LUMID

Design of the Lunar Micrometeoroid Impact Detector

C.C. Brunt	4307372	M. Misin	4275004
B. van Dam	4220889	P.S. Sengalrayan	4206525
H. Frericks	4301102	A.F. Vandenberghe	4274075
A. Karagiannis	4280164	J. Vanwesenbeeck	4189299
T. Koppenaal	4143396	J.M. Westenberger	4233425
B. Krijnen	4232143		

Final Report

Design Synthesis Exercise

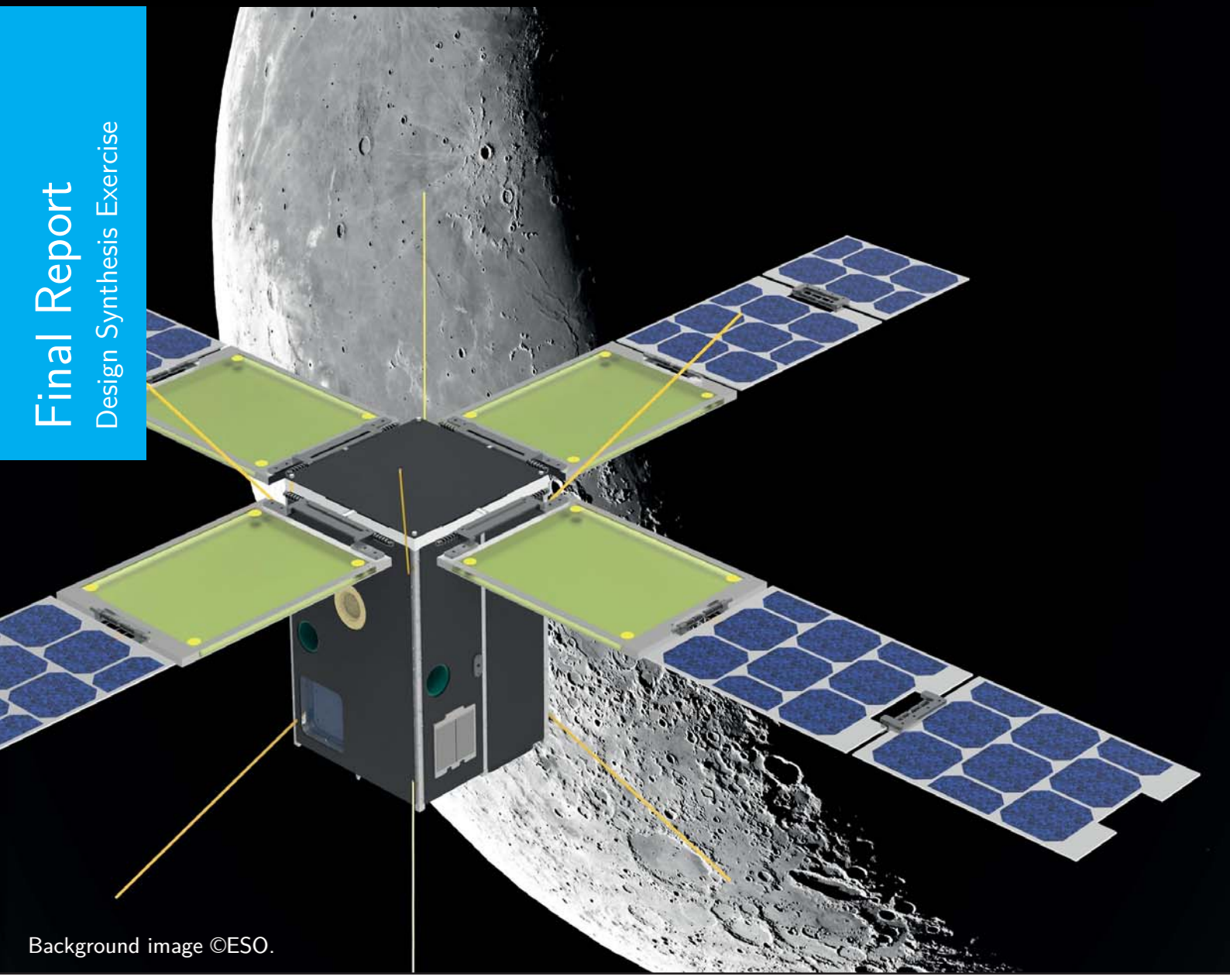

TU Delft Delft University of Technology

Aerospace Engineering

January 31, 2017

(This page is intentionally left blank.)

TU Delft Delft University of Technology

LUMID

by

C.C. Brunt, B. van Dam, H. Frericks, A. Karagiannis, T. Koppenaal, B. Krijnen, M. Misin, P.S. Sengalrayan, A.F. Vandenberghe, J. Vanwesenbeeck, J.M. Westenberger

Supervisors: Ir. P.P. Sundaramoorthy — Space Systems Engineering
Dr. G.A. Bohlin — Flight Performance and Propulsion
Ir. J. Geul — Astrodynamics and Space Missions

Version	Date	Pages Affected	Brief Description
1.0	January 23, 2017	All pages	Draft Version
1.1	January 24, 2017	All pages	Spelling checks and general quality control
1.2	January 25, 2017	All pages	Major changes in CH2-CH4, CH14. Changes of the design reflected in all subsystems.
1.3	January 31, 2017	All pages	Implemented supervisors' feedback.

Preface

This report is the fourth in a series written by the LUMID design group for the fall 2016 “MoonSat” Design Synthesis Exercise. The group consists of eleven bachelor students from the faculty of Aerospace Engineering at the Delft University of Technology. During the past ten weeks, the effort got us to the point where we can proudly present this design.

We would like to extend our greatest gratitude to the group’s tutors; ir. Prem Sundaramoorthy, dr. Alexis Bohlin and ir. Jacco Geul, for guiding us through this project in pursuit of a successful result. We would also like to thank all other PhD students and academic staff on whom we could rely for providing us with inputs and feedback during this project. Lastly we want to address you, the reader, and wish you a pleasant reading.

Delft, January 2017

Contents

List of Abbreviations

Abbr.	Description	Abbr.	Description
2SID	2-Stage Impact Detector	LO	Lunar Orbiter
ADCS	Attitude Determination & Control System	LPA	Low Pressure Assembly
AOCS	Attitude & Orbit Control System	LRO	Lunar Reconnaissance Orbiter
AOP	Argument of Periapsis	LUMID	LUnar Micromicrometeoroid Impact Detector
AU	Astronomic Unit	MM	Micrometeoroid
BER	Bit Error Rate	MMI	Micrometeoroid Impact
BOL	Begin of Life	MMOI	Mass Moment of Inertia
BPSK	Binary Phase Shift Keying	MOI	Moment of inertia
CAD	Computer-Aided Design	MOQ	Minimum Order Quantity
CDHS	Command & Data Handling System	NASA	National Aeronautics and Space Administration
CMG	Control Moment Gyroscope	NEI	Noise Effective Irradiance
c.o.m.	Centre of mass	PLS	Payload
COTS	Commercial Off-The-Shelf	PPU	Power Processing Unit
CR	Contrast Ratio	PROP	Propulsion
DC	Direct Current	PCB	Printed Circuit Board
DMIPS	Dhrystone Mega-Instructions Per Second	qe	Quantum efficiency
DOD	Depth of Discharge	q_{max}	Maximum aerodynamic pressure
DOT	Design Option Tree	RAAN	Right Ascension of the Ascending Node
EDAC	Error Detection and Correction	RAMS	Reliability, Availability, Maintainability and Safety
EMI	Electromagnetic Interference	s/c	Spacecraft
EOL	End-of-Life	RSS	Root Sum Square
EPS	Electrical Power System	SEE	Single Event Effect
ESA	European Space Agency	SF	Solar Flux
EU	European Union	SLOC	Source line of code
FEA	Finite Element Analysis	SMAD	Space mission analysis and design
GEO	Geosynchronous Equatorial Orbit	SNR	Signal to Noise Ratio
GMAT	General Mission Analysis Tool	STR	Structures
GNCS	Guidance Navigation and Control System	TA	True Anomaly
HPA	High Pressure Assembly	TC	Thermal Control
HVPS	High Voltage Power Supply	TID	Thermal Imaging Device
IR	Infrared	TRL	Technology Readiness Level
ISIS	Innovative Solutions in Space	TTC	Telemetry, Tracking & Command
ISL	Inter-Satellite Link	UHF	Ultra High Frequency
IPS	Instructions per Second	WBS	Work Breakdown Structure
LEO	Low Earth Orbit	WFD	Work Flow Diagram
WOD	Whole Orbit Data		

List of Symbols

Symbol	Description	Unit
A_S	Solar radiated area	m^2
A_{Ss}	Solar radiated area side surface	m^2
A_{Su}	Solar radiated area upper surface	m^2
A_{cell}	Solar cell area	m^2
C	Charge	C
c	Speed of light in vacuum	m/s
$c_{ps} - c_m$	Solar radiation pressure arm	m
$Delta - v$	Delta-v	m/s
d	Diameter	m
e	Specific energy	J/kg
e^-	Number of electrons	[-]
E	Kinetic energy	J
E_B	Battery-stored energy	J
f	Frequency	Hz
f^{-1}	Period	s
F_{sr}	Solar radiation perturbation	μN
F_{ext}	External forces and perturbations	μN
$F(m)$	Number of meteoroids	$1/m^2$
g_0	Gravity acceleration of Earth	m/s^2
g	Gravitational force	N
g	Gravitational acceleration of orbited body	m^2/s
G	Gravitational constant	$m^3/(kgs^2)$
h	Altitude	km
h_p	Planck's constant	m^2kg/s
H	Momentum	Nm
H_{tot}	Total momentum	Nm
i	Inclination	°
I	Mass moment of inertia	kgm^2
I_{tot}	Total impulse	Ns
I_{ne}	Total impulse needed to dump momentum	Ns
I_{sp}	Specific impulse	s
I_{ssp}	System specific impulse	s
J_{sun}	Solar irradiance	W/m^2
J_{th}	Thermal flux	W/m^2
J_2	Oblateness effect constant	[-]
k_g	Boltzmann constant	$m^2/(kgs^2K)$
l	Length	m
L	Momentum arm	m
L	Life degradation	[-]
L_{impact}	Power flux per wavelength	W/m^3
m	Mass	kg
m_0	Starting mass	kg
m_b	Expelled mass	kg
m_{dry}	Dry mass	kg
m_e	Empty Mass	kg
m_{EI}	Mass of the electrical power system (PROP)	kg
m_f	Final mass	kg
m_i	Initial mass	kg
m_p	Propellant mass	kg
m_t	Tank mass	kg
m_T	Thruster mass	kg
m_{wet}	Wet mass	kg

n	Number of components	[-]
$p_s r$	Solar radiation pressure	N/m^2
P	Power	W
P_{sci}	Used power during the science phase	W
P_{sun}	Used power during power generation phase	W
P_{man}	Used power during the manoeuvre phase	W
P_{impact}	Impact power	W
P_{noise}	Noise power	W
P_c	Critical storage pressure	Pa
P_{tot}	Total power	W
P_u	Average used power	W
P_d	Average delivered power	W
P_g	Average generated power	W
P_m	Maximum available power	W
q	Reflectance factor	[-]
r	Position vector of s/c	[-]
r_s	Radius of the spherical tank	mm
R	Distance s/c and centre of orbited body	km
R_{total}	Total reliability	[-]
$R_{parallel}$	Parallel reliability	[-]
S	Total data storage	Gb
SF	Solar flux	W/m^2
t	Time	s
$True_a g$	True anomaly at the begin of an eclipse	rad
$True_a h$	True anomaly at the end of an eclipse	rad
t_a	Begin time of slew manoeuvre 1	s
t_b	Begin time of slew manoeuvre 2	s
t_c	Begin time of burn time	s
t_d	End time of burn time	s
t_e	Begin time of slew manoeuvre 3	s
t_f	Begin time of slew manoeuvre 4	s
t_g	Begin time of eclipse	s
t_h	End time of eclipse	s
t_{exp}	Exposure time	s
t_{impact}	Impact time	s
t_m	Mission time	s
T_s	Thickness of the spherical tank	m
t_{wcs}	Worst case slew manoeuvre time	s
T	Temperature	°C
T_f	Thrust	μN
Tt	Torque	Nm
Tt_{gg}	Gravity gradient torque	Pa
Tt_{sp}	Solar radiation torque	Pa
U	Electric potential	V
U_d	Energy density	J/m^3
v	Velocity	km/s
v_{error}	Velocity error	km/s
V_{eq}	Equivalent exhaust velocity	km/s
V	Volume	m^3
α	Angular acceleration	rad/s^2
α_i	In orbit plane incidence angle	°
β	Beta angle	rad
β_i	Out of orbit plane incidence angle	°
γ	Burn direction angle	°
δh	Momentum change	Nms
ϵ	Emissivity	[-]
ϵ_{be}	Battery charge and discharge efficiency	[-]
ϵ_{pm}	Power management and conversion efficiency	[-]

η_{BOL}	Solar cell begin of life efficiency	[-]
η_{charge}	Charge efficiency	[-]
θ	True anomaly	°
θ_i	Impact angle	°
ϑ	Max. angle between local vertical and z-axis	°
κ	Radiation focused on chip	[-]
λ	Wavelength	m
μ	Standard gravitational parameter	m^3/s^2
ρ	Density	kg/m^3
ρ_p	Density of the projectile	kg/m^3
ρ_{prop}	Density of the propellant	kg/m^3
ρ_t	Density of target bulk	kg/m^3
σ_y	Yield strength	Pa
τ	Orbit period	s
τ_{sun}	Time in sun	s
ω	Argument of periapsis	°
Ω	Right ascension of the ascending node	°

Summary

Ambitious plans for a near-future human colony on the Moon are currently impeded by a lack of understanding of various aspects of the Lunar environment. The LUMID (LUnar Micrometeoroid Impact Detector) mission aims to cast light upon one of these aspects: it uses three CubeSats to characterise the flux of impacts on the lunar surface by micrometeoroids (MM) in the mass range of smaller than 1 g. Reaching the surface with energies exceeding those of bullets, they are capable of catastrophic damage to ground assets and even personnel. The quantification of the involved hazards is, therefore, a necessary stepping stone for future missions.

The concept employs a commercially available remote sensing thermal imaging camera to capture the heat radiated upon a MM impact as main payload, supplemented by a series of in-situ 2-stage Impact Detectors to measure the strikes of MM on the spacecraft (s/c) itself. The camera is only effective at a low altitude and when on the night side, constraining the orbital periapsis on that side. Observations will be limited to characterising the MM hazards within the $\pm 50°$ latitudes, motivated by the abundant presence of potential future landing and settlement sites in this region. Aimed for deployment in late 2019, it will use its 2-year mission to detect impacts of MM as small as 2.6 mg on-surface and 7.72×10^{-15} g in-situ, over a total time-area product of roughly 1.8 billion km^2s, before it is crashed on the surface in early 2022.

The s/c are piggybacking the mission of a larger Lunar Orbiter, intended as a relay and support station. Deployed at a 500 km circular orbit, it uses a series of low-thrust finite burns over 110 days to descend to its operational periapsis x apoapsis elliptical orbit of 15×300 km , at an inclination of 50°, with an orbit period of 123 min. The Lunar Orbiter itself is at a 800×8000 km orbit at an assumed inclination of 86°, raising an average available total contact time of 706 s per orbit. The LUMID s/c will perform one station-keeping manoeuvre per orbital revolution to maintain operational orbit. The mission will conclude with a controlled impact on the surface, induced by another series of finite burns over roughly 2 days, raising a total mission Δv budget of 679.25 m/s over the mission duration, including a 30 % contingency factor.

The Command and Data Handling system uses a quad-core radiation hardened processor, benchmarked at a throughput of 1.06×10^3 DMIPS and 3 SD cards for a redundant and fault-tolerant 2 GB of storage. Flight software and the scientific data processing software are used, to account for s/c functionality and payload data processing, respectively.

Telemetry, Tracking and Command is achieved by virtue of two turnstile antennas at a frequency range of 130 MHz to 500 MHz with a bandwidth of 10 MHz to 13 MHz. The total contact time during the first 27 days of orbit data is approximately 2.61 days, roughly 10 % of the total 27 days.

A total of four reaction wheels in pyramidal configuration, two 0.01 N cold-gas thruster units, eight sun sensors distributed over the top and bottom corners of the s/c and three star trackers compile LUMID's Attitude and Orbit Control system, capable of providing 3-axis stabilisation, slew manoeuvre management and guidance/navigation at any point of operation. A maximum pointing accuracy of 10 arcsec is achieved. Every set of sensors/actuators has accounted for redundancy in its number of components.

The propulsion system uses two commercially available gridded ion thrusters, with a thrust of 1.4 mN and an I_{sp} of 3500 s at 0.39 kg of Xenon propellant stored in a spherical Aluminium tank with radius of 40.47 mm and wall thickness of 2.58 mm. The two thrusters will never operate simultaneously and are placed opposite to each other to relieve the workload of the AOCS system and for redundancy.

For electrical power provision, a set of 4 longitudinally spring-deployable, rotatable (about their longitudinal axis) solar panels with a 0.257 m^2 effective area are placed in a cross-shape, coplanar configuration at the top of the CubeSat. The panels are capable of providing a maximum of 95 W at the beginning of life, with an assumed decay rate of 1.1 %. Three 12-cell Li-Ion batteries, with a 53.2 Whr storage each are employed, one for redundancy.

For achieving Thermal Control of the s/c a 1mm kapton film with silver-aluminium oxide overcoating, coupled with a 7.5×7.5 cm, high emissivity radiator are employed to maintain the s/c subsystems within their 279 K to 307 K temperature range. Additionally, a 20W electrical resistance heater protects the systems during the freezing temperatures of the deployment phase, together with a 5 W heater for the mini-thrusters only.

All aforementioned subsystems are distributed within the $246 \times 246 \times 366$ cm structure, in turn encompassed within aluminium-plate radiation shields. Extra radiation packaging protects the inner electronic systems. Finite element models have guaranteed the s/c structures and mechanisms' integrity against all expected loads and vibrations.

The mass and power budgets of every subsystem are summarised in the table 3.

Table 3: LUMID mass and power budget (per s/c)

Subsystem	**Mass Budget [kg]**	**Power Budget [W]**
PLS	1.893	4.20
CDHS	1.030	8.00
TTCS	0.200	2.04
AOCS	3.532	4.53
PROP	1.686	107.14
EPS	2.523	n/a
STR	5.500	-
TCS	1.730	25.00
Total:	**18.094**	**150.91**

The LUMID mission is projected to find its place in the rapidly growing CubeSat market, drawing from the abundant commercial availability of its components, its increased reliability and significantly lower cost. It aims to help in the endeavour of the nanosatellite concept to occupy a large portion of the space market in the coming decades. LUMID's return of investment stems from the scientific data value, the demonstration of state-of-the-art nanosatellite technologies and the establishment of CubeSat's potential for interplanetary missions.

Lastly, the mission uses the highly flexible modularity of its composure, the green propulsion systems encompassed, the piggyback deployment concept and a no-orbital-debris end-of-life approach to secure a long-term sustainable realisation of its mission.

CHAPTER 1

Introduction

Decades after the last man stood on the Moon, the plans for further human exploration and colonisation have been brought up by space agencies like ESA [1] and NASA [2]. Being Earth's closest celestial body, the Moon offers an excellent platform for developing and refining the scientific knowledge and technology that will open new paths in human exploration of the solar system and beyond. At the same time, the space sector is turning its attention to the principles of miniaturisation and distributed space systems, as a promising alternative to the often prohibitive costs of today's missions. The off-the-shelf composition of CubeSats® offers admirable reliability and functionality, but at a fraction of the size and, most importantly, the cost of current s/c. This concept of standardised nanosatellites has come to stay and as their potential for space missions continues to impress, the space market is shifting its attention on their appreciable prospects for profit. The amount of nanosatellites that will be launched in the upcoming years increases rapidly due to the aforementioned opportunities. The announced launches can be seen in the figure below. One of the major upcoming events scheduled in 2017 is the launch of 89 nanosatellites on February 13th with main influence from Planet Labs. [3]. In an attempt to merge these trends into an innovative concept, the current document presents the design of the LUMID mission, a CubeSat® system to assist in the exploration of the Moon. Among the vast array of opportunities for research, the concept focuses on characterising one of lunar missions' most formidable threats: the impacts of micro-meteoroids on the Lunar surface. These minuscule fragments of rock, often of size so small as is barely visible with the naked eye, can accumulate enough kinetic energy to deliver the equivalent strike of a .22 caliber bullet upon impact [4]. Characterising their flux, impact velocities and physical properties is instrumental in protecting future assets on the lunar surface and this is where the LUMID mission fits in the picture. The background of Lunar MMs is further elaborated in section 2.1.Additionally, the effects of the deep space environment on CubeSats® will be further characterised and its capacity for near-Earth interplanetary scientific missions will be demonstrated. The subsequent chapters will guide the reader through the mission set-up, s/c hardware design and auxiliary aspects of the design, in pursuit of providing a complete image on the capacity of the proposed concept.The structure of the document follows the steps of the design process, starting with the mission and trajectory designs in chapters 2 and 3, respectively.The design of every subsystem of the s/c start with a global analysis in chapter 4, followed by a detailed analysis in chapters. 5-12. The system performance is assessed in chapter 13, before chapter 14 outlines the post-design phase. The report concludes in chapter 15 with conclusions and recommendations for further development.

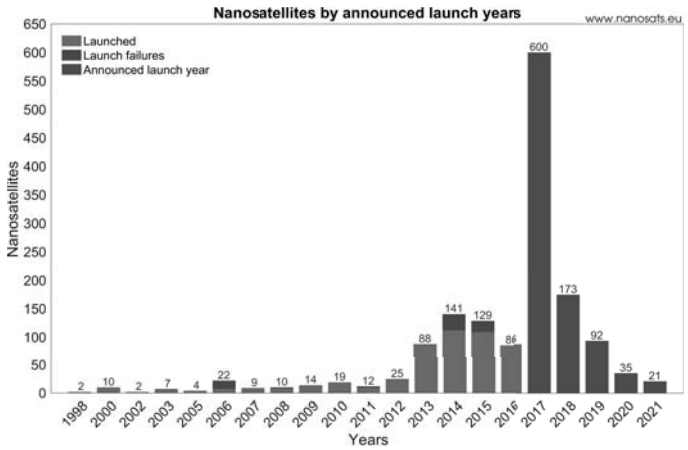

CHAPTER 2

Mission Considerations

This chapter aims to offer a brief, albeit comprehensive overview over the main aspects of the space mission proposed in this document. Much of the information presented below is elaborated in greater depth in subsequent chapters (the reader is referred to, accordingly). However, the following lines focus mostly on the "soft", mission-related aspects of the design, rather than the trajectory and hardware specifications.

The mission comes with a set of predefined requirements, which are listed and described table A.1 in appendix A.

2.1 Background on Lunar Micrometeoroids

Interest in the flux of micrometeoroids (MMs) on the lunar surface gained momentum in the late 1960s, when research conducted by Pettersson [5] estimated the amount of cosmic dust descending on the Earth in the order of several million tons/year, implying that comparable amounts would reach the lunar surface. As the plans for a mission to the Moon had just started to take shape, Pettersson's results sparked concerns about the potential issues these tiny rocks would impose.

A number of space missions were used to subsequently characterise this phenomenon. Observations in both the near-Earth and the lunar environments, by the "Pegasus" and "Surveyor" programmes respectively, disproved the estimations and showed that the actual flux of MMs on the Moon was much lower, in the order 10 000 tons/year to 20 000 tons/year [6].

Samples returned by the Apollo missions offered an even deeper insight into the matter. The samples featured large numbers of microscopic cavities, referred to as "zap pits", results of the intense MM shelling of their past. The samples allowed scientists to extract a number of conclusions on the flux of micrometeroids and their evolution over time. [7]

Since the completion of the Apollo programmes, a number of statistical models have been developed aiming to provide an ever improving estimation of the flux of these small fragments on the lunar surface. The downside of virtually all models is the large factor of uncertainty involved and it is not uncommon for new research to emerge only to disprove the conclusions of its predecessors. It was only in 2016 that a team of NASA scientists used data extracted from the LRO over seven years to deduce that the flux of meteors is at least 33% larger than previously estimated [8].

It follows that despite decades of efforts, the flux of micrometeoroid impacts (MMIs) on the lunar surface is still poorly characterised. Given the catastrophic force these minuscule particles can inflict upon a target on impact, this deficiency is a major drawback in the pursuit of protecting future long-term mission and assets on the surface or local environment. Characterising the related hazards is, in fact, one of ESA's top priority objectives for the exploration of the Moon [1].

In this spirit, the LUMID mission serves to fill the gap by providing the most comprehensive study to date into the matter. And in doing so, it further aspires to establish the potential of nanosatellites for low-cost, sustainable interplanetary missions.

2.2 Objectives

The objectives of the mission draw from three main areas where room for innovation is abundant: the emerging CubeSat® market, the scientific benefits in exploring the lunar MM phenomenon and the eager interest in characterising the capacity of nanosatellites for interplanetary missions. On these grounds, the objectives of the mission are established as listed below:

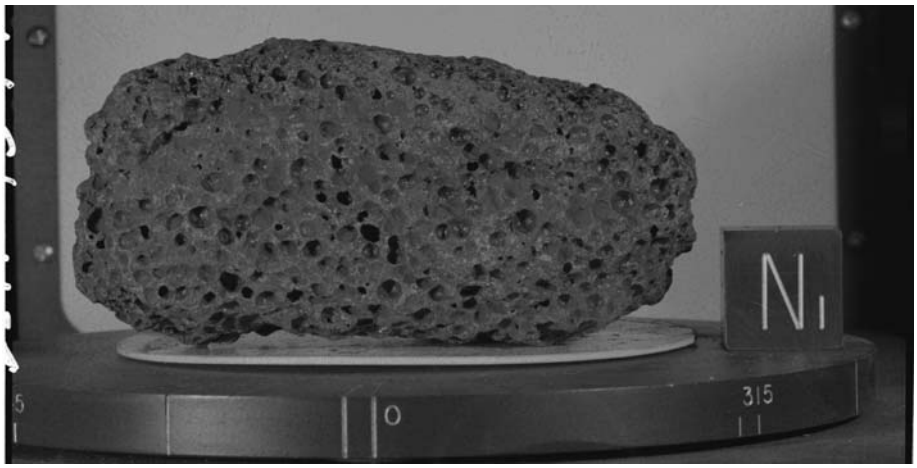

Figure 2.1: Lunar basalt sample collected during the Apollo programme, bearing numerous “zap pits” by MMIs (Photo by: Smithsonian museum, [9])

1. To support human exploration of the Moon by characterising the flux of micrometeoroids on the lunar surface and in low-lunar orbit
2. To demonstrate the capacity of CubeSats® for near-Earth interplanetary scientific missions, at a reduced cost compared to mainstream size satellites
3. To further characterise the effects of the deep space environment on CubeSats®

2.3 Mission Overview

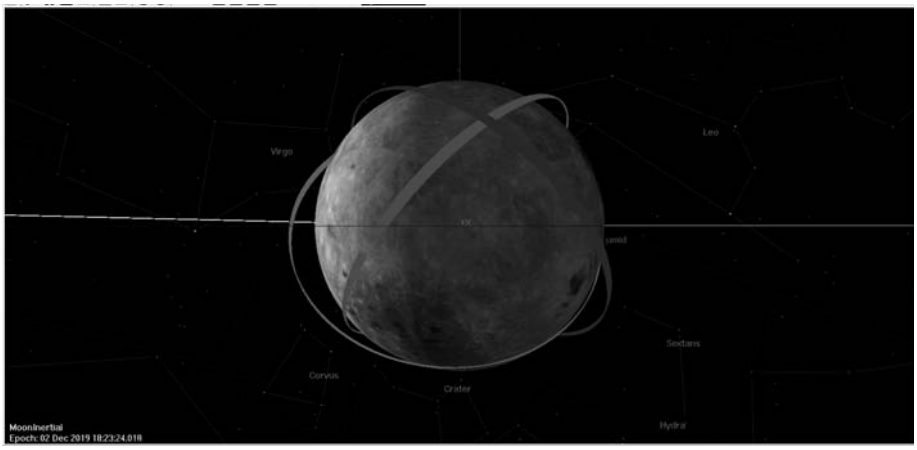

Figure 2.2: Example overview of the trajectories of the three CubeSat® in orbit around the Moon

The LUMID mission concerns the deployment of three CubeSats® in a low elliptical orbit around the Moon. The s/c will travel as a piggyback to a non-defined future lunar mission of a larger orbiter, referred to as a “Lunar Orbiter”, which will function as a relay and support unit for the CubeSats®.

Each s/c will bear a thermal imaging camera and use its time on the night side of the Moon to capture the thermal flashes created by a MM upon impact. The payload can detect smaller impacts at a lower altitude. It detects these flashes when they make a strong contrast to the darkness of the Moon’s night side. This imposes a stringent requirement for the periapsis to be on this side. This proved inconveniently hard to time for a single unit, therefore three satellites will be positioned at the same orbit but different starting positions, to ensure a larger coverage and to ensure that at much larger fraction of the time at least one of the satellites has its periapsis in the night side.

In addition, the s/c are equipped with a number of in-situ impact detectors, to extract information such as the trajectory and velocity components of micrometeroids in the vicinity of the s/c's orbital position.

It is currently estimated that impacts of micrometeroids of mass as small as 2.6 mg will be detectable on the ground and of 7.72×10^{-15} g on the s/c itself. It is expected that over the two year duration of the mission, a total area-time product of 1.8 billion km^2s (see chapter 5) will be covered. As such the observations made are expected to be sufficient to significantly improve the existing statistical models on the matter and shed light upon these otherwise inconclusive estimations.

No requirements have been set regarding the launch dates, launcher vehicles or mission start epochs. Still, in accordance with ESA's aspirations for the establishment of a lunar base within the next decade [10], the current plans aim at deploying the CubeSat® in operational orbit (see figure 2.2 in late 2019, with the mission concluding in early 2022.

Further elaboration on all the matters involved in the mission design is given in the subsequent chapters.

2.3.1 Lunar Region of Interest - Orbit Inclination

While a number of constraints on the orbit configuration where imposed by other subsystems (e.g. payload, power subsystem, etc), a major point of research regarded the inclination which would best suit this mission. A large number of candidates arose, but the absence of relevant constraints or requirements obscured the lines that would define an appropriate from an inappropriate orbit.

For example, a polar orbit, a highly popular choice for lunar orbiters to this date, offers global coverage, as well as superior illumination and contact-time conditions. Yet, it is less stable than orbits in lower inclinations. Furthermore, this is an orbit where both current and future missions are targeted (e.g. LRO and Lunar Flashlight respectively [11, 12]), which would then raise the necessity to examine the possibility of collisions or interferences. On the other hand, orbits at 86° or lower appear to have superior stability characteristics when configured properly, however the total ground coverage is not as high and illumination conditions not as favourable.

No strong arguments could be found to favour one orbit configuration over another. Also, there is no strong evidence in existing literature to suggest that certain regions of the Moon are bombarded with higher intensity than others by the MMs and, thus, would be a deciding factor in choosing an inclination.

Eventually, the criterion came down to what the designers regarded as an observation region of interest. Literature study indicated that the region of the Moon confined between the ± 50 latitudes are of increased scientific interest. The region appears to contain the majority of observed lunar pits and suspected lava tubes (see figure 2.3). These are large sub-surface cavities, assumed to have been created in the Moon's primordial past, when volcanic activity was still present. Today, they are regarded as strong candidates as future landing sites and areas for human settlements [13]. These tubes are assumed to be as large as 300 m in diameter and covered beneath 40 m or more of basaltic material [14]. This means they would be capable of providing a human settlement with a hospitable thermal environment of $-20°C$, protection from cosmic radiation and shielding from meteor impacts [15]. Furthermore, they appear to remain unaffected by the extreme temperature variations on the lunar surface and abound with mineral resources [16].

As such, the design team concluded that future lunar landing/settlement missions are highly likely to focus their efforts and resources within this region. Coincidentally, this appears to be a region of superior orbital stability performance, one of the frozen orbits. On the grounds of the above information, it was decided to place the LUMID s/c at a 50° inclination, so that the results of the mission could assist future designers in characterising the micrometeroid hazards to be expected in their endeavours.

As a final remark, one could argue that the deployment of multiple satellites in different inclinations is also an option, so that various lunar regions can be scanned at the same timeframe. This is indeed true, however the limited time and computational resources allocated for the development of the design treated here has not allowed room for exploring these options in depth. Possible com-

plications such as timing and coordination of the s/c, transmission time allocation, station-keeping requirements at different inclinations, resources required on the ground station on Earth for the simultaneous monitoring of the s/c at the different operating conditions etc, demand for a thorough investigation, which is beyond the capacities of the current design process.

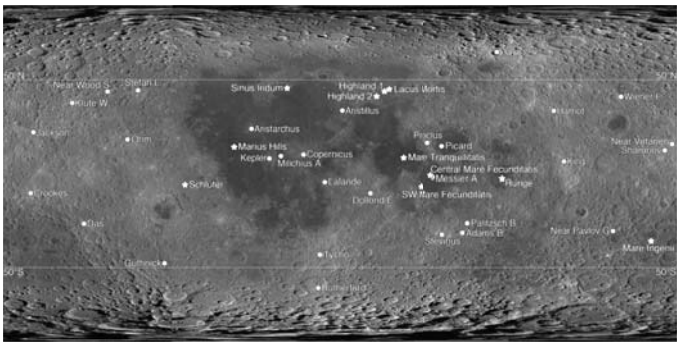

Figure 2.3: Location of (suspected) lava tubes across the lunar surface [17]

2.4 Mission and Operations Design

Orbit insertion By the project definition, the s/c will be realised at a 500 km circular orbit. It will then use a series of finite burn manoeuvres over a 113 day period to descent to its nominal operational orbit, an elliptic trajectory with its periapsis at 15 km and its apoapsis at 300 km. The total Δv cost of the manoeuvre is currently predicted at 155 m/s.

Upon release, the s/c will enter into the so-called "recovery mode". This mode is used to recover the s/c from its tumbling condition after ejection from the deployment dispenser, and instate it to its nominal state. The AOCS is responsible for this operation.

Payload Operations The concept employs a commercially available remote-sensing thermal imaging camera to capture the heat radiated upon a MM impact. This is supplemented by a series of in-situ 2-stage Impact Detectors, as secondary payloads, to measure the strikes of MM on the spacecraft (s/c) itself and extract data on their velocity components and trajectory.

The camera itself makes use of the stark heat difference caused by the tiny flashes against the cold lunar surface, therefore it is only effective at a low altitude (<40 km) and only when on the night side, constraining the orbital periapsis on that side. Observations will be limited to characterising the MM hazards within the $\pm 50°$ latitudes, motivated by the abundant presence of potential future landing and settlement sites in this region, as explained previously.

The payload will use its two year mission to detect impacts of MM as small as 2.6 mg on-surface and 7.72×10^{15} g in-situ, over a total time-area product of roughly 1.8×10^9 km^{2}s, before it is crashed on the surface in early 2022.

Attitude Control and Navigation The AOCS facilitates 3-axis stabilised control throughout the mission, as well as navigation for orbit determination. The attitude control subsystem consists of (excluding redundant components) 4 sun sensors, 2 star trackers, 3 reaction wheels, and 1 cold-gas thruster unit.

The star trackers employ an on-board star catalogue to match the patterns observed in flight, to precisely determine the inertial attitude of the s/c. The measurement is supplemented by the sun sensors' determination of the sun location. The sun sensors are also able to determine the direction to the Sun in case of a star tracker failure, to orient the solar panels and ensure power provision. All attitude changes are facilitated by the reaction wheels, however the accumulation of angular momentum necessitates the operation of the cold-gas thruster unit once every roughly 5 days for de-saturation.

No conclusive design decision has been made on the Guidance and Navigation subsystem. The dominant current concept concerns the employment of the Iris V2 CubeSat® Deep Space Transponder, developed by NASA's Jet Propulsion Laboratory. Similarly to the arrangement used for NASA's INSPIRE mission, two pairs of patch antennas, one for reception and one for transmission, will be placed on the top and bottom face of the s/c, respectively, so that two roughly hemispherical views of the sky can be obtained, offering communications from any s/c orientation. Communication for navigation will take place directly between the s/c and the ground station on Earth. Computations have indicated that the link budget closes for the data rate required, assuming that the Deep Space Networks 32m antenna is used on the ground. [18]

Power Handling For electrical power provision, a set of 4 longitudinally spring-deployable, rotatable (about their longitudinal axis) solar panels with a 0.257 m^2 effective area are placed in a cross-shape, coplanar configuration at the top of the CubeSat®. The panels are capable of providing a maximum of 136 W at the beginning of life, with an assumed decay rate of 3.6 %. Three 12-cell Li-Ion batteries, with a 53.2 Wh storage each are employed, one for redundancy.

Thermal Control For achieving Thermal Control of the s/c a 1 mm Kapton Film with silver-Aluminium Oxide overcoating, coupled with a 7.5 x 7.5 cm, high emissivity radiator are employed to maintain the s/c subsystems within their 279 K to 307 K temperature range. Additionally, a 20 W electrical resistance heater protects the systems during the freezing temperatures of the deployment phase, together with a 5 W heater for the mini-thrusters only.

Command and Data Handling The Command and Data Handling system uses a quad-core radiation hardened and radiation tolerant processor, benchmarked at an SoC of 1.06×10^3 DMIPS and 3 SD cards for 6 GB of triple redundant storage. A flight software and the scientific data processing software are included, to account for s/c functionality and payload data processing, respectively.

Telecommunications Telecommunications are achieved by virtue of two turnstile antennas at a frequency range of 130 MHz to 500 MHz. They are capable of transmitting data at a maximum of 24 kbit/s, within roughly 10 % of the orbital period.

Station Keeping Lunar orbits can be defined by the evolution of their eccentricity and argument of periapsis over time. The Moon's irregular gravity field significantly perturbs these two parameters. In absence of station keeping, these perturbations would cause the s/c to hit the lunar surface within roughly 6 days (worst case simulated scenario). [11, 19]

The LUMID station-keeping strategy is to perform one finite burn, centred about the apoapsis, on every orbital revolution, to correct for the deviation of the periapsis. The operational orbit and manoeuvre are configured such that the apoapsis requires no corrections, mainly due to the fact that its deviation always stays within acceptable margins. The maximum burn duration as a fraction of the orbit is currently estimated at 36%, corresponding to about 182 m/s per year. A far more in-depth elaboration is presented in chapter 3. The fuel quantity amounts to roughly 0.4 kg. All manoeuvres are delivered by a low-thrust, gridded ion thruster.

End-of-life Operations Once the decision has been taken to decommission the s/c, its thruster will use the remaining propellant for a final series of finite burns, leading the CubeSat® to crash on the Lunar surface. The manoeuvre will closely resemble spiral descent to the surface and allows for a controllable impact, in the sense that the final location can be selected and targeted. Simulations conducted have shown this final impact location to be highly sensitive to the initial conditions (start epoch of the manoeuvre and a number of orbital parameters, such the argument of apoapsis and latitude of the ascending node), therefore the relevant decision is projected to be made at a later stage of the development process or even during the mission itself.

From a scientific point of view, the crash could be used by the Lunar Orbiter for a number of observations. For example, it could study the composition of the plume ejected from the regolith following impact, similarly to the NASA Lunar CROSS mission [20]. Alternatively, it could use the dispersed area of fragments to estimate the size of some geological feature, similarly to for the same mission. A large array of possibilities exist, but in absence of any information on the nature/configuration of the orbiter, these options cannot be explored. They are left for a subsequent stage of the analysis.

Possible Mission Extension Currently, no considerations for a mission extension has been included in the design. While contingency factors have been included in the design of all subsystems, these are to account for anomalies and unexpected circumstances, rather than a prolonged mission. The designers have estimated that:

- The two year mission duration will provide enough data for an extrapolation of the observations and an extension of the mission
- The limited-scope science payload on board (only MM impact detectors) would mean that little scientific interest would stem from an extension of the mission. Any extra observations made would be directly analogous to the ones performed over the preceding two years, with little, if any, additional data of intriguing scientific value

The room for extended the mission further, if so it is decided later in the development process, is there. The design treated in this document indicated that mass/power/Δv budgets are relatively simple to adjust upwards to provide for an extended mission duration. Still, due to limited time and resources, such prospects have not been explored here.

2.5 Mission Timeline

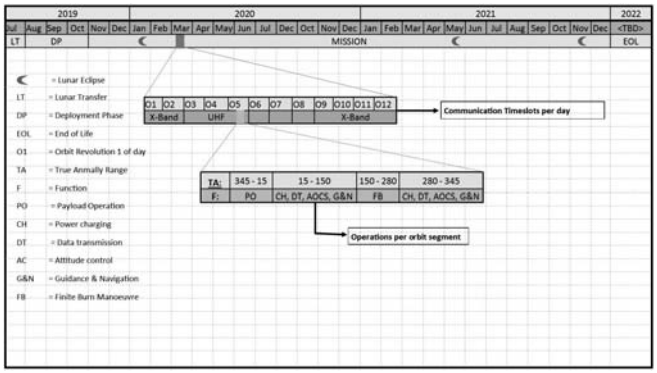

Figure 2.4: Simplified example overview of the LUMID mission timeline

The definition of the sequence which the various phase of the LUMID phase will follow is a continuously iterative process that is not limited to the current design process but is instead expected to continue until the very last phases of the s/c's flight certification.

Early in the sizing process of the EPS, it became apparent that it would not be possible to have all subsystems functioning simultaneously. For example, when the energy-devouring thrusters will have to be activated for station-keeping manoeuvres, other systems have to be shut down or put in idle mode, due to lack of available power. Similarly, some subsystems have specific time slots within they need to operate. A characteristic example is that of the thermal imaging instrument, which is only effective when there surface is on the night side. As such, the various subsystems imposed requirements and constraints calling for the segmentation of operations and the definition of a fixed timeline for each.

This timeline has been defined in three different levels. The first concerns the entire mission duration and regards phases such as deployment, science mission etc. The second delves into more

detail, outlining the sequence of operation over a single orbital evolution. The final one covers the more rare occurrences of a lunar eclipse and insertion into a safe mode.

Figure 2.4 offers a simplified version of the mission timeline. The main mission phases have been split over the duration of the mission. A randomly selected day in March 2020 has been selected and broken down into the orbital revolutions during the day, and the communication time slots during the day are shown. It is to be noted that these have been indicated in a randomly defined basis, as the exact operational conditions on the date itself cannot be known so far in advance. Subsequently, the 5th orbital revolution on that day has been broken into the defined segments and the operations conducted per phase are shown.

2.5.1 Timeline over the Mission Duration

It is given by the project description that the transfer from the moment of launch to the moment of injection to the 500 km orbit lasts one month. Furthermore, simulations have shown that roughly 113 days are needed for the descend from this deployment to the operational orbit.

Since no requirements or constraints whatsoever are giver regarding the launch epoch or mission execution, it was decided to use the following as a concept for demonstration of a potential mission: The s/c is deployed at an epoch such that it is already in operational orbit when the Geminids meteor shower takes place in late 2019. The event is projected to peak on December 13-14, 2019. Given considerations for post-deployment operations and the necessity for some contingency in this transfer period, it was decided to set the epoch for simulations on November 22, 2019. When deployed on this date, at least one of the LUMID s/c will find itself with its periapsis on the night side on December 13. This, in turn would mean that release from the carrier Lunar Orbiter would take place at approximately the final week of July 2019.

Subsequently, upon attaining nominal orbit, the s/c is simulated for another two years, before the decommissioning phase starts in early 2022. The exact epochs or sequences have not been set for this phase since the uncertainty in the eventual evolution of the mission is too high to make allow safe predictions. Still, given no extension of mission has been accounted for and the budgets have been sized for the two year duration, it is estimated that the mission will be forced into its conclusive phase at approximately January 2022.

2.5.2 Timeline over an Orbital Revolution

The main payload requires to be active during the passage from the periapsis, assuming that the periapsis is positioned in the night side. When this is not the case, no effective observations are possible and therefore the s/c can deactivate the instrument and focus on other operations, such as data transmission or on-board data processing. The 2SID can and is planned to remain active at all times, so that possible impacts on the CubeSat® itself can be detected at any instant.

A second major operation regards station-keeping. The current mission design predicts on finite burn centred about the apoapsis on every orbital revolution, to prevent the s/c from being pushed into a non-recoverable orbit by the irregular gravity field. The thruster therefore needs to be activated at the same time as the AOCS (which controls the thrust direction) and it is to be taken into account for power and thermal management requirements.

A further important operations concerns the transmission of observation and system maintenance data to the Lunar Orbiter. The antennas used are non-directional and the involved subsystems have been designed to support their function at any time, therefore no constraints are imposed on the timing of data transmission.

Lastly, the s/c needs to orient its solar panels towards the Sun for energy provision. As explained in chapter 10, the panels are mounted on a rotatable mechanism at their end, providing the capacity to orient them towards the Sun with minimal requirements from the AOCS. In chapters 10 and 12 it is explained that the two subsystems have been designed to accommodate for the simultaneous function of all aforementioned subsystems, if necessary. As such, no constraints are imposed in that regard, provide great freedom in the configuration of the orbital operations. As such, the following

protocol has been compiled, as a preliminary indication of operations sequence in nominal orbit (all points assume nominal operation):

- The main payload is only activated when the spacecraft finds itself in eclipse while descending towards the periapsis. Observations start and end when the altitude is lower and exceeds 40 km, respectively.
- The PROP system is only activated when the s/c is ascending towards its apoapsis, for a single finite burn per orbital revolution. If needed, data transmission can take place at the same time as the manoeuvre. While not expected in the operational design, the payload is not to take measurements during operation of the thruster, as the disturbances will render the observations useless.
- Data transmission can occur at any time desired, given the Lunar Orbiter is within view and maximum allowable distance. It is however to be kept in mind that the greater the deviation of the antennas from the direction of the Lunar Orbiter, the greater the signal noise involved.
- The TC system is passive, so an "on/off" mode is not applicable.
- The 2SID is always active, regardless of the orbital state.
- The AOCS sensors are always active, at least those necessary for determining the required accuracy at each instant.
- The CDHS is always active. The system's multi-core processor allows it to perform multiple operations in parallel, such as activating the AOCS actuators for attitude correction and processing data collected by the payload at the same time.

2.5.3 Timeline on Extraordinary Events

Lunar Eclipses

The Earth passes between the Sun and the Moon every month. Although the Earth usually crosses at an angle high above or low beneath the Sun-Moon line enough such that its shadow is not cast on the Moon, twice a year (see figure 2.5) (on average) it pass close enough to this line to effectively cause a lunar eclipse. [11]

The effects of these eclipses on the LUMID spacecraft have been accounted for in the trajectory simulations, as explained in chapters 3 and 10. The amount of solar power received during each event has been computed and tested against the power requirements both for the operation of the main thrusters and the rest of the s/c bus. These results have been used to size the spacecraft battery and design the power management schemes to ensure LUMID can survive the eclipses.

The worst of these will occur in Jan 10, 2020 (refer to table 2.1 resulting in a worst case battery depth of discharge of 70 %, which has been accommodated for in the operating modes of the s/c. During these lunar eclipses, energy consuming activities such as payload observations, thrusted trajectory manoeuvres, data transmission, etc.,will be ceased, so that the s/c can remain power positive. The thermal system's heating tubes will be activated instead to ensure all subsystems remain within operating temperatures.

Table 2.1: Lunar eclipses in the period 2019-2022

Calendar date	Eclipse type	Total Duration
2019 Jan 21	Total	04h 19m
2019 Jul 16	Partial	02h 58m
2020 Jan 10	Penumbral	04h 05m
2021 May 26	Total	03h 22m
2021 Nov 19	Partial	03h 28m
2022 May 16	Total	04h 52m

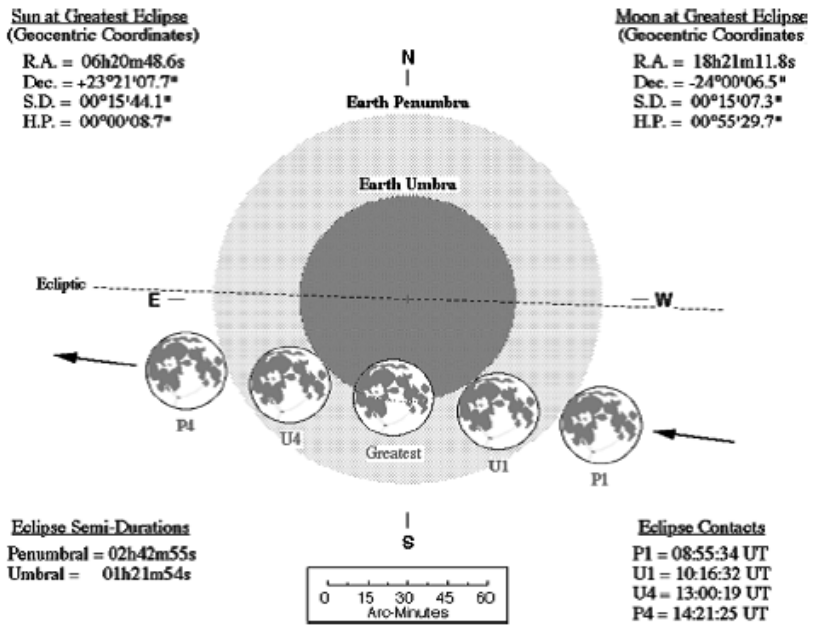

Figure 2.5: Example eclipse data—June 26, 2010 Lunar eclipse [11]

Safe Mode Protocol

Upon an anomaly in the system, the s/c will enter safe mode and retain this condition until the problem has been identified and fixed or another course of action is decided upon. The safe mode will aim to achieve the following:

- Prevent loss of power
- Maintain communication with the Lunar Orbiter
- Maintain attitude pointing capability towards the Sun
- Preventing accumulation of momentum in the AOCS system

The safe mode will unfold in the following fashion, per subsystem:

- AOCS configuration: The cold gas thrusters will remain inactive, since they are only intended to de-saturate the wheels once every roughly 5 days. Furthermore, since experience with previous missions has shown star trackers to fail with increased frequency [21], it is imposed as an extra requirement during the safe mode that the s/c is to retain its attitude with its star trackers disabled.

  In such a situation, the s/c will rely on its 4 operational sun sensors and 3 reaction wheels. As explained in chapter 8, these components are still adequate to provide 3-axis attitude determination until operational mode has been recovered.

- Command and Data Handling: The computer will remain operational, but a portion of its functionality will be deactivated. The rest will be powered by a reduced 6.2 W, enough to facilitate communication with the Lunar Orbiter, attitude control and on-board maintenance operations.

  A further measure will be to ensure the computer is connected via analog cables (next to the digital ones) to the wheels, so that open-loop commands can still activate them (for gyroscopic stiffness [22] if the digital parts of the computer need to be deactivated.

- Communications: The subsystem's operation is reduced to merely the telemetry function and the payload data transmission utility is deactivated. This means that the required power is reduced to 0.52 W and the bit rate to max 0.7 bits/sec. Computations have indicated that, if

necessary, the bit rate can be further reduced to a max of 0.4 bits/sec, beneficial in terms of power requirements and ease of link-budget closing, while the telemetry function is still effective.

- Thrusters: The main thrusters will be deactivated, as their power consumption is prohibitive during a safe mode. Depending on the time of occurrence of the anomaly and its duration, this may have an effect on the guidance and navigation capabilities of the s/c; if it deviates from its orbit, a correction will be unfeasible until recovery from the safe mode. Still, the configuration of the trajectories is such that sufficient stability is provided over the course of several days, so that enough time is provided for any anomalies to be tackled (refer to 3).

CHAPTER 3

Astrodynamics

The current chapter treats the trajectory design for the LUMID mission. Given the s/c travel in a piggybacking configuration, no lunar-transfer trajectories are applicable and the treatment instead starts at the moment of deployment.

The overview of requirements given in section 3.1 is followed by a presentation of the main challenges the design is called to overcome. The methodology used in the analysis follows in section 3.3 and the subsequent results and their correspondent discussion are presented in 3.4 and are then used for the definition of the final trajectory configuration and conclusion/recommendations in 3.5.

3.1 Requirements

In table 3.1 the requirements that have been set for the astrodynamics part of the LUMID design can be seen. The far right column indicates whether the corresponding requirement is met or not.

Table 3.1: Astrodynamic requirements

Identifier	Requirement	Section	Compliance
R-SC-AD-1	The s/c shall be placed at an orbit with an apoapsis at 2038.2 and a periapsis at 1853.2 km from the centre of the Moon	3.4.1	✓
R-SC-AD-2	The s/c shall be able to achieve R-SC-AD-1 when released at a circular orbit at 500 km altitude	3.4.2	✓
R-SC-AD-3	The s/c shall provide orbit correction for maintaining the periapsis altitude from its nominal value, as described in R-SC-AD-1	3.4.1	✓
R-SC-AD-4	The s/c shall be able to remain operational for at least 2 years, counting from the moment of deployment	x, x	✓
R-SC-AD-5	After deployment, the s/c shall be able to assume its nominal inclination when released at any inclination between 50° to 90°	3.4.2	partly
R-SC-AD-6	The s/c trajectory shall prevent impact to the surface until a temporary thruster failure has been fixed	3.4.4	✓
R-SC-AD-7	The s/c shall be capable of assuming its nominal orbit after a temporary thruster failure has been fixed	3.4.4	✓

3.2 Challenges

To perform the astrodynamics simulation, the challenges that the system will encounter during its mission have to be assessed. These challenges are due to the Moon's and the lunar environments' characteristics.

3.2.1 Perturbations

Non-uniform Gravity Field The lunar gravity field is highly irregular. Mass concentrations (often abbreviated as "mascons") with high density are distributed unevenly over the surface of the Moon, further intensifying the irregularity of its gravity field. As a result, orbit propagation is chaotic and unstable in most cases [23]. Characteristically, the satellite FPS-2 released during the Apollo 16 mission was projected to stay operational for 1.5 years, but instead crashed in the surface after 35

days, victim to the destabilising gravitational field [24]. Therefore, accurate knowledge of the gravity field becomes a necessity for scientific missions at an orbit close to the surface.

NASA's GRAIL mission in 2011 eventually characterised the gravity field on the entire lunar surface for the first time, producing the most detailed gravity field map of any alien body in our Solar System to date. An overview can be seen in figure 3.1, courtesy of NASA's Jet Propulsion Laboratory.

It is important to examine if there are specific orbits that are favourable over others with respect to their behaviour under the irregular gravity field. Such orbits, referred to as "frozen", maintain an approximately constant average eccentricity, inclination and periapsis along a given period, thus minimising the required station keeping manoeuvres. It is important to understand that perturbations are still heavily present in these orbits. The advantage lies in that the orbits' configuration drives these perturbations to cancel each other out, producing a virtually undisturbed trajectory.

D. Folta et al. [25] used the data from the LP and Clementine missions to produce a comprehensive overview of these orbits. While their analytical and numerical models span a variety of cases and conditions, the bottom line is that there are four main inclinations where frozen orbits can be established: 27°, 50°, 76° and 86°.

Modelling of this gravity field for orbit trajectory design and prediction will be implemented in the simulation model that will be used, what kind of gravity model is used is treated in more detail in section 3.3.

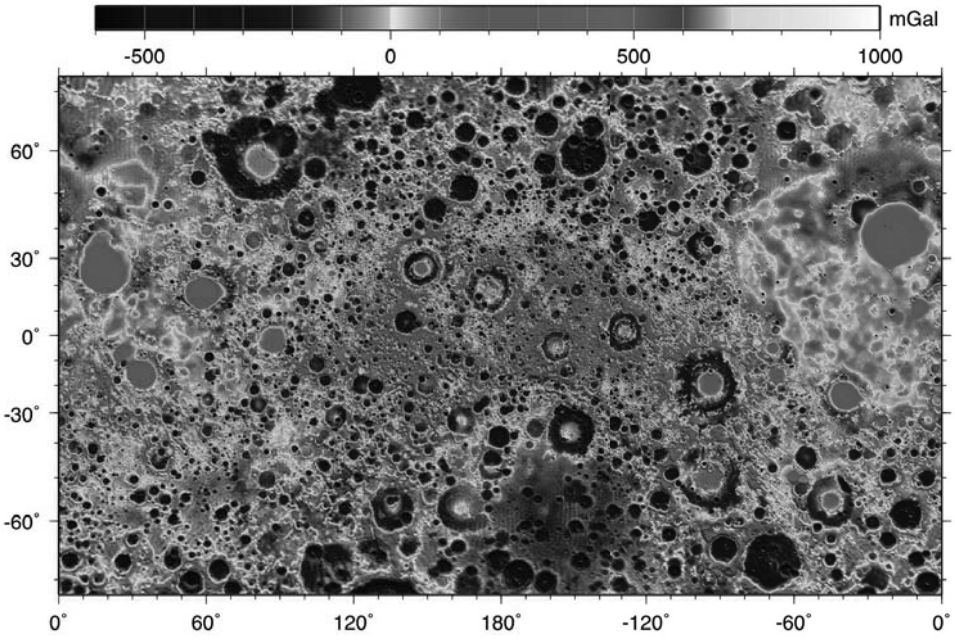

Figure 3.1: The gravity field of the Moon as measured by NASA's GRAIL mission. The viewing perspective shows the far side of the Moon in the centre and the near side (as viewed from Earth) at either side.

Third-body Perturbations D. Folta et al. [25] also investigated the effect of Earth-induced third-body perturbations on lunar trajectories. According to their account, operational experience has demonstrated this effect to be dominant for orbits higher than ~750 km above the lunar surface. Below this altitude, gravitational effects caused by the presence of the mascons start to downgrade the significance of third-body perturbations and below 100 km the difference is such that perturbations can virtually be neglected. D. Folta et al. have further applied a number of simplifying assumptions (Earth/Moon treated as point masses, circular orbits, etc.) to develop analytical relations describing the effect of third-body perturbation forces on orbital parameters such as eccentricity, inclination and argument of periapsis.

Representative of these formulations is NASA's Lunar Prospector (LP) mission. D. Folta et al. were involved in the trajectory design for the satellite, orbiting the Moon at roughly 100 km altitude. Their validated model for the mission profile included third-body perturbations not only from the Earth and Sun, but also Jupiter. Assuming the Sun to be a point mass and the Moon to be non-spherical, they showed that the ratio of the relative third-body effects of the Sun over the gravitational effects of the Moon are only 0.5 %. For the case of the Earth, this increases to 1:15 when comparing the $C_{2,2}$ terms and over 1:50 when comparing the J_2 terms. [26]

Since the elliptical orbit that will be concluded in the following sections has an apoapsis above 100 km, the third-body perturbations will have to be taken into account.

Solar Radiation Pressure The perturbation, p_{sr}, is the result of the pressure exerted by solar radiation on the exposed area of the spacecraft. This perturbation is only present when the s/c is directly impacted by sunlight, and absent in eclipse. It is assumed that this pressure is modelled with the appropriate accuracy.

Lunar Albedo Radiation Pressure The portion of solar radiation emitted back into space from the lunar surface acts on the spacecraft in similar manner as the direct solar radiation. The magnitude of the respected pressure on the Moon is between 7 % to 24 % of the incoming solar radiation [27]. The force produced by this pressure is thus a small percentage of the total Solar Pressure radiation force. The effect has been neglected in the current analysis. At a later stage, when the analysis will have reached a more mature level, its potential inclusion in the model will be re-evaluated.

3.2.2 Other Challenges

Relativistic Effects Relativistic effects generally refer to the effects of time dilation. Time dilation is the difference in elapsed time measured by two observers that either move relative to each other or are located at a different distance from a gravitational mass. According to chapter 5 of [28] the relativistic effect is very small (especially in comparison with other perturbations) and can be neglected. The Schwarzschild solution, the geodesic precession and the Lens-Thirring precession together can form relativistic correction and are included in GMAT, but including these corrections in a simulation script drastically increases the running time and sometimes even jams the simulation. The previous two arguments lead to the conclusion to not include the relativistic correction in the LUMID simulations.

Deployment Constraints From the requirements it can be seen that the inclination deployment range varies from 50° to 90°. A preferred inclination will be set on the basis of payload requirements. However, when the system is not deployed at this inclination, this presents a challenge since performing an inclination change will be costly in terms of Δv. Next to this possible inclination variation the orbit will need to be manoeuvred from the circular 500 km deployment orbit to the mission orbit.

3.3 Methodology

This section will provide the methodology used for the astrodynamic analysis of the system. First the way the mission is segmented for faster simulation is treated. The simulation tool that has been used for the analysis will be treated next. Last the set-up of the manoeuvres that will be performed during the mission phases will be explained and the way a mission start date has been established will be elaborated upon.

3.3.1 Mission Segmentation

The mission is divided into three separate elements. These three elements correspond to the three different phases the system will encounter. The first phase is the deployment phase in which the orbit will be transferred to the mission orbit. After this, the second phase will be performing station

keeping manoeuvres to keep the satellite in this orbit. Finally, the third phase will be the end of life phase. These three different phases were previously explained in 2.4 by the paragraphs of Orbit Insertion(deployment phase), Payload Operation and Station Keeping (mission phase) and End of Life Operations (end of life phase) For a final astrodynamics simulation, it is necessary to attach these mission segments together, making sure that the end and begin points of these phases coincide and a continuous mission is obtained.

3.3.2 Modelling

The software and its components, such as force models, numerical integrator schemes, differential corrector schemes, targeters and the LUMID script will be elaborated upon in the next section.

Software To perform simulations of the complete mission of LUMID the open-source tool GMAT (General Mission Analysis Tool) was used. GMAT is an open-source space mission design tool developed by a team of NASA, private industry, and public and private contributors. The program is based on MATLAB® and therefore has similar functionality. The program lets the user create one or multiple spacecraft, for which the user can design all the hardware, set its reference frame and modify its initial parameters. The user can add propagators, solvers, burns and custom coordinate systems. After this the mission tree can be edited to design the simulation. There are many possibilities for commands, such as propagating, targeting and multiple others. In the following paragraphs there will be elaborated upon the choices made for the LUMID mission simulations.

Force Models To create a representative simulation of an orbit around the Moon, the perturbations described in section 3.2.1 need to be included in a so called force model. In lunar precision orbit determination, the perturbation caused by the lunar non-spherical (non-uniform) gravity has a major role. That is why it is important to have gravity field model of high resolution. The lunar gravity field model used in the force model is the 40th degree and order LP165P model. This model is created using tracking data of the Lunar Prospector together with historical tracking data (including data from Clementine, upon which the GLGM-2 model is based) [29]. For the third-body perturbations Earth, Jupiter and the Sun are included as point masses. Solar radiation pressure is also taken into account for the force model used. In the model no relativistic correction is used and also drag is neglected since the density of the atmosphere around the Moon is very low [30]. Furthermore, as mentioned before, the lunar albedo radiation pressure is omitted in the model.

Numerical Integrator To model the motion of a satellite a propagator command is used. The one used is a numerical integrator type. This type of propagator requires a force model, such as described in the previous subsection and a numerical integrator. In the LUMID simulations the RungeKutta89 integrator is utilised. This is an adaptive step, ninth order Runge-Kutta integrator with eighth order error control. The coefficients that GMAT uses are developed by J. Verner [31]. The RK89 integrator is picked over other integrators available in GMAT because this integrator scores good both in run time and in error magnitude for multiple different orbit types according to the GMAT User Guide. [31] In the calculations an accuracy of 9.999×10^{-12} is set and the step size have a minimum and maximum of 1 and 100 seconds, respectively and an initial guess of 20 seconds. The maximum number of step attempts is set to 50. These values are chosen to achieve acceptable simulation times, due to the time constraint of the mission design, the accuracy of the simulations is limited.

Differential Corrector In GMAT a differential corrector is used to solve boundary value problems. To achieve desired orbital conditions regularly a differential corrector is adopted to determine the manoeuvre components that are required. The Newton-Rhapson algorithm is chosen for the LUMID simulation as it takes less iterations than the other two supported algorithms, Broyden and Modified Broyden. The maximum number of iterations is set to 50, because it is expected that more steps than that will not improve the result of the solver, but will slow the simulation down. Because of the time available for the design of this mission, faster simulations are preferable.

Targeter The target function in GMAT is used when it is desired to solve for (a) certain condition(s) by varying one or multiple parameters. An example that also occurs in the LUMID simulations is the varying of the Δv of a manoeuvre at the apoapsis to achieve a desired altitude at the periapsis. If there is a quantity of which the value is unknown, but that needs to be determined, that is defined as the control variable. Secondly, there are the constraints, which are the conditions that need to be satisfied. Now the target sequence will numerically solve the boundary value problem and thereby determine what the value of the control variable needs to be to meet the set constraints. The *Vary* and *Achieve* commands are used to define the control variables and constraints, respectively.

Script The script to simulate LUMID uses the force model, integrator and differential corrector described before. To set the way the simulation behaves, first the spacecraft has to be defined, this includes the mass, orbital characteristics, the coordinate system it is positioned in, the hardware, etc. After this the force model and numerical methods are implemented. To let the simulation operate according to the requirements that will be determined in the remainder of this chapter, the mission sequence has to be defined. The mission sequence starts with a 730 day loop, while the number over elapsed days in the simulation is below 730 days, LUMID will take a "step". After every propagation step the script will check if the satellites' magnitude of radius (RMAG) falls below a set value or is higher than a certain threshold. These values are the determined radius of periapsis (RP) and the determined radius of periapsis plus one kilometer (RP+1). This way it is made sure that every orbit, the following orbital correcting progress will be triggered. In the next section it will be explained why this is necessary. First the satellite will propagate to the apoapsis, where the burn manoeuvres are most efficient. At the apoapsis GMAT will start a *Target* run and using the differential corrector it will *Vary* and eventually determine the Δv required to *Achieve* a predetermined radius of periapsis with a tolerance of 0.1 km. After propagating to the periapsis, the if loop is closed and the satellite will continue to propagate until 730 elapsed days are reached or until the altitude condition is violated. The script is visualised in figure 3.2.

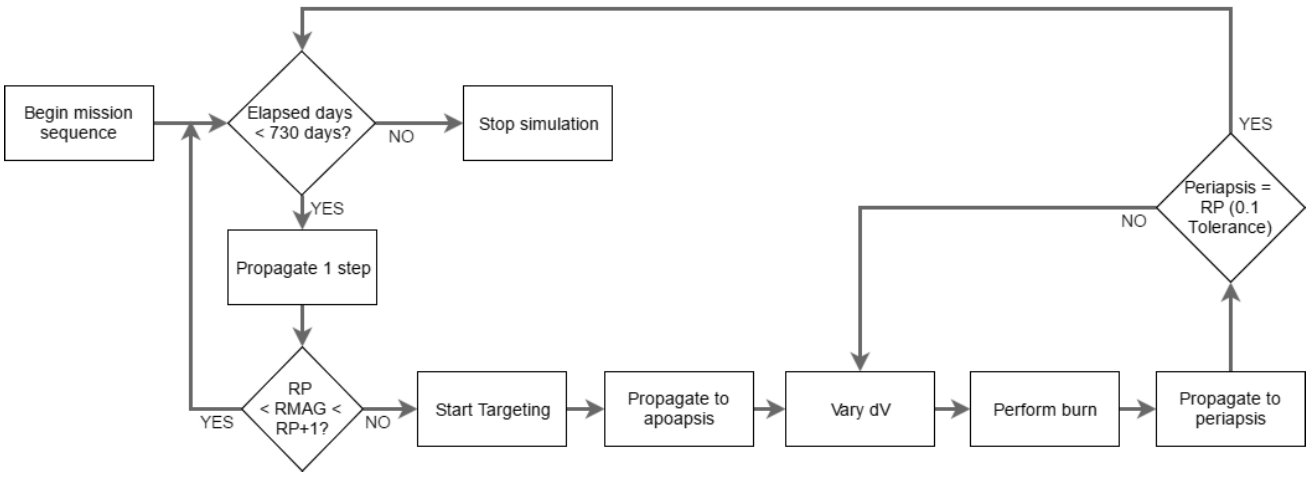

Figure 3.2: Visualisation of the GMAT mission sequence

3.3.3 Manoeuvres

By propagating the mission without performing any manoeuvres it can be seen in figure 3.3 that the mission orbit is not stable and station keeping is required to maintain the nominal orbit. Since the deployment orbit also differs from the mission orbit, the system needs to perform manoeuvres during the deployment phase as well. Finally to perform a controlled impact on the lunar surface, manoeuvres are required as well.

These manoeuvres have to simulated in the model of the mission. This can be done in two ways. Using impulse burns which assume infinite thrust and therefore can perform instant manoeuvres at

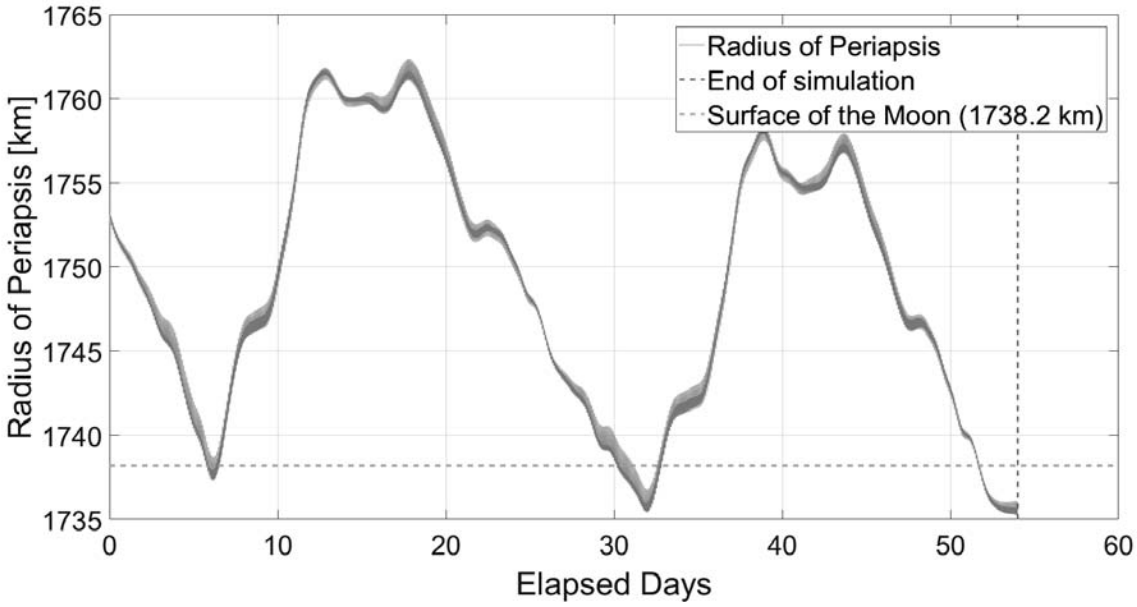

Figure 3.3: The radius of periapsis of a LUMID satellite vs the elapsed days. Horizontal line is the radius of the lunar surface [Mission Phase]

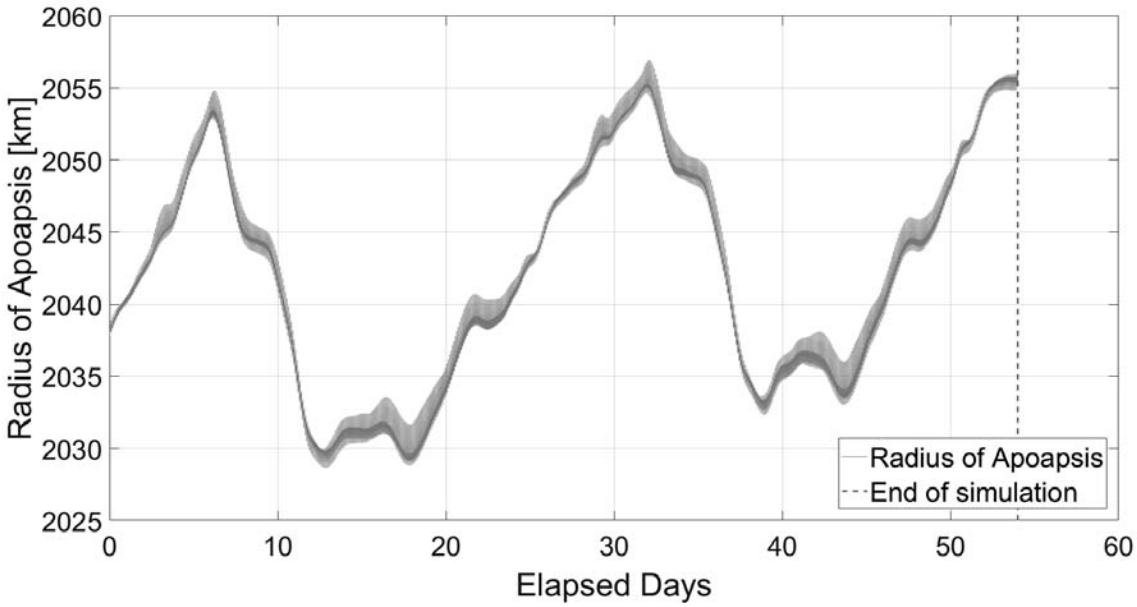

Figure 3.4: The radius of apoapsis of a LUMID satellite vs elapsed days [Mission Phase]

user specified locations. The second, more accurate method is using finite burns, which does not assume infinite thrust and therefore also has to take burn time into account.

For these two ways the required Δv is calculated by using the target and vary command together in the mission sequence in GMAT. Both types of burns can be varied in three directions. These directions are specified by the VNB axis system. The VNB or Velocity-Normal-Binormal coordinate system is non-inertial coordinate system based upon the motion of the spacecraft w.r.t. a chosen origin, here the Moon. That means that the x-axis is pointed in the direction of the velocity of the spacecraft w.r.t. the Moon, the y-axis is along the instantaneous orbit normal (hence Normal axis). The z-axis completes the right-handed set and is orthogonal to the other axis and is directed away from the Moon. For the finite burn method the burntime also has to be incorporated in the vary commands. Because of our CubeSat® system a large thrust propulsion system will not be available, see section 9 and

therefore a large burntime will be required to achieve the necessary Δv for performing manoeuvres. However, this burntime can differ by a significant amount for each orbit. This also changes the required directions corresponding to this burn. Since the vary command is heavily dependent on the initial parameters that have to be set by hand, it can be noticed that the target loop will only converge for one to three orbits per simulation and then crashes because the initial parameters are too far off the required directions and burntime of the burn. Therefore the approach of using finite burns for the simulations are deemed infeasible and the impulse burns are chosen to model the manoeuvres that will be done during the mission. The output of the impulse burns is measured in Δv. This Δv is calculated by the vary and achieve command in GMAT. For each burn, the model will vary the Δv in the desired directions to achieve a certain condition. For other subsystems, not only the Δv is of interest, but the burntime as well. Therefore the burntime values should be calculated using the Δv values. This is done using equation 3.1, where m_0 is the initial mass, Isp the specific impulse, g_0 the gravitational parameter and T_f is thrust.

$$\Delta t = \frac{m_0 \cdot I_{sp} \cdot g_0}{T_f} \cdot \left(e^{\frac{\Delta v}{Isp \cdot g0}} - 1 \right) \tag{3.1}$$

To model the impulse burns it has to be decided when and where these impulse burns will be performed.
When is mostly important for the mission phase, where station keeping is required to stay at the nominal orbit. When also specifies what range of altitudes are considered to be a nominal orbit. From figure 3.3 it can be seen that the orbit's periapsis not only lowers due too perturbations but is also raised in the mission phase. Part of the payload system can only function when below a certain altitude above the lunar surface to detect MMI. Therefore, it is desired to not only perform manoeuvres to raise the orbit's periapsis but also lower it to ensure the scientific value of the mission.
In figure 3.4 it can be noted that the apoapsis shows around the same altitude variation as the periapsis, within a band of around 25 km. Although the apoapsis varies as well, it is deemed not benificial for the mission to perform manoeuvres to keep the apoapsis at the nominal altitude. This ensures a smaller constraint for the propulsion, AOCS and correspondingly the power system. In short, the decision is made to only perform manoeuvres to keep the periapsis at the nominal altitude of 15 km. Because of the low thrust propulsion system (section 9), large variations in the altitude cannot be compensated for in one orbit. Long term this can lead to the system not being able to maintain the periapsis' nominal altitude. From this the conclusion can be made that station keeping will be necessary every orbit, this ensures each manoeuvre only has to compensate for relatively small differences in the periapsis' altitude.
In figure 3.5 it can be seen that the inclination of a LUMID satellite starting from 50° inclination will remain within a range of 48 to about 52.5 ° for the mission phase of two years. Therefore no inclination station keeping burns will be performed.

For the deployment and end of life phase the required manoeuvres will be performed for as long as is necessary to achieve the desired goal of each specific phase.

Where the manoeuvres will be performed in the orbit is a question of efficiency. In other words, where is it most efficient to perform these manoeuvres. When it is desired to only change the altitude of the periapsis or apoapsis, the best location to apply a Δv correction is at the opposite side of the orbit, so for the periapsis this is the apoapsis and vice versa. These locations are most efficient since performing a tangential manoeuvre here will only change the altitude of the periapsis or apoapsis and not different parameters.

From the payload system the requirement flows that measurements can only be performed in the night side of the Moon and under 39 km, see section 5.2.3. It would therefore be ideal to have a sun-synchronous orbit with the periapsis at the night side. To achieve this however, a higher performance propulsion system would be required to perform the corresponding manoeuvres. The fact that the system's mass allows for three satellites to be deployed ensures that the scientific return is still sufficient while not achieving this sun synchronous orbit

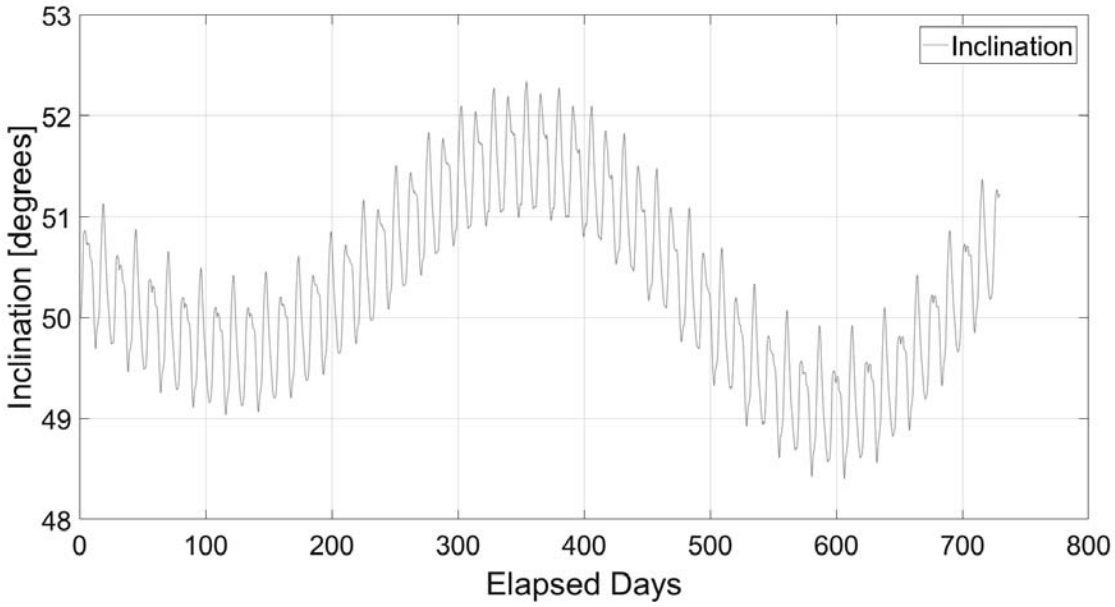

Figure 3.5: The inclination of a LUMID satellite vs elapsed days [Mission Phase]

Impulsive Burns to Finite Burns

From the simulations a data set is obtained containing the Δv values corresponding to each manoeuvre that is done to maintain the nominal orbit. These Δv values are created by performing impulsive burns at either the apoapsis or the periapsis. During the mission phase the only location of these burns is at the apoapsis since it is only desired to correct the altitude of the periapsis. An impulsive burn however, is not truly representative of the real life burn for the LUMID satellites, since a low thrust propulsion system is incorporated, see chapter 9. This means a generally long burn time is required and the assumption of impulsive burns is no longer valid. The Δv values that are obtained from the simulation can be used to estimate finite burns. This should be done by incorporating the gravity losses. First the burntime is calculated using equation 3.1. By centering these burntimes around the apoapsis the locations in orbit during the burn can be estimated.

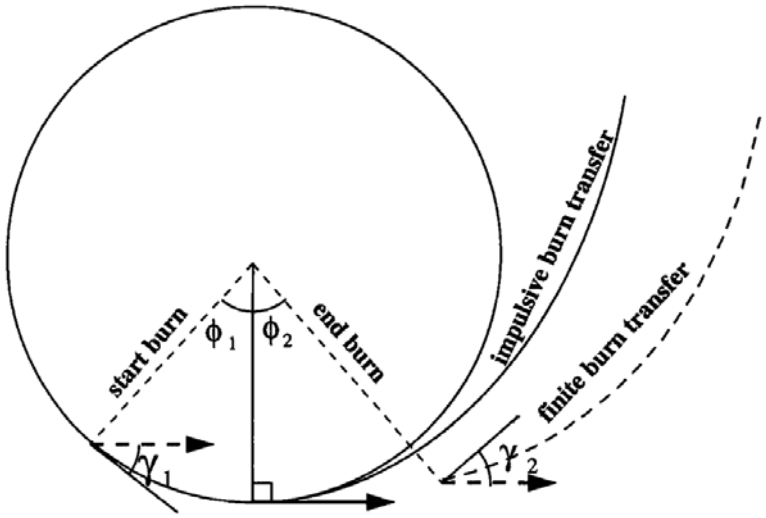

Figure 3.6: Comparison of impulsive- and finite-burn transfers: solid lines = impulsive-burn characteristics; dashed lines = finite-burn characteristics [32]

The first value that is obtained is the altitude the satellite is at during the burn. Using equation 3.2 the gravitational force acting on the satellite for a specific altitude can be calculated.

$$\frac{g_1}{g_2} = \left(\frac{r_1}{r_2}\right)^2 \tag{3.2}$$

Next the final mass of the satellite after the burn should be calculated. The expended mass (m_b) is calculated using equation 3.3, where m_i is the initial mass and m_f the final mass.

$$m_b = m_i \cdot \left(1 - e^{\frac{\Delta v}{Isp \cdot g0}}\right) m_f = m_i - m_b \tag{3.3}$$

Using the calculated values the Δv incorporating the gravity losses can now be calculated using equation 3.4 (from chapter 6 of [32]). In this equation the value for time t is the time value dependent on where the satellite is at in the orbit. The value for g is the gravitational force acting at a satellite dependent on the satellites position. γ is the angle from the tangential vector at that specific position in orbit towards the vector along which the thrust of the satellite will be pointed. This thrust vector is in the same direction along the entire duration of the burn and this direction is defined to be along the velocity vector at the apoapsis as can be seen in figure 3.6. In other words when the burnduration becomes longer, the positions where the burn starts and ends will be further away from the apoapsis and the γ angle will become greater. This angle can also be calculated by using the true anomaly values of the location the satellite is at. Since the true anomaly is the angle between the direction of periapsis to the location of the satellite the θ angles as shown in figure 3.6 can be calculated by substracting the true anomaly values by 180 °. These θ angles are directly correlated using trigonometry to the γ angles used in equation 3.4.

$$\Delta v = g_0 \cdot I_{sp} \cdot \log\left(\frac{m_i}{m_f}\right) - \int_{t_1}^{t_2} g \cdot sin\gamma \cdot dt \tag{3.4}$$

The Δv values that would be calculated using this equation (3.4) can be used for another iteration using the same equations. After enough iterations it will be noticed that the values will start to converge to certain values dependent on the starting Δv values. However, due too time constraints the calculation of the gravity losses was not finalised and therefore the impulsive burn method is used without taking gravity losses into account in this iteration of the LUMID design. In section 3.5 the expected impact of this assumption can be read.

3.3.4 Choice of Start Date and Location

The space weather plays an important role in determining the initial values for the mission. Through the entire year multiple meteoroid showers occur, because of the high density of particles during these periods, these are interesting moments for LUMID to perform measurements. The Geminids meteor shower, that contains meteors with a average velocity of 35 km/s, has a very density and offers a good opportunity to collect data. The Geminids shower peaks around the 13th and 14th of December, so the aim is that at least one of the LUMID satellites is at the optimal position to perform measurements at that moment [33].

In section 5.2 it is stated that the flashes of the meteorite impacts are best detected the surface of the Moon is not illuminated, i.e. when the side of the Moon where the pictures are taken is in eclipse. The other requirement of the payload is the distance to the surface, which should not exceed 40 km. With the elliptical orbit, this altitude requirement is only satisfied when the satellite is in its periapsis. To determine if LUMID meets both requirements one should first imagine a spin-axis-referenced coordinate system with its origin in the centre of the Moon. In this coordinate system the x-axis is always pointed to the Sun, the y-axis is computed as the cross product of the x-axis and the spin axis of the body and the z-axis is pointed in the direction so that it completes the right-handed set. Now, by definition, if the RAAN and the AOP summed are 180° the periapsis will lie in the negative x-direction and since the x-axis is pointed towards the Sun, this means that the periapsis is located in the shadow side of the Moon. It should be noted that during the revolutions around the Moon both the RAAN and AOP travel around the planet, the rates of these variation will be covered in result section 3.4.1. To have optimal measurement possibilities for the Geminids meteor shower

the previous described condition should be met around December 13 and 14. The mission orbit should be initiated three weeks before the event of the meteor shower to allow for miscalculations or anomalies during the transfer orbit that causes it to take longer to lower the orbit.

After running a two year simulation with an epoch three weeks before Geminid peak, November 22 2019, with inclination at 50°, the periapsis and apoapsis as determined and the other orbital elements at zero, the average $\Delta\Omega$ and $\Delta\omega$ are determined. Now it could be guessed what the initial values for the rest of the orbital parameters should be, so that the satellite naturally drifts off to the desired location in three weeks. The average $\Delta\Omega$ and $\Delta\omega$ depend on the start location due to the non-uniform gravitational field of the Moon, that is why the determination of the start location is an iterative process. After some trial and error the best location to start from is determined and will be discussed in section 3.5.

Figure 3.7 shows the idea of the travel of the relative positions of the Moon, Sun and the satellite. The lighter contours of the orbit are the contours of the orbits at the start of the mission phase, as is the case with the lighter coloured Sun in the top of the figure. The arrow indicates the travel direction of the sum of the RAAN and the AOP and the Sun. In the figure it is visible that at 14 December or the moment of the Geminids shower, three weeks after the start of the mission phase, the satellite is in its periapsis and at the shadow side of the Moon at the same time.

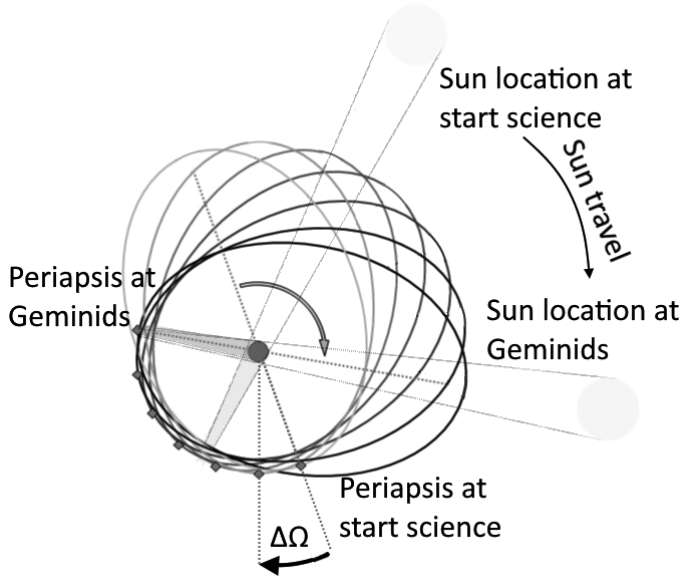

Figure 3.7: The travel of the RAAN and the AOP of the satellite and the position of the Sun (Adapted from reference [34]

The initial parameters of the other two satellites that will be used in the mission, will be determined based on the fact that the satellites have to be identical and on the fact that as much coverage as possible is desired. The first constraint is met by keeping as much orbital parameters as possible the same.

3.3.5 Verification and Validation

Most of the calculations for the astrodynamic part of the LUMID mission are done within GMAT. The designers used GMAT to simulate the trajectory of the orbit by filling in the initial parameters and the commands to propagate or to achieve certain target parameters. The General Mission Analysis TOOL is in use from 2011 [31] by its developer. The program and all the functions, equations and coefficients it uses are verified and validated by NASA. That is why it will not be necessary to repeat this V&V procedure. However the models that GMAT uses should be validated. The force models that are used should be validated, an example of which is the gravity field model which GMAT uses, this model can be validated by looking up the source of this model and validating how this model is

created. In principle all models of perturbations (section 3.2.1) have to validated in this way. Due too time restriction, it was chosen to assume these models have been validated by GMAT's creators because it is a tool that is still being updated and therefore has an active and dedicated developer team behind it. The origins of the gravity field model is elaborated upon in section 3.3.2.

3.3.6 Sensitivity Analysis

A sensitivity analysis has been done on the deployment phase to see what would change if the satellites are deployed in a different orbit configuration. The sensitivity to changes in the "drop" orbit inclinations is calculated in section 3.4.2. A change in the altitude the satellite is dropped at will increase or decrease the amount of Δv and time necessary to achieve the mission phase orbit dependent on whether the change is positive or negative in amount. Since the higher the altitude is at where a manoeuvre is performed, the more efficient the manoeuvre is and therefore an increase in altitude will not directly translate to the same percentage of increase to the total Δv cost. A lower percentage is expected. For a lower deployment altitude a certain percentage decrease is expected to translate to a smaller percentage decrease to the total Δv cost. Some of the results presented in section 3.4.4 also can be seen as means of sensitivity analysis. This section shows how the mission could be influenced by sudden hardware failure during the mission.

3.3.7 Error Control

Error control is a function included in GMAT and is incorporated in the propagator. The error control determines the way the error in the current step is calculated. All the errors are relative errors, but the reference for the relative error is determined by the selected error control. In the LUMID simulations it was chosen to use RSSStep. This is the Root Sum Square (RSS) relative error measured w.r.t. the current step in the propagation.

3.4 Results & Discussion

In this section the results of the different phases in the design process are shown. First the mission phase will be discussed since this is the main phase of the system and therefore will be the driving phase for the design. After that the deployment phase and the difference in this phase for the three LUMID satellites will be elaborated upon. Lastly the approach to the end of life phase is shown.

3.4.1 Mission Phase

In this section the results of the two types of mission phases simulations are shown. The primary goal of the astrodynamic analysis for the mission phase is to achieve an orbit that has the largest possible fraction of the orbit period that the satellite spends in the lunar night but still complies with all other subsystems that are related to the astrodynamics, mainly the PROP and correspondingly the EPS subsystems.

Circular Orbit Results & Discussion

Since the primary mission payload requires a maximum altitude of 39 km as will be explained in section 5.2.3. The ideal mission orbit would be a circular orbit that satisfies this altitude requirement, because this way measurements can be performed during a larger fraction of the orbit since the time the spacecraft spends in the night side of the orbit will become larger in respect to the orbital period than for an elliptical orbit of which the apoapsis is greater than this 39 km altitude. Not only will the fraction of the orbit that the satellites will spend in night time become more optimal, an elliptical orbit with only its periapsis beneath the 39 km boundary will have this periapsis in the day side of the lunar surface for half of the time it takes the RAAN to travel 360° back to its initial condition. This means the scientific value will be reduced if an elliptical orbit is necessary. In figure 3.8, the radius

of apoapsis and periapsis for a 38 km circular orbit are shown. In this simulation, only the periapsis is kept at its nominal altitude by performing manoeuvres.

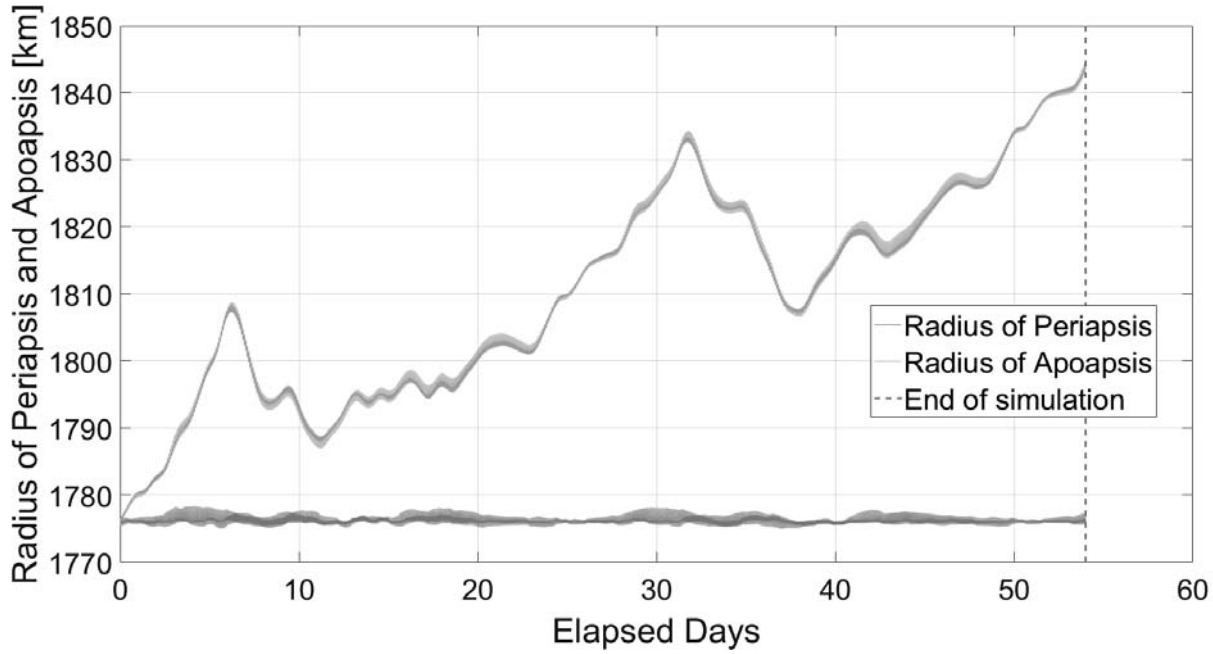

Figure 3.8: The radius of the periapsis and apoapsis for LUMID in a circular orbit at an altitude of 38 km for two months (54 days)

In table 3.2 the corresponding manoeuvre parameters for maintaining the nominal periapsis altitude can be seen for the same 38 km circular orbit.

Table 3.2: Manoeuvre parameters for a 38 km circular orbit

Periapsis Altitude [km]	**Apoapsis Altitude** [km]	**Maximum burntime** [min]	**Orbital period** [min]
38	38	42.43	112

Figure 3.8 shows the radius of the apoapsis and periapsis of the orbit of a LUMID satellite if it is simulated with a circular orbit at an altitude of 38 km. In this simulation only impulsive burns to maintain the periapsis' nominal altitude are performed. However, it can be seen in this figure (3.8), that the radius of apoapsis has an upward motion. Therefore, to maintain the circular orbit not only manoeuvres to correct the periapsis are required, but also manoeuvres to correct the apoapsis. When this is not done, the orbit will become elliptical and its eccentricity will increase over time and achieve a certain relatively stable value. This means that two burns are required to stay in the desired orbit, leading to about twice as much Δv and with this also twice the amount of maximum burntime that is shown in table 3.2 over the entire mission. For the orbital period from 3.2 this would lead to a maximum burntime fraction of the total orbit period of 0.75. This is the burntime without the gravity losses included and therefore it is likely that this fraction will become larger than 1 with the gravity losses included. Such a fraction shows that a circular orbit at 38 km will decay even when burning for the full duration of the orbit and therefore is infeasible for the LUMID system in combination with a duration of two years.

Elliptical Orbit Results & Discussion

In section 3.4.1 it is explained why a circular orbit is not feasible for the LUMID design. Therefore an elliptical orbit is required to perform the mission. The altitude requirement of the primary scientific payload determines the range of periapsis altitudes to look in to. The altitude of the apoapsis can

be determined by looking at the consequences, in terms of the required sum of Δv, maximum Δv and fraction of the orbit spent below 39km for the TID of a higher or lower apoapsis altitude. The first two of these parameters are shown in figure 3.9 and table 3.3.
In figure 3.10 the variation of several orbital parameters are shown with impulsive burns performed for two months (or 54 days).

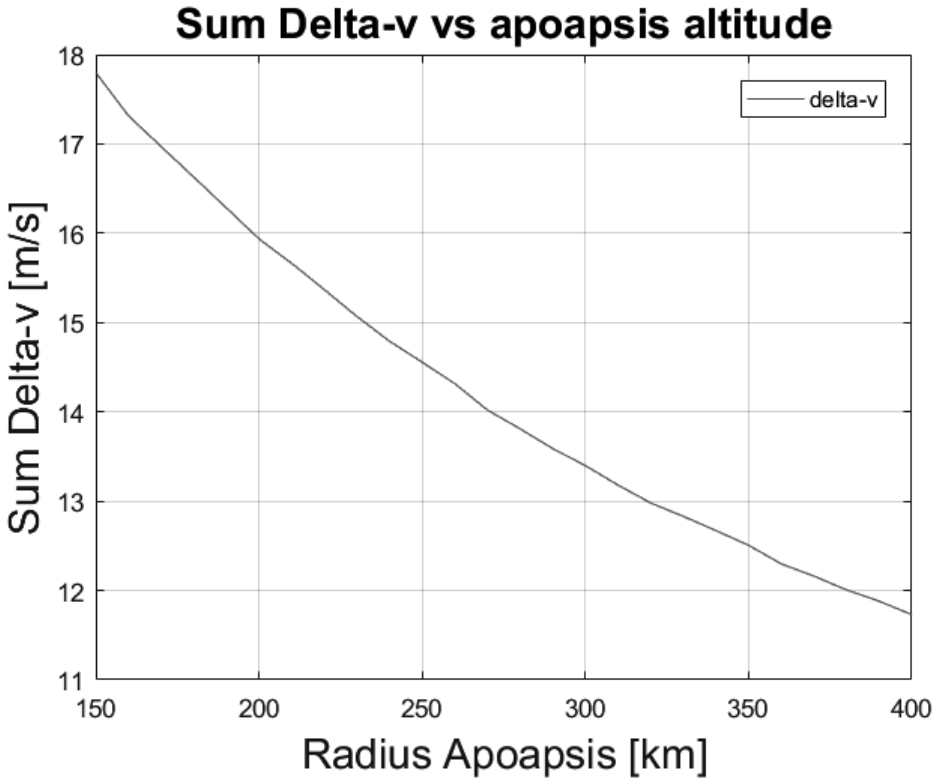

Figure 3.9: The sum Δv cost over one month for different altitudes of apoapsis

Table 3.3: Maximum Δv for the outer ranges of the analysed apoapsis altitudes

Periapsis altitude [km]	**Apoapsis altitude** [km]	**Maximum Δv** [m/s]
15	150	0.145
15	400	0.143

To select the parameters of the elliptical orbit two things are considered. The results from figure 3.9, table 3.3 and the velocity at the periapsis. The velocity at the periapsis will be used to calculate the motion blur. The higher this velocity, the higher the motion blur and therefore it becomes harder to detect MMI. The rule of thumb is for the same periapsis altitude if the apoapsis altitude increases the velocity at the periapsis increases.
The periapsis altitude has been chosen as such to accommodate the largest possible time beneath the 39km maximum altitude for the TID to perform measurements in, see section 5.2.3. This means a low value for the periapsis altitude. However this value should not be so small that the satellites might crash into the lunar surface due to the natural tendency of the altitude periapsis to deviate slightly from the nominal altitude even when performing station keeping burns, which can also be seen in figure 3.10a. Except for the deviation in the periapsis altitude, one should consider the deviation of the altitude of the Moon surface, which is highly irregular. The highest point on the Moon lies 10 786 m above the mean radius, therefore a large margin is required [35]. This lead to a periapsis altitude of 15 km, since this value has a relatively large margin to the surface and can accommodate a high maximum measurement time for the TID.
The apoapsis altitude was determined by looking at a range of altitudes vs sum Δv as can be seen in figure 3.9. The apoapsis radius ranges from 1888 to 2138 km wich corresponds with a 150 to 400 km

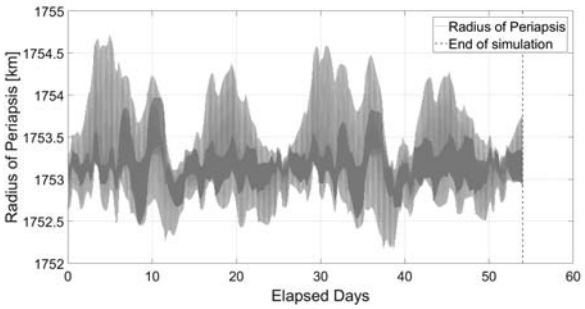

(a) Radius of periapsis vs elapsed days

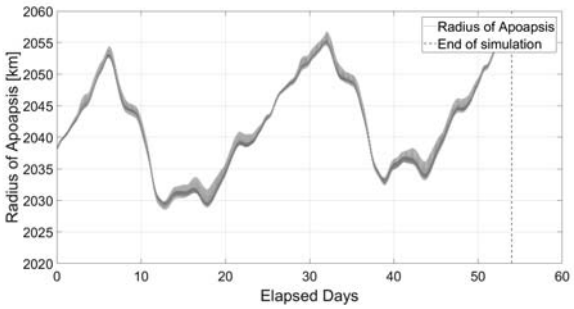

(b) Radius of apoapsis vs elapsed days

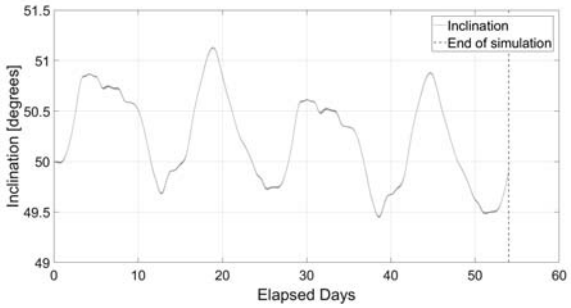

(c) Inclination vs elapsed days

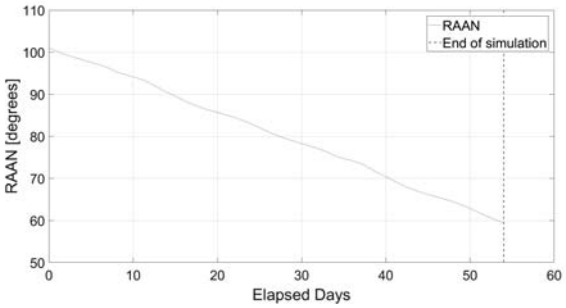

(d) RAAN vs elapsed days

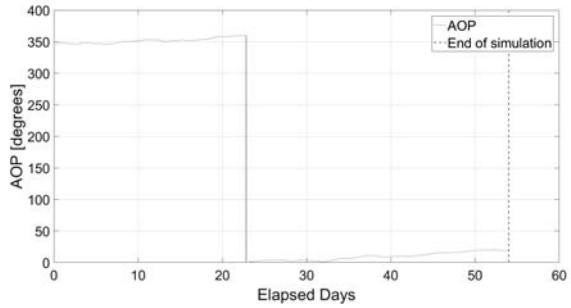

(e) AOP vs elapsed days

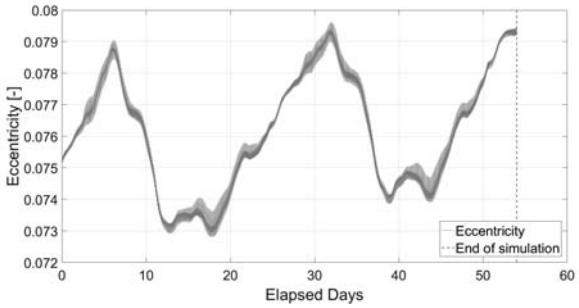

(f) Eccentricity vs elapsed days

Figure 3.10: Different orbital elements plotted over two months (54 days)

altitude. This range, with interval of 10km has each been simulated for a month. What can be seen in this figure is that the sum of Δv drops steeply for the first part of this range and evens out when the radius of the apoapsis becomes larger. The same trend can be seen for the average burntime. The maximum Δv and therefore correspondingly the maximum burntime for each radius of apoapsis does not decrease significantly, as can be seen in table 3.3. Since this maximum burntime has to be performed in a reasonable fraction of the total orbital period in order to not put too much of a strain on the EPS and AOCS, the radius of apoapsis cannot be too low, because this would decrease the orbit period. Another factor to take into account is that the higher the apoapsis is, the higher the velocity at periapsis is, of which a too high value is undesirable. A low burntime to perform station keeping and a low velocity at the periapsis therefore have to be balanced out. The altitude of the apoapsis that was concluded to achieve best of both factors of this balancing after analysis is an altitude of 300km. This comes down to the values of the altitude of the periapsis and the apoapsis have been analysed, concluding with the values of 15 and 300km, respectively.

In figure 3.10a, the variation of the radius of the periapsis in 54 days is shown. In the plot it is visible that due to the burn manoeuvres that are performed every orbit, the periapsis deviates only slightly from the desired value of 1753.2 km (15 km altitude). The maximum range of the periapsis radius is about 2.5 km.

The change in the radius of the apoapsis of the LUMID satellite for two months is shown in figure

3.10b. As is shown in the plot is the deviation between the highest apoapsis and the lowest apoapsis a lot bigger than the differences for the periapsis. The smallest value is 2013.54 km and the largest value is 2056.72 km, that means a range of 43.18 km. These large variation are not problematic since there are no requirements bound to the apoapsis, as long as the periapsis stays between the desired values. This is why no manoeuvres are performed to adjust the apoapsis.

The inclination, RAAN, AOP and eccentricity development over two months are displayed in figure 3.10c, 3.10d, 3.10e and 3.10f, respectively. The inclination plot shows that the inclination only deviates one degree over the time of two months, this means that inclination station keeping will not be necessary. Figure 3.10d shows a graph with a negative slope that indicates that the RAAN travels in the opposite direction of the Moon rotation. In figure 3.10e one can see that the AOP increases in time, which means that the argument of periapsis travels in the same direction of the rotation of the Moon. The jump in the graph at around 22.67 days is because of the fact that the argument of periapsis is always expressed in 0° to 360°, so when the AOP exceeds 360° it starts over from 0°. The travel of the RAAN and of the AOP are in opposite direction and since the average $\Delta\Omega$ is bigger than the average $\Delta\omega$ the periapsis location travels in negative direction around the axis that points upward through the Moon. The change in the eccentricity is displayed in figure 3.10f and shows very similar behaviour to the radius of apoapsis plot. This is legitimate since the radius of periapsis stays about the same, so when the apoapsis increases, the orbit gets more eliptical and thus an increase in eccentricity occurs.

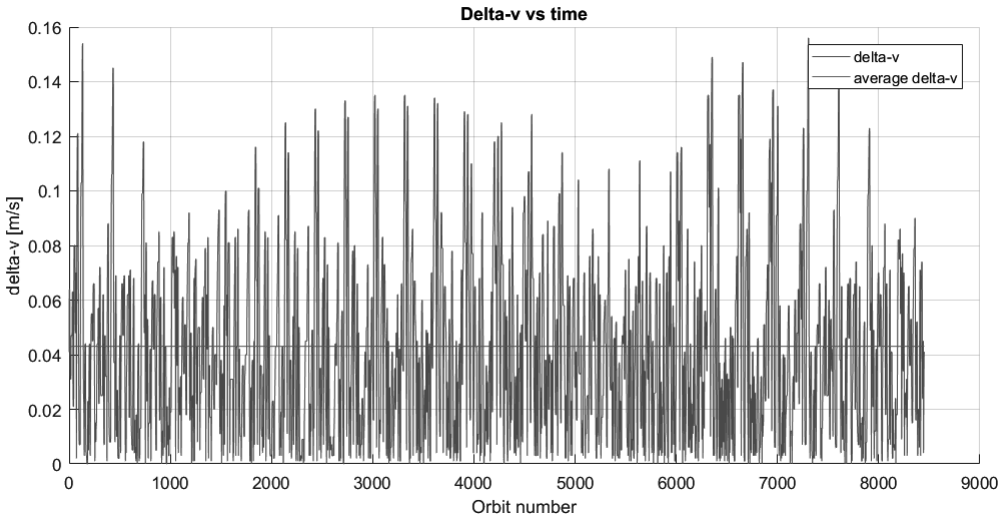

Figure 3.11: Δv values in m/s per orbit over the mission phase

In figure 3.11 the amount of Δv required for each burn during a simulation of the entire mission phase of two years for the orbit configuration with its periapsis at 15 km and apoapsis at 300 km and the average Δv of these 2 years can be seen. The values in this figure are the absolute Δv values. GMAT will also output negative Δv values which correspond to the manoeuvre being a manoeuvre where the periapsis needs to be lowered to the nominal altitude. For graphical illustration the absolute values have been taken and shown in figure 3.11. As explained previously a manoeuvre is performed every orbit as to keep the maximum required Δv for station keeping as low as possible, this translates to a total of 8450 burns. This results in a maximum Δv value is 0.156 m/s and the minimum value approaches zero. The average Δv value is 0.0431 m/s. These Δv correspond to an average and maximum burntime of 12.3 and 44.6 minutes respectively.

Now the orbital parameters have been configured, the way the three satellites' orbit is going to vary will have to be considered. The desired difference in orbital parameters will be for the RAAN to vary 120 ° between each satellite. This, together with a difference in deployment AOP will ensure that at at least 1 satellite will have its periapsis in the nightside of the Moon and therefore ensure that at least 1 satellite will be able to perform measurements during the mission.

3.4.2 Deployment Phase Results & Discussion

When the satellite(s) are deployed, they will be deployed at a circular orbit of 500 km. The inclination at which the satellites are deployed may differ though. For scientific reasons, the desired deployment inclination is 50° as mentioned in section 2.3.1.

Since the satellites may be deployed at another inclination, research has to be done whether the system can handle other inclinations as well and if possible, perform manoeuvres to achieve the desired inclination of 50° or another inclination. In table A.2 the different inclinations for which this research has been done can be seen. In this table the first column represents the possible deployment inclinations. The second column is the calculated Δv values for station keeping in this respective orbit. The third column is the difference in Δv with respect to the desired 50° inclination over two years. The two year value for each inclination is assumed by multiplying the second column's value by 12. A positive value in the third column means more Δv is required to stay in the nominal orbit. Negative value means less Δv is required. The last column shows whether an inclination change is desired or not.

It is assumed that all 3 satellites will be deployed almost simultaneously, their starting orbital parameters however are different with respect to the starting RAAN angle as discussed in section 3.4.1. Therefore their deployment phases will differ after a possible inclination change has been performed. The desired difference in RAAN angle is 120 degrees between each satellite. This was formulated as such to accommodate the desired fact that when 1 satellite its periapsis has gone into the dayside of the moon another satellite would have its periapsis in the night side and therefore ensure that at least 1 satellite will be able to perform measurements during the mission. To achieve this change in RAAN the second and third satellites will stay in the circular orbit of 500 km. However as can be seen in figure 3.12 it takes one month for a change of slighty more than 9 ° in RAAN between the mission and deployment orbit. If this result is assumed to be representative and is extrapolated for the whole mission, to achieve a 120 and 240 ° difference the waiting period would then be one and two years, respectively. Since this would defeat the purpose of having such a difference in RAAN this option is therefore not valid.

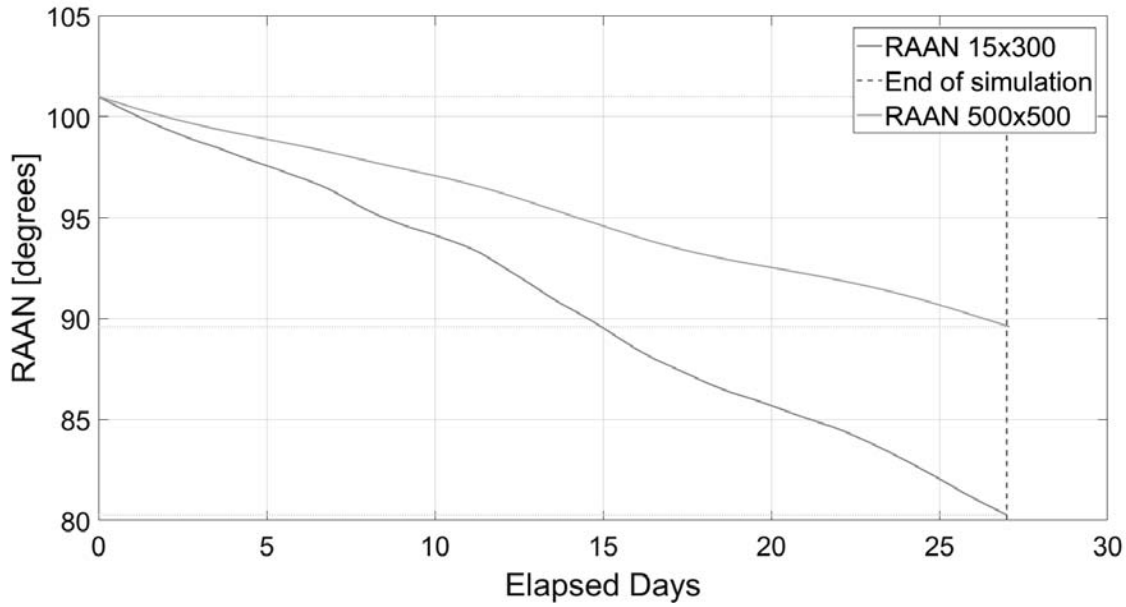

Figure 3.12: Travel of RAAN for the nominal and deployment orbit due too natural perturbations over a month

For this stage of the design further options for the difference in the deployment parameters for the three satellites have not been assessed. However, the following options have been identified.

- Decreasing the difference of the RAAN angle between the three satellites will decrease the time that the second and third satellites will spend in the deployment orbit. In figure 3.12 it can be seen that one month will result in a change of around 9 °. Depending on the new desired difference in RAAN the waiting time in the deployment orbit can be decreased.

- A drastic change from having a difference in the RAAN angle is having no change for this angle but having the satellites fly in the same orbit. The approach would be as such: all satellites should be deployed in the same direction to ensure the resulting orbits are mostly alike. To make sure no collision occurs between two satellites the time of separation for all three satellites should vary slightly. After this the first satellite will start its deployment phase. Dependent on how far the three satellites have to be separated the other two satellites will wait for a certain amount of orbits before performing the same deployment phase starting at the exact same position. This will ensure the satellites fly in a comparable orbit but phased slightly off from each other. This approach would mean however that for certain periods of time no measurements will be able to be performed by the TID since none of the satellites will be in the night side while below 39 km.

Lowering the orbit is divided into two stages. First the orbit is lowered from the 500 km circular to a 300 km circular orbit. After that the periapsis is lowered to the nominal periapsis' altitude of 15 km. Due too power constraints the propulsion system can only be used for a certain amount of time each orbit. The amount of Δv that is applied each orbit is corresponded to the maximum burntime of the mission phase, which is shown in 3.4.1, since the EPS (chapter 10) will be able to handle this burnduration for the mission orbit, even when in eclipse and thus will be able to perform the required power to the propulsion system during the deployment phase as well. For this phase of the design it is assumed for the deployment phase that first one side of the orbit is lowered to a 300 km altitude and after that the other side. In table 3.4 the results of this approach can be seen.

Table 3.4: Deployment phase - Lowering the orbit to nominal mission orbit

Stage	**Action**	**Required Δv [**m/s**]**	**Time [**days**]**
1	Lower Periapsis to 300 km	43.3	26,4
1	Lower Apoapsis to 300 km	44.4	46,2
2	Lower Periapsis to 15 km	67.4	37,2
Total:		**155**	**110**

In table A.2 various parameters of the possible deployment inclinations can be seen. The nominal orbit is a 50° orbit. Because of the dependence for the deployment inclination on the Lunar Orbiter, the deployment inclination might not be the nominal one. Therefore it should be considered at what inclinations the mission can no longer be completed. This is shown in table A.2. The system is designed for a 50° inclination orbit, however the propulsion system takes a contingency factor into account for unforeseen circumstances. This translates to an extra Δv value of 113 m/s, which can be used for extra station keeping or performing inclination changes. The third column indicates what extra Δv is required or is freed over the course of two years for each inclination in the mission orbit. When this value is larger then the contingency Δv of 113 m/s the deployment inclination is deemed not feasible. There are some exceptions to this rule, this is the case when it is still possible to perform an inclination change to get to a feasible orbit. From this it can be concluded that the inclination range the LUMID system can be deployed at is from 50° to 67° and from 83° to 90°. For the inclinations between 67° and 83° it is not possible for the system to complete the full mission duration of two years.
The last column shows whether an inclination change manoeuvre is desired or not. In table 3.5 an indication of the Δv cost of performing an inclination change can be seen. Between 48° and 52° an inclination change is possible. Outside this range the time that is required outweighs the fact that is possible and is thus possible, but not desired.

Table 3.5: Δv change for various inclination changes

Inclination difference from nominal inclination[°]	**Δv [m/s]**	**Number of orbits**
-1	28,673	201
0	0,000	0
1	20,249	144
2	54,095	374

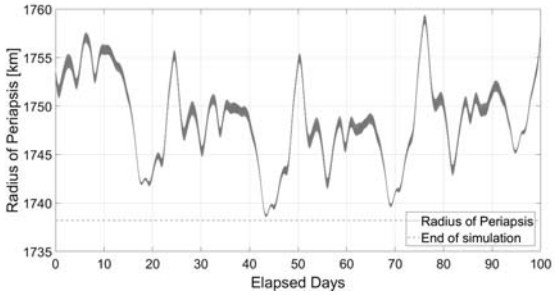

(a) Radius of periapsis vs elapsed days without burns

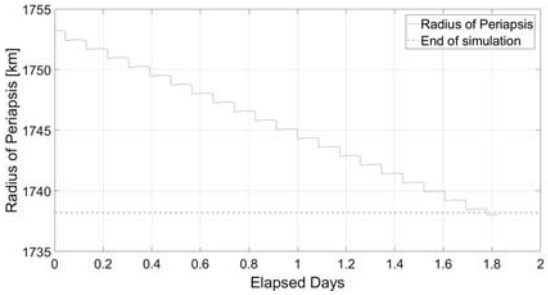

(b) Radius of periapsis vs elapsed days with burns

Figure 3.13: Radius of periapsus of end of life phase without (a) and with (b) burns to perform a controlled impact

3.4.3 End of Life Results & Discussion

As stated in section 3.3.1 the satellites will, after the mission phase, asses how much propellant is left in the system. As a result of this value the mission could be extended for a certain amount of time. In figure 3.13a the radius of periapsis is plotted versus the elapsed days if no propellant is left in the system and no crash burn is performed. However, since this would imply the impact of the satellite is not controlled it is desired to perform a crash burn. Figure 3.13b shows the radius of periapsis versus the elapsed days when a maximum burn is performed to lower the radius of periapsis. Table 3.6 shows the corresponding values.

Table 3.6: End of life phase cost estimation

Periapsis starting altitude [km]	**Total Δv cost [m/s]**	**Total time required [days]**
15	3.5	2

In figure 3.13a and 3.13b the difference between a non-controlled and controlled (with burns) impact on the lunar surface can be seen. The corresponding values for performing these burns can be seen in table 3.6. The conclusion that can be drawn from these values that the required Δv and amount of time is not large with respect to the total mission Δv cost and duration. The end of life phase does depend on the amount of propellant that is left in the tank. The values in table 3.6 will have to be recalculated according to the amount of time the mission can possibly be extended and the corresponding new end of mission parameters. To make sure there will be no uncontrolled impact of the satellites into the lunar surface, a certain amount of Δv, dependent on the end of mission parameters, should always be left for the end of life phase. In this way a controlled impact in a predetermined location on the lunar surface can be ensured.

3.4.4 Orbit Control Failure

There is always a chance of orbit control failures, which can cause the inability of the satellite to perform manoeuvres. To see the impact of these anomalies simulations at different events in the satellites lifetime are made. To have a diverse view on the effects of these failures 13 different situations are evaluated. The first ten events in the mission phase are picked randomly and the other three are “extreme” cases. The latter are based on possible risky moments to lose the ability to perform manoeuvres. These are the events when the periapsis or the apoapsis are at their minimal value as

seen over the entire two year simulation and when the semi-major axis is at its smallest value for the whole mission phase. For every of these 13 cases the related orbital parameters are set as initial values of the simulation and the timestamp of that event is set as epoch. The script is set that it will perform a simulation till the satellite crashes, i.e. orbital altitude drops below zero, or until it travels for a period of 14 more days, which is assumed to give enough time to fix any errors. The different cases are displayed in table 3.7.

Table 3.7: Different events at which no burn simulations are performed

Event	Epoch	Radius of Periapsis	Radius of Apoapsis	Inclination	RAAN	Argument of Periapsis	True Anomaly
Random 1	28 Nov 2019 18:53:24.990	1753.0637	2052.7404	50.7228	96.9334	345.7721	257.5702
Random 2	26 Jan 2020 09:23:54.340	1753.0674	2039.9958	49.2675	51.4000	26.6854	302.5725
Random 3	18 Mar 2020 18:46:15.213	1752.8405	2060.6806	49.1949	9.8351	57.1797	62.7278
Random 3	02 May 2020 10:56:37.921	1753.0913	2075.7667	50.1292	334.9362	72.8622	12.6629
Random 5	03 Jul 2020 01:11:32.848	1753.4984	2077.5731	50.7546	285.1995	104.1803	218.1799
Random 6	02 Oct 2020 16:26:50.270	1753.4463	2041.0535	51.9271	214.9906	145.4264	65.9098
Random 7	21 Jan 2021 03:52:39.095	1753.3041	2037.8107	50.5190	131.3007	215.5022	25.9099
Random 8	01 Apr 2021 14:27:47.737	1753.1684	2030.6938	50.5038	78.5125	284.5430	313.3893
Random 9	02 Jul 2021 02:37:21.814	1754.2279	2031.9900	49.7917	7.79190	354.6649	200.6521
Random 10	23 Sep 2021 23:57:47.748	1753.0183	2067.3933	49.2220	301.8414	47.8079	155.4955
Lowest Periapsis	10 Sep 2021 21:52:09.505	1752.0434	2045.2975	48.8752	312.4930	42.4269	234.6660
Lowest Apoapsis	28 Mar 2021 00:16:43.482	1753.1039	2013.5434	49.7021	81.3484	276.8048	343.6826
Smallest Semi-Major Axis	28 Mar 2021 00:10:54.353	1753.0632	2013.5765	49.7030	81.3516	276.8414	324.1832

From the simulations the conclusion can be drawn that the situation when the apoapsis is at its lowest point is the most critical point, because the satellite will crash after only 4.08 days. The other results are documented in table 3.8.

In figure 3.14 the change in the radius of both the periapsis and the apoapsis when there are no manoeuvres performed are shown. The periapsis decreases at the same rate for approximately two and a half days until it dropped 5 km. After that the slope increases and drops the remainder 10 km in 2 days. The apoapsis deviation shown in figure 3.14b follows the opposite motion and increases over time. This means that the orbit is getting more and more elliptical and thus that the eccentricity increases. In table 3.8 it is also visible that in seven of the thirteen cases, the satellite crashes in around ten days. This proves that a Moon orbit is indeed vary unstable and that frequent station-keeping is indeed required. By this means, these results can also be seen as sensitivity analysis.

3.5 Conclusions

Final Trajectory Configuration

The final trajectory of the LUMID system is the three different mission segments, deployment, mission and end of life phase, stitched together. The parameters for these different segments are shown in tables 3.9 to 3.11. In the tables the initial parameters are shown for the first satellite that will enter

Table 3.8: Results of no burns simulation

Event	Epoch	Time elapsed till crash or 14 days	Crash event or 14 day event
Random 1	28 Nov 2019 18:53:24.990	13.9996	12 Dec 2019 18:52:51.125
Random 2	26 Jan 2020 09:23:54.340	10.3019	05 Feb 2020 16:38:36.908
Random 3	18 Mar 2020 18:46:15.213	10.2745	29 Mar 2020 01:21:34.120
Random 3	02 May 2020 10:56:37.921	13.9997	16 May 2020 10:56:11.443
Random 5	03 Jul 2020 01:11:32.848	13.9991	17 Jul 2020 01:10:16.304
Random 6	02 Oct 2020 16:26:50.270	5.39166	08 Oct 2020 01:50:49.976
Random 7	21 Jan 2021 03:52:39.095	13.9997	04 Feb 2021 03:52:17.361
Random 8	01 Apr 2021 14:27:47.737	13.9995	15 Apr 2021 14:27:03.079
Random 9	02 Jul 2021 02:37:21.814	8.76062	10 Jul 2021 20:52:38.998
Random 10	23 Sep 2021 23:57:47.748	14.0000	07 Oct 2021 23:57:45.464
Lowest Periapsis	10 Sep 2021 21:52:09.505	10.5987	21 Sep 2021 12:14:19.784
Lowest Apoapsis	28 Mar 2021 00:16:43.482	4.07878	01 Apr 2021 02:10:09.719
Smallest Semi-Major Axis	28 Mar 2021 00:10:54.353	4.08283	01 Apr 2021 02:10:10.975

the deployment phase. The RAAN and AOP values of the other satellites are dependent on what deployment method is chosen and are therefore not shown.

Table 3.9: Deployment phase parameters

Element	Value
Epoch	1 Aug 2019
RadPer	2238 km
RadApo	2238 km
Preferred Inclination	50°
RAAN	161°
AOP	347°
TA	0-360°
Required Δv	155 m/s
Phase duration	110 days

Table 3.10: Mission phase parameters

Element	Value
Epoch	22 Nov 2019
RadPer	1753 km
RadApo	2038 km
Inclination	50°
RAAN	101°
AOP	347°
TA	0°
Required Δv	364 m/s
Phase duration	2 years

Table 3.11: End of life phase parameters

Element	Value
Epoch	21 Nov 2021
RadPer	1753 km
RadApo	2077 km
Inclination	51°
RAAN	256°
AOP	72°
TA	0°
Required Δv	3.5 m/s
Phase duration	2 days

Conclusions

Using inputs from the payload and the propulsion subsystems an optimal orbital configuration has been configured. This optimal orbit is an elliptical orbit of 15×300 km altitude above the lunar surface. Since the gravity field of the Moon is a highly irregular field, see figure 3.1, manoeuvres have to be performed to maintain the orbit. These manoeuvres have been simulated using impulsive burns. Next to the station keeping during the mission phase that is required to maintain the nominal orbit, the deployment phase consists of performing manoeuvres to lower the orbit from a 500 km circular

orbit. The desired inclination for the LUMID satellites is 50°, however since the deployment inclination might vary between 50-90 °, an analysis was done to see what deployment inclinations are allowable for the LUMID satellites. This is shown to be between 50-67° and 83-90°. Inclination changes to achieve the desired inclination will only be performed at the inclinations of 48-52 °. After the mission phase, the end of life phase is entered during which the satellites will perform a controlled impact onto the lunar surface on a predetermined position. In total these manoeuvres have a Δv cost of 522.5 m/s. A 120 ° difference in RAAN angle between the three satellites with the approach of the second and third satetellites waiting in the deployment orbit has been deemed infeasible. The following other options have been defined; decreasing the difference in RAAN angle between the satellites or having the satellites fly in the same orbit but separated by a certain amount.

Recommendations

For the astrodynamics of the LUMID design, some assumptions and observations were made that will have impact on the design.

- The largest of these is that the current Δv cost is calculated using impulsive burns, which is not a realistic assumption for a LUMID satellite. This is mostly due to the fact that the design incorporates a low thrust propulsion system. The result of which is that the burnduration of burns will increase greatly and thus making the assumption of impulsive burns invalid, since the relatively low altitude orbit means the fraction of the total orbit period the burn needs to be performed is high and therefore is not neglible. The implications of which would be that Δv cost will increase when implementing all the calculations of 3.3.3. These calculations should be done for a couple of iterations and a convergence of the total Δv cost to a certain value should become apparent. When a designer specified accuracy on this convergence is obtained, the new required burntime for a manoeuvre can be calculated. This gravity loss induced Δv is expected to have a significant impact on large Δv values. In figure 3.11 the Δv values for the entire mission phase can be seen, it can be noticed that there are peaks of relatively large Δv values. However the mean Δv is a factor of three smaller than these peaks. Therefore it can be concluded that the gravity losses will definitely have to implemented to achieve a more realistic design, however the impulsive burn method can be used for first estimations of the design. If the gravity losses are taken into account, it will have the following impact: burnduration will be longer which will put larger requirements on the PROP, EPS, AOCS system which in turn will increase the mass and size of these subsystems.
- In future work the deployment parameters should be further looked at. In simulations for two years it can be seen that not only the RAAN travels around the Moon, which causes the unwanted effect of having the periapsis not in the night side, but also the AOP will vary, which can also cause the same unwanted effect with the added affect of the probability that the time spent in the measurement range of the TID can decrease by this varying AOP. Further research should include doing research in the deployment angle of the AOP of each satellite seperately. It should be calculated what the optimum configuration of deployment AOP angle is in order to maximise the time that can be spent taking measurements with the TID in the night side of the Moon.
- To gain or increase the scientific value of the end of life phase, options as discussed in section 2.4 like using the crash as source of data collection should be explored. One can investigate the crash site or the plume that the crash leaves, for example.
- To improve the mission design even more, time should be spent investigating the safe-mode option. In section 3.4.4 the situation of orbit control failures are discussed. In the section a time span of 14 days is assumed to be enough to solve any problems, this claim should be looked into and also other options should be explored. Furthermore, the section concluded that in the worst case scenario the satellite will crash in slightly more than four days. It should be determined if fixes can be found and executed in such short time periods.

- The final action which should be made if further time is spent on the astrodynamic analysis is making sure the components that are used for the simulations are on a higher degree of accuracy. For the current simulations the accuracy is set at such a value that running the simulations don't take up too much time. If more time were available, the accuracy of the simulation could go up since the runtimes can be longer.

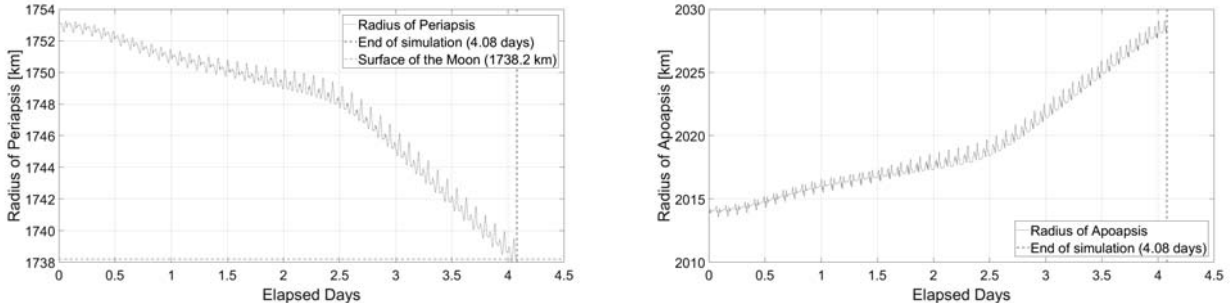

(a) Radius of periapsis

(b) Radius of apoapsis

Figure 3.14: Radius of periapsis and apoapsis vs elapsed days in the case of orbit control failure at the lowest apoapsis

CHAPTER 4

LUMID Design Specification

With the mission and the astrodynamic characteristics known, the LUMID-satellite can be defined. In this chapter, the spacecraft will be defined in terms of functions (section 4.1), subsystem definition and system architecture (section 4.2).

4.1 Functional Diagrams

The starting point of the design is to define the functions of the LUMID. In figures 4.1 and 4.2 the functions are described in two ways. The Functional Breakdown Structure shows the overall functions the satellite has to perform and the Functional Flow Diagram shows the chronological ordering of the functions of the breakdown structure and adds the pre-operation phases as well as the end-of-life phase. There are also certain subsystems that have to be maintained continuously during the operations phase. These functions are specified with the starting code of 3.C. The functional analysis is of a top-level view. The subsystems (which will be defined in the next section) will have a detailed functional analysis in their respective chapter

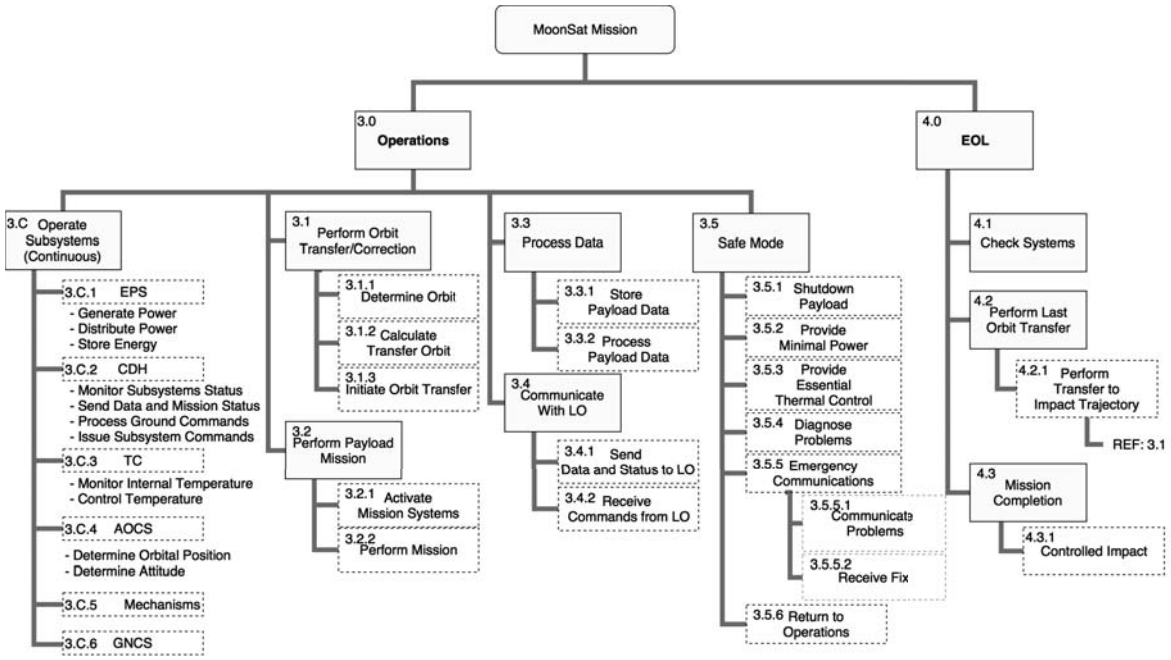

Figure 4.1: Functional breakdown structure of the LUMID

4.2 Subsystem Definition

To start of with the design, the satellite will be split into subsystems. The first systems are defined according to functions 3.3 to 3.5, which consists of obtaining measurements and getting the data to the ground. This critical path of data will be supported by the rest of the subsystems, which correspond to the continuous functions in figures 4.1 and 4.2. The top level interactions between the subsystems and the ground station is given in a mission architecture, which is given in figure 4.3. The order of the subsystems corresponds to the order from chapters 5 to 12.

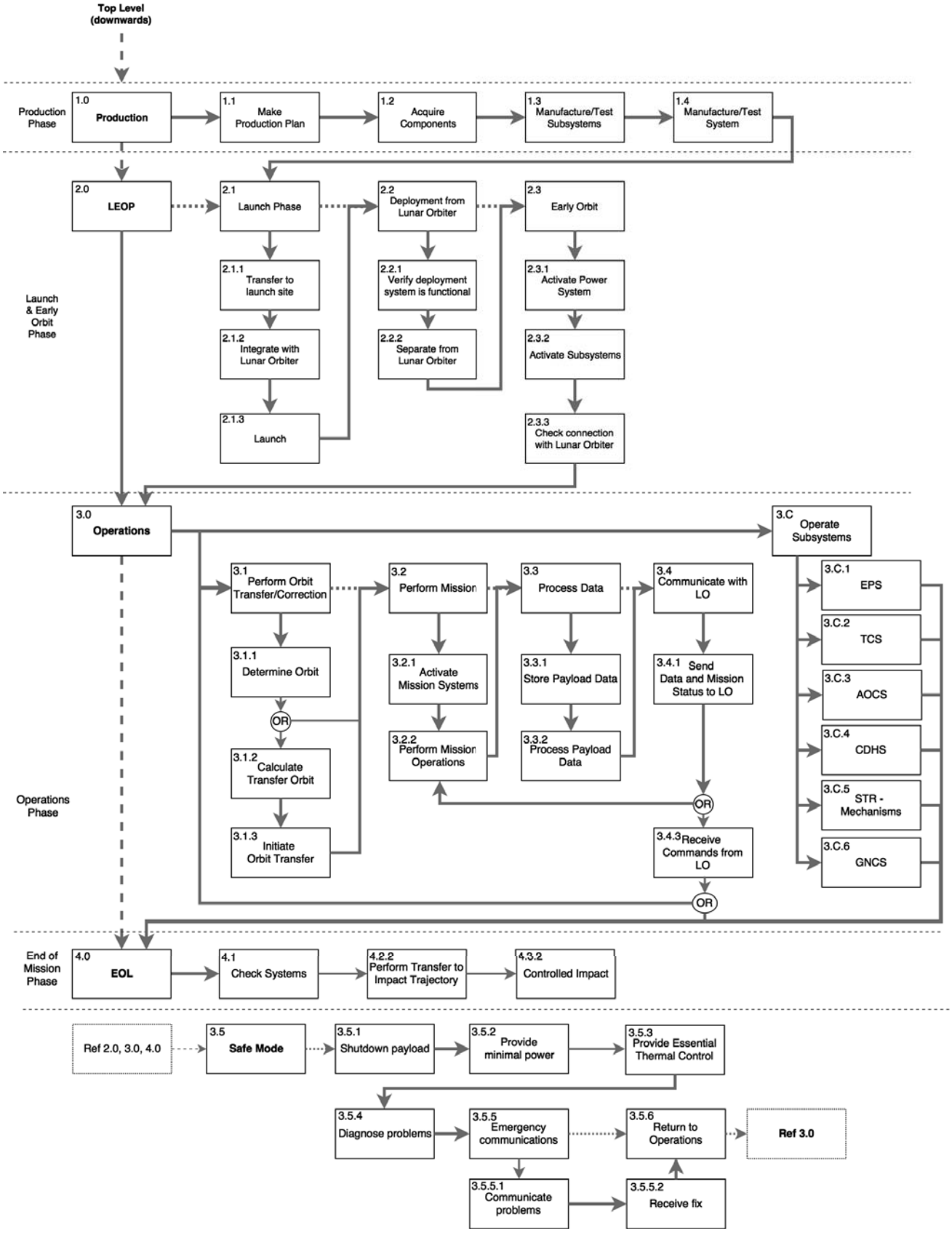

Figure 4.2: Functional flow diagram of the LUMID

Payload System (PLS) This design starts by defining the payload used of measurements. This system will measure the micrometeoroid impacts and will record the data.

Command and Data Handling System (CDHS) The data generated by the payload will be processed and stored on board by the CDHS. Besides that, the system will also monitor the status of other subsystems, issue commands, and process ground control commands.

Telemetry, Tracking and Command System (TTCS) The TTC will send and receive signals from the Lunar Orbiter. The commands and data will be sent to and from the CDHS.

Attitude and Orbit Control System (AOCS) The AOCS combines the functions of attitude determination, attitude control, orbit determination, guidance and navigation. The AOCS will provide the information to the CDHS and will rotate the spacecraft such that the spacecraft can point towards the Sun and lunar orbiter and the payload can point towards the lunar surface.

Propulsion (PROP) The propulsion for the LUMID will provide the means to transfer the orbit from deployment to the mission orbit. Besides that, the system will also provide the station-keeping necessary to maintain a 15 km periapsis.

Electrical Power System (EPS) The EPS will provide all electronic systems with the power needed.

Structures and Mechanisms (STR) The structure will contain all on-board satellite components and protect them from launch loads and radiations. It will also include mechanisms needed for deployment.

Thermal Control System (TCS) The TCS will control the temperature of the LUMID and will ensure that the temperature stays in the operational temperature range.

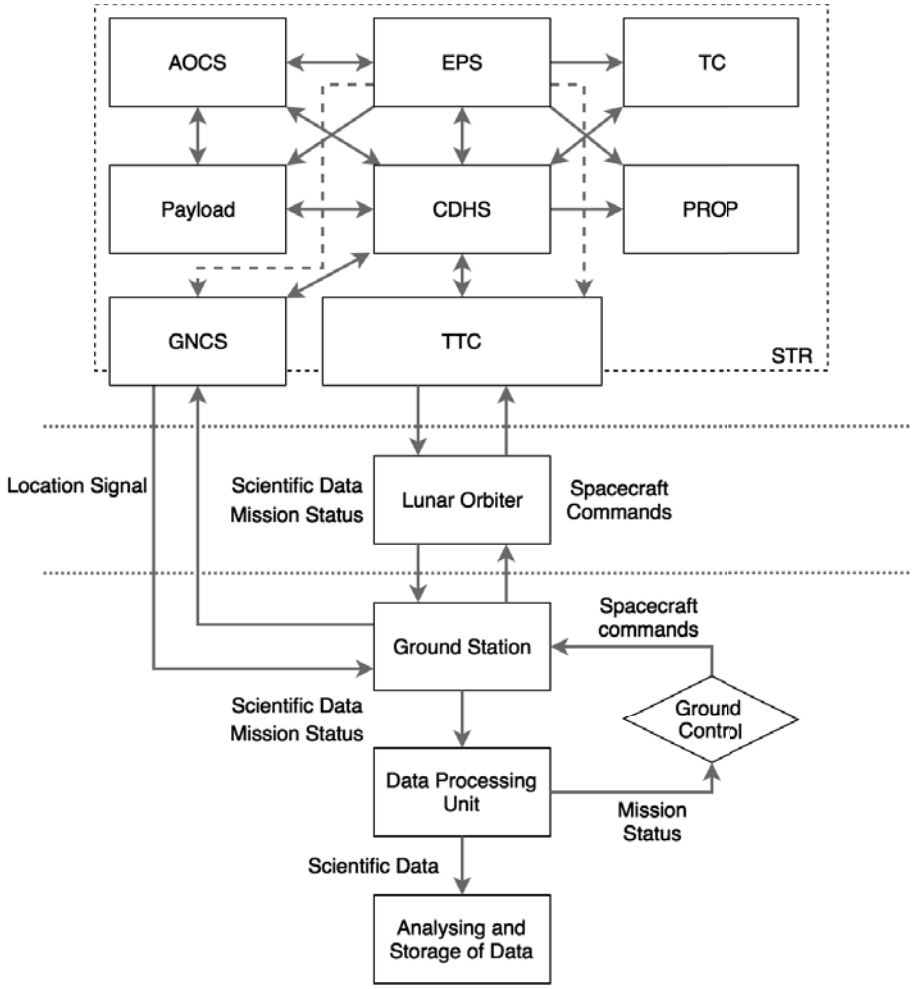

Figure 4.3: System architecture

CHAPTER 5

Payload System

The Payload System is the subsystem of the LUMID that will perform the scientific part of the mission, which is measuring the frequency and characteristics of micrometeoroid impacts. This chapter includes the design process that has been followed and the final design specifics will be presented. Additionally, recommendations for future work and improvements will be given.

5.1 Subsystem Description

The payload system will measure micrometeoroid impacts in two different locations in the lunar region. Firstly, the lunar surface will be scanned for heat spikes that are caused by the high-energy impacts. The Thermal Impact Detector (TID) has been designed to fulfil this function. Secondly, in addition to scanning the surface, in-situ measurements will be performed. A 2-stage impact detector has been designed that will detect micrometeoroid impacts that occur on the device itself.
It has been decided that two distinct devices will be used to measure characteristics of micrometeoroid impacts (MMI). As main payload system a thermal impact detector has been designed. This system is able to measure the meteoroid impact flux on the surface on the Moon. The secondary payload system consists of four 2-stage impact detectors per satellite. This system will measure the flux of MMIs that will hit the device itself, but also estimate their velocity, incidence angle and mass. These characteristics can be combined and show the correlations between the meteoroids in-orbit and the impacts on the lunar surface.
In table 5.1 the requirements for the payload systems are listed, as well as the section in which their compliance is verified. Most of the requirements were established in the baseline report [36]. Requirements R-SC-SI-2, R-SC-SI-3, R-SC-SI-4, R-SC-SI-5, R-SC-SI-7 and R-SC-SI-8 have been discarded because they were no longer deemed to be necessary requirements.

Table 5.1: Payload requirements

Identifier	Requirement	Section	Compliance
R-SC-PL-1	The SI subsystem shall detect in real-time the impacts of micrometeoroids at least as small as 1 µm in it's longest dimension	5.3.4	✓
R-SC-PL-6	The SI subsystem shall not exceed the dimensions of the cubical units on the s/c allocated to it.	5.2.2	✓
R-SC-PL-9	The SI subsystem shall relay the science data to the CDHS at a maximum data rate of 275.25 Mbps	5.2.4	✓
R-SC-PL-10	The SI subsystem shall be capable of shutting for entrance in safe mode and resume nominal operation upon command from the CDHS	5.2.4	✓
R-SC-PL-11	The surface-projected plane of view shall not increase more than 3% in width due to a pointing offset from the nadir.	8.2.4	✓

5.2 Thermal Impact Detector

The thermal impact detector is a device that will sense the lunar surface for heat, generated by micrometeoroid impacts. This section describes how this heat has been modelled and how the thermal impact detector will measure this heat. Additionally, the detection performance of this device will be assessed.

5.2.1 Measurement Model

In order to assess the performance of the Thermal Impact Detector a model the represent an impact on the moon must be created.

Signal Model

As soon as a MMI occurs on the surface of the Moon the projectile's kinetic energy is converted into heat, which will dissipate to a large part into electromagnetic radiation. Part of this electromagnetic energy lies in the infrared band. The radiated heat is modelled following Planck's law of black-body radiation. The model assumes that a meteoroid impact creates a heat-affected crater with a certain surface temperature and a diameter (d) that is based on the following scaling law: [37]

$$d = 0.25 \cdot \rho_p^{0.167} \rho_t^{-0.5} g^{-0.165} E^{0.29} \sin^{\frac{1}{3}} \theta_i \tag{5.1}$$

In which ρ_p and ρ_t are the densities of the projectile and the target bulk, respectively. Their values can be assumed to be 2000 kg/m^3 and 3000 kg/m^3 respectively [37]. g is the lunar gravitational constant and E is the kinetic energy of the meteoroid. θ_i is the incidence angle of the impact, which is assumed to be a constant 45°. According to Bouley et al [37] impact heat is dissipated within 10 ms and 1 s. Therefore, it is assumed that the impact heat of the smallest detectable meteoroid lasts 10 ms at minimum. An additional assumption is that during this flash the surface temperature of the crater is constant and has a temperature of 3500 K [37]. This energy is radiated away, which can be estimated using Planck's law of black-body radiation:

$$L_{\text{impact}}(\lambda) = \frac{2\pi h_p c^2}{\lambda^5} \left(e^{\frac{hc}{\lambda k_g T_e}} - 1 \right)^{-1} \text{ (W/m}^2\text{)/m} \tag{5.2}$$

Equation 5.2 shows the power flux per wavelength. Here are h_p, c, λ and k_g the Planck's constant, the speed of light in vacuum, the wavelength and the Boltzmann constant, respectively. When integrating this over the bandwidth to which the camera sensor is sensitive the total power flux that reaches the camera can be calculated:

$$P = S_e \int_{\lambda_1}^{\lambda_2} \frac{L_{\text{impact}}(\lambda, T_e(t))}{2\pi d^2} \text{W/m}^2 \tag{5.3}$$

In equation 5.3, S_e is the area of the crater. It is assumed that the radiation is emitted isotropically. Furthermore, d is the distance between the impact and the camera, which is the current altitude of the satellite. These equations are used to determine the power of an impact that is received by the sensor. An example: when a meteoroid of 2.5 mg impacts the surface of the Moon with a velocity of 19.4 km/s from equation 5.1 a crater with an area of 50 cm^2 is estimated. Inputting this area in equation 5.3 together with a temperature of 3500 K, a bandwidth of 900 - 1700 nm and an altitude of 15 km, gives a signal power flux of 0.76 mW/m^2.

Noise Model

The signal power is not the only power that affects the measurement. The radiation of noise sources will be registered as well in the measurements and has to be accounted for in the model. Three sources of noise are included in the model:

- Black-body radiation from the portion of the surface that is not affected by an impact.
- Cosmic background radiation.
- Internal system noise of the camera.

The field of view of the camera will cover a certain area on the Moon. In this area only a small portion will be affected by a meteoroid impact. The rest of the area also radiates black-body radiation which is also sensed by the sensor. Equations 5.2 and 5.3 can be used again to estimate the power flux of this

radiation. But now, S_e is equal to the surface area on the Moon that is represented by one pixel and T_e is the average lunar surface temperature during the night, which is 150 K [38]. Assuming that the Moon's surface has a homogeneous emissivity allows to take this temperature value as a constant. Just as for the calculation of the impact power, the wavelengths will be related to the camera's sensitivity spectrum. Calculating the power flux, using the same example as used in the section above a power flux in the order of 10^{-27} W/m^2 is found. This magnitude is negligible to the signal power flux and also constant for all altitudes. It is constant because the value decreases quadratically with the altitude, but simultaneously increases with the covered ground area that increases quadratically on the altitude.

The cosmic background radiation is also included in the bandwidth to which the camera sensor is sensitive and therefore to be taken into account as well. Even at low altitudes this source of noise has a large influence on the measurements because the Moon has a high albedo that reflects a significant portion (13.6%) of the incoming background radiation [39]. From this high albedo follows that on the light side of the Moon almost all infrared radiation that origins from the Sun is reflected. This makes it very unlikely that meteoroid impacts will be detected on the light side of the Moon. The background radiation's intensity in the 900 - 1700 nm bandwidth (which is the sensitivity range of the selected camera in section 5.2.2) can be estimated to have a magnitude of 249 W/m^2/sr [40]. The internal systems noise is a specification of the camera. It is often given as a value of "noise equivalent irradiance" (NEI) which represents how many photons should incident the sensor on a unit of area every unit of time to match the system's internal noise generation. This can be transformed into a unit of power using the energy of a photon [41] [42]:

$$P = \text{NEI} \cdot \frac{hc}{\lambda} \tag{5.4}$$

Where t is a unit of time and for λ the lower limit of the sensors spectrum sensitivity is selected. In figure 5.1 the received power of the signal and noise sources that irradiate the thermal impact detector's sensor is shown. This figure represents the performance of the camera system that has been selected in section 5.2.2. For this graph the defined "minimum" impact is used for the calculations. It can be seen that the noise sources will overcome the signal source near 125 km. At this altitude the signal-to-noise ratio would become smaller than 1 and detection would be impossible.

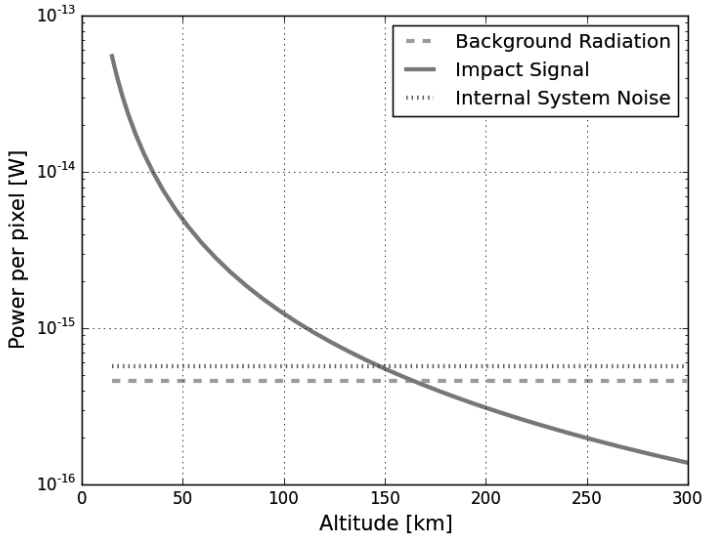

Figure 5.1: Received signal and noise power

Exposure Model

Now that the signal and noise power sources are included, the fashion in which the camera sensor will sense this energy is modelled as well. Firstly, the exposure time of the sensor will be taken into account. To minimise the probability of missing an impact the exposure time is set to be equal to the duration of one image frame (t_{exp} is equal to the inverse of the frame rate). This implies that when the camera system is active the sensor will be exposed and radiated continuously, charging the pixels. The pixel charges are reset every time a frame is stored. During one exposure time, signal energy from the impact and energy from the noise sources is collected in the pixels of the image sensor. These two types of energy must be compared with respect to each other in order to assess the system's detectability performance. The signal to noise ratio (SNR) is a parameter that indicates the system's detectability performance. Equation 5.5 has been derived to estimate the signal to noise ratio.

$$\text{SNR} = \frac{\kappa \cdot P_{\text{impact}} \cdot t_{\text{impact}}}{\left(\kappa\left(2\pi \cdot P_{\text{noise}_{\text{cosmic}}} + P_{\text{noise}_{\text{Lunar}}}\right) + \text{NEI} \cdot \text{qe}\right) \cdot t_{\text{exp}}} \tag{5.5}$$

Here qe equals the quantum efficiency of the sensor. This relates the energy of the photons to the electrical energy that the sensor generates from these photons. P_i indicates the power flux of each source i. Usually the power flux must be multiplied with a unit area and time before it can be related to energy, but in this equation the unit area disappears in the fraction. The power flux of the cosmic background radiation is multiplied with 2π because its radiation intensity is given in power flux per steradian a value of 4π would be used if the sensor would be hit from all directions. All the power flux coefficients that are based on radiation are multiplied by κ. This is a factor that is related to how much the radiation is concentrated on the chip. It is estimated by the ratio of the lens area over the focal plane area, multiplied by the transmissivity of the lens. The focal plane area can assumed to be the area of a circle with a diameter that is equal to the diagonal length of the chip. In this way the focal plane covers the complete sensor, while maximising the the level of increased concentration. For simplicity, an additional assumption is made that states that the all the radiation sources are focused on the chip. This means that it is assumed that the radiation beams enter the lens in a parallel fashion and that the lens is focused on an infinite distance. In reality the focal points of the different sources lie slightly in front or behind the chip, which can either be beneficial or disadvantageous to the measurements. Equation 5.5 has the condition that t_{impact} is smaller than t_{exp}. As mentioned in 5.2.1 a minimum impact is defined by a flash duration of 10 ms (t_{impact}) and P_{impact} is calculated using equation 5.3.

A meteoroid impact is detected on the sensor by comparing the pixels charge levels to each other. If one pixel is a certain amount more charged than the other pixels it counts as an impact detection. A pixel that senses an impact is irradiated by the signal as well as the noise while the other pixels are only irradiated by the noise. The ratio between the charge level of a pixel that detects and impact and an other pixel is defined as the contrast ratio and is simply calculated as:

$$\text{CR} = \frac{C_{\text{signal}} + C_{\text{noise}}}{C_{\text{noise}}} = \text{SNR} + 1 \tag{5.6}$$

Where C represents the charge of a pixel. The contrast ratio is the parameter that will be used to assess the detectability of the system. An impact will be detected if the contrast ratio reaches a certain threshold value. In practice the pixels will not be compared to the charge level of any other pixel, but to the average value of any other pixel. This reduces the influence of any peaks that occur randomly in noise. One important aspect that greatly influences the detectability of the system is motion blur. This is caused by the shift of the field of view during the exposure time due to the velocity of the satellite. Officially an image can said to be free of motion blur if during the exposure time the field of view shifts one tenth of a pixel, maximally [43]. On the other hand, this is a standard for visual photography where high quality of images is required. For this mission a frame is defined to be free of motion blur if the field of view has maximally shifted half a pixel during the exposure. If motion blur occurs the "effective" contrast ratio, which is the contrast ratio compensated for motion blur, can be estimated by using the derived equation 5.7:

$$\mathrm{CR}_{\mathrm{effective}} = \mathrm{CR} \cdot \frac{\mathrm{shift(pixel)}}{0.5} = \mathrm{CR}\frac{V_{\mathrm{sat}} \cdot \frac{r_{\mathrm{moon}}}{r_{\mathrm{moon}}+h} \cdot t_{\mathrm{exp}} \cdot \mathrm{res}_{\mathrm{nadir}} \cdot \mathrm{res}_{\mathrm{sensor}}}{0.5} \tag{5.7}$$

Since motion blur decreases the contrast ratio it could be said that detectability performance is reduced. However, since the the signal power will be spread across more pixels it could be argued that the statistical value of the measurements is increased. Section 5.2.3 discusses how the design performs in respect to motion blur and in section 5.8.1 methods to reduce motion blur are discussed.

5.2.2 Design

Camera Sensor

The device that senses these impacts will be a camera system that measures the infrared radiation that is emitted after an impact. The camera core consists of the FLIR TAU SWIR. This is a commercially available camera that enhouses an Indium Galium Arsenid (InGaAs) sensor which is sensitive to the 900-1700 nm electromagnetic spectrum (Short Wave Infrared). This camera core is very small and lightweight. Impounding only 49 cm^3 and 81 g,respectively. In table 5.2 the most relevant parameters of the camera can be found [44].

Table 5.2: FLIR Tau SWIR specifications

Chip Resolution	640 × 512 pixels	**Pixel dimension**	15 µm
Quantum efficiency	>65 %	**Framerate**	60 fps
NEI	1.78×10^9 photons/cm^2	**Spectral range**	900 to 1700 nm
Power consumption	<3.2 W		

Lens System

The systems described in the previous section only consists of a camera core. In order to get a clear measurement a lens is required that focuses the radiation on the chip. Two important parameters of the lens are the area and the focal length. A larger area gives a larger amount of radiation to be concentrated on the chip. The focal length is directly related to the field of view of the system. A larger focal length gives a smaller field of view. Which decreases the coverage of the system. By keeping this parameters in mind a lens was selected from [45]. The selected lens has a diameter of 100 mm and a focal length of 75 mm. Furthermore, the lens has coating that functions as a band-pass filter for the infrared spectrum from 900 to 10 000 nm. Additionally, the transmissivity of the lens is 90 %. A custom housing for the lens has been designed. It consists of a shell that enhouses the lens and connects the camera system to the satellite's structure. The shell is connected via a cone to the camera core. The shell is designed in such a way that the distance between the center of the lens and the chip is equal to the focal length. It has been assumed that the lens will be focused on an infinite distance. Between the connection of the shell to the structure a silicone rubber layer is placed to damp any vibrations from the satellite [45]. The dimensions of the TID complies to the space allocated in the satellite structure. Which means that requirement R-SC-SI-6's compliance is verified.

5.2.3 System Performance

Detection Performance

In this section the performance of the thermal impact detector will be assessed. The most important performance aspect is how well the system can detect a micrometeoroid impact. This can be quantified in terms of the measured contrast ratio when a minimum impact occurs. Using the equations described in the previous section and the astrodynamical data of the satellite the contrast ratio can be calculated at any altitude of the satellite, provided that it is measuring the dark/eclipse side of the Moon. It has been decided that a minimum impact is defined by an impact area of 16 cm^2 which

radiates at a constant temperature of 3500 K for 10 ms. According to equation 5.1 this corresponds to a micrometeoroid which has a volume of 0.18 mm^3 and a mass of 0.36 mg that impacts the surface with a velocity of 19.4 km/s and at an angle of 45°. The pericenter of the satellite's orbit lies at an altitude of 15 km. At this altitude a contrast ratio of 25 has been calculated. This seems to be a high value. However, when taking motion blur into account the "effective" contrast ratio is only 3.6. Because the satellite's ground speed is close to it's large orbital velocity at such a low altitude. From an altitude of 70 km motion blur no longer occurs because the ground speed will be low enough to shift less than half a pixel during the exposure time. In figure 5.2 the contrast ratio and the "effective" contrast ratio at the full range of the satellite's altitude can be found assuming that the satellite is always positioned at the dark side of the Moon. A threshold value of 2 has been defined for the contrast ratio to count as a impact detection. The "effective" contrast ratio is contrast ratio that will define the detection performance. In the figure can be seen that this value is reached at an altitude of 39 km. This means that from higher altitudes only meteoroids with higher kinetic energies can be detected. For instance, at the apocenter altitude of 300 km a effective contrast ratio of 2 is only reached when the heat affected area is equal to 850 cm^2 which corresponds to a meteoroid of 168.8 mm^3 and 336.6 mg.

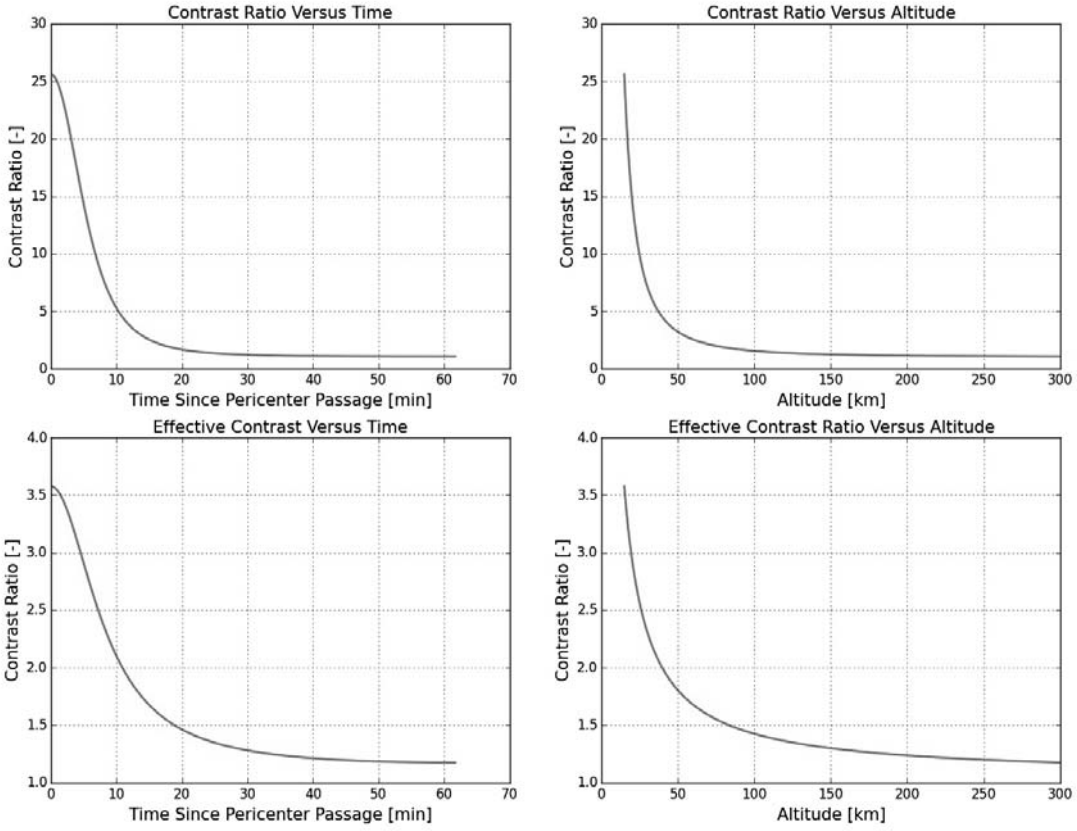

Figure 5.2: Contrast ratio and effective contrast ratio

Coverage

From the focal length of the lens the field of view is calculated to be 7.32°. Together with the resolution of the sensor and the altitude the covered area on the lunar surface can be calculated. At the pericenter one pixel represents an area of 3×3 m^2 on the surface. The full chip then covers an area of 2.95 km^2. Since the exposure time of the sensor is equal to the duration of one frame measurements are taken continuously without interruptions between frames. In figure 5.3 can be seen how the

covered area propagates as the orbit's altitude varies. Since the coverage area is not constant and the satellite is not always located in an eclipse an "effective" coverage area of 166 km^2 per satellite is estimated by multiplying the time average coverage area with the ratio of the average eclipse duration over the orbital period. The three satellites that will orbit the moon at different locations, but with similar orbit characteristics. Therefore the effective coverage are of the three satellites combined is simply three times larger, or 498 km^2 The expected frequency to which impacts are detected will be assessed in section 5.4.

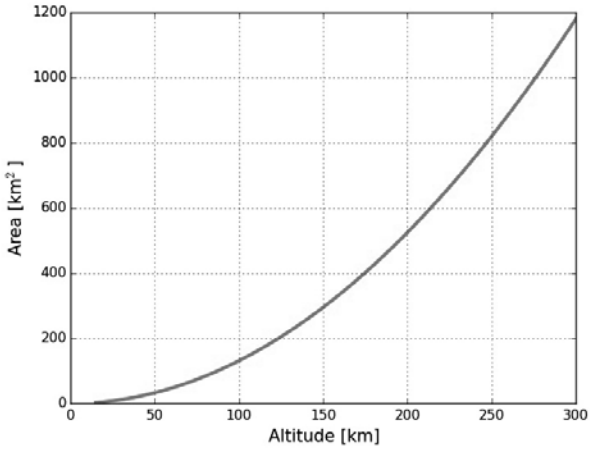

Figure 5.3: Ground coverage area vs altitude

5.2.4 Data Handling

In this section the method in which the scientific data is handled will be described.
The thermal impact detector is activated as soon as the satellites is orbiting above the dark side of the moon. Images will be taken at a rate of 60 frames a second. The frames are send to the CDHS to be temporarily stored for image processing. The camera sensor has a resolution of 640x512 pixels and a bit depth of 8, which means that data will be sent to the CDHS at a rate of 157.3 Mbit/s [44]. Image processing includes noise reduction, based on the statistical properties of the noise model, and motion blur reduction based on the dynamics of the satellite. Finally, the signal from every pixel will be compared to the average value of all pixels from the last minute. If one pixel gives a signal larger than 2 times the average value an impact is detected. The time of impact, the current position and orientation of the satellite, and the location of the related pixel are stored for transmission to Earth. Additionally, part of one frame from before the impact and a frame from after the impact will be compressed and (temporarily) stored as well and only be sent to Earth if requested by the ground station. This part consists of an area of 15×15 pixels, surrounding the impact affected pixel. The CDHS will also send commands to the TID to request housekeeping data and to activate/de-activate the device when transferring from or to an eclipse or when entering safe-mode.
In terms of scientific value, the frequency and location of the impacts will be the main parameters that can be deducted of the measurements. However, the intensity of the charged pixel may also be of value in determining the projectile characteristics for example.

5.3 2-Stage Impact Detector

The secondary function of the scientific mission includes a 2-Stage Impact Detector (2SID) that will perform in-situ measurements to detect micrometeoroids that impact the device while being in-orbit. It implements two techniques to estimate the impact characteristics and the mass of the meteoroid, respectively.

5.3.1 Impact Detection

The 2SID consists of two stages that detect impacts by measuring the vibrations that are generated from such an impact. The two stages consist of sheets that have sensors placed on them that are sensitive to vibrations. When a meteoroid impacts the device it is necessary that it penetrates the first stage and then hits the second stage in order to be able to derive the impact characteristics. The vibrations that are generated by an impact reach the sensors at different times, depending on the propagation speed of the vibrations in the material. From these timing differences the impact location can be derived using multilateration techniques. The thickness of the plates will be ignored in the localisation of the impacts. From this it can be assumed the location of impact is placed in the 2-dimensional space, which means that at least three sensors are required on each stage to determine the locations of impact. Corsaroa et al. mentions that there are many multilateration techniques available, but most use iterative techniques that require a significant amount of computing power [46]. In order to limit the required computing power to a minimum [46] suggests an analytical expression which performs well localising the origin of impact while minimising required computing power. The only constraints in using this expression are that the surfaces are planar and that the sensors are located orthogonally. This method is described in [46]. Another aspect that needs to be considered in the placement is the occurrence of evanescent waves at the edges of the foil. Impact vibrations in plates will propagate as Lamb waves. These waves generate evanescent waves by reflecting on the edges of the foil and will resonate close to the edges. This will interfere with the measurements. In [47] is explained that almost resonance can be neglected at a distance of half a wavelength from the edges. This means that in the design the piezoelectric sensors shall be placed at a distance larger than half the wavelength of the impact vibrations from the foil edges.

Minimising Location Errors

The separation distance and the measurement sample frequency have a large influence on the accuracy of the impact location determination. Impact location errors are translated from errors that occur in timing the impacts. Samples of the sensors signals are only stored at certain clock ticks. In the worst-case, a sensor provides a signal just after a clock tick has passed. A full clock period is then passed before a new tick occurs at which the signal can be registered. It is possible to store the signal in the mean time such that the signal is not lost, by using a capacitor for example, but there is no way of telling at which time the signal arrived between the two clock ticks. This means that the maximum timing error of a signal is equal to the duration of a full clock pulse [48]. In the 2SID this timing error translates to an error in timing the impact between the two stages, which means that there will be an error in the estimated velocity. Furthermore, it also translates to an error in the location of impact on the stage itself, which will give an error in the calculated angle of impact. According to Corsaroa et al. [46] the most common micrometeoroids have a velocity between 10 and 70 km/s. Now a requirement has been defined that states that the 2SID shall be able to estimate the velocity of a micrometeoroid that impacts with a velocity of 70 km/s with an accuracy of 5 km/s at an angle perpendicular to the plate. Equation 5.8 has been derived to calculate the minimum required sample frequency, given a target velocity and accuracy.

$$f^{-1} = \frac{s}{V_{\text{error}} + 3V} = \frac{s}{215000} \tag{5.8}$$

This equation is derived from what clock period f^{-1} would be required to measure v when the meteoroid would impact the stages, separated at distance s, exactly when a clock tick would occur and simultaneously satisfy a maximum error in of velocity v_{error}.

5.3.2 Mass Estimation

Meteoroids are known to generate a small ionising plasma cloud with a certain charge after an impact. According to L. Foschini [49] about 1 % of the kinetic energy is portioned into ionisation. In the cloud electrons are generated that move a certain distance before an electric field is developed to restore

charge neutrality. The magnitude of this electric field can be calculated by measuring how much it interferes with an electric field with a known magnitude [50]. This implies that if in one of the stages an electric field is generated and it's disturbances are measured the kinetic energy of an impacting meteoroid can be estimated. Since the velocity of the meteoroid is already estimated by using the method described in the previous subsection the mass of the projectile can simply be estimated using the standard kinetic energy equation:

$$m = \frac{2E}{v^2} \tag{5.9}$$

Where E and v are the kinetic energy and projectile's velocity, respectively. A electric field is easily generated by a grid of wires with a potential difference between the wires. To simplify the measurements it is suggested to use a static electric field. This means that the potential difference between the wires will be held at a constant voltage. When an impact occurs the value of the potential difference will change a small amount. This change translates to a small change at the voltage supply that tries to keep the electric field at a constant voltage. This change can be measured and related to the kinetic energy of the meteoroid. In a static electrical field no electrical current flows, this means that this system would only require a negligible amount of power correct the disturbances once a field is generated [50].

5.3.3 Design

Since the satellite operates in the gravitational sphere of influence of the Moon it can be expected that most meteoroids will impact from a direction perpendicular to the surface of the moon. Therefore, the 2SID will be directed away from the lunar surface to increase the probability of being hit by an impact. It has been decided to connect 2SID units to the solar panel arrays. One unit will have the same length and width as a solar panel unit which are 320 mm and 220 mm, respectively. It will have a total thickness of 1 cm and the two stages will be separated by 0.8 cm which by equation 5.8 requires a sample frequency of 26.9 MHz to comply with the measurement accuracy. The first stage consists of a aluminium frame that holds a foil of the material "kapton" of a thickness of 25 µm. This foil will not be in tension in order to have better sensor response. Additionally, penetrations of meteoroids will affect the structural integrity less when the foil is not in tension [46]. In [46] it was suggested that both kapton and mylar foils are both good candidates for a 2SID. However, it has been calculated that the thermal expansion coefficient of the kapton fits better to the thermal expansion of the aluminium frame that will be created due to the large thermal fluctuations during the mission. This ensures that no extra tension will be introduced during the mission. Extra tension influences the propagation speed of vibrations and the structural integrity of the foil in a negative way [46]. The second stage consists of two layers of aluminium with a thickness of 0.5 mm. Between those layers a grid of wires is placed that will generate the static electrical field. The power supply will be enclosed in the satellite's core together with a Volt-meter and an amplifier to measure the disturbances. Additionally a high-pass filter will be added to filter out structural vibrations.

From a set of different types of sensors piezoelectric sensors have been selected for both stages. This type of sensors generates a electrical current as it deforms. Which means that a signal will be generated as soon as a structural vibration from the impacts deforms the sensor. Piezoelectric sensors can be made to be very accurate and is very lightweight and require no power. Another type of sensor that was considered is the fiber optic sensor. This type of sensor has a very high accuracy and would not be placed in contact with the stage itself which is beneficial for the vibration propagation and the structural integrity. However, fiber optic sensors require a small amount of power, which makes them less reliable and increases the integration complexity [46]. On the surface of each stage, four piezoelectric sensors are placed perpendicular to each other in the corners of the stage. Three sensors would have been enough for impact localisation, but extra sensors have been added to increase redundancy and an increased statistical value for impact location determination.

5.3.4 Coverage

The coverage of a 2SID unit is determined by the surface area of the upper stage. This area is equal to 540 cm^2. There are four 2SID units placed on each satellite, giving a total measurement area of 0.648 m^2 to total of three satellites. The devices will start to perform measurements continuously from the beginning of the science phase. Most micrometeoroids in the vicinity of the satellite will have a velocity between 10 and 70 km/s [46]. The 2SID will be able to detect a meteoroid with a size of 10 µm when it impacts with a velocity of 12 km/s [46]. By scaling this with the kinetic energy it is estimated that a particle of 1.7 µm and 12 µm related to a velocity of 70 and 10 km/s, respectively.

5.3.5 Data Handling

The 2SID will provide a electrical signals from the piezoelectric sensors device to the CDHS. Here the signals will be analysed and impacts will be detected. From the timing differences the locations, velocity and incidence angle will be estimated. The voltage of the EM power supply will be measured as well and matched with the impact events. From the disturbance the mass will be estimated.

5.4 Expected Results

5.4.1 Meteoroid Flux Model

To know what results can be expected an estimation of the meteoroid flux density has to be made. For this, the Grün interplanetary flux model is used. This model gives a relation between meteoroid mass and meteoroid flux at 1 AU. It is considered to be accurate for meteoroids in the mass range of 10^{-18} to 1 g [51]:

$$F(m) = 3.15576 \cdot 10^7 \left[F_1(m) + F_2(m) + F_3(m)\right] \tag{5.10a}$$

$$F_1(m) = (2.2 \cdot 10^3 m^{0.306} + 15)^{-4.38} \tag{5.10b}$$

$$F2(m) = 1.3 \cdot 10^{-9}(m + 10^{11}m^2 + 10^{27}m^4)^{-0.36} \tag{5.10c}$$

$$F3(m) = 1.3 \cdot 10^{-16}(m + 10^{6}m^2)^{-0.85} \tag{5.10d}$$

$F(m)$ represents the number of meteoroids per m^2 per year of mass m or larger under a viewing angle of 2π. In these equations F_1 corresponds to meteoroids with a mass larger than 10^{-9}G. F_2 refers to particle masses between 10^{-14} and 10^{-9}g and F_3 refers to particles smaller than 10^{-14}g. These equations are used to estimate in which frequency impacts will be detected for both the thermal impact detector as the 2-stage impact detector. It is assumed that both systems can be represented as flat plates with an surface area equal to the system's coverage area and a viewing angle of pi.

5.4.2 Thermal Impact Detection Frequency

As described in section 5.2.3 the coverage area and detectable mass of the meteoroid vary with altitude. The related meteoroid flux is calculated by calculating the average meteoroid flux during one orbit and multiplying this value with the average eclipse over orbit duration ratio over the full mission. Since the mass varies between 336.6 mg and 2.6 mg only F_1 needs to be taken into account. An average flux of 0.07 (impacts/m^2)/year is found. When multiplied with the average coverage area of 166 km^2 (from section 5.2.3, which also includes the average measurement time) during an orbit an estimated impact detection frequency of 109580.257 per year is found. Which corresponds to 1 impact every 28 seconds on average, or 3 impacts every 28 seconds for three satellites.

5.4.3 2-Stage Impact Detection Frequency

As described in section 5.3.4 the total measurement area of the 2SID equals 540 cm^2. It has also been determined that meteoroids as small as 1.7 µm can be detected. Assuming a spherical geometry

and a density of 3000 kg/m^3 this corresponds to a mass of $7.72 \cdot 10^{-15}$g. A meteoroid flux of 2030 meteoroids per m^2 per year is found. Which corresponds to 109.7 impacts per year, or 219 impacts after the entire 2-year mission.

5.4.4 Scientific Return

The two payload systems both measure distinct characteristics of MMIs. The TID will return the meteoroid impact frequency on the surface as well as the intensity of the pixels that measure these impacts. The 2SID will provide the MMI frequency on the satellite and also estimate the mass, velocity and incidence angle of the impacts. This data can be combined with the location and orientation of the satellite, and analysed to show the correlation between meteoroids that are detected in-orbit and the detected impacts on the surface.

5.5 Mass and Power Budgets

In table 5.3 the estimated total mass and power consumption of the total scientific payload is presented.

Table 5.3: Scientific payload mass and power budget.

Component	**Amount**	**Total Mass [kg]**	**Total Power [W]**
TID	1	0.229	3.2
2SID	4	1.644	1
	Total:	**1.893**	**4.2**

5.6 Verification

In this section the verification of the calculations that are used in the design process of the payload is verified. In this, the verification of the calculations that have been performed in this chapter are verified.

5.6.1 Numerical Calculations

During the design phase many of the calculations had to be repeated as design parameters changed. Therefore most calculations have been implemented in a Python script to minimise the total effort and probability of the occurrence of calculation errors. However, this means that some calculations have to be performed using numerical methods, which introduces the possibility of discretisation errors and floating-point errors. To verify that no significant discretisation errors occurred the results from a high level of discretisation were compared to the results from a low level of discretisation. If the absolute difference is within 1% of the value from the high level of discretisation the numerical method is deemed to be accurate enough.

5.6.2 Thermal Impact Detector Calculations

Equations 5.1,5.2 and 5.3 have been verified by inputting the parameters from [37] and comparing if the same results were produced as in [37]. Additionally, sense-checks were performed by checking whether the results changed in a logical sense when changing the parameters of the equations. For instance, increase the temperature in equation 5.2 to see whether or not the radiation power increases.
Equations 5.5, 5.6 and 5.7 are derived based on the functioning of basic photovoltaic sensors. However, there was no reference data available to compare the results to. Which means that only sense-checks were performed to verify the calculations.

Any for some calculations the satellite's orbit had to be modelled. For the orbit simulation in chapter 3 the GMAT tool has been used. Although more accurate, it is a more time demanding method of estimating orbit characteristics than using methods that are based on Kepler orbits. Therefore, in some calculations, such as the average coverage area calculation in section 5.2.3, the orbit was estimated using Kepler methods to minimise processing time. To verify the precision of the results, some orbit characteristics that follow from the Kepler calculations were compared to the orbit characteristics that resulted from the GMAT tool. The values of these characteristics were always in close vicinity to each other which both verifies and validates the use of the Kepler methods. To verify the correct average area calculations, the coverage area at a distinct time instant was calculated using the python script and verified by performing a calculation by hand for the same time instant.

5.6.3 2-Stage Impact Detector Calculations

The most calculations performed for designing the 2SID are generic and were performed by hand. Repeated calculations verified that the calculations were indeed performed correctly. The calculation of the required sample frequency is derived from a method on determining the required clock frequency for digital systems based on a propagation delay [48]. The calculations in the examples in [48] were compared to the calculation of the required sample frequency. It verified that a certain timing error in the 2SID would require the same frequency as a digital system with a minimum propagation time of the same magnitude.

5.6.4 Mass and Volume Calculations

For both scientific payload devices the mass en volume have been calculated. These calculation have been verified as follows. Firstly, for the TID information about the mass and volume for the camera and lens was already available in the official data sheets [44] [45], which are assumed to be a reliable source. A CAD model of the shell that connects the lens to camera has been designed. Inside Catia the volume of the model was estimated and this was verified by performing hand calculations, assuming that the shell could be approximated by generic shapes such as a cone and a cube. The mass was then estimated by multiplying the volumes by the densities of the used materials.
The 2SID has also been modelled in Catia. The volume was estimated and verified in the same way as described above for the shell of the TID.

5.7 Sensitivity Analysis

In this section the sensitivity analysis will be performed. Firstly, in section 5.7.1 the sensitivity analysis on the performance of the Thermal Impact Detector design will be performed. Then, in section 5.7.2 the sensitivity of design of the 2-stage impact detector will be treated.

5.7.1 Thermal Impact Detector

The sensitivity analysis on the TID is performed by changing the input variables and relate this to a change in detection performance, which is expressed in the contrast ratio. Since an extensive amount of parameters are used in the calculations not all variables will be assessed in this chapter. For instance, in section 5.2.1 the power of the black body radiation of the unaffected surface of the moon was found to be constant and negligibly small compared to the other radiation sources. So this parameter will not be used. However, the parameters that have shown the highest sensitivity will be discussed, in addition the parameters that are based on the least valid assumptions will be discussed as well.
Firstly, the effect of altitude on the detection performance will be discussed. Section 5.2.3 shows the contrast ratio of a minimum impact detection versus the altitude in figure 5.2. It can be seen that the contrast ratio decreases quadratically and the "effective" contrast ratio follows a path that is closely resembles a quadratic relation. It differs slightly since it includes a term of ground speed,

which scales to the altitude,h according to $1 + \frac{r_{\text{moon}}}{h+r_{\text{moon}}}$.
Secondly, in section 5.2.1 has been explained that it was assumed that a minimal impact leaves a heat affected area with an equivalent black-body temperature of 3500 K in an area of 16 cm^2. Although the value of the temperature is confirmed by [37], the area is determined assuming that the area of the crater is equal to the heat affected area, which may not be a valid assumption. In figure 5.4 the change in effective contrast ratio can be seen when doubling the temperature or making the are 10 times larger. Doubling the temperature gives a contrast ratio that is 5.2 times larger at an altitude of 15 km. At the same altitude, the contrast ratio is 5.4 times larger when making the impact area 10 times larger.

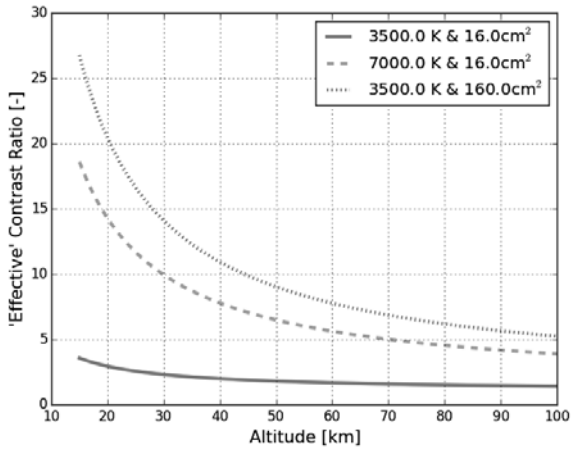

Figure 5.4: Sensitivity analysis impact temperature and area

The next parameters that will be assessed are the lens properties. It is investigated how the contrast ratio changes as the diameter of the lens changes and also if the focal length changes. In figure 5.5 the corresponding graph can be found. It can be seen that at an altitude of 15 km the contrast ratio increases 2 times as the diameter increases 3 times. Where it decreases with an factor $\frac{1}{2.8}$ as the focal length increases 10 times. The next set of parameters is being assessed consist of the frame rate of

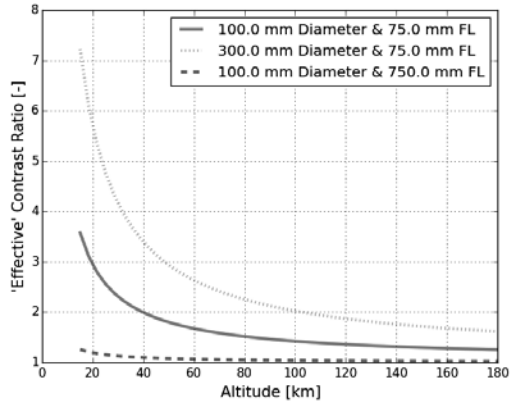

Figure 5.5: Sensitivity analysis lens diameter and focal length

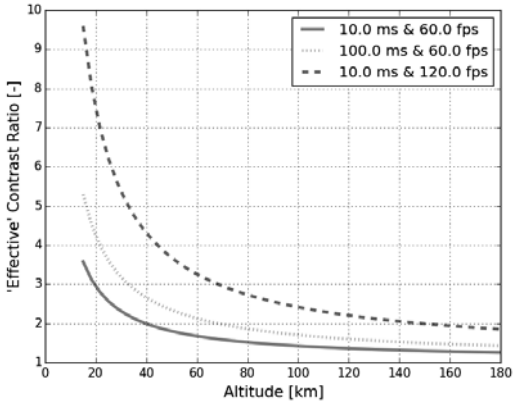

Figure 5.6: Sensitivity framerate & dissipation duration

the camera and the shortest heat dissipation time of the heat affected area. In figure 5.6 the results can be found. It can be seen that as the framerate is doubled the contrast ratio is almost 2.7 times higher. This seems counter-intuitive, but can be explained by the fact that a larger time fraction of the exposure time of an impact to the smaller exposure time of the frame. A limit will occur if the frame rate is so high that the charge level becomes smaller than can be represented by the bit depth of the pixels. In that case the pixel remains black. Maximum heat dissipation duration becomes 10

times larger the contrast ratio increases only 1.5 times. This is because an increase in duration of the heat dissipation will only improve the contrast ratio up to the point that the time equals the frame duration. Since the frame duration is the maximum time the signal can irradiate the sensor for 1 frame. Finally, the parameters in equation 5.1 are responsible to the sensitivity of the volume and mass estimation of the projectile. The equation is used the calculate the diameter of the meteoroid based on the crater size. From the equation it can directly be seen how the diameter will change by changing a parameter. For instance it has been assumed that the projectile has a velocity of 19.44 km/s. It can be seen that the diameter will change quadratically with the velocity.

5.7.2 2-Stage Impact Detector

In the sensitivity analysis of the 2SID the sensitivity of the required sample frequency is investigated. The required minimum sample frequency is described by equation 5.8. In figure 5.7 the variation of the required sample frequency on changing the maximum to be detected velocity, the separation gap between the two stages and the maximum error that may occur. It can be seen that the required frequency behave linearly with respect to the maximum velocity and error, and inversely to the separation gap between the two stages.

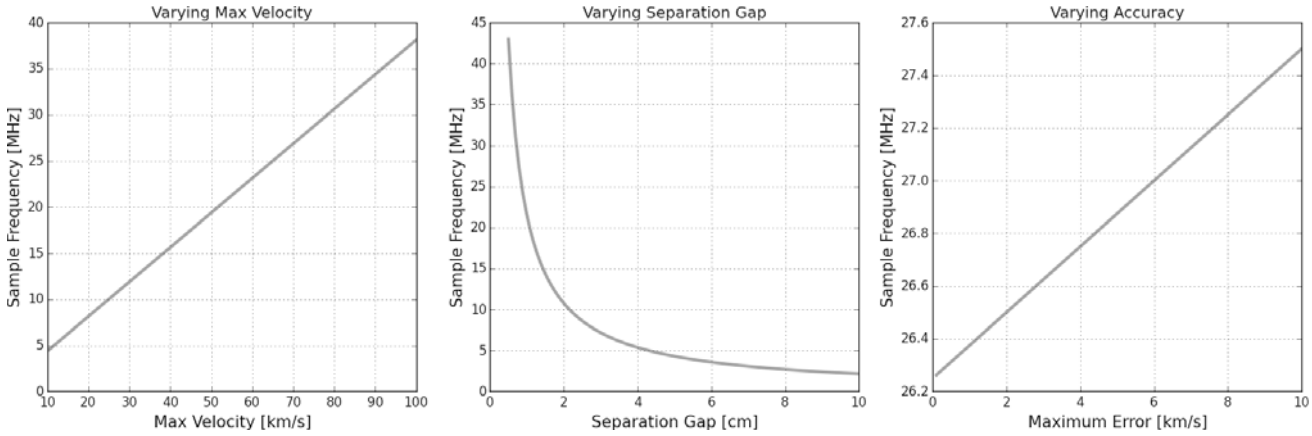

Figure 5.7: Sensitivity on sample frequency

5.8 Future Improvements

In this section some actions are described that have not yet been performed, but could improve the design if carried out in the future.

5.8.1 Motion Blur Reduction

As can be seen from figure 5.2 the motion blur has affects the contrast ratio significantly at lower altitudes. Motion blur can be reduced by using several methods. Firstly, motion blur can be reduced by stabilising the focal plane that falls on the sensor. This can be done by actively tracking the camera's movement, or by predicting the satellite's movement, and the counteract these movements. For this design active tracking will not be a feasible option since it requires a lot of detail in the images, which is not possible with the current system at the dark side of the Moon. Predicting the movement of the satellite could be feasible however. Stabilising the focal plane to counteract the movement can also be performed in several ways. Firstly, the whole satellite could be stabilised using the AOCS. This would mean that for every frame the satellite would have to rotate to centre it's view to area of interest on the lunar surface and then perform a manoeuvre to keep this view on the centre during the exposure time. Subsequently, it would have to rotate rapidly to the area of interest of the next frame. It has been calculated that, even if the satellite would use the full exposure time to rotate to

the next frame, it would require almost 30 Nm of torque to realise this. Which is significantly more than the AOCS can deliver. Therefore it is not feasible to use the AOCS to stabilise the whole satellite.

The next option is to create a smaller AOCS for the camera system only. This would mean that the camera should be able to orient itself independently of the satellite to stabilise the focal plane. However, the structure that has been selected for the satellite does not provide enough space to design a system that can move in such a way. The last option that is considered is to implement a mirror in the camera system that can translate the focal plane across the sensor to keep the plane stable with respect to the sensor. This is the most feasible option of active stabilisation since it requires only a small actuator system for a mirror. Certain Algorithms exist that can compensate for motion blur in image processing. The satellites movement still needs to be known to correctly compensate for motion blur. This system could be assessed more thoroughly in the future.

5.8.2 Components Investigation

More thorough investigation has to be performed is certain components.
For instance, the response of the piezoelectric sensors in the 2SID has not yet been investigated, but will be required to design the additional component such as the amplifier that will amplify the signal for better detection performance.
More investigation in the camera core has to be performed. The FLIR Tau SWIR has not yet been flight-proven for operation in the space environment. The influence of the radiation on the electronics will need to be determined. Additionally, the influence of vibrations on the structural integrity and the measurement performance has to be assessed. Also it has to be assessed whether or not the core will be able to handle intense duty cycle that is required during the mission. After a 2 year mission it will have been activated and de-activated roughly 8500 times. This may negatively impact the performance of the device.
Additionally, as mentioned in section 5.4.3 it is estimated that the stages will be hit by meteoroids about 200 times after 2 years. This may have an impact on the structural integrity of the materials that are being used. Especially for the thin kapton foil it will need to be investigated how many penetrations it will be able to withstand and also how penetrations affect the propagation of the vibrations.

5.8.3 Model Improvement

The calculation that have been performed in this chapter include many assumptions. More research can be spent on minimising the assumptions and improving accuracy of the models.
Firstly, the characteristics of vibrations that will be generated in the 2SID must be investigated more thoroughly such that measurement performance can be optimised by applying band-pass filters. It is known that the vibrations will have the characteristics of Lamb waves [47]. A property of such waves is that the propagation is not only dependent on the material of the foil, but also on the frequency of the vibration. Knowing the correct propagation speed is essential in localising the impact location on the stages.
Secondly, the statistical properties of the noise sources that have been used in model to design the TID could be investigated more thoroughly. When more accurate information is known, filters could be improved to minimise the influence of noise power sources on the measurements.

CHAPTER 6

Command and Data Handling System

6.1 Subsystem Description

The CDHS subsystem is often called the brain of the CubeSat®. It is responsible for controlling and managing all functions of the spacecraft which should allow for a high degree of autonomy. It stores the data obtained by the payload and determines the location and orientation of the spacecraft with the data provided by the AOC system.
The subsystem requirements are listed in table 6.2, they are derived from the functions (that can be seen in figure 6.1) and the mission requirements.

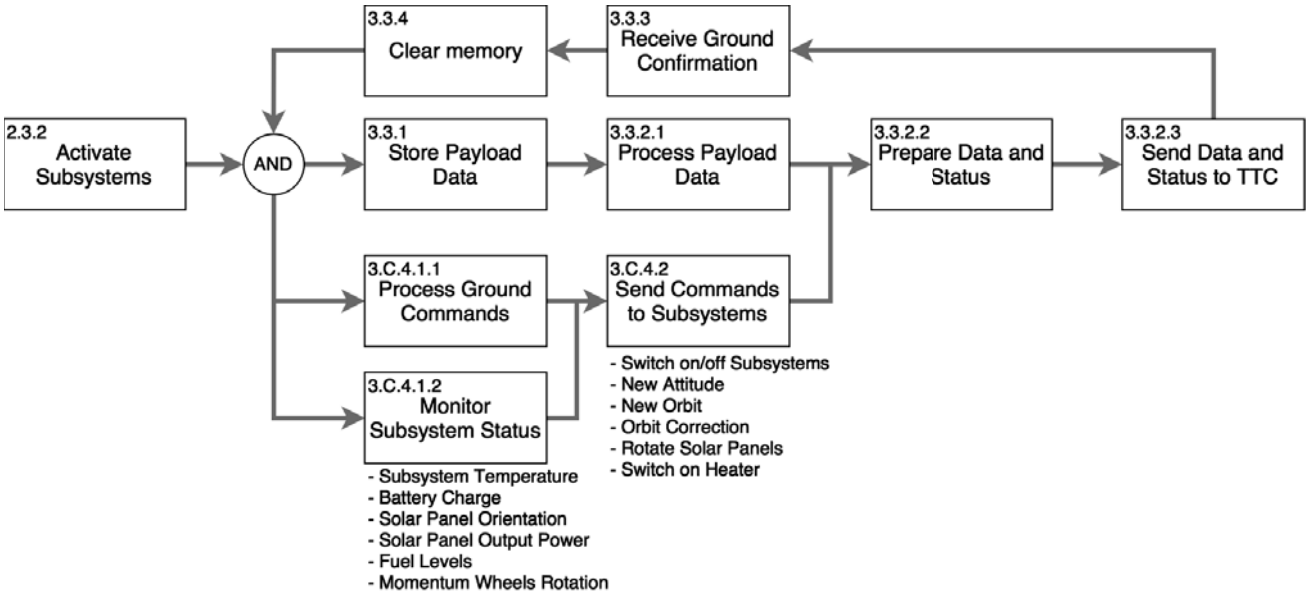

Figure 6.1: Functional flow diagram of the CDHS

An estimation of the processing power, code and data size for the software is made using reference data from SMAD [52].

Table 6.1: Concept phase processing capacity budget

Function	**Code** [Kwords]	**Data** [Kwords]	**Throughput** [KIPS]
Communication	2.0	6.5	10.0
Attitude sensor processing	3.3	15.6	12.0
AOCS	22.3	6.4	84.
Autonomy	2.0	1.0	1.0
Fault detection	6.0	11.0	20.0
Scientific Data Processing	10.9	22.0	2.1×10^3
Other functions	2.0	2.0	8.0
Estimated total	48.7	64.5	2.2×10^3
Contingency factor	0.1	0.1	0.3
Allocated total	53.6	71.0	2.9×10^3
Allocated total [Kbits]**:**	**857.1**	**1117.6**	

It can be seen in table 6.1 that the largest contributors to code size and data size are the AOCS subsystem, the fault detection algorithms and the scientific data processing. It should be noted

that the actual scientific data produced by the scientific data processing is not included in the Data column, as this concerns the data needed to run the software, rather than the data generated by the software. By far the largest contributor to the throughput requirement is the image processing software.

Table 6.2: CDHS requirements

Identifier	Requirement	Section	Compliance
R-SC-CDH-1	The s/c shall be able to store 6GB amount of data before overwriting.	6.2.1	✓
R-SC-CDH-2	The CDHS subsystem shall bear a processing unit that handles all the real time operations of the satellite.	6.2.1	✓
R-SC-CDH-3	The CDHS subsystem shall provide data interfaces to all other systems.	6.2.2	✓
R-SC-CDH-4	Upon command from the ground, the CDHS subsystem shall enter safe mode after a single-event failure.	6.2.2	✓
R-SC-CDH-5	The CDHS subsystem shall provide temperature monitoring of critical locations of the CubeSat®, as defined by the mission design.	6.1	✓
R-SC-CDH-6	The CDHS subsystem shall record all sensor data from temperature sensors, as well as from ADCS and EPS.	6.2.2	✓
R-SC-CDH-8	The CDHS subsystem shall not produce more than 1500MB/day of data to be sent.	6.2.2	✓

6.2 Design

In this section, the design choices for the CDHS will be made and explained. This will concern the hardware and software architecture of the system. The design of this subsystem will be preliminary as a detailed design would fall out of the scope of this project.

6.2.1 Hardware

The hardware choices will be made according to the requirements for throughput and data storage in table 6.1. The mass and power budget of the system will be kept as low as possible and special attention will be given to the radiation hardness of the components.

When choosing a processor, the main requirement will be the throughput. The system shall be able to process at least 2.9 MIPS, the largest part of which comes from the image processing algorithms used to detect impacts from the thermal images. These algorithms will have to continuously process the stream of data coming from the thermal imaging device. This datarate will be 157.3 Mbps.

The hardware for the CDHS will be based around the Cobham Gaisler GR740 [53], this system on chip (SoC) includes a powerful LEON-4 quadcore radiation-hardened processor, is designed to be fault-tolerant, and was designed as ESA's next generation MicroProcessor. The throughput capability of this SoC is benchmarked to be 1.06×10^3 DMIPS and the image processing will be distributed among its 4 cores to cope with the large datarate coming from the payload. This is several orders of magnitude bigger than what is required for this mission, but the low mass and power usage of this system justifies this amount of overdesign. The GR740 also includes two computer watchdogs and can use radiation hardened SD-cards as memory storage. The use of SD-cards for storage is justified mainly by the radiation tolerance and their size and power usage. The GR740 has 4 LEON4 cores, 4 timer units and a timer unit watchdog which increases reliability of the system. The ROM interface includes Error Detection and Correction (EDAC) protocols. This can correct errors which occur due to radiation, such as flipped memory bits.

When deciding upon the amount of data storage needed, a basic estimation is made assuming a no contact time with the Lunar Orbiter of 10 days during which housekeeping and payload data has

to be stored on board. The payload data rate, after image processing, is 6.5 Kb/s and a housekeeping data rate of another 10 Kb/s is assumed. This leads to a total data storage (S) of at least

$$S = (6.5 + 10) \cdot 60 \cdot 60 \cdot 24 \cdot 10 = 14.256\text{Gb} \tag{6.1}$$

Using this requirement, the choice is made to use 3 standard size SD card with a capacity of 2 GB, which equates to 16 Gb per card. The SD card will have a write/read speed of 10 MB/s. This speed is higher than both the generated data rate as well as the maximum data rate for communications, which means it is more than sufficient. The 3 SD-cards will operate independently and a voting mechanism will decide whether the data received from them is correct, to prevent errors in the memory due to radiation from reaching the system.

6.2.2 Software

The software will consist of two main parts, i.e. the flight software and the scientific data processing software. The flight software includes functions such as thermal control, attitude and orbit determination and control, power management, communications, etc. A general architecture of this software is shown in figure 6.2.

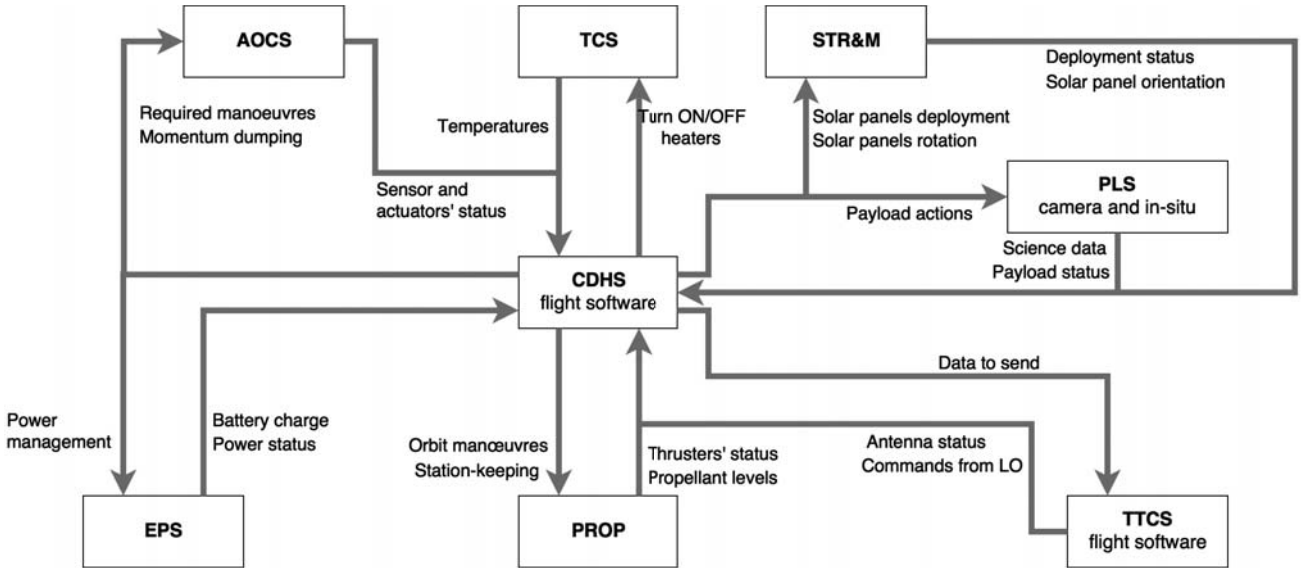

Figure 6.2: General CDHS flight software architecture

The flight software will also process and execute commands, either coming from the Lunar Orbiter or from the data storage. This process is shown in figure 6.3. The software will decode the commands, determine the time of execution, the destination of the command and will then either send the commands directly or place them in the queue if they are to be executed at a later time.

Another function of the flight software is to keep track of the housekeeping data and provide the TTC subsystem with the necessary data to be transmitted. A general protocol has been established to determine what housekeeping data will be transmitted to the lunar orbiter.

General housekeeping data will be stored in a format specified in the WOD format. [54] In this format, important housekeeping data is stored once every minute in a fixed 1856 bit format. In the case of unforeseen events, a special detailed report of all housekeeping data will be generated and sent to the lunar orbiter with the highest priority.

In table 6.1 it can be seen that the total code size will be 857.1 Kb. At an average of 4 KB per 1000 SLoC (SLoC: Source Lines of Code). This equates to roughly 27 KSLoC. At a cost of 500 EUR per SLoC, this amounts to 10 M EUR.

6.2.3 Mass and Power Budgets

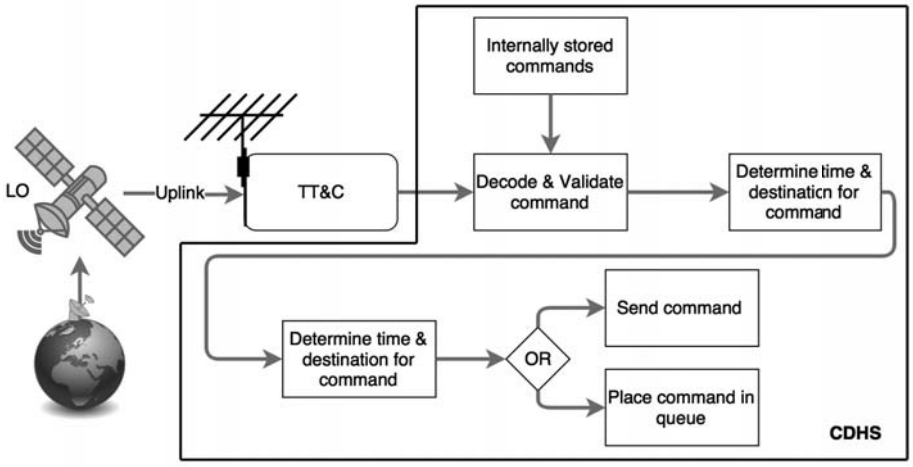

Figure 6.3: CDHS command process

Table 6.3: Command and data handling mass and power budget

Component	**Amount**	**Total Mass [kg]**	**Total Power [W]**
System on Chip	1	0.2	8
Data Storage	3	0.03	0
	Total:	**1.02**	**8**

6.3 Verification

The estimations performed in this chapter are based on estimations used in SMAD [52]. On top of this, an estimation for the scientific data processing software was done using the FireSat as an example. This was done because of the comparable scientific payload of the FireSat and the LUMID, i.e. a Thermal Imaging Device. The proposed contingency factor in SMAD for code size of 30% was used to account for increase in size during the next design phases. The estimated code sizes were checked against reference CubeSat missions to assess the validity of the estimation. The verification of the code cost estimation is harder. It seems that reduction of software cost when compared to regular satellites, does not scale with the reduction in size. This can be partially mitigated by using COTS software, which will significantly reduce the cost. Due to the prices of this software not being publicly available, the estimation of 500 EUR per SLoC is still used in this phase.

6.4 Sensitivity Analysis

The most important inputs for the design of the CDHS subsystem are the data rates provided by the other subsystems, the scientific data rate coming from the payload, the required processing power for the flight software and the science data processing, and the contact times with the lunar orbiter for the data storage requirement.

If data rates should change, the system shall most likely still be able to handle this, since the throughput of the system is much higher than what is required as of now. The processing power is also not used to its fullest so this can be increased. This would however increase the power required and therefore increase the strain on the EPS. If the longest duration of no contact would increase, this would increase the required data storage linearly. If the storage requirement would go up to the point where a single SD-card is unable to store everything, extra data storage can be created by decoupling the 3 SD-cards and using them independently, at the expense of reduced redundancy.

CHAPTER 7

Telemetry, Tracking and Command System

In this chapter, the process of choosing the most suitable antenna for communications is discussed. It is followed by the description of the parameters of the antenna and contact time calculations. Next, a link budget is presented and calculations for the TTC subsystem are verified. The chapter culminates with the sensitivity analysis of the link budget and the contact times.

7.1 Subsystem Description

In table 7.1, the requirements for the TTC subsystem are presented. As one can see, all the communication requirements have been met and can be looked at more closely in the sections that are indicated in the 3rd column of the table. As it can be seen from subsection 7.2.1, two specific frequency ranges were given for different data links. To fulfil this requirement, two UHF antennas were chosen with suitable frequency ranges that also has right hand circular polarisation and maximum RF power up to 2 W. While creating and closing the link budget for the data links, the gain to noise ratios, and the 3 dB link budget margin was taken into account, which can be looked at more closely in subsection 7.2.2.

Table 7.1: TTC requirements

Identifier	Requirement	Section	Compliance
R-SC-TTC-1	Frequency range (Telecommand: 390 - 405 MHz)	7.2.1	✓
R-SC-TTC-2	Frequency range (Telemetry and Payload: 435 - 450 MHz)	7.2.1	✓
R-SC-TTC-3	Data rate less than 512 kbps	7.2.2	✓
R-SC-TTC-4	Modulation/coding: as per Proximity-1	7.2.1	✓
R-SC-TTC-5	Polarisation: right hand circular	7.2.1	✓
R-SC-TTC-6	RF power: up to 2W	7.2.1	✓
R-SC-TTC-7	Antenna G/T: −17.4 dBW/K (TM return link)	7.2.2	✓
R-SC-TTC-8	Antenna G/T: −7.8 dBW/K (payload data return link)	7.2.2	✓
R-SC-TTC-9	Lunar orbiter antenna EIRP: 5.5 dBW (1 W RF power)	7.2.2	✓
R-SC-TTC-10	Link budgets shall have a nominal margin of 3 dB.	7.2.2	✓

7.2 Design

In this section the design, together with the corresponding design choices, of the TTC system will be given.

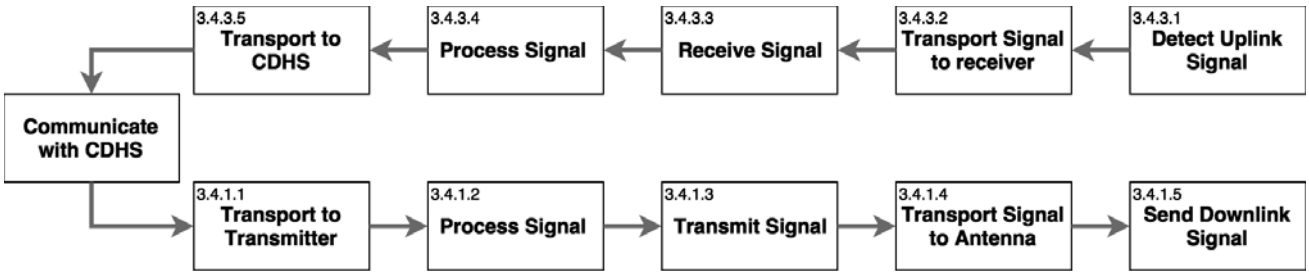

Figure 7.1: The TTC functional flow diagram

7.2.1 Antenna Selection

In order to guarantee effective communication between the three spacecraft and the lunar orbiter, of which functional flow diagram can be seen in figure 7.1, a proper antenna had to be selected for them. The choice came down to be between a spacecraft microstrip patch antenna developed by the Antenna Development Corporation [55] and a deployable turnstile antenna built by Innovative Solutions in Space® company (ISIS®) [56]. Both of them operate in the required UHF frequencies and can have right hand circular polarisation [55], [56]. The advantage of the patch antenna would be higher gain and bigger capability to transmit power, which would be at least 10 W [55]. That means that if the antenna is directly pointed towards the lunar orbiter, then one would need less power to transmit something at a given distance.

However, the vulnerability of the patch antenna is that if it is not directed towards the lunar orbiter, then the communication will be much more sophisticated. One always needs to account for antenna pointing losses and the capabilities of the AOCS subsystem to be able to keep the antenna directed towards the orbiter at all times. Since the turnstile antenna can be approximated to be omni-directional, the biggest disadvantage is that lots of transmitted power is wasted by sending it where it is not needed. However, if one can close the link budget with a turnstile antenna then the spacecraft communication ability can be assumed to be independent of its attitude. That would be a great advantage which would allow the AOCS subsystem to direct its focus on aiding other subsystems. Therefore, it was decided to select a turnstile antenna if one can close the link budget.

In table 7.4, one can see that the link budget can indeed be closed with the aforementioned deployable UHF turnstile antenna, therefore the microstrip patch antenna was abolished. The parameters of the selected turnstile antenna are given in table 7.3 [56]. There are 3 different data links - one for Telecommand feeder link, one for Telemetry return link, and one for payload data return link. The first operates in the frequency range of 390 - 405 MHz, the last two operate in the frequency range of 435 - 450 MHz. [57] The antenna operates within the frequency range of 130 - 500 MHz; however, the operational bandwidth of the antenna is only 10 - 13 MHz [56]. That means that one antenna can only be used for one data link frequency range at the same time. To solve this problem, a second antenna of the same type was included in the design. The antennas would be positioned on the opposite sides of each other on the 200 mm x 200 mm side. The downlink antenna (spacecraft to lunar orbiter) will be on the side where the solar panels are positioned and the uplink antenna (lunar orbiter to spacecraft) will be on the side where the camera is. Both antennas will consume 2 W during the deployment phase at the beginning. The uplink antenna will be there to receive signals from the lunar orbiter. Since it does not transmit power, its nominal electrical power consumption will be continuously 20 mW or less. However, the downlink antenna will consume 2.02 W of power while transmitting data (0.5 W for Telemetry and 1.5 W for payload, of transmission power for both, and 20 mW of nominal power that is always present). When data is not transmitted, it will also consume 20 mW or less [56].

The link budget in table 7.4 closes at a maximum communication distance of 4300 km. Knowing that, one can calculate maximum, minimum, and average orbit times. A program was created to calculate these times. It takes the Cartesian coordinates of the spacecraft relative to the center of the Moon and creates a cone-shaped line of sight around and beyond the Moon. The program calculates in which instances there is contact and where there is not. The conditions for contact are that the distance between the spacecraft and the lunar orbiter shall not be more than 4300 km and the Moon shall not block the communication link. In table 7.2, one can see the information on contact time based on the first 27 days of orbit data in seconds and in days. The main takeaway from the table is that the total contact time compared to the entire first 27 days is approximately 10 %. In figure 7.2, one can also see the contact times per each orbit of the spacecraft vary a lot. In some orbits, there is no contact time; however, in some orbits, one can communicate for longer than 3500 s.

One should note that the antenna will be off the shelf; however, there will be modifications. Instead of the platform with dimensions of $98 \times 98 \times 7$ mm that connects the four rods, a bigger platform will be used with dimensions of $198 \times 198 \times 7$ mm. That is due to the fact that the side which the antenna is on has the size of 200×200 mm. On the camera side, the platform will have a cut-out for

Table 7.2: Contact times based on the data during the first 27 days of the mission.

	Seconds	**Days**
Total time	2 360 595	27.3
Total contact time	225 457	2.61
Total non-contact time	2 135 138	24.7
Maximum consecutive contact time	7 208	0.0834
Minimum consecutive contact time	93	0.00108
Maximum consecutive non – contact time	42 849	0.496
Minimum consecutive non – contact time	1 464	0.0169
Arithmetic average of contact time	3 758	0.0435
Median of contact time	3 099	0.0359
Arithmetic average contact time per orbit	707	0.00818

Total contact time [%]	**9.55**
Amount of orbits	319

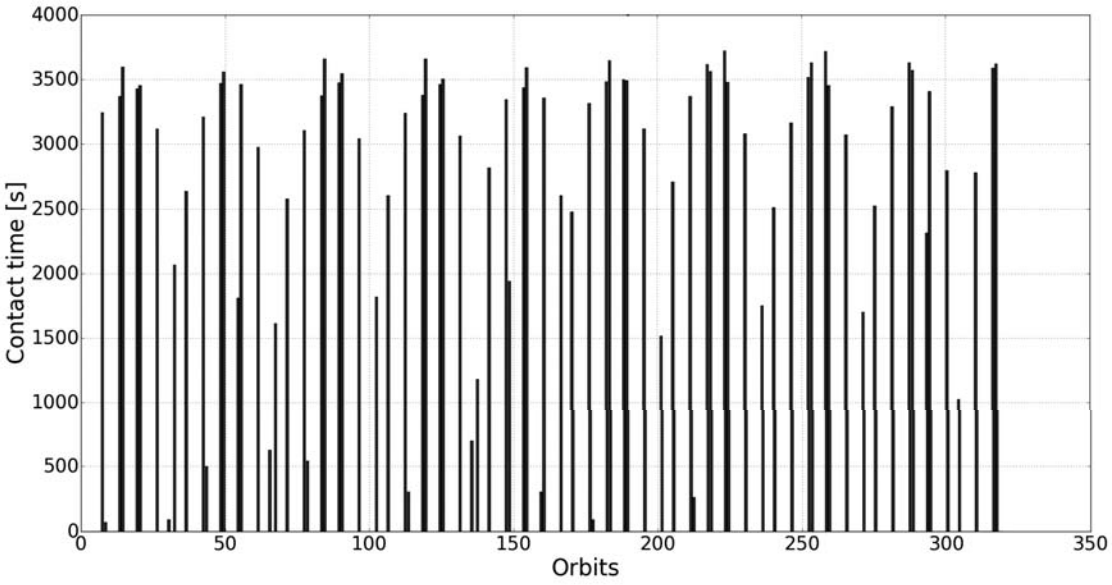

Figure 7.2: Contact times per each orbit in seconds

the camera. The four antenna rods will be positioned perpendicular to each other just like the four solar panel limbs. They will be 45 ° from the deployed solar panels and they will also be turned 45° up away from the spacecraft. That will approximate omni-directionality even more. The lengths of the rods of the downlink and uplink antennas were calculated to be 35 cm and 39 cm, respectively. Since the rods are half-wave dipole antennas, their lengths are one half of the signal wavelength. The lengths can be calculated in equation 7.1 [58], where λ is the signal wavelength, c is speed of light in free space (3×10^8 m), and f is the minimum frequency of the required data link frequency range [57].

$$l = \frac{\lambda}{2} = \frac{c}{2f} \tag{7.1}$$

7.2.2 Link Budget

The communication happens between the lunar orbiter and each spacecraft individually. It must be noted that the three spacecraft do not communicate with each other, but only directly with the lunar orbiter. The data link budget for the data links can be seen in table 7.4. It consists of three data links: A telecommand link from the orbiter to the spacecraft, a telemetry link, and a payload data

Table 7.3: Final design antenna parameters

Parameter	Value
Max Radio Frequency Power (W)	2
Nominal Electric Power (W)	0.02
Electrical Power during deployment (W)	2
Frequency Range (MHz)	130-500
Operational Bandwidth (MHz)	10-13
Mass (g)	100
Envelope stowed: [length x width x height] (mm)	198 x 198 x 7

rate link from the spacecraft to the orbiter. For every data link, the data is presented in decibel and SI units. For the required signal to noise ratio, the bit error rate (BER) of 10^{-5} and the Binary Phase Shift Keying (BPSK) modulation with R-$\frac{1}{2}$ coding is selected to increase the performance of BPSK. The margin closes when the received signal to noise ratio surpasses the one of the required ratio by 3 dB. [59]. The data rate was obtained by first multiplying the amount of data per second by the total time, also in seconds, and then dividing the number by the total contact time. The data rate turned out to be 23.4 kbps for the payload. The minimum data rate for Telemetry was found to be 0.324 kbps. Since the system is largely autonomous, one does not need to send many Telecommands from the ground to the lunar orbiter and then to the three spacecraft. Therefore, the data rate in the Telecommand data link was budgeted as it was for the one of Telemetry. The Telecommand data link would be mainly used for unforeseen instances, when something needs to be altered in the mission. However, once the link budget was closed, it was possible to increase the data rate for TC and TM data links a bit while still keeping the budget closed. The TC and TM data rates were increased by 4.5 and 1.5 dB(bps), respectively. The system noise for the data links was obtained from the gain-to-noise ratios in the project description [57]. To the aforementioned noise, 60 K of Galactic noise was added which has to be accounted for in the UHF frequency ranges [60].

Table 7.4: Final design data link budget

Link Budget: Crosslink	**Command: LO to s/c**		**Telemetry: s/c to LO**		**Payload: s/c to LO**	
	dB	SI Unit	dB	SI Unit	dB	SI Unit
Transmitter Power (W)	0.00	1.00	-3.01	0.50	1.76	1.50
Loss factor transmitter (-)	-1.00	0.794	-1.00	0.794	-1.00	0.794
Transmitting antenna gain (-)	5.50	3.55	0.00	1.00	0.00	1.00
Loss factor receiver (-)	-1.00	0.794	-1.00	0.794	-1.00	0.794
Receiving antenna gain (-)	0.00	1.00	5.50	3.55	5.50	3.55
Space loss (-)	-157	2.03×10^{-16}	-157	2.03×10^{-16}	-157	2.03×10^{-16}
Antenna pointing loss (-)	0.00	1.00	0.00	1.00	0.00	1.00
Required data rate (s/bit)	-32.3	5.88×10^{-4}	-29.3	1.17×10^{-3}	-43.7	4.27×10^{-5}
Boltzmann constant (K/J)	229	7.24×10^{22}	229	7.24×10^{22}	229	7.24×10^{22}
Noise temperature (1/K)	-35.2	3.03×10^{-4}	-35.2	3.03×10^{-4}	-25.6	2.77×10^{-3}
Received SNR (-)	7.68	5.86	7.67	5.85	7.65	5.83
Required SNR [BER = 10^{-5}] (-)	4.40	2.75	4.40	2.75	4.40	2.75
Margin (closes if ≥3 dB) (-)	**3.28**		**3.27**		**3.25**	

7.2.3 Mass and Power Budgets

In table 7.5, one can see the mass and power budget of the TTCS subsystem. As one can see, the total mass and consumed power compared to other subsystems is relatively low.

Table 7.5: Mass and power budgets

Component	**Amount**	**Total Mass [kg]**	**Total Power [W]**
Uplink antenna	1	0.1	0.02
Downlink Antenna	1	0.1	2.02
	Total:	**0.2**	**2.04**

7.3 Verification

To ensure that the calculations in the link budget were performed correctly, a series of checks were performed. The first thing was the unit check from normal units to dB. A special calculator was created that converts the units automatically. All the parameters in the link budget were put in that calculator in dBs as an input and the output non-dB units were obtained, checked, and verified. Also, the link budget was peer reviewed to make sure that the correct data in all data links would have been inserted. In many cases, an input data in a data link is the same for all three data links; however, special care had to be taken to make sure where input data would differ.

To verify the codes for calculating contact times, one had to make sure that the information in the lists was handled correctly. Therefore, two different algorithms were created to calculate contact and non-contact times. They would extract necessary information from orbit data lists differently. However, the output had to be the same. At the beginning, it was not and then a programming logic error was discovered and then corrected. Then, the calculations from both algorithm versions became the same and the code for contact time was verified.

7.4 Sensitivity Analysis

To investigate how sensitive outputs are to changes in inputs in TTC subsystem, sensitivity analysis for the link budget and contact times was performed as shown in tables 7.6 and 7.7, respectively. In the link budget sensitivity analysis, certain values in SI units that could change were increased by 1 %. The percentage changes of the link budget margins in dB were calculated. As one can see in table 7.6, in certain cases, the margin changes are positive and in other occasions, they are negative. However, one can see that the margin is most sensitive in a negative way when the maximum communication distance increases. Therefore, it clearly has a negative effect for the link budget.

In table 7.7, one can see the changes of contact, non-contact, and average contact times when the maximum allowed communication distance does change by 1 %. It can be seen that for contact times, such change is positive. By far, the minimum consecutive contact time is positively influenced by the communication distance change increasing by 153 %.

Table 7.6: Link budget sensitivity analysis

	dB Margin value change in percentages (%)		
Values in SI Units are changed by 1 **%**	**TC**	**TM**	**Payload**
Transmitter Power change	1.32	1.32	1.33
Transmitting antenna gain change	1.32	1.32	1.33
Receiving antenna gain change	1.32	1.32	1.33
Communication distance change	**-2.63**	**-2.64**	**-2.66**
Required data rate change	-1.32	-1.32	-1.33
System noise temperature change	-1.32	-1.32	-1.33
Required SNR change	-1.32	-1.32	-1.33

Table 7.7: Contact time sensitivity analysis

Maximum allowed distance: increased by 1 %	**Original time [s]**	**New time [s]**	**Change [%]**
Total time	2360595	2360595	0.00
Total contact time	225457	231918	2.87
Total non-contact time	2135138	2128677	-0.303
Maximum consecutive contact time	7208	7316	1.50
Minimum consecutive contact time	**93.2**	**236**	**153**
Maximum consecutive non – contact time	42849	42662	-0.438
Minimum consecutive non – contact time	1464	1464	0.00
Arithmetic average of contact time	3758	3802	1.18
Median of contact time	3099	3157	1.88
Arithmetic average contact time per orbit	707	727	2.87
Total contact time as a percentage of total time	9.55	9.82	2.87
Amount of orbits	319	319	0.00

CHAPTER 8

Attitude and Orbit Control System

The Attitude and Orbit Control System (AOCS) can be divided in the Attitude Determination and Control System (ADCS) provided by actuators and sensors and the Guidance Navigation and Control System (GNCS) to determine the location of the spacecraft. First, the requirements are stated followed by the design choices made, then the verification is performed and finally the sensitivity to input parameters will be analysed.

8.1 Subsystem Description

The requirements concerning the AOCS are given in table 8.1. Some requirements cannot be verified in this stage and are indicated with <tdb> in the compliance column. The method used for verifying this requirements is elaborated in section 8.3.

Table 8.1: AOCS requirements

Identifier	Requirement	Section	Compliance
R-SC-AO-1	The AOC subsystem shall provide during all phases of the mission the capability to acquire and keep all attitudes necessary to perform the mission, as defined by the mission design.	8.2.3, 8.2.7	✓
R-SC-AO-2	The initial attitude acquisition shall be performed as an automatic sequence, without input from the ground station.	8.3	<tbd>
R-SC-AO-3	The maximum providable torque of the reaction wheels shall be sufficient to counteract the worst case disturbance torque.	8.2.3	✓
R-SC-AO-4	The worst case slew manoeuvre duration shall not exceed 100 s (flows from EPS)	8.2.3	✓
R-SC-AO-5	The AOC subsystem shall be able to perform all needed slew manoeuvres each orbit	8.2.3	✓
R-SC-AO-6	The AOC subsystem shall process and deliver, at the frequency specified by the mission design, the attitude and orbit related information to other on-board functions.	8.3	<tbd>
R-SC-AO-7	The AOC subsystem shall be able to retain full operation in case of failure of one of its components.	8.2.3, 8.2.7	✓
R-SC-AO-8	The AOC subsystem shall be able to provide three axis determination and control.	8.2.3, 8.2.7	✓
R-SC-AO-9	Upon ground request, the flight software shall provide the capability for in-flight update of the AOCS design parameters.	8.3	<tbd>
R-SC-AO-10	The sun sensors shall be able to locate the sun at every time instant independently of the spacecrafts orientation.	8.2.7	✓
R-SC-AO-11	The s/c shall have a pointing accuracy better or equal to 36 arcsec (flows from the propulsion system)	8.2.7	✓
R-SC-AO-12	The thruster units shall have sufficient propellant mass to dump all the accumulated momentum of the reaction wheels during the mission lifetime.	8.2.3	✓
R-SC-AO-13	The thruster units shall not occupy more volume than one unit of the satellite	8.2.3	✓

8.2 Design

The spacecraft orientation is to be kept stable in order to obtain the scientific data and manoeuvres has to be fulfilled. The location of the sun is essential for solar panel pointing and the orientation

accuracy is required for the propulsion manoeuvres for station keeping. In this section, there will be elaborated on the design and all its functions. The relation between the different components and the corresponding functions is given in figure 8.1. The GNC determines the position dependent on the chosen method, the location is propagated when contact is impossible. The reaction wheels and the thruster units receive commands from the CDH system, while the sensors only sent the obtained orientation data to the CDH system where the orientation is determined. The relation of the AOCS with the CDH system is important since the sent data is converted into commands to other subsystems and vice versa. In other words, the CDH system connects the AOCS to the rest of the spacecraft. It is important to note that the reaction wheels only sent the momentum status when the orientation is kept the same, this has to do with momentum change and momentum storage which will be explained in subsection 8.2.2.

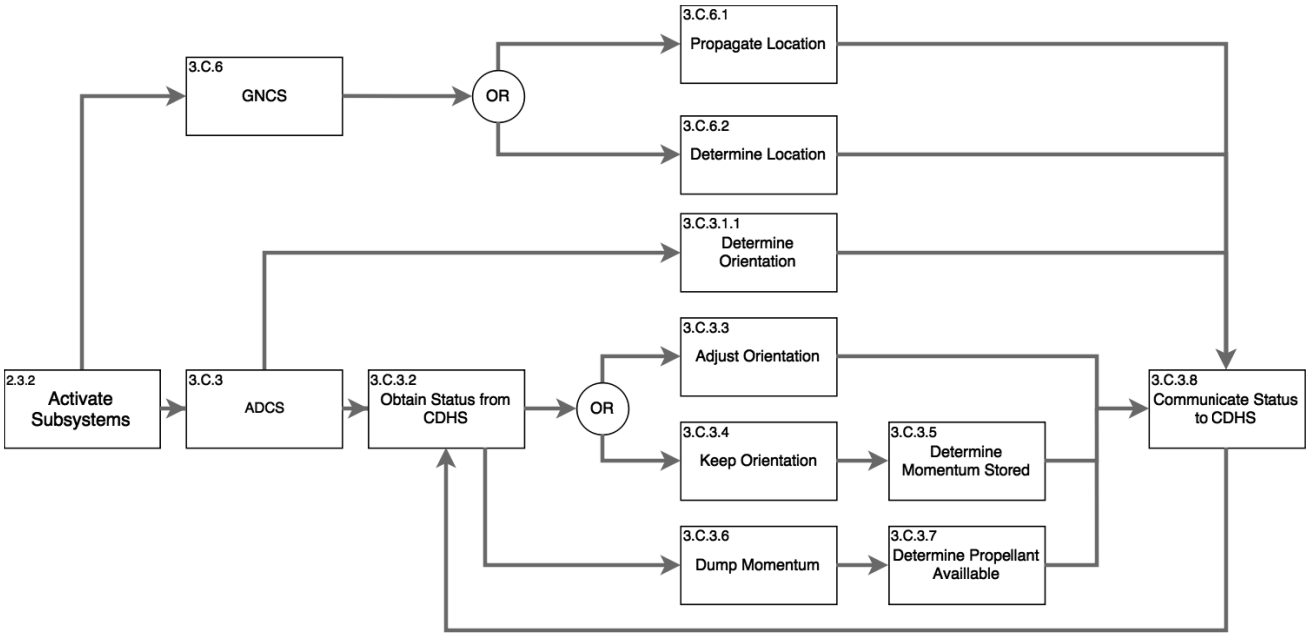

Figure 8.1: AOCS flow diagram

8.2.1 Disturbances

During the mission lifetime, several sources create disturbance torques, introducing external momentum to the spacecraft. This external momentum is stored in reaction wheels and when saturated, thrusters are used for momentum dumping. The four main disturbance torques originating from these sources are the solar radiation pressure, the atmospheric drag, the magnetic field disturbance and the gravity gradient disturbance respectively. The lunar environment is characterised by the absence of an atmosphere making atmospheric drag inapplicable. Also, the lunar magnetic field is weak resulting in a negligible magnetic field disturbance torque. This means that only two disturbance torques will be taken applicable for this mission, namely, the solar radiation pressure and the gravity gradient torques.

Solar Radiation Pressure

The torque caused by the solar radiation pressure is estimated using 8.1 [61]. Where SF is the solar flux at 1 AU distance from the sun [62], c the speed of light, A is the radiated area, q is the reflectance factor, $cp_s - cm$ is the solar radiation pressure arm indicated by the difference between the centre of mass and the centre of solar pressure of the spacecraft, β is the incidence angle w.r.t. the sun which varies during the mission. The reflectance factor range is from 0 (no reflectance) to 1 (total reflectance) of the solar radiation. The solar panels, which cover most of the area in the worst case

scenario, absorb most of the solar radiation making the value of 0.6 a maximum reflectance factor introducing a safety margin.The solar radiation pressure arm, $cp_s - cm$, is minimised by placing the components in the structure based on the mass, positioning the centre of mass as close to the axes of symmetry as possible. The corresponding values originate from the CAD model with the components integrated from chapter 11. All values used in the equation are stated in table 8.2.

$$T_{sp} = \frac{SF}{c} A_s (1 + q)(cp_s - cm) \cdot cos(\beta) \tag{8.1}$$

Gravity Gradient Torque

The gravity gradient torque w.r.t. a celestial body can be estimated using 8.2 [61]. Where μ is the gravitational constant of the orbited body. The parameter R denotes the distance from the spacecraft to the centre of the orbited body, for this mission the radius of the moon plus the spacecrafts altitude. Since an elliptic orbit is chosen, the distance to the centre of the moon is varying from the periapsis of 15 km to the apoapsis of 300 km. The mass moment of inertia in kgm^2 is indicated by I where the subscripts denote the corresponding axes; the body, normal and velocity axes. The gravity gradient torque is the highest around the axis with the lowest mass moment of inertia, in this case around the normal axis. The configuration is such that the extending solar panel and two stage impact detector combination is longer in the normal than in the velocity direction. The mass moment of inertia values stated in table 8.2 are based on the CAD model of the satellite of chapter 11. ϑ is the maximum angle between the nadir direction and the body-axis.

$$T_{gg} = \frac{3\mu}{2R} |I_b - I_n| \cdot sin(2\vartheta) \tag{8.2}$$

Since the moon is the orbited body, the corresponding gravity gradient torque is the highest. The torques regarding the earth and the sun are evaluated for comparison.

Disturbance Torque Results

The values of the parameters used in 8.1 and 8.2 are given in table 8.2. The parameters β and R are variables such that the disturbance torques vary in magnitude during the orbit and the mission. For the worst case disturbance torques the incidence angle β is 90 ° such that the solar radiation is perpendicular to the satellite. The worst case solar radiation pressure is calculated when the upper face, denoted by subscript u, and the side face, subscript s, is in the sun respectively. The gravity gradient torque is maximised when the distance to the orbited body is minimised, in the case of the moon, the minimum distance (R) is 1752 km.

Table 8.2: Disturbance torque parameters

Parameter	Value	Unit	Parameter	Value	Unit
μ_m	4.905×10^{12}	m^3/s^2	ϕ	1367.5	W/m^2
μ_e	3.986×10^{14}	m^3/s^2	c	3×10^8	m/s
μ_s	1.327×10^{20}	m^3/s^2	A_{Su}	0.842	m^2
I_v	1.163	kgm^2	A_{Ss}	0.072	m^2
I_n	0.987	kgm^2	q	0.6	-
I_b	1.635	kgm^2	$(cp_s - cm)_u$	4×10^{-4}	m
ϑ	2	°	$(cp_s - cm)_s$	5.47×10^{-2}	m

The maximum disturbance torques are determined and the values can be found in table 8.3.

Total Momentum During the Mission

The disturbance torques introduce external momentum to the spacecraft which is to be dumped by thrusters. First, the total momentum to be stored in the reaction wheels during the entire mission lifetime is estimated. This estimation is done using equation 8.3 from [61]. This approach uses the

Table 8.3: Worst case disturbance torques

Solar radiation pressure (upper face)	2.46×10^{-9}	Nm
Solar radiation pressure (side face)	2.87×10^{-8}	Nm
Gravity gradient Moon	6.18×10^{-8}	Nm
Gravity gradient Earth	4.83×10^{-13}	Nm
Gravity gradient Sun	2.71×10^{-15}	Nm

worst case disturbance torque assuming it accumulates over a quarter of the orbit time leading to a value of n of 4. The value 0.707 is the root-mean-square of of the sinusoidal disturbance torque function since this depends on the incidence angle β. It may seem that the additional total momentum is underestimated. However, the gravity gradient torque is also based on the angle ϑ between the local vertical and the z-axis where 2 ° is already a worst case value.

$$H_{tot} = \frac{0.707 \cdot T_{max} \cdot t_m}{n} \tag{8.3}$$

Where T_{max} is the maximum torque, in this case the maximum gravity gradient torque of the moon of 6.18×10^{-8} Nm, t_m is the mission lifetime of 6.31×10^{7} s.

This estimation leads to an total external momentum of 0.690 Nms during the mission lifetime.

8.2.2 Slew Manoeuvres

During an orbit several slew manoeuvres have to be performed. In figure 8.2 these slew manoeuvres are visualised together with the orientation of the spacecraft for a certain orbit. The orbit manoeuvres w.r.t. eclipse time and location change accordingly to the explanation in subsection10.2.1.

During one orbit, four slew manoeuvres have to be performed. Two for pointing the solar panels perpendicular to the sun and two where the camera is pointing to the lunar surface, one for the payload phase in eclipse and one allowing the propulsion system to perform the needed station keeping. The first solar panel slew manoeuvre is at t_h, the propulsion manoeuvre takes place from t_c to t_d, symmetrically around the apoapsis. This is followed by a solar panel manoeuvre again at t_d and finally the manoeuvre to initiate the payload phase takes place at t_g.

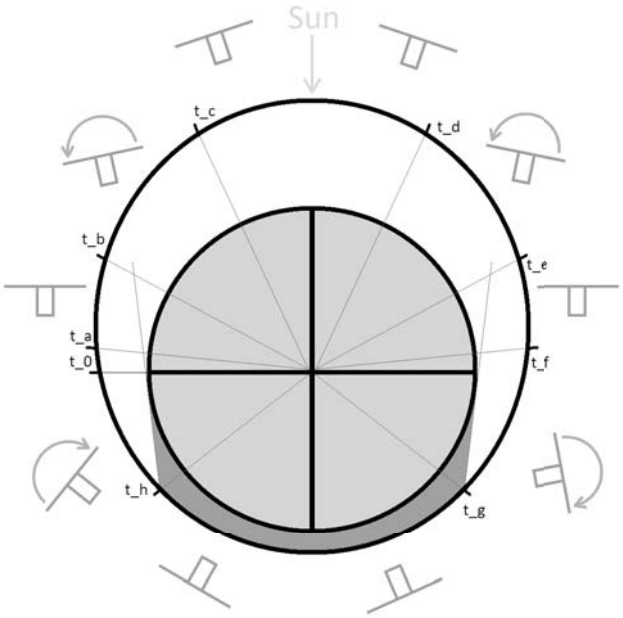

Figure 8.2: Attitude of s/c during one orbit

The slew manoeuvres result in a momentum change assuming that the reaction wheels accelerate and decelerate half of the manoeuvre time. This means that the build up momentum is zero after

the manoeuvre, such that the number of manoeuvres does not influence the momentum storage. Disturbance torques create external momentum which fills up the momentum storage of the reaction wheels, while slew manoeuvres create internal momentum. This internal momentum has a maximum which is equal to the momentum change, occurring at half the time of a slew manoeuvre.

There are several aspects determining if a particular slew manoeuvre is achievable. The momentum change may not be larger than the possible momentum storage of the reaction wheel. Taking into account that disturbance torques store momentum as well a factor of 10 % is used that may not be used for internal momentum. This results in the fact that the momentum change may not exceed 90 % of the total momentum storage. This also means that momentum created by the disturbance torques has to be dumped before 10 % of the wheel momentum storage is exceeded, resulting in more thrusters burns for momentum dumping. It is decided that the disturbance torques are dumped when adding up to 5 % of the momentum storage, leaving a safety margin of 5 % for underestimated momentum storage. Also, the maximum providable torque for the reaction wheel is to be considered, since this influences the manoeuvre time. When the maximum torque is the limiting factor for the manoeuvre time, the momentum storage will be lower than 90 %, introducing an additional safety margin. For the reaction wheel choice elaborated on later, this turns out to be the case adding a safety margin of another 5 % to the momentum storage. This in combination with the aforementioned safety factor of 5 % results in a total safety factor for momentum storage of 10 %. The manoeuvre time is important for the solar panel pointing as it directly affects the power generation. The manoeuvre time is determined for the maximum manoeuvre angle of 180 ° using 8.4, the torque is related via 8.5, or equivalently via 8.6 and the momentum change is defined by 8.7. Where θ denotes the true anomaly, α is the angular acceleration in rad/s, t is the time in seconds, T indicates the torque in Nm, I is the mass moment of inertia with unit kgm^2, in this case around the normal axis for the manoeuvres. Note that the normal axis is preferred as slew manoeuvre axis (I_n<I_v) as it keeps the manoeuvre time relatively low, see equation 8.5. δh is the momentum change in Nms. With the determined manoeuvre time another worst case aspect is used, namely compensating for the maximum rotational velocity of 9.90×10^{-4} rad/s, if an manoeuvre is to be achieved at the perioapsis. During the manoeuvre time, an additional angle is travelled which increases the manoeuvre time even more. The final worst case manoeuvre times are given in table 8.4.

$$\frac{\theta}{2} = \frac{1}{2}\alpha \cdot (\frac{t}{2})^2 \tag{8.4}$$

$$T \cdot t = I_n \cdot \alpha \tag{8.5}$$

$$T = \frac{4 \cdot \theta \cdot I_n}{t^2} \tag{8.6}$$

$$\delta h = T \cdot \frac{t}{2} \tag{8.7}$$

The true anomaly, the angular velocity, the angular acceleration and the required torque the reaction wheels need to provide to point the camera to the lunar surface are plotted versus the time and are visualised in figure 8.3. This figure verifies that during one orbital period, the reaction wheels accelerate and decelerate half of the time, such that no net momentum is created. Therefore, there is a momentum change to be accounted for by the reaction wheel momentum storage, but there is no need to dump momentum from orbiting. The slew manoeuvres require more momentum change, such that the reaction wheels have to be designed for that.

The maximum providable torque and the total momentum storage are properties of the reaction wheels. It turns out that for some reaction wheels the maximum torque defines the manoeuvre time, while for others this will exceed the momentum storage such that a lower torque is applied. Using a MATLAB® code the worst case slew manoeuvre of 180 ° times are determined based on equation 8.4 to 8.7 and stated in table 8.4.

8.2.3 Actuator Choice

The actuators consist of reaction wheels used for momentum storage and slew manoeuvres while the thrusters are used desaturate the reaction wheels. For the actuators, the choice is made not to use control moment gyroscopes (CMGs), because CMGs combine a short life (the bearings suffer from wear and tear) with high cost, mass and power needs, they are generally used only on large spacecraft and only when absolutely necessary to achieve the mission goals [61]. Magnetorquers will not be used since it consists of electromagnetic coils working together with the magnetic field of the

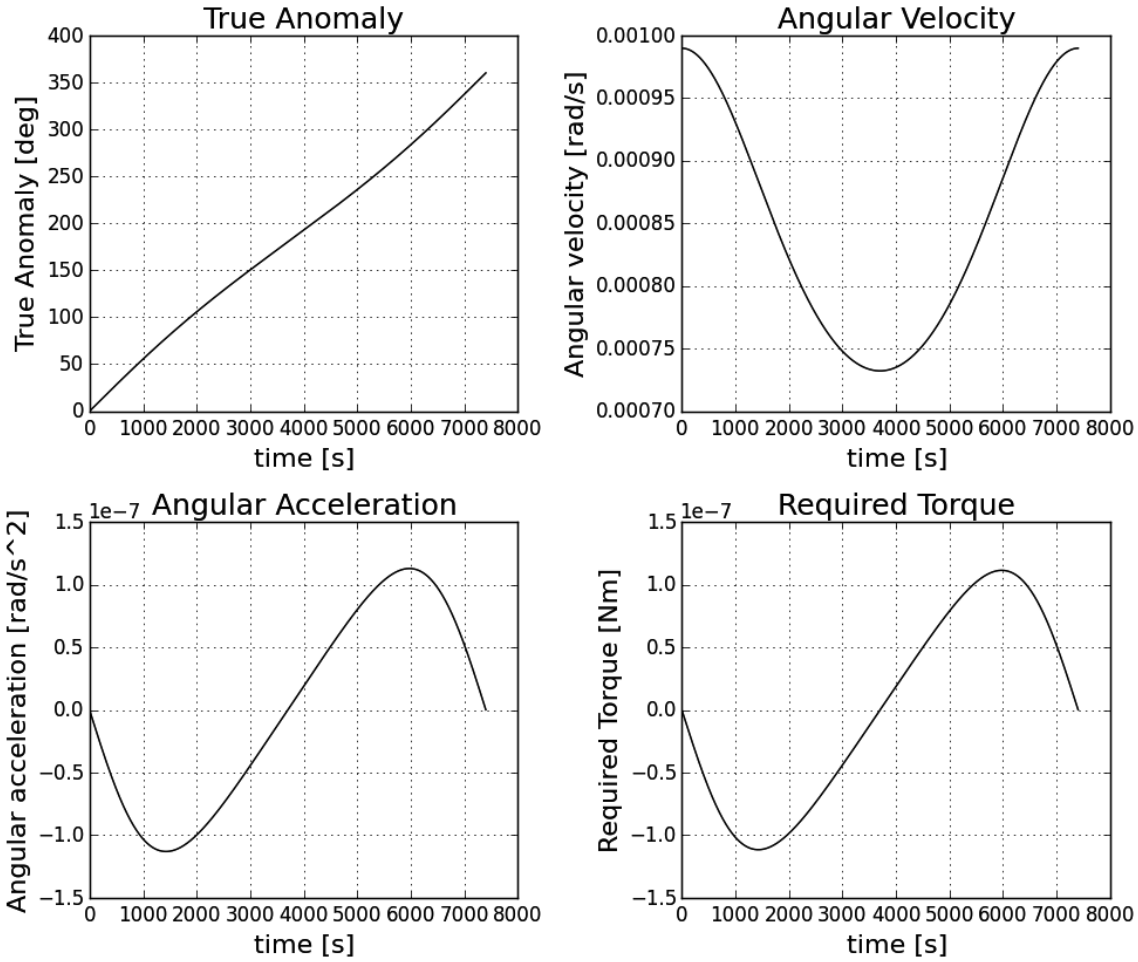

Figure 8.3: Reaction wheel parameters during orbit

orbited body to create torque. The lunar magnetic field is too weak to be able to produce large enough torques.

Reaction Wheels

Reaction wheels provide attitude control by rotating at a certain speed and are capable of rotating in two directions. In this way, the external momentum of disturbance torques are stored and slew manoeuvres are performed.

One property of reaction wheels is the maximum achievable torque. From table 8.3 it can be seen that all reference reaction wheels can deliver the torque needed for counteracting the highest worst case disturbance torque. This torque plays also a role in combination with the momentum storage for slew manoeuvres which together define the worst case slew manoeuvre times indicated with t_{WCS} in table 8.4. In general, the accumulated momentum is dumped when the momentum storage is reached. As is explained in the previous subsection this does not hold in this case, taking into account the momentum storage needed for the momentum change of slew manoeuvres. Therefore, the momentum storage in reaction wheels is mainly important for the slew manoeuvre time instead of the total momentum to be dumped during the mission lifetime.

The possible reaction wheel options and their performances can be seen in table 8.4.

In agreement with the power subsystem it is decided to use the RWP100 of Blue Canyon Technologies [63] to have a worst case slew manoeuvre time of 74.5 sec combined with a total mass of 1.4 kg and a total power of 2.0 W. This is decided to be the optimal combination between slew manoeuvre time, mass and power performance.

Table 8.4: Reaction wheel performance

	h [Nms]	$\mathbf{T_{max}}$ [mNm]	**n**	$\mathbf{t_{WCS}}$ [s]	**Total mass** [kg]	**Total power** [W]
RWP015	0.015	4	4	526	0.52	2.4
RWP050	0.05	7	4	151	0.96	2
RWP100	0.1	7	4	74.5	1.4	2
RWP500	0.5	25	4	22.4	3	12
RWP1	1.5	40	4	17.7	6.4	12
RWP4	4	60	4	14.4	10	12
RWP8	8	110	4	10.6	14.4	12
RSI 01-5/28i	0.12	5	4	62.0	2.8	8
bradford-space RW	18	248	4	7.08	29.2	560

Thrusters

The thrusters are used to dump the momentum stored in the reaction wheels at regular times. It is important to note that the thruster system is entirely independent of the propulsion system where electrical propulsion is used. Depending on the reaction wheels chosen, the momentum to be dumped may vary slightly as the end of life momentum is not required to be dumped. For the reaction wheel considered, a momentum of 0.690 Nms is to be dumped. The total impulse needed for a thruster unit to dump momentum (h) is determined using equation 8.8.

$$I_{ne} = \frac{h}{L} \tag{8.8}$$

$$M_p = \frac{I_{tot}}{I_{sp} \cdot g} \tag{8.9}$$

Where L is the moment arm of the thruster, assuming a value of 0.1 m which is the worst case moment arm when dumping w.r.t. the z-axis. Since a thruster unit is considered, the thruster with the most effective moment arm is used. This leads to an impulse needed of 6.90 N − sec which is well fulfilled by all thruster units.

For the reference thrusters found the performance results are summarised in table 8.5. All reference thrusters use cold gas as propellant since this is suitable for delivering precise and small thrust pulses. As explained previously, the external momentum will be dumped when adding up to 5 % of the possible momentum storage. For the reaction wheel chosen, this means that each time a momentum of 5×10^{-3} Nms has to be dumped. Therefore, in the total mission lifetime 137 momentum dumping thruster burns are necessary. The nominal thrust is 0.01 N for all thrusters. The impulse needed per momentum dumping considering a thruster moment arm (L) of 0.1 m is 0.05 N − sec. The Vacco thrusters [64] have a minimum impulse bit of 5×10^{-5} N − sec and the the nanosatellite micro-propulsion system [65] of 2×10^{-9} N − sec. This minimum impulse allows for the impulse needed per momentum dumping of 0.05 N − sec to be delivered accurately. For the nominal thrust of 0.01 N of all thruster units, the burning time per momentum dumping is 5 s.

It is to be noted that all references consider thruster units, the Vacco thrusters have propellant storage and five thrusters, the nanosatellite micro-propulsion system system needs a storage tank for the propellant and has three thrusters but still provides three axis control.

The propellant mass needed for the thruster units can be determined using equation 8.9 from [61].

Where the total (I_{tot}) and specific impulse (I_{sp}) are properties of the thruster units and g is taken as the mean gravitational acceleration, which varies with altitude, in lunar orbit. The propellant mass needed to dump the momentum is determined using the same equation but instead of the total impulse the impulse needed is used. The propellant mass values can be seen in table 8.5.

Since for the Vacco reference thruster units already propellant is accounted for in the mass, an estimation for this is made assuming a gravitational acceleration of 9.8 m/s^2. This leads to the thruster unit dry mass values stated in table 8.5. The propellant and dry mass values consider two thruster units, so already account for redundancy.

The total mass of the redundant thruster system is given in 8.5 as well. The stars indicate that a propellant tank is needed since the propellant mass storage of the unit itself is insufficient. To fit the trade-off in the table, subscripts are sometimes used instead of written out parameters.

The nanosat micro-propulsion system has the lowest mass, however, the volume is large and the power consumption is the highest. Moreover, an additional propellant tank is needed (indicated by

Table 8.5: Thruster performance.

Thruster unit type	I_{tot}	I_{sp}	n	Volume [U]	M_{Dry} [kg]	M_p [kg]	M_{tot} [kg]	P_{tot} [W]
Vacco X14029003-1	44	40	2	0.6*	0.86	0.25* (0.22)	1.11*	0.5
Vacco X14029003-4	103	40	2	1	0.96	0.25 (0.52)	1.21	0.5
Vacco X14029003-7	191	40	2	1.6	1.11	0.25 (0.97)	1.36	0.5
Vacco X14029003-9	250	40	2	2	1.21	0.25 (1.28)	1.46	0.5
nanosat microprop. syst.	250	75	2	2*	0.6	0.13*	0.73*	4

the stars in the table) increasing the volume and mass even more. Besides the increase in mass and volume, it also introduces complexity, for example, valves are needed and the tank shape for stress distribution is not preferable for volume efficiency. Since the volume is a limiting factor in the system design and an additional propellant tank is required, this option is not chosen.

For the Vacco thruster units, the two smallest types are the most promising since the mass and volume are relative low, while still fulfilling the requirements. The smallest type requires an additional propellant tank. Besides the disadvantages discussed previously, the propellant tank has to be connected to both thruster units. It is unknown what the connection possibilities for an external propellant tank to these closed units is. The volume and mass of the second type, the Vacco X14029003-4, are not much higher than for the first type, and since no additional propellant tank is required inducing extra complexity, this type is chosen for the design. Finally, a safety margin is introduced for this thruster unit. For momentum dumping 0.25 kg propellant is needed while the propellant capacity of two units is 0.52 kg, this is indicated in 8.5 between brackets. A safety margin of 20 % is incorporated although the propellant mass needed is not very sensitive to changes, as is shown in 8.4, resulting in a total propellant mass of 0.30 kg. This concludes a total mass of 1.26 kg, a total power of 0.5 W and a total volume of 1 u for the thruster units.

8.2.4 Sensor Choice

The sensors needed for navigation will be dealt with from here on. For the sensors, sun sensors and star trackers are used. The sun sensors are needed to be able to sense the direction of the sun directly after deployment from the lunar orbiter. The star trackers have a higher accuracy and are used for more precise attitude determination such as pointing of the camera to the lunar surface, tracking the lunar orbiter for communication purposes and the exact orientation needed for station keeping by the propulsion system.

It is decided not to use horizon sensors since the availability of small components is still limited nowadays and flight-proven reliable sensors are preferred. Furthermore, Earth sensors are not feasible since Earth sensors sense the reflected radiation. The albedo coefficient of the Earth is approximately 0.30 [66] while the reflected radiation by the Moon is between 7 % to 24 % of the incoming solar radiation [27]. The lunar reflected radiation is smaller than Earths, making it an unfeasible option. A gyroscope contains rotating parts, which causes complexity; especially for a limited sized CubeSat® mission this can affect the reliability. Magnetometers cannot be used due to the weak lunar magnetic field. Finally, Inertial Measurements Units (IMUs) are not chosen since different sensors are combined, also containing sensors that cannot or are not preferred to be used for this mission such as gyroscopes and magnetometers.

An aspect to be taken into account is that the star trackers may be blinded by the bright sunlight. As three star trackers on different sides are used for redundancy, as explained later, not all star trackers can be in the sunlight at the same time. Moreover, the solar panels are pointed to the sunlight during daytime such that the star trackers will not be in the sunlight as well. When this issue still occurs, Sun sensors can be used despite the lower accuracy and the orbited can be adjusted to solve the problem.

The radiation pattern of the antennas used for the TTC subsystem is omni-directional, resulting in the fact that no pointing accuracy requirement flows from this subsystem. For the payload a pointing accuracy of 10 ° is defined, which is independent of the altitude, based on the fact that the image width may not increase more than 3 %. Finally, the pointing accuracy needed for the propulsion

system manoeuvres turns out to be decisive. The direction of thrust needs to be regulated precisely and when the position is incorrectly determined this may lead to an thrust offset. Since the thruster is active over a time period, this offset will add up and lead to an in-preferred position after the manoeuvre. Therefore the required pointing accuracy is defined as 36 arcsec.

Sun Sensor Choice

For the sun sensors the reference components with their performance are shown in table 8.6 With the field of view the number of sun sensors needed to create a full redundant system is indicated in table 8.6 by n. With this the total mass and power for the sun sensors is determined.

Table 8.6: Sun sensor performance

	Accuracy [deg]	**Field of view** [deg]	**n**	**Total mass** [kg]	**Total power** [W]
Newspace CSS	0.5	57	9	0.045	0.45
nano SSOC A60	0.5	60	8	0.032	0.08
nano SSOC D60	0.5	60	8	0.052	0.92
MTASS	0.15	60	8	0.192	8
Mini FSS	1.5	64	8	0.4	0
Adcole MSSS	0.25	87.5	7	1.75	3.5

The accuracy of the sun sensors is preferred to be as high as possible and all accuracies are found well in the range to determine the position of the sun precisely enough. The total mass and power performance combination of a full redundant system is evaluated and the nano SSOC A60 [67] turns out to have the best combination with a total mass and power of 0.032 kg and 0.08 W respectively.

Star Tracker Choice

The reference star trackers found are listed in table 8.7 with their corresponding properties. Star trackers can cover two axes with high accuracy and one with low accuracy. This means that two components are sufficient for accurate three axis determination, one extra is used as back-up of the other two accounting for redundancy. The star trackers are placed on three different sides such that there are always two star trackers with high accuracy on a particular axis, accounting for redundancy. Although star trackers are relatively costly, redundancy is necessary for reliability of the whole mission, coming to a choice of three star trackers.The most decisive pointing accuracy is defined before as 36 arcsec flowing from the propulsion system. All existing star trackers found fulfil this requirement such that the mass and power combination is used for the design choice.

Table 8.7: Star tracker performance

	Accuracy [arcsec]	**n**	**Total mass** [kg]	**Total power** [W]
ST400	10	3	0.84	1.95
SSC03-X-7	<100	3	0.9	3
Microasc MST	2	3	1.28	3
MIST	30	3	1.5	12
Procyon ST	5	3	3.6	19.5

Based on the mass and power combination the ST400 of Berlin Space Technologies [68] is chosen as star tracker used for this mission. The total mass and power accumulate to 0.84 kg and 1.95 W respectively.

8.2.5 Component Location in Spacecraft

The location of the chosen components is shown in figure 8.4. The four reaction wheels in pyramid configuration are located in the bottom left and the two thruster units are the blue boxes in the bottom corners. The three star trackers are the camera looking devices on three different sides of the satellite and the sun sensors are too small to be indicated in the figure. The configuration of the 8

sun sensors used consists of 2 sensors on the top side, 4 on the bottom corners and 2 on the middle of the opposite bottom edge seen from the other two corners.

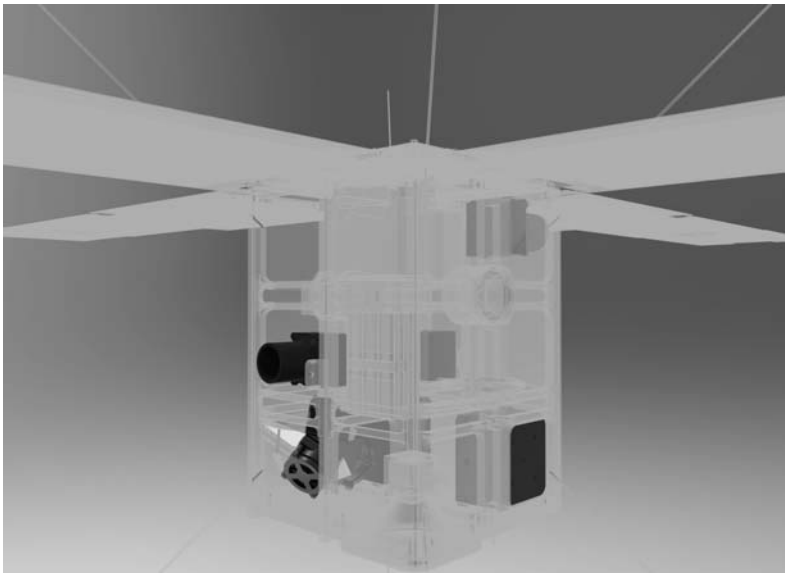

Figure 8.4: AOCS component location

8.2.6 Mass and Power Budgets

The mass and power budget for the AOCS is summarised in table 8.8 where component is shortened to comp. All components incorporate redundancy and can withstand the launch loads and radiation since they are flight-proven.

Table 8.8: Mass and power budgets for the AOCS.

Component	**Amount**	**Total Mass [kg]**	**Total Power [W]**
Reaction wheel	4	1.4	2
Thruster unit	2	1.26	0.5
Sun sensor	8	0.032	0.08
Star tracker	3	0.84	1.95
	Total:	**3.532**	**4.53**

8.2.7 Guidance Navigation and Control System

The Guidance Navigation and Control System determines the position of the spacecraft. This is essential for ending up in the preferred position after station keeping, for switching on the camera when in eclipse and below the altitude of 39km and to perform manoeuvres at the right moment. In case of orbiting the Earth, GPS can be used. However, the possibilities when orbiting the moon are limited. The options found will be briefly discussed below. Due to time constraints there is to be investigated on a specific design. From similar missions, the optical guidance and navigation method turns out to be more applied. It turns out that the optical guidance and navigation method is mostly applied in similar missions.

Optical Guidance and Navigation Optical guidance and navigation is performed by means of a camera to take measurements of the Moon and stars. In case of the moon, landmarks can be identified and this data is compared to a digital map of the CDHS. With this iterative process the altitude, longitude and latitude are obtained. A Star based method is also possible, it determines the position of the centre of the moon via a sequence of collected images. The pointing errors are removed using background stars. Additional attitude constraints also flow from this second camera. Dust storms

and eclipses can prevent the camera from scanning landmarks and therefore determining the position. It is possible to propagate the data from the latest known position, but the accuracy decreases and is to be investigated. The spacecraft performs four slew manoeuvres per orbit and the camera is only pointing to the surface in the payload phase in eclipse and in the propulsion phase. Since landmarks can be identified only in daylight, the position is measured in the propulsion phase only and is to be propagated for the rest of the orbit.

Radiometric Guidance and Navigation Another possibility is radiometric guidance and navigation where radio communication links between the Earth and the satellite are used to determine the relative position and velocity of the spacecraft. A signal is transmitted from the satellite to the ground station which position is accurately known and a signal is sent back. Accounting for the Doppler shift the s/c's position can be determined. The position and velocity are deduced by minimising the residuals between the tracking and modelled data, such that mathematical models have to be used. This method requires two antennas, one for transmitting and one for receiving the signal from and to Earth. A constraint is the visibility of the ground station, at regular times, the moon blocks the signal such that the location is unknown. This requires propagation as explained before. The propagation time in this case is shorter. The difference in spacecraft and ground station clock times is a factor to account for, as a small time difference leads to a large position off-set. An example making use of radiometric navigation is the Saturn orbiter Cassini [69]. Also, the lunar orbiter can be used for radiometric navigation, as it measures its location as well. Due to time constraints no prediction about the propagation accuracy is provided. This is a point of further investigation.

Location Accuracy Required All systems require a specific accuracy to operate properly and the main influencing systems turn out to be the payload system, the propulsion system and the AOCS. For the propulsion system it is estimated that the highest location accuracy is needed in combination with the astrodynamics to determine the burn time and not propagating the position error after station keeping. The payload is only active during eclipse which has variations in time and position making it difficult to determine the required position accuracy. However, it is estimated less decisive than the propulsion position accuracy since it only determines when the camera is turned on or off. Furthermore, it does not influence the 2SID at all as the orientation is here the driving factor. The required accuracy needed for the AOCS is regarding the attitude, when a location off-set is present, the attitude is determined incorrectly and a manoeuvre may be performed at the wrong moment.

8.3 Verification

The AOCS calculation and requirement verification are addressed together with the model validation.

8.3.1 Verification of Calculations

The equations used to obtain the results and to perform the component trade-offs are given in the concerned sections. The parameters used and the corresponding values are stated as well. A MATLAB® code is written for optimisation of the component trade-offs in parts per calculation to create unit tests. The results of these parts were verified by inspection and by reviewing intermediate results of parameters calculated, the given inputs resulted in expected outputs.

8.3.2 Requirement Verification

The requirements with identifier R-SC-AO-2, R-SC-AO-6 and R-SC-AO-9 have to be complied by verification methods. R-SC-AO-2 will be verified by testing and demonstration. First, a simple controlled test will be executed, when fulfilled successfully, demonstration is needed to verify that this can be done without input from the ground station. Requirement R-SC-AO-6 will be verified by analysis and demonstration. First, the frequency can be agreed on by analysis, afterwards, the attitude and orbit

related information can be sent to other on-board functions to inspect if this works properly. Finally, R-SC-AO-9 will be verified by testing. The validity will be verified by creating a similar situation.

8.3.3 Validation

At this mission phase, it is difficult to analyse the difference between the reality and the methods used. The equations used are applicable but simplified using assumptions, so validation of the model is still to be performed. This can be done by testing and demonstration on component and system level.

8.4 Sensitivity Analysis

In the sensitivity analysis, the output results are evaluated when an input parameter changes.

Suppose that the power subsystem requires more power generation and the total number of solar panels and two stage impact detectors panels increases from 9 to 12 panels, a growth of 33.3 %. Note that this example is based on old iteration values. As first consequence, the total satellite mass goes up with 1.8kg. The upper face area of the spacecraft rises by 28.9 %. This area is directly related to the solar pressure disturbance torque, which goes up with 28.9 % as well. The momentum to be dumped by the thrusters is based on the worst case disturbance torque, which still is the gravity gradient torque exerted by the moon, which therefore remains the same. The additional solar panels are situated far away from the centre of mass of the spacecraft, increasing the mass moment of inertia around all axes significantly. The mass moment of inertia around the velocity, normal and body axes increase with 30.9, 93.6 and 72.2 % respectively. As a consequence, the gravity gradient torque exerted by the moon grows with a factor of 3.30. The total momentum to be dumped during the mission lifetime, as well as the total impulse needed for the thruster units are linearly related so also rise with a factor of 3.30. It turns out that 3.33 times more thruster burns for momentum dumping are needed, this varies slightly due to the integer number of burns. This leads to an expansion of the propellant mass of a factor 3.33 as well, resulting in updated propellant mass of 0.307 kg. Now, an additional propellant tank is needed for the thruster unit chosen such that the Vacco X14029003-4 would be chosen. The new thruster unit choice increases the volume from 0.6 u to 1 u which has to be incorporated in the structure of the satellite.

The torque needed for this slew manoeuvre to not let the momentum change exceed the momentum storage of the reaction wheel is inversely related to the mass moment of inertia about the normal axis, diminishing by the same amount of 93.6 %. This same holds for the required time to perform the slew manoeuvre only which rises by this percentage. However, compensating for the maximum rotational velocity an additional angle is to be travelled. This angle is also 93.6 % larger. So, with the same angle travelled, the new slew manoeuvre time will be 93.6 % higher, compensating for the additional angle increase the total slew manoeuvre time will go up with a factor 2.02. This results in a minor decrease in power generation due to the slew manoeuvre time. From this example, it can be concluded that when designing a certain system the effects on other systems and components can have drastic effects. Therefore, the communication and interrelation between the different systems is of uttermost importance.

CHAPTER 9

Propulsion System

In this chapter the propulsion subsystem is explained. Starting with a description of the subsystem, continuing with the requirements, then the design of the subsystem and ending with verification methods and a compliance matrix.

9.1 Subsystem Description

Starting with deployment from the Lunar orbiter the CubeSats® will have to perform some orbital manoeuvres at first to inject it in the preferred orbit and second to perform orbit maintenance throughout the whole mission. This is why a propulsion subsystem is needed to introduce certain Δv's as explained in the astrodynamics chapter 3. The requirements of the propulsion subsystem are listed in table 9.1.

Table 9.1: PROP requirements

Identifier	Requirement	Section	Compliance
R-SC-PROP-1	The PROP subsystem shall provide required Δv of567.33 m/s for given functional requirements.	9.2; 9.3	✓
R-SC-PROP-2	The PROP subsystem shall provide a specific impulse in vacuum of at least 2500 s.	9.2	✓
R-SC-PROP-3	The total wet mass of the PROP system shall be less than 3 kg, including all propellant required for all Δv, as well as subsystem residual propellants and uncertainties in propellant loading.	9.2	✓
R-SC-PROP-4	The PROP subsystem shall withstand all mechanical loads during all phases of launch, deployment and operation.	11.2.1 9.3	
R-SC-PROP-5	The PROP subsystem shall utilise "green" technology.	9.210	✓
R-SC-PROP-6	The design and development phases of the PROP system shall conform to the standards of the "European Cooperation for Space Standardization" [70].	9.2	
R-SC-PROP-7	The PROP subsystem shall not exceed a volume of 2 l.	9.2	✓
R-SC-PROP-9	The maximum propellant quantity used shall encompass worst-case subsystem performance.	9.2	✓
R-SC-PROP-10	The propellant tank shall be designed such that fluid motion inside the tank does not produce a spacecraft/launch vehicle nutation time constant outside the launch vehicle specification.	9.2	✓
R-SC-PROP-11	The propulsion subsystem shall thrust with a pointing accuracy of at least 36 arcsec	8.2.7	✓

The propulsion subsystem consists of several functions. The functional flow diagram of the propulsion subsystem is presented in figure 9.1.

9.2 Design

This section explains the design of the propulsion subsystem. Starting with a thruster selection followed by tank sizing and closing with the subsystem architecture.

9.2.1 Thruster Selection

There are a lot of different types of thrusters available at the moment. However, not all of them are applicable to the LUMID so it is important to choose the thruster that is the most suitable for the

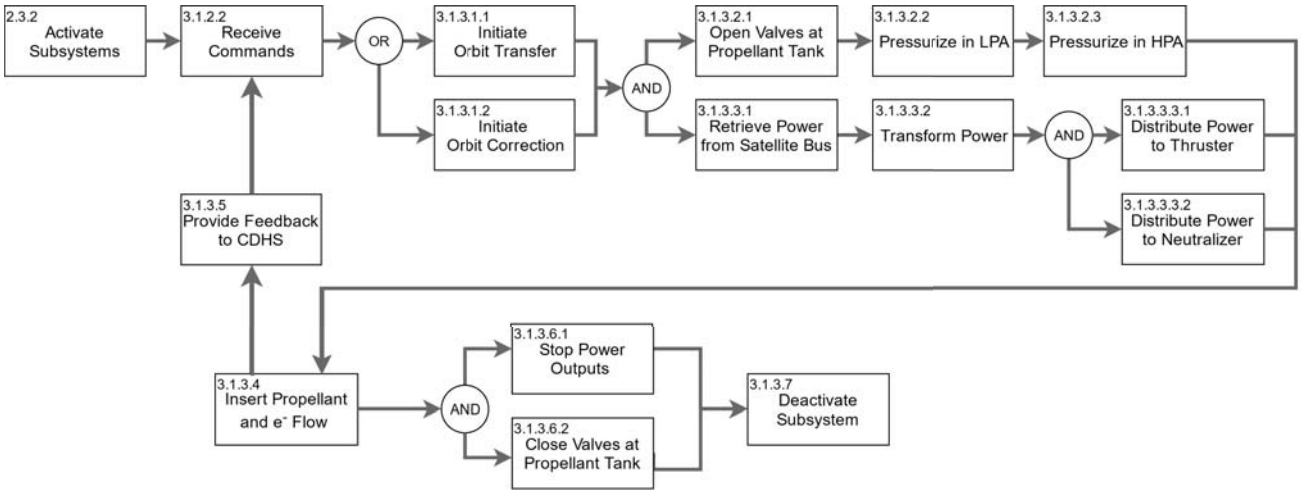

Figure 9.1: Flow diagram for propulsion subsystem

design. In order to do this, one needs to calculate the system specific impulses (I_{ssp}) for each possible thruster, which is the ratio of the total impulse delivered by the system over the system mass. The parameter was used to compare the efficiency of the propulsion system. Firstly, the minimum and maximum propellant masses are calculated using the specific impulse ranges of the thrusters and the required Δv obtained in the astrodynamics section 3. To be able to compensate for unforeseen circumstances a contingency factor of 30% will be added to this Δv. This is done because the Δv calculated in the astrodynamics chapter did not take any gravity losses into account. Also another contingency factor (10%) [71] for the propellant mass to account for pressure losses. The Δv budget and propellant masses for the thruster that was chosen are presented at the end of this chapter in table9.2.

Secondly, tank-to-propellant mass ratios were computed for Xenon. Since Xenon is a noble gas, the ideal gas law starts to fail at much higher temperatures. In order to estimate the tank over propellant mass, the "Redlich-Kwong" 9.1 equation was used [71]. R being the gas constant here, T the temperature, V_s the volume and P the pressure.

$$R \cdot T = (V_s - b)\left[P + \frac{a}{V_s(V_s + b)) \cdot \sqrt{T}}\right] \tag{9.1}$$

From the aforementioned equation, the expressions for pressure and tank-to-propellant mass ratios were derived for a spherical tank. For the tank material density one choose the density of aluminum (see section 9.2.2 and table 9.3). The derived equations can be seen in 9.2 and 9.3 [71].

$$P = \frac{R \cdot T \cdot \rho_p}{m - b \cdot \rho_p} - \frac{a \cdot \rho_p^2}{m(m + b \cdot \rho_p) \cdot \sqrt{T}} \tag{9.2}$$

$$\frac{m_t}{m_p} = \frac{3 \cdot \rho_t \cdot \beta}{2 \cdot \sigma_y}\left[\frac{R \cdot T}{(m - b \cdot \rho_p)} - \frac{a \cdot \rho_p}{m(m + b \cdot \rho_p) \cdot \sqrt{T}}\right] \tag{9.3}$$

Now it is important to find the storage density ρ_p that minimises the tank mass. This can be done by taking the derivatives of the tank-to-propellant mass ratios with respect to ρ_p as in equation 9.4 [71]. The resulting expression for ρ_p is presented in equation 9.5 [71]. The outcome of ρ_p is the same for a spherical and cylindrical tank. The constants a and b are the Redlich-Kwong parameters and are given by equations 9.6 and 9.7, respectively [71]. These constants are independent of the tank shape as well.

$$\frac{\partial(m_t/m_p)}{\partial \rho_p} = 0 \tag{9.4}$$

$$\rho_p = \frac{(4R \cdot T^{3/2} b \cdot m^2 a)^{1/2} - R \cdot T^{3/2} b \cdot m - a \cdot m}{R \cdot T^{3/2} b^2 - a \cdot b} \tag{9.5}$$

$$a = \frac{R^2 \cdot T_c^{5/2}}{9(2^{1/3} - 1)P_c} \quad (9.6) \qquad b = \frac{(2^{1/3} - 1)R \cdot T_c}{3P_c} \quad (9.7)$$

$$I_{ssp} = \frac{I_{tot}}{m_p + m_t + m_{EI} + m_T} \quad (9.8)$$

Next, using specific impulses and propellant masses, total impulses were obtained. When using electrical propulsion, the mass of the electrical system also becomes relevant when calculating system specific impulse. By knowing required power for each thruster, mass of the electrical system required for the propulsion subsystem is determined in electrical power subsystem chapter 10. By knowing all the above parameters about each thruster, system specific impulses were calculated 9.8. Here I_{tot} is total impulse, m_p is propellant mass, m_t is tank mass, m_{EI} is electrical system mass and m_T is thruster mass [71].

In figure 9.2, one can see that the BIT-3.2: 3 cm RF ion thruster (figures 9.3 and 9.4 [72],) turned out to be the best option in terms of the highest system specific impulse. The thruster has a thrust of 1.4 mN and consumes a power of 60 W while delivering that thrust. The amount of propellant needed to fulfill the Δv requirement is presented in table 9.2. Please note the contingency factor in the Δv to allow for unforeseen circumstances. To account for pressure losses in the tank as well, an extra contingency factor of 10% was added to the propellant mass [71]. This results in a final propellant mass of 0.3905 kg. Please note that this does not take into account the amount of propellant needed for momentum dumping of the reaction wheels. This is discussed in chapter 8.

In order to prevent that the CubeSat® gets negatively charged and starts re-attracting the positive ions, the thruster can be paired with a BHC-1500 neutraliser [73]. Both thruster and neutraliser are manufactured by "Busek space propulsion and systems" [74]. To minimize the need for AOCS manoeuvres, the choice was made to place two thrusters on two opposing sides of the LUMID. This would have no effect on the required power since the thrusters will never be firing at the same time.

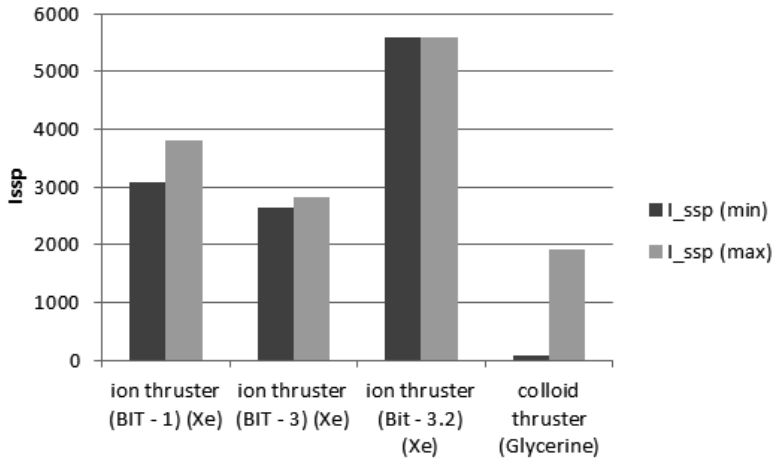

Figure 9.2: Comparing system specific impulses

Table 9.2: Δv budget

	From model	**Including contingency**		**Final**
Phase	**Δv** [m/s]	**Δv** [m/s]	**m_p** [kg]	**m_p** [kg]
Maintenance	364	473.2	0.2536	0.2790
Transfer	155	201.5	0.0976	0.1073
De-orbit	3.5	4.55	0.0038	0.0042
Total:	522.5	**679.25**	0.3550	**0.3905**

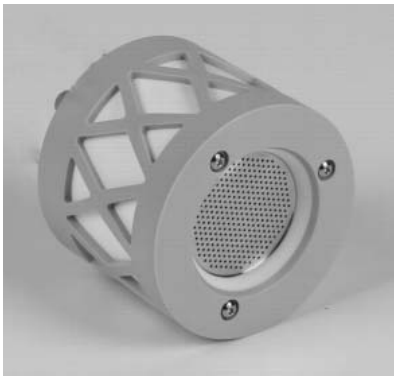

Figure 9.3: Bit 3.2 RF ion thruster

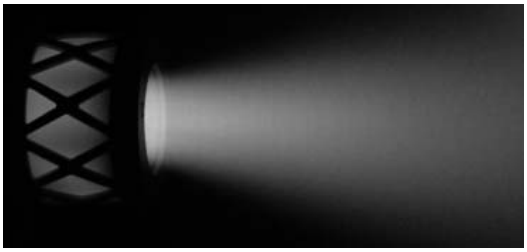

Figure 9.4: Bit 3.2 RF ion thruster operational

9.2.2 Tank Sizing

The chosen propellant is Xenon. After iterations done on every subsystem, the total spacecraft mass, propellant mass and moreover the complete mass budget is set. All the propellant needs to be stored in a tank located in the near vicinity of the thruster. For mass efficiency, one considered two options, a spherical- and a cylindrical tank. They where calculated simultaneously to allow for iterations. With a required radius of 40.47 mm it turns out that the spherical tank still fits inside one cube. Since a spherical tank is the best for mass conservation there is no need for elaboration on the design of a cylindrical tank. However, during the trade-off phase calculations on a cylindrical tank were also performed. Equations 9.9 and 9.10 were used to calculate the radius and thickness.

$$t_s = \frac{P \cdot r_s \cdot \beta}{2\sigma_y} \tag{9.9}$$

$$r_s = \left(\frac{3m_p}{4\pi \cdot \rho_p}\right)^{\frac{1}{3}} \tag{9.10}$$

In table 9.3, the trade-off of the tank material is presented. The trade-off criteria chosen were tank mass, material cost and the degradation due to the radiation environment. Taking this into account, one can conclude that the spherical Aluminium tank with radius of 40.47 mm and wall thickness of 2.58 mm is the most suitable for our design.

Table 9.3: Tank material trade-off

Trade-off table - Materials	m_t	Mat. cost (EUR)	Degradation life (-)
Steel (AM-350)	0.393	1.728	60% decrease in strength
Al (7075-T6) ✓	0.163	1.247 ✓	YS (+) & TS (+) & EL (-) ✓
Ti (Ti-6Al-4V)	0.137 ✓	3.48	YS (+), TS (+) & EL (-)
Quasi-isotropic composite	0.199	40.625	20% decrease TS

9.2.3 Architecture

The basic architecture of the propulsion subsystem is illustrated in figure 9.6. Please note that in figure 9.6 only one thruster is presented. In the final design of the CubeSats®, two thrusters and two neutralisers will be installed. However since they are both placed on parallel sides of the CubeSats® they will never be activated together. The red arrows in the figure represent power supply or in case of the neutraliser, electron supply (which are the same thing in this matter). The blue arrows are the Xe flow, passing both the high- and low pressure assembly (HPA and LPA) before being injected in the thruster. Both pressure assemblies represent an arrangement of filters, pressure transducers, service valves, latching valves, etc. [75]. Designing in such a sub-level is considered outside the scope of this project so won't be treated here but can and should be treated in later stages of the design.

The double black arrows represent the command and telemetry lines. They deliver all the commands to every part and provide feedback. [75]. The PPU|DClU unit is designed to process powers from the EPS to the required thruster inputs. For this a rad-tolerant, miniaturised PPU was used. It requires a 28 V to 37 V unregulated input [76] and uses RS-485 [77] as communication path (which basically means it uses two cables to communicate between parts instead of everything through one cable). Since the power is generated by the solar arrays, all voltages and currents processed are direct current (DC). The PPU is designed for a power draw of 55 W to 75 W [76] which complies with the required thruster input power. An example of a power distribution within the propulsion subsystem per load is illustrated in figure 9.5 [76]. To account for this (supplying the 60 W to the thruster), a total input power of 107 W is required. This does not take into account all the efficiencies of the PPU which will result in a higher required input power. The main power loads are the thruster, the neutraliser and the feed load.

The PPU described above is an off the shelf component, manufactured by the company named "Busek space propulsion and systems" [76].

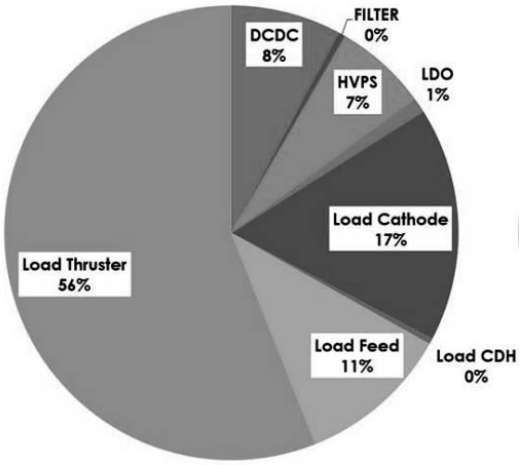

Figure 9.5: Propulsion subsystem power distribution

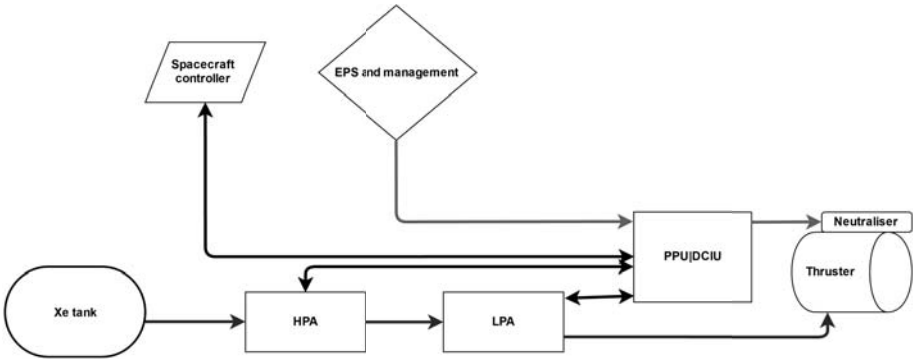

Figure 9.6: Propulsion subsystem architecture

9.2.4 Mass & Power Budgets

The complete mass and power budget of the subsystem is presented in table 9.4.

9.3 Verification and Sensitivity Analysis

In this section the verification methods for the design and the requirements the propulsion subsystem .

Table 9.4: Mass and power budget of the propulsion subsystem.

Component	Amount	Total Mass [kg]	Total Power [W]
Thruster	2	0.4	60 (from PPU)
Tank	1	0.163	11.785
Propellant	1	0.395	0
Neutralizer	2	0.30 [78]	18.21
PPU and others	1	0.428	11.07
	Total:	**1.686**	**107.14**

9.3.1 Verification of Calculations

The calculation that were performed to make the trade-off in 9.2.1 and to size the tank in 9.2.2 were verified with unit and system test. For example the input Δv was set to zero, returning zero values for m_p, m_t, t_s and I_{ssp}. Some calculations were done using two different methods. Comparing the two answers, it turns out they are the same.

Requirement Verification The requirements with identifier R-SC-PROP-4 and R-SC-PROP-6 need to be verified. The first being: "The PROP subsystem shall withstand all mechanical loads during all phases of launch, deployment and operation." This requirement will be verified by analysis, demonstration and testing. During the design, the launch loads are calculated. Then tests are performed simulating those loads. In the end the requirement is fully verified by demonstration after the launch and deployment phase when the propulsion subsystem is operational. The second one "R-SC-PROP-6: The design and development phases of the PROP system shall conform to the standards of the "European Cooperation for Space Standardization" [70]" shall be verified by analysis.

Thruster Selection Validation As the choice of thruster came down to be the "BIT 3.2 RF ion thruster"9.3 it is important that this is validated. This is done by looking for reference missions with comparable mission characteristics and where the same thruster is chosen. The LunarCube mission (a deep space 6U CubeSat® with mission enabling ion propulsion technology) that is going to be launched in 2018 is planning on using this same thruster sized for injecting a Δv of 3.2 km/s to a 12 kg or 6U CubeSat® [79]. As the LUMID is slightly comparable (higher mass but lower Δv) to this mission however not operational yet, at least the thruster "selection" is considered to be validated.

9.3.2 Sensitivity Analysis

The most relevant inputs of the propulsion subsystem are the required Δv and the available power. If more power is available, a more powerful thruster can be used with a higher specific impulse, which lowers the burntime and also the required propellant mass. The lower propellant mass translates itself in a lower total mass of the satellite which also lowers the propellant mass and so on.

Lets suppose that an additional Δv of 10% is requested, this means that the propellant mass will also increase with 10%, resulting in 4.3% increase in total subsystem mass or 0.29% in total satellite mass. This increase in total mass translates itself in an additional increase in propellant mass and so on. Introducing an increase in total mass of 10% (keeping the Δv constant) results in a increase of 10% for the propellant mass.

The reverse happens when the Δv and/or mass budget are lowered. It could even be that the Δv becomes so low that even for cold- or hot gas thrusters the amount of propellant that one can store in the CubeSats® is not a limiting factor. This could mean that electric propulsion is not the most suitable option for the design and cold or hot gas thrusters become more weight efficient in terms of operational power. If the power required for the propulsion subsystem lowers in such a matter, since it is the main driver in the power budget, the amount of required solar panels and batteries lowers which means that the total mass of the satellite lowers as well. The lower total mass translates itself again in a lower propellant mass.

CHAPTER 10

Electrical Power System

The Electrical Power System (EPS) is the electrical interface between all on-board components. The main function is to provide the power needed for the operation of all systems that together form the spacecraft bus. In this chapter, the design of the EPS will be split into three parts: power generation, power storage and power management.

10.1 Subsystem Description

The EPS concept generation described the different types of methods of power generation and storage. At the end of the concept phase, the decision to use a photovoltaic–battery system was made. The requirements that were defined beforehand plus the relevant mission requirements are given in table 10.1.

The starting point of the EPS design is the mission power budget, given in table 10.2. This budget shows the total power consumption of the different subsystems. The breakdown of each budget is given in their respective chapter.

A functional analysis of the EPS shows that there are four essential power related functions: power generation, storage, conversion and distribution. The latter two will be combined into power management. This can be seen in figure 10.1.

Table 10.1: EPS requirements

Identifier	Requirement	Section	Compliance
R-MI-EOL-2	Spacecraft shall not pollute the lunar environment with hazardous substances in case of an end-of-mission impact.		✓
R-SC-EPS-1	The EPS subsystem shall enable the operation of all subsystems for the full duration of the mission.	10.2.3	✓
R-SC-EPS-2	The EPS subsystem shall deliver an average power of at least 35 W during one full orbit.	10.2.1	✓
R-SC-EPS-6	The EPS subsystem shall autonomously adjust the power provision and distribution upon a ground command to enter safe mode operation.		
R-SC-EPS-7	The power storage shall account for the worst case scenario.	10.2.2	✓
R-SC-EPS-8	The solar panel degradation shall be lower than 10 % over the mission lifetime.	10.2.1	✓

Table 10.2: Total power budget at subsystem level

Subsystem	Power [W]				
	Total	Manoeuvre Phase	Science Phase	Communication Phase	Safe Mode
AOCS	4.53	4.53	4.53	4.53	1.54
CDHS	8.00	6.20	8.00	6.20	6.20
PLS	4.20	1.00	4.20	1.00	0.00
PROP	107	107	0.00	0.00	0.00
TTCS	2.04	0.04	0.04	2.04	0.04
TCS	25.0	0.00	0.00	0.00	0.00
Total:	**151**	**119**	**16.8**	**13.8**	**7.78**

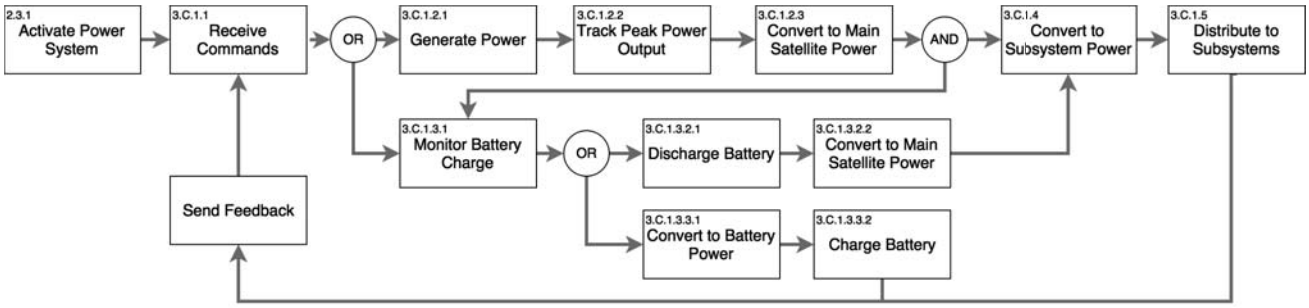

Figure 10.1: EPS functional flow diagram

10.2 Design

The design and design process of the EPS are presented below.

10.2.1 Solar Panel

Before a solar panel can be designed it is important to know whether it is beneficial to have small panels or not. This is because it might be better to have a larger solar panel, for instance to have a low mechanical natural frequency in the first mode of vibration which is good for the AOCS [80]. However, this benefit for the AOCS is countered by the added control needed due to the possibly higher MOI caused by larger solar panels. Another downside of a larger solar panel is the STR integration and deployment systems that are needed to fit it to the s/c which increases the costs and complexity. Furthermore, larger solar panels can also increase the irradiated area which increases the solar pressure. To counter this, the AOCS and PROP systems need to be enlarged for torque compensation and additional station keeping respectively. Lastly, a larger panel means more mass which increases the launch costs.

To design a small solar panel it is important to have a high solar panel performance. More efficient solar cells increase the generated power per unit area. The positions or configuration of the solar panels have a large effect on the performance too, because the power that is generated decreases with an increasing incidence angle. Lastly, the solar cells need to be positioned such that the effective area and therefore the packaging factor is high.

Solar Cell Selection

As stated before, the EPS needs to provide power to all subsystems for the entire lifetime. The efficiency of solar cells decreases due to ageing, radiation degradation, micro-meteoroid impacts etc. Therefore it is important to design the solar panels for the minimum lifetime of two years. This is why not only the maximum efficiency at beginning-of-life (BOL), but also the efficiency at the end-of-life (EOL) is of importance. The cost is of importance too, as one of the design goals is to optimise the performance to cost ratio.

Types of Solar Cell Materials Photovoltaic cells or solar cells convert sunlight in the form of photons into electricity. Electric potential is created when the energy of a photon is absorbed by the common junction of two dissimilar materials. The energy of the photon creates charge carriers that are separated at the junction. They are electron–ion pairs in a liquid electrolyte, or electron–hole pairs in a solid semiconducting material. They create a potential gradient and a current when the circuit is closed, the product of which is the power [80]. Semiconductor materials and semiconductor alloys that are used in the photovoltaic industry include elements like; CdS, $CdSe$, $CdTe$, Cu_2S, Cu_2SnS_3, FeS_2, $GaAs$, GaN GaP, Ge, InN, InP, $a-Si$, $c-Si$, SnS, $ZnTe$, $Al_xGa_{1-x}As$, $CdZnTe$, $Cu(In,Ga)Se_2$, $CuInSe$, $InGaN$, and $In_xGa_{1-x}P$. A selection of solar cell materials are compared in table 10.3.

However, each type of solar cell can only absorb a specific amount of energy corresponding to small range of wavelengths of the solar spectrum, this energy is known as the band gap. Photons with energies less than the band gap pass right through the material without generating electricity and photons with excess energy dissipate it in the form of heat [81]. The band gaps of the semiconductor materials can also be seen in table 10.3, however this property is not used in the trade off as it is already integrated in the conversion efficiency.

Although the most used solar cells in the space industry are monocrystalline single-junction silicone and GaAs/Ge-based multi-junction solar cells. However, for the sake of completeness and a fair trade-off, several other solar cell technologies are also considered.

Semicrystalline and polycrystalline are created using fast and inexpensive manufacturing processes. However, their conversion efficiencies are lower than single crystalline cells and are therefore not applicable to space applications for now. There is an increasing interest in the application of thin film materials in the space industry. These materials can be added directly on compatible substrate materials and increase the band gap resulting in a higher efficiency. They are relatively cheap, because a small amount of material is required as the thickness is typically a few micrometres or less.

Amorphous technology based solar cells have too low efficiencies for the space industry. Instead of a crystalline structure it forms a random bond structure resulting in these lower efficiencies. However, a steep learning curve is anticipated, resulting in higher efficiencies and lower manufacturing cost.

The efficiency of a single solar cell is limited by the band gap. To achieve higher efficiencies, solar cells of different band gaps are stacked, creating what is known as 'multi-junction cells'. This way the energy of photons that would pass through a certain semiconductor, because its energy is less than the band gap can now be absorbed by another semiconductor with a lower band gap. Tunnel junctions are used provide a low electrical resistance to mitigate the voltage drop between two tandem cells. Multi-junction cells generally have higher efficiencies as can be seen in table 10.3. Today, the $GaInP/GaAs$ on Ge substrate multi-junction cells are being increasingly used in the space industry [80].

Solar cells degrade over time due to radiation, thermal cycling in and out of eclipses, micro meteoroid strikes, plume impingement from thrusters, and material outgassing, and material property degradation such as darkening of solar cell cover glass [61]. However, the xenon leaving the thruster is inert and will therefore not cause damage to the solar cells. Furthermore, the cold gas thruster used to desaturate the reaction wheels (part of the AOCS) need only 140 g of propellant (see subsection 8.2.3) and therefore their contribution to the life degradation of the solar cells is neglectable as well.

Of these the radiation degradation is most variable over different solar cells as some are more sensitive to radiation than others. This is why the radiation hardness of solar cells is used as a trade criteria. A comparison of the normalised efficiency Pmp/Pmp_0 for various solar cells at different levels of electron fluence can be seen in figure 10.2. This figure is based on data from references; [82] [83] [84] [85]. Here it can be seen that silicon and indium phosphide solar cells types are more sensitive to high fluence. More severe radiation damage is however caused by protons, but it can be seen in the references that the relative differences in sensitivity between solar cells are close to the sensitivity to electron fluence. A cover glass can be used to decrease the radiation degradation of solar cells. This decrease depends on the thickness of the cover glass and the amount and type of radiation that the solar cell experiences. Several factors can be found in Spacecraft System Engineering [22].

As can be seen from the trade off table 10.3 the $GaInP/GaAs/Ge$ solar cells are the best option. The efficiency was given the highest weight, because this changes the required affective area.

COTS Solar Cell Choice

With the previous trade-off focusing on the general characteristics of the solar cells, the COTS choice compares the real characteristics of different types of triple-junction $GaInP/GaAs/Ge$ solar cells. A trade-off between various $GaInP/GaAs/Ge$ solar cells that are suitable for CubeSats® is made in table 10.4. The packaging factors are calculated using one of the panels used on the LUMID spacecraft and

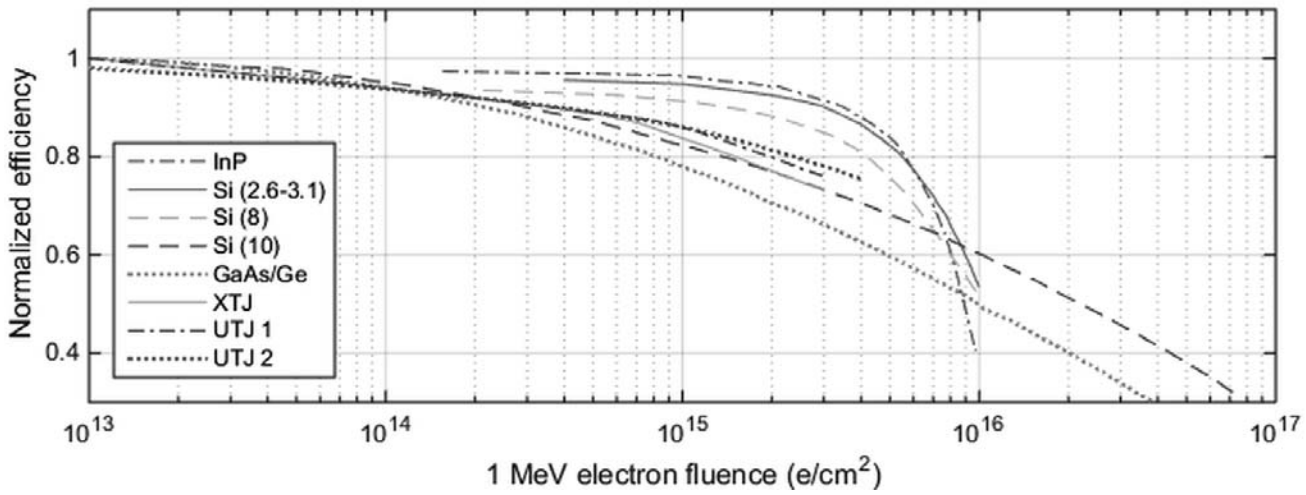

Figure 10.2: Radiation degradation of solar cells due to electron fluence

Table 10.3: Solar cell characteristics and trade-off matrix

Trade Criteria / Characteristics	**Weight**	**Semiconductor Materials**							
		$CdTe$		$GaAs$		$a-Si$		$c-Si$	
		Value	Score	Value	Score	Value	Score	Value	Score
Band Gap (eV)	x	2.1 [22]	x	1.35 [22]	x	1.7-1.8 [86]	x	1.12 [22]	x
Efficiency (%)	60	16.7 [87]	4	18.5 [61]	5	8.0 [61]	1	22 [61]	7
Radiation Hardness	25	High [88]	8	Med [89] [90]	5	High [80]	8	Low [80]	2
Cost ($/W)	15	<100 [91]	8	300 [92]	2	<100 [80]	8	100 [80]	4
Total:	**100**		**560**		**455**		**380**		**530**
Trade Criteria / Characteristics	**Weight**	**Semiconductor Alloys**				**Multi-junctions**			
		$Cu(In,Ga)Se_2$		$CuInSe$		$GaInP/GaAs/Ge$		$GaAs/Ge$	
		Value	Score	Value	Score	Value	Score	Value	Score
Band Gap (eV)	x	1-1.7 [93]	x	1.05 [81]	x	0.6-1.86 [81]	x	0.67-1.35 [94]	x
Efficiency (%)	60	15 [95]	3	10 [80]	2	30.0 [61]	8	19 [80]	6
Radiation Hardness	25	Low [96]	2	High [80]	8	Med [80]	5	Med [80]	5
Cost ($/W)	15	<100 [80]	8	<100 [80]	8	250 [97]	3	300 [80]	2
Total:	**100**		**350**		**440**		**650**		**515**

the solar cells dimensions. The costs are unknown. As can be seen in the trade-off table there is a clear winner, namely the Azur Space TJ 3G30C [98]. The weight given are based on the magnitude in which the differences of the characteristics impact the required solar panel area, however the winner will not change during the sensitivity analysis it scores high on all trade criteria.

Table 10.4: COTS solar cell characteristics and trade-off matrix

Trade Criteria / Characteristics	**Weight**	**Spectrolab**						**Azur Space**	
		ITJ [99]		UTJ [100]		XTJ [101]		3G30C [98]	
		Value	Score	Value	Score	Value	Score	Value	Score
BOL efficiency (%)	50	26.8	1	28.3	2	29.5	3	30	4
Radiation Degradation Pmp/Pmp_0 at 10^5 fluence 1MeV (e/cm2)	20	0.84	1	0.86	3	0.85	2	0.89	4
Packaging factor (%)	30	0.85	4	0.792	2	0.792	2	0.828	3
Total:	**100**	**190**		**220**		**250**		**370**	

The Azur Space TJ 3G30C cells come in different sizes. The most useful sizes for the 12 Unit s/c are 30.18 cm^2 or 60.36 cm^2 and their dimensions are 40 by 80 mm and 80 by 80 mm respectively. From now one the large solar cell will be considered as two cells. Therefore a maximum of 15 cells fit on one panel of 220 by 320 mm. The damage equivalent 1 MeV fluence ($e/cm^2/yr$) over orbit altitude is given is Spacecraft System Engineering [22]. However this is for orbits around the Earth. The radiation in a lunar orbit is smaller compared to the radiation in the Van Allen belts. The actual amount of radiation in lunar orbit over a period of two years is not known. Therefore a fluence of 3.0×10^{14} e/cm^2 is assumed. A cover glass is already included in the solar cell and with it degrades by 1.1% over two years. The life degradation caused by thermal cycling, MMIs, and material property degradation is assumed to be an extra 1.25% per year [61]. This value is given for silicon and gallium-arsenide cells, but as thermal cycling and MMIs are not dependant on the material it is close to the actual degradation of the triple junction $GaInP/GaAs/Ge$ solar cells.

Solar Panel Configuration

Firstly, as said before, the power that is generated decreases with an increasing incidence angle. The s/c is 3-axis stabilised, so it is possible to point one surface of s/c towards the Sun. This is why all solar panels are placed on one plane. During the eclipse and manoeuvres the s/c attitude needs to be controlled for the payload and thrusters respectively. Therefore, a few attitude changes need to occur during one orbit which causes added requirements on AOCS and system complexity. However, the added amount of power per unit area results in a smaller solar panel area which results in a smaller MOI which is beneficial to the AOCS. For a majority of orbits the eclipse will not overlap the manoeuvre.

During the manoeuvre a lot of power is required (see table 10.2), that is why during these scenarios the solar panels will be able to turn relatively to the s/c to decrease the incidence angles. The solar panels will rotate on one axis like the orientable solar panel system for nanospacecraft by Fabio Santoni et al. [102, 103]

The solar panels will be placed on the sides of the spacecraft and will deploy by using spring-loaded hinges and can rotate as explained in subsection 11.2.4. This way the solar panels on one axis, the velocity body axis, can correct for the beta angle and will have an incidence angle equal to the in orbit plane angle from the sun to the s/c = α_i and panels on the other axis, the velocity body normal axis, can correct for this angle and its incidence angle is therefore equal to the beta angle.

The solar panels are deployed in the longitudinal direction instead of lateral so that when the solar panels turn the moment required is low.

Solar Panel Sizing

To determine the required amount of solar cells a simulation is created in MATLAB®. This model estimates the average generated and used power per orbit over a period of two years. It does so by

taking an average orbit during one day, calculating the power during that orbit and integrating this over the orbit period and dividing this by the orbit period. A flow diagram of the model can be seen in figure 10.3.

The variable inputs of the simulation are; the average orbit time per day, the average beta angle per day, the maximum burn time during one orbit per day and the average true anomalies of the begin and end of an eclipse per day. Furthermore, the constant values that are used are; the solar irradiance, J_{sun} of 1367 W/m^2 [62], an area, A_{cell} of 30.18 cm^2 of one solar cell [98], the solar cell BOL efficiency, η_{BOL} of 30% [98], the life degradation, L_d of the solar cell of 3.6%, the maximum time for a slew manoeuvre, t_{wcs} of 74.5 s (see table 8.4), the used power during the science phase, P_{sci} of 16.85 W, the used power during the manoeuvre phase, P_{man} of 118.9 W, the used power during power generation phase, P_{Sun} of 11.85 W, the battery charge and discharge efficiency, ϵ_{be} of 98% [104], and the power management and conversion factor, ϵ_{pm} of 0.85 [52]. Due to an assumption mentioned below the power of the manoeuvre phase and science phase is different from the power budget. The assumptions and their impacts for the solar panel sizing model are given below.

Assumptions

- During the penumbra of the eclipse the solar panels will not generate power.

  The additional energy that can be generated during the penumbra is negligible as it is a small period during which the solar irradiance is low. Furthermore, the s/c has to start to point towards the centre of the Moon to prepare the science phase and so incidence angles will not be optimal.

- The orbit is assumed to be circular.

  The orbits are relatively close to circular orbits as the average eccentricity of the orbits is 0.0784 *(chapter 3). This changes the values of α_i, the begin and end times of an eclipse and station keeping manoeuvres change by a small amount, which cause small changes in the generated and used power.*

- The solar pointing accuracy is a perfect one hundred percent.

  As the pointing accuracy is high the difference in incidence angle is negligible (subsection 8.2.7)

- The solar pointing of the solar panels is assumed to be perfect.

  The stepper motor can only vary the solar panels per degree (see subsection 11.2.3), this however marginally changes the generated power due to different incidence angles

- The solar panels will turn towards the Sun during the attitude changes.

  Turning the solar panels during the slew manoeuvres decreases the incidence angles and thereby increases the generated power. The maximum slew time is 74.5 s *which is low compared to the orbital period. Therefore, if the solar panels will not turn during this manoeuvre the change in average power over one orbit is minimal.*

- During the attitude manoeuvre the angle rate of change is assumed to linear.

  As the slew time is small the difference in energy generation over one orbit is minor.

- The station keeping manoeuvre is centred around the apoapsis.

  It might be that the thrusters will start and stop operating earlier or later, however the time the solar panels will be pointed towards the Sun remains the same, so the changes in the generated power are small. Furthermore, this might cause the manoeuvre to coincide with an eclipse for a longer time and cause the used power increase due to battery charge and discharge efficiencies.

- During manoeuvre phase the s/c is assumed to be pointing towards the centre of the Moon.

  Pointing towards the camera towards the centre of the Moon in a circular orbit means that the thruster would be pointed in the velocity direction. However, the thruster should more often be pointed perpendicular to the semimajor axis. Therefore the incidence angles will be different. Therefore depending on the orbital parameters the generator power might be higher, but can also be

lower. When this coincides with a large burn duration this might impact the time that the thrusters can operate for. This can be however, compensated for over time, since the peaks of the burn durations last for a maximum of 15 *orbits (see chapter 3). When this peak decays extra burn time can be allocated since the power system is designed for these peaks.*

- The power for communication is assumed to be continuous and equal to $1/24^{th}$ of 2 W plus the 0.04 W due to the maximum communication time constraint of one hour per day (see table 7.1).

  It might occur that the lunar orbiter is in communication range during a manoeuvre and therefore more power is required. However, this does not influence the average power per orbit, so there will be enough energy generated during the orbit to provide power by the use of stored energy in batteries.

- The s/c is assumed to be never operating in the safe mode.

  This causes the average used power to be slightly higher than the actual value as the safe mode is only an exceptional case.

- The life degradation is assumed to be linearly.

  As can be seen in figure 10.2, the radiation degradation is not linear. However, the life degradation is only 3.6 % *of a total BOL efficiency of* 30 %*. Therefore the difference in efficiency at a certain point in time will be minor.*

As explained in section 8.2.2 the s/c will turn towards the Sun in various phases of one orbit. However, due to Moon phases the eclipse will not be centred around the periapsis during all orbits. By comparing the average true anomalies of the beginning and end of the eclipses for each day and the calculated true anomalies of the beginning and end of the manoeuvres it is decided if and when attitude changes will occur and how the s/c is oriented during the entire orbit.

There are eight different scenarios. Firstly the burntime can be smaller or greater than the eclipse time. Next the eclipse period might overlap (can be on two different sides of apoapsis), coincide or differ from the manoeuvre phase. The last being the situation as seen in figure 8.2.

The incidence angles α_i, which is defined as the in orbit plane angle between the solar panel and the Sun, and β_i, which is defined as the out of orbit plane angle between the solar panels and the Sun, are determined for each second of every simulated orbit. Examples can be seen in figure 10.4.

As said before there are solar panels that are able to turn on the axis that is tangential to the velocity vector, (x-axis), and others that can turn on the normal to velocity vector axis, (y-axis). This means that during the manoeuvre phase the incidence angle for the panels on the y-axis is equal to the beta angle, because it cannot turn out of the orbit plane, and the incidence angle for the other panels is equal to α_i. The incidence angles are also determined for the different orbit phases.

The used power is determined during every simulated orbit too. For different phases in one orbit different amounts of power are used. This is done for all eight scenarios. Furthermore, if the s/c is in an eclipse and manoeuvre the required power is higher due to the battery charge and discharge efficiencies.

To calculate the maximum available power per unit area, P_m, equation 10.1 is used. Here η_{cell} is the planar cell theoretical efficiency and J_{sun} is the solar irradiance. At the BOL, the solar panel's power per unit area, P_{BOL}, is given by equation 10.2 [61]. Where I_d is the inherent degredation and θ_i is the incidence angle. The life degradation of solar cells, L_d, is given by equation 10.3 [61]. Where t is time in years and D is the degradation per year. Finally, the solar panel's power per unit area at during the mission, P_t, is given by equation 10.4 [61]. The available power is calculating assuming that the incidence angle is 0deg. Lastly, the generated power is with the power management and cable loss efficiency to get the delivered power. Examples of these can be seen in figure 10.5.

$$P_m = \eta_{cell} \cdot J_{sun} \quad (10.1) \qquad P_{BOL} = P_0 \cdot I_d \cdot \cos\theta_i \quad (10.2) \qquad L_d = (1-D)^t \quad (10.3) \qquad P_t = P_{BOL} \cdot L_d \quad (10.4)$$

The average available power, average generated power, average delivered power, average used power are calculated by integrating over the orbit period and dividing by the orbit time. These were plotted over the required total life time of two years which can be seen in figure 10.6. The oscillations are due to the different burn times. The burn times have a larger effect on the used power compared

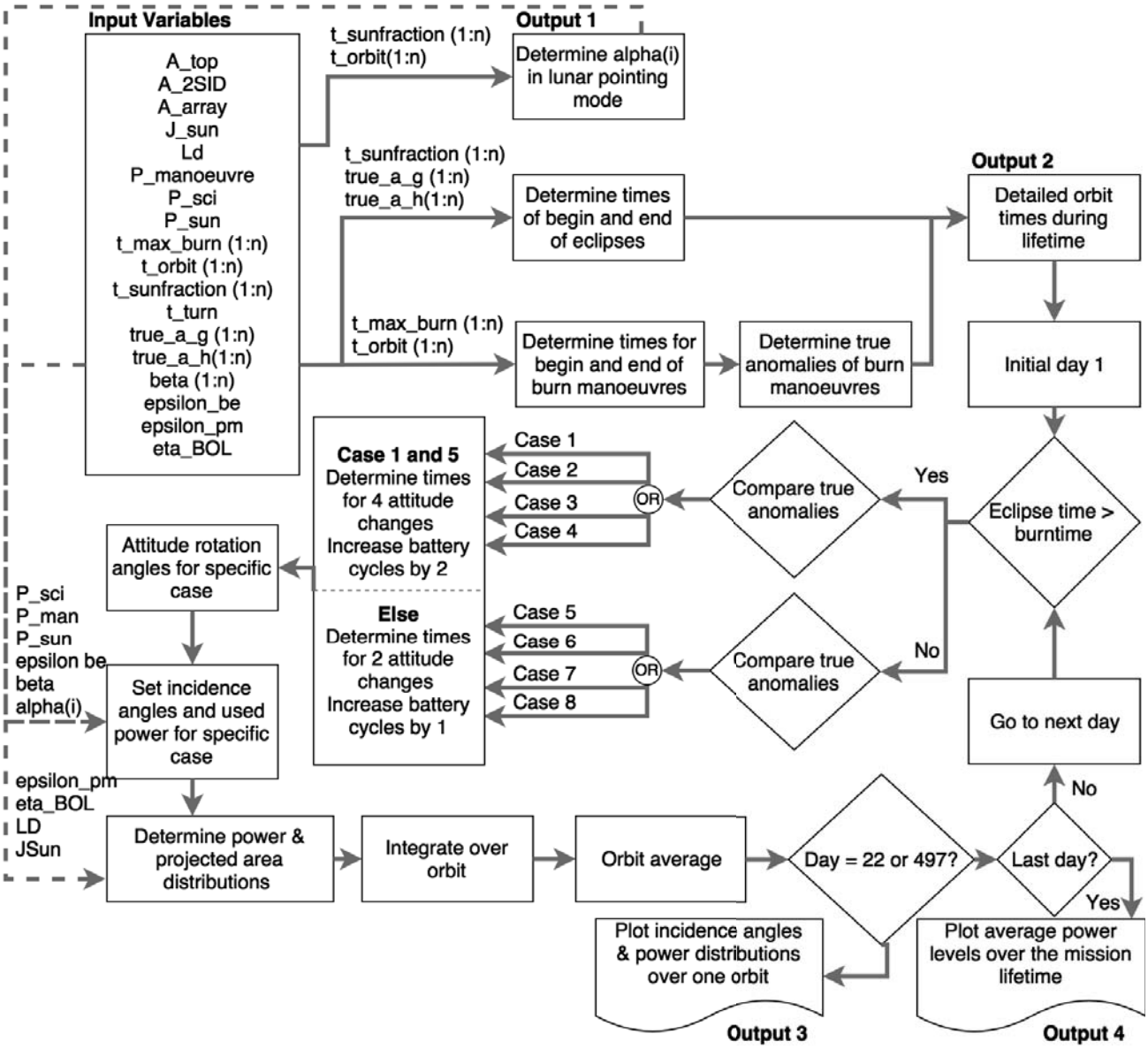

Figure 10.3: Schematic of the model used for the solar panel sizing

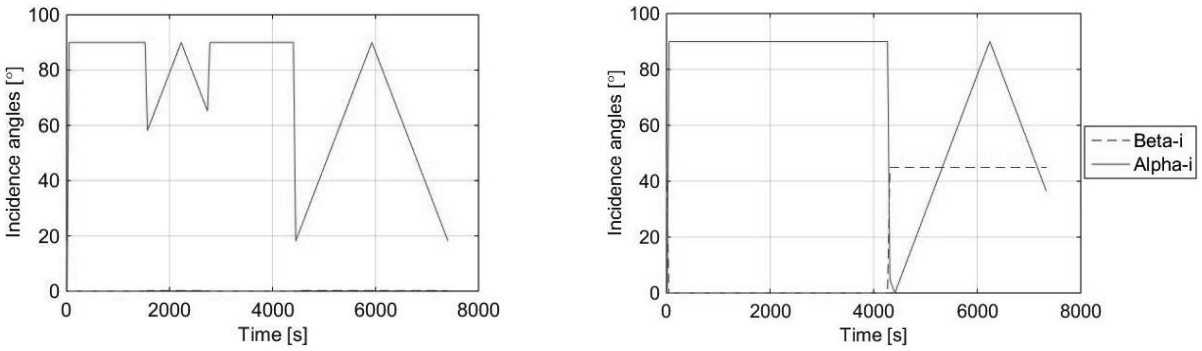

(a) Average orbit on day 22

(b) Average orbit on day 497

Figure 10.4: Incidence angles during one orbit

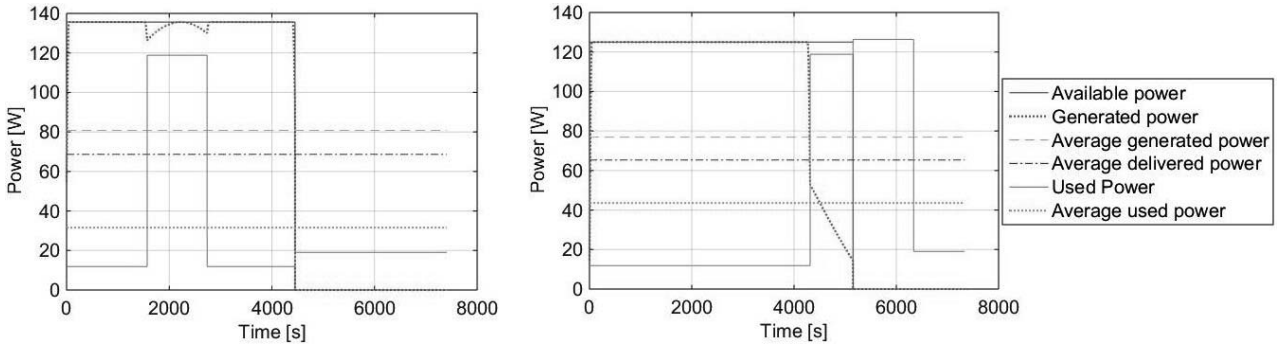

(a) Average orbit on day 22

(b) Average orbit on day 497

Figure 10.5: Power levels during one orbit

to the generated and delivered power. This is because of the power required for the PROP system is larger than the difference in generated power due to different incidence angles during the manoeuvre phase. Next the number of solar panels was adjusted and allocated over multiple axis until the used power distribution just touches the delivered power distribution. An additional of 10% is added a safety factor. This results in an optimum, when also considering the packaging factor and the allocated panels, of 50 required solar cells, four panels on the x-axis and 60 required solar cells, four panels, on the y-axis. A maximum of 15 cells can fit on one panel as in figure 10.7a. In order to have 50 cells spread symmetrically a panel of 10 cells is used as can be seen in figure 10.7b. With this many solar cells a maximum power of approximately 136 W can be generated.

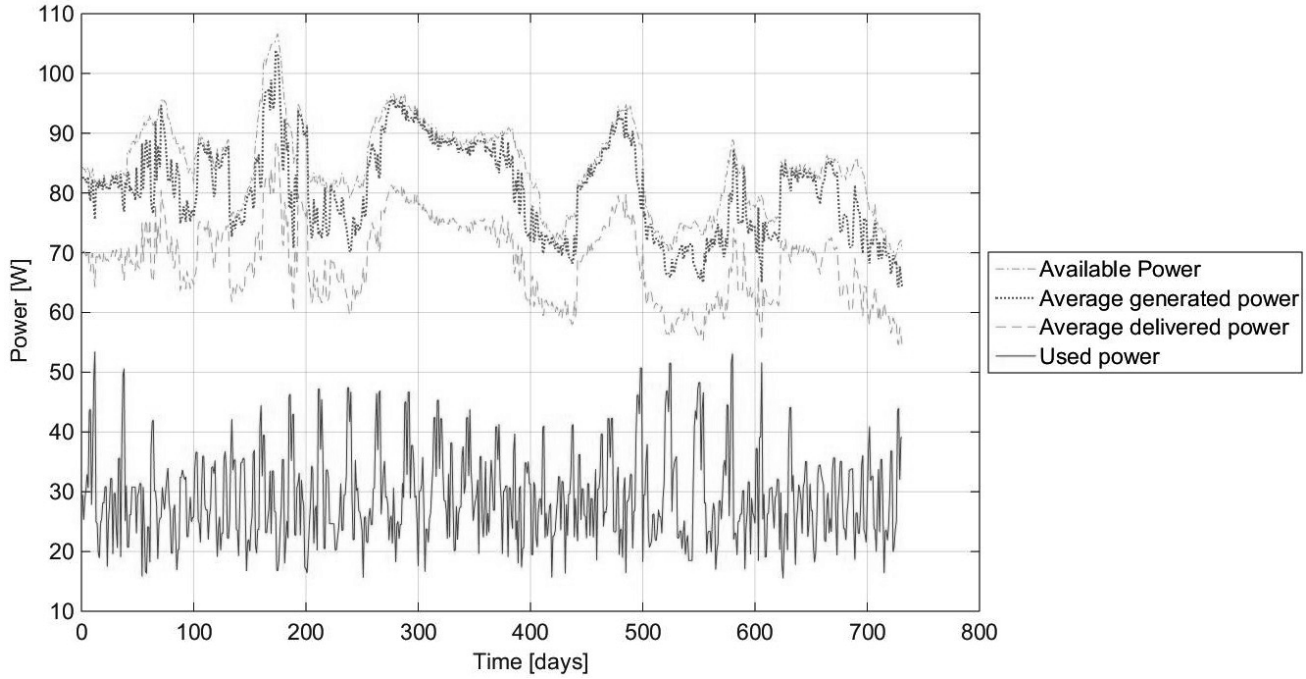

Figure 10.6: Power distributions during the mission operation phase

Furthermore, a counter is used, which determines the amount of cycles for the batteries. It does so using the eight scenarios described before. The batteries are used during eclipses and during manoeuvres, so the counter adds two cycles when in one orbit these phases happen separately and it adds one cycle when they coincide or overlap. The count is then multiplied by 24 hours and divided by the mean orbit period as the simulation only runs one orbit per day. This results in a total number of 12 324 cycles.

Lastly the projected area of the s/c by the sun is also calculated using the simulation. This area is used by the thermal control to calculate the temperature levels of the s/c. It is calculated using the

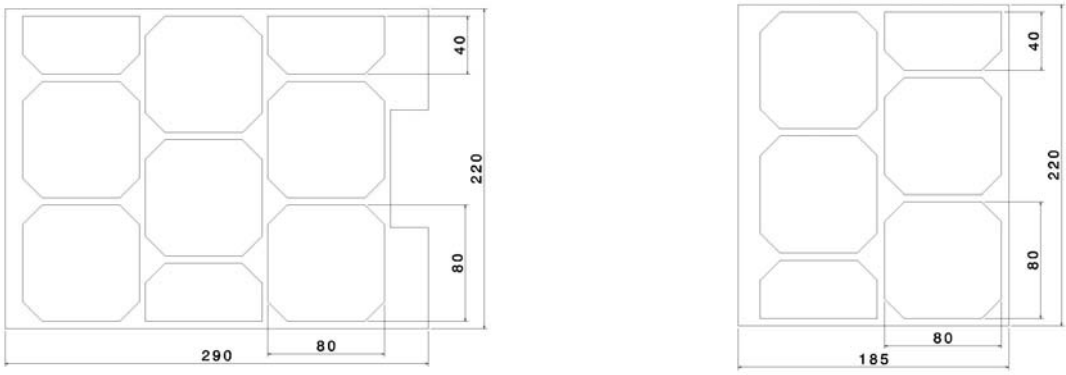

(a) Solar panel with 15 cells

(b) Solar panel with 10 cells

Figure 10.7: Types of used solar panels

total area of the panels, both 2SID and solar, and the top of the s/c as for the majority of the time the panels will be pointed towards the Sun and/or the camera will point towards the centre of the Moon. The incidence angles of the 2SID panels are the same as for solar panels, but the incidence angle of the top is the maximum of α_i and β_i. This results in an average projected area per orbit which is used in chapter 12. The average projected area over the entire two years is 0.802 m^2.

This simulation designs the power system for the mission time during which the s/c is already deployed and in operational orbit. However, at deployment and during the transfer orbit the EPS should also deliver enough power to the subsystems. At deployment an additional amount of power is needed for the thermal control system. It requires 25 W to heat the s/c. The batteries can provide power for the initial deployment after which the solar panels can take over. After the s/c is heated the orbit transfer will start during which the maximum required burn time is approximately 32 min (see section 3.5) which is lower than some burn times required for station keeping. Also at the BOL there will be more power generated due to a high solar panel efficiency. Therefore, the average generated and delivered power at the orbit transfer are higher than the average required power. This means that is some orbits the burntime can be increased to decrease the transfer time.

The size of the solar panels might need to be increased slightly due to the added degradation of the solar cells during the deployment phase. This effect is larger for the second and third s/c that will be deployed at a different right ascension of ascending node which is explained in section 3.4.2. As the degradation per year is 1.8% and the BOL efficiency is 30%, the increase in extra solar panel area will be around 6% per extra year in orbit.

10.2.2 Battery Selection & Sizing

The power generated with the solar panels needs to be stored for the time in eclipse. In the Midterm report [105] the choice for chemical batteries was made. Before the COTS choice for the battery is made, first a trade-off for various battery types is made. Then the COTS

Battery Type Trade-off

Before looking at the characteristics, a selection of space-suitable rechargeable batteries was made. These include the $Ni-Cd$, $Ni-H_2$, $Ni-MH$, $Li-ion$, $Li-poly$, and $AgO-Zn$ types of batteries.

The killer criteria is the cycle life of the battery. During the life time of at least two years, the number of cycles is about 12 000, see subsection 10.2.1. This amount of cycles is to large for $AgO-Zn$ types of batteries, and therefore it is not considered suitable for the mission. The values and properties of the remaining battery types are presented in table 10.5. In this table the weight of each criteria and the scores are also presented.

One of the most important characteristics are the specific energy in Whr/kg and the energy density in Whr/L, as they determine the mass and size of the battery.

Another important characteristic is the energy efficiency. This is a figure for the amount of energy lost when charging and discharging the battery. For power loss, the self discharge of a battery is also considered. The self discharge is a figure for the amount of energy lost in a battery over time due to an internal reaction when the battery is not used for extended periods of time. The longest phase where the battery is not used is the launch and deployment phase.

The temperature range is a major influence point on the thermal control subsystem. The operating temperatures for batteries is narrow compared to other subsystems and even within that range, battery efficiencies may vary.

A major effect on the nickel based batteries is the memory effect. It is an effect that occurs when the battery is not fully discharged repeatedly. The result is that it 'remembers' the point where it is recharged. The end result is a partial loss of capacity after repeated shallow discharge cycles. This memory effect is a disadvantage in cycles where the battery is not fully discharged every time like in a satellite.

Lastly, the cost are of mayor importance, older battery compositions are generally cheaper in costs per kWh than newer systems [80].

Table 10.5: Battery characteristics & trade-off matrix

Trade Criteria / Characteristics	**Weight**	$Ni-Cd$		$Ni-H_2$		$Ni-MH$		$Li-Ion$		$Li-poly$	
		Value	Score	Value	Score	Value	Score	Value	Score	Value	Score
Specific Energy (Whr/kg) [80]	15	40-45	1	45-65	2	50-70	3	90-150	4	100-200	5
Energy Density (Whr/L) [80]	15	50-100	2	35-50	1	140-180	3	150-250	4	150-300	5
Energy Efficiency (%)	20	72 [61]	3	70 [61]	2	66 [106]	1	98 [61]	5	98 [104]	5
Self Discharge (% per month)	10	20 [61]	2	20 [61]	2	30 [104]	3	2 [61]	5	2 [80]	5
Temperature Range (∘C) [80]	20	−20 to 50	5	−10 to 50	4	−10 to 50	4	10 to 45	2	50 to 70	1
Memory Effect [104]	5	yes	1	no	5	no	5	no	5	no	5
Relative costs ($/kwh) [80]	15	1500	5	1500	5	2000	3	3000	2	>3000	1
Total:	**100**		**305**		**285**		**290**		**365**		**360**

The trade-off shows that the COTS option for batteries can be focused on Lithium-Ion.

COTS Battery Choice

With the previous trade-off focusing on the general characteristics of the battery types, the COTS choice compares the real characteristics of different types of Lithium-Ion batteries. The values for each battery can differ due to different configuration of cells, efficient packaging and standard size of one battery.

The important characteristics for choosing the battery is the packaging of the battery for CubeSat®, the battery capacity and the mass. The limiting factor for this design is the packaging for CubeSat®, since there are few options that are commercially available. Out of the remaining options, one battery was found suitable for this design: The EXA BA01-D battery. The characteristics of this battery can be found in table 10.6.

Table 10.6: Characteristics of the BA01-D battery

Characteristic	**Value**
Number of cells	12
Mass (kg)	0.155
Energy storage (Whr)	53.2
Voltage (V)	3.7
Capacity (Ahr)	14.4
Dimensions (mm)	100x100x7
Maximum discharge rate (C)	20
Maximum charge rate (C)	3

Battery Sizing

The size of the battery depends on: the eclipse time, the power required during the entire orbit, the depth-of-discharge (DOD) for the standard battery cycle and the degradation of the solar panels. The number of batteries needed to store is calculated with equation 10.5.

$$n_{batteries} = \frac{E_{required}}{E_{battery}} = \frac{1}{E_{battery} \cdot \eta_{EOL} \cdot \eta_{charge} \cdot DOD} \int_0^{t_{eclipse}} P(t)dt \tag{10.5}$$

The battery will be designed for the ideal DOD-EOL charge efficiency. The power consumption changes during various stages of the orbit and during the mission lifetime. The worst case for the battery is during a full lunar eclipse. However, designing the entire power storage on this single event in the mission lifetime results in an over-designed EPS. A decision was made to not use thrusters during any eclipse, which is allowed since the spacecraft will survive three orbits without station-keeping (section 3.4.4). The second-worst case is when the eclipse time is the longest and the full station-keeping burn time is in the eclipse as well. The largest fuel burn time is estimated to be 33 min and the largest eclipse time is estimated to be 75 min. Using the power budgets from table 10.2, the estimated energy used is 68 Whr (equation 10.6).

$$E_{required} = \int_0^{t_{eclipse}} P(t)dt = 87.3 \cdot \frac{33}{60} + 15.93 \cdot \frac{75}{60} = 68Whr \tag{10.6}$$

The DOD of a normal discharge cycle affects the degradation of the battery during its lifetime: reducing the DOD increases the battery size overall, but reduces the size needed at the end of the mission lifetime. Through experimental analysis [107], the values from table 10.7 are found. For these estimations, a total of approximately 13000 life cycles is taken from the astrodynamic models. The final variable is the charge efficiency, which was defined in the trade-off as 98%. The number of batteries is given as result of table 10.7

Table 10.7: Number of batteries used for different battery DOD-EOL combinations

DOD (%)	**50**	**60**	**70**	**80**
EOL capacity (%)	82	77	72	62
EOL capacity one battery (Whr)	43.71	41.04	38.37	33.05
Number of batteries needed	3.25	3.65	2.98	3.02

The end result is that the ideal solution for the batteries is taking three batteries at DOD of 70%, which leaves some design margin. This margin allows for unexpected circumstances or possibly an accelerated wear-out failure of the batteries.

10.2.3 Power Management

With the two main components chosen for the EPS system, it is possible to decide the configuration of the complete electrical system. The design of the power management is summarised in figure 10.10.

Solar Panel Schematics The solar panels will consist of multiple solar cells on a 20x30 cm panel. The schematic of 3x3 solar cells is given in figure 10.8. This is an illustration of the solar panels. The actual panels will be multiples of 5 cells in series (either 2 or 3). The configuration of 5 cells in series results in a peak voltage of 12.5 V. Every solar cell will get a bypass diode and a blocking diode that is used to prevent the short circuiting of individual solar cells.

The solar panel generates more power at higher voltage at the beginning of life and when cold coming out of an eclipse. For the satellite power system, one voltage needs to be generated during the entire mission life-time, which should be lower than the maximum power producing voltage of the solar cells. A suitable switching regulator between the solar panel and the load, as shown in figure 10.8, remedies the disparity between the maximum power producing voltage and the constant load voltage. [80] The series regulator input voltage is then maintained at the maximum power producing

level with the peak power tracker, and the output voltage is stepped down to the constant load voltage by varying the duty ratio as required.

The excess power must be diverted (shunted) from feeding into the bus in order to control the bus voltage. There are two possibilities for shunts on a spacecraft. The shunt load can be a dump resistor, converting the solar panel power into heat. An alternative is to shunt (some of) the solar panel strings to the ground. This forces the string to operate under short circuit condition. In this mode, no power is delivered to the load or to the ground. The differences between the two methods is the location of the heat dissipation: in the spacecraft or on the solar panels. The choice was made to place a MOSFET transistor as a shunt, which will switch on when instructed when the peak power tracker measures that V_{min} and V_{max} of the solar panels is equal (i.e. no power is used to charge the batteries or when the battery is solely used).

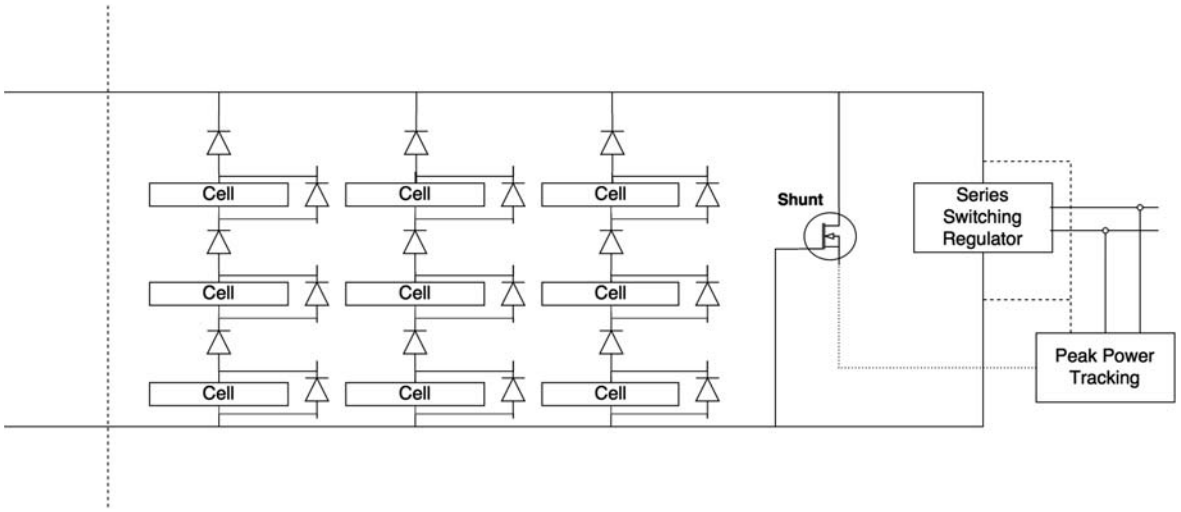

Figure 10.8: Schematic overview of one solar panel consisting of 9 solar cells

Battery Charging The charging of the batteries requires constant monitoring. The charging process changes the overall voltage, current and the charge over time. To accompany this constant changing requirement, a battery (dis-)charge regulator will be implemented in the EPS architecture.

The battery charge regulator will measure: Two cell temperatures per battery (lowest and highest), two cell pressure readings per battery, all cell voltages for comparative performance analysis and each battery voltage and charge/discharge current

Through a dedicated micro controller and the measurements above, the battery regulator will also determine the state of charge and discharge, rate of charge and discharge, depth of discharge and the number of charge and discharge cycles.

The battery is charged only if the battery voltage is lower than the bus voltage. A dc–dc voltage converter is required to buck (step down) the bus voltage to the battery voltage during charging. In the same way, a voltage converter is required to boost (step up) the battery when it is discharging.

Power Distribution and Conversion In the previous section, the need for battery charge converters was described. But during the subsystem design, more electrical components were chosen, with each component a different rated voltage and current. The result is that the EPS will include power conversion from the main satellite bus. The component used for the conversion is the dc-dc converter. A dc-dc converter can either buck or boost the voltage, as shown in figure 10.9. The switch in the schematics will alternate between open and closing in a so-called “duty cycle” and the resulting voltage fraction is shown in equation 10.7.

$$V_2 = V_1 \cdot M(D) \tag{10.7}$$

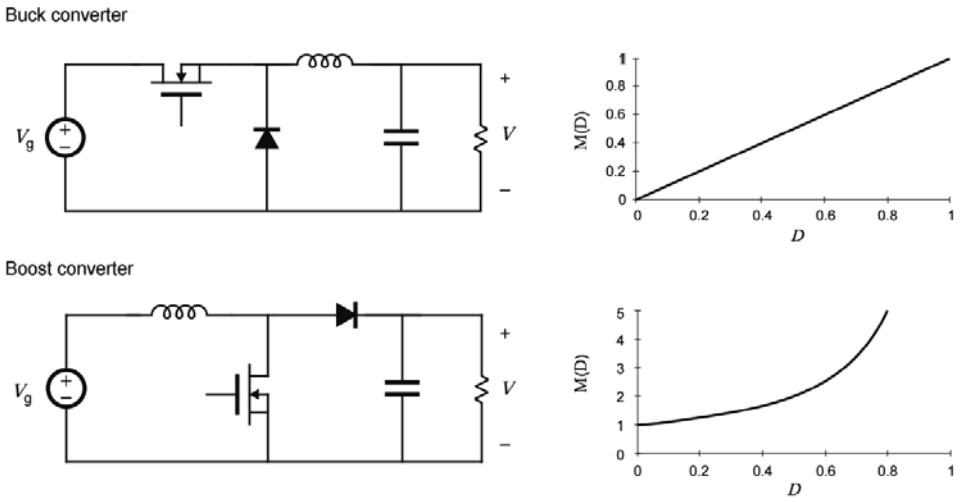

Figure 10.9: Schematics of two types of dc-dc converters

For the total power conversion, a total of eight converters are necessary. Table 10.8 shows the required current-voltage combinations.

Table 10.8: Required current-voltage combinations for the different electrical systems

System	Current (A)	Voltage (V)
PLS TID	0.68	5
PLS 2SID	<0.01	5
PROP	2.5	30
CHDS port 1	1.88	3.3
CDHS port 2	2.48	2.5
AOCS thruster	0.042	12
AOCS star tracker	0.39	5
AOCS sun sensor	<0.002	3.3-5

All EPS design choices can be summarised in an electric block diagram. The block diagram is given in figure 10.10.

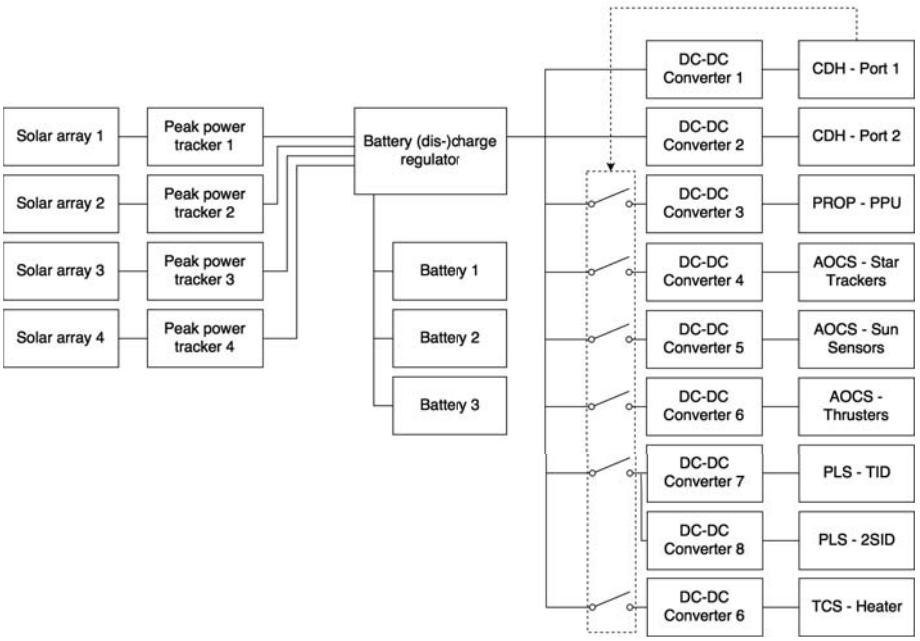

Figure 10.10: LUMID electrical block diagram

Other Factors in Power Management and Architecture The choice of the two main elements (panels and batteries) and the power management elements combine into an overall EPS design. However, there is one level of detail deeper than the current design steps. This level concerns with the designing of Printed Circuit Boards (PCB), electrical schematics for the entire satellite and the satellite wiring harness and protection. These design steps need to be considered in future design iterations.

The wiring harness includes the wiring, connectors and shielding. The harness design is influenced by the following factors: the rated current and the allowable voltage drop, the bundle size and steady state temperature, the rated voltage, temperature rise, derating requirement, specific power of the source and the reliability goal of the design. In this stage, the power conversion and distribution efficiency can be determined. [80]

The last consideration for future design is the protection of all electric components. Both in physical protection with insulation and casings for PCB's, and in protection for Electro-Magnetic Interference (EMI). There are two EMI sources: conducted and radiated. Active components, such as switches and diodes, are the main sources of conducted EMI. High-frequency conducted EMI arises due to parasitic ringing in voltage following a current switching, as seen in e.g. the dc-dc converters.

The power system harness is a major source of low frequency electro-magnetic radiated EMI. This is due to the fact that every wire has its own electric and magnetic field, thereby being a source of EMI.

The following steps can be taken to supress the impact of EMI [80]:

- Minimize the EMI generation by: minimising the current loop area in switching circuits and minimizing the switching transients' dI/dt rate in large current loops.
- Minimize the E-field and B-field couplings between the culprit and the victim equipments by: minimizing the inductive coupling by twisting wires or using coaxial cables, minimising the capacitive coupling by using shields and by reducing area of exposed metal and keeping it far from the ground.
- Divert the energy impinging on the victim equipment to ground by using a proper grounding scheme and a Faraday shield, single or double.
- Protect the equipment from the coupled energy by using L-C filters for conducted EMI and an enclosure shield for radiated EMI.

10.2.4 Mass and Power Budgets

The mass and power budget of the EPS can be seen in table 10.9.

Table 10.9: Mass and power budgets of the EPS

Component	Amount [-]	Total Mass [kg]	Total Power [W]
Battery	3	0.465	n/a
Solar cells	110	0.286	n/a
Solar panel structure	8	1.772	n/a
	Total:	**2.523**	

10.3 Verification & Validation

The calculations and simulations that are used need to be verified and validated.

10.3.1 Verification

First of all zero input test were performed to verify the MATLAB® model that is used for the solar panel sizing. The calculation of the available power that can be seen in figures 10.5 and 10.6 is actually already a zero input test for the incidence angle. It can be seen that the generated power is

always less than the available power as it should. Next the orbit time was set to zero which caused an average power of zero. The sun fraction, was set to zero which caused the power generation to be zero as this means that the entire orbit would be in an eclipse.

Unit test were performed for different orbit scenarios. For all eight scenarios plots were created like the figures 10.4 and 10.5. For instance for day 22, the power generation is equal to the available power when the β_i is 0 and α_i is 90 degrees as the incidence angle is 0 degrees. During the manoeuvre the generated power changes due to different incidence angles as the s/c is assumed to be pointing towards the centre of the Moon, it also touches the available power when the s/c is at the apoapsis. Furthermore, the generated power is zero during an eclipse and the used power is higher during an eclipse because of the TID that is turned.

Finally, constant values were used for the burn times and orbit parameters. This resulted in linear distributions which can be seen in figure 10.11. The average generated power decreases linearly with time as the remaining influence is the life degradation of the solar cells and the average used power is constant as expected.

10.3.2 Validation

The MATLAB® model is an approximation of reality. How close it matches to reality is mostly dependent on the assumptions and their effects which are given in subsection 10.2.1. Furthermore, it is dependent on the validation of the inputs of the model which are generated using GMAT. This validation can be found in subsection 3.3.5.

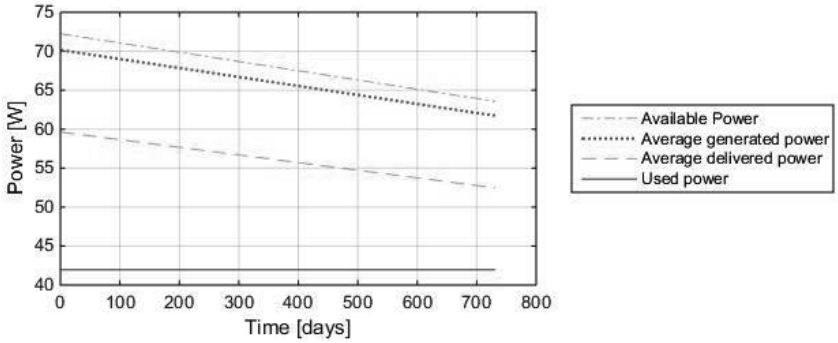

Figure 10.11: LUMID electrical block diagram

10.4 Sensitivity Analysis

The design of the EPS is influenced by many other subsystems. The main issue is that any deviation from the current design will result in a change somewhere in the EPS. The analysis will be split into three parts: change of power demand, change of burn time and change of orbit.

10.4.1 Change in Power Demand

The main driving parameter in the design is the total power consumption. The average power consumption is dependant on what subsystems require more power as some subsystem do not operate continuously and others require a different amount of power for various phases of the orbit. However, in general it can be said that the power generation changes linearly with the affective solar panel area, so changes in the power consumption would cause a linear change in the amount of solar cells. An increase in power demand can also increase the amount of the batteries needed to provide enough energy during the eclipse.

When the total power budget would be increased with 10 % the number of required solar cells becomes 123. This would increase the mass and area of the solar panels which increases the MOI

which influences the AOCS. Furthermore, the configuration should be changed because only a maximum of 120 solar cells fit on the s/c with the current configuration. For the power storage, increasing the load demand by 10 % will result in needing an extra battery, increasing the mass of the EPS by 0.155 kg.

10.4.2 Change in Burn Time

Another driver for the EPS are the burn times during which the thruster is active for the station keeping manoeuvres. This increases the average required power, because the thruster operates for a longer period, but it also decreases the average generated power during one orbit, because less time is left in which the s/c will direct all solar panels towards the Sun. However, the difference in inclination angles, when the apoapsis is in the Sun and the s/c is pointing towards the centre of the Moon in the manoeuvre phase, are low. Therefore there is just a small decrease in average power generation.

A change in burn time also effects the amount of batteries required as batteries are used as a buffer in some orbits during the manoeuvre phases.

When the burn times are increased by 10 % the number of required solar cells becomes 123 too, this shows that indeed the main influence is the used energy during one orbit.

10.4.3 Change in Maximum Slew Rate

A 10 % change in the maximum slew rate or turn time has only a small influence on the EPS. This is, because the s/c is able to turn quickly compared to the total orbit period. The temporarily decrease in generated power during this attitude change due to larger incidence angles barely influences the average generated power. Therefore the number of required solar cells stays the same.

CHAPTER 11

Structures and Mechanisms System

In this chapter the structures and mechanisms of the CubeSats® is explained. Starting with the subsystem description stating all the requirements and functions, then extended elaborated on the design and closing the chapter with the verification methods and sensitivity analysis.

11.1 Subsystem Description

The requirements of the structures and mechanisms of the CubeSats® are listed in table 11.1.

Table 11.1: STR requirements

Identifier	Requirement	Section	Compliance
R-SC-STR-1	The s/c shall withstand all mechanical loads during launch.	11.2.1	✓
R-SC-STR-2	The s/c shall withstand all mechanical loads during separation from mothership and deployment.	11.2.1	✓
R-SC-STR-3	The design of structural assemblies shall be compatible with internal and external interfaces.	11.2.2	✓
R-SC-STR-4	Inertia properties shall be compliant with the requirements stemming from the mission design <tbd>.	11.2.2	✓
R-SC-STR-5	The s/c bus structure shall accommodate for the scientific payload, as defined by the mission requirements.	11.2.2	✓
R-SC-STR-6	The s/c bus structure shall allow the removal and replacement of any hardware subsystem at any stage during production.		✓
R-SC-STR-7	The s/c bus structure shall protect the internal subsystems from solar radiation.	11.2.5	✓
R-SC-STR-8	The s/c bus structure shall contain the spread of shrapnel within a <tbd> area in case of an end-of-mission impact on the lunar surface.		
R-SC-STR-9	The s/c bus structure shall not involve any flammable, toxic or unstable materials.		
R-SC-STR-12	The STR subsystem shall keep the Total Ionizing Dose of the s/c during the entire lifetime below 10 Gy.	11.2.5	✓
R-SC-STR-13	The s/c bus structure shall have no modal frequency below 25 Hz.	11.2.1	✓

The structures and mechanisms subsystem comprises several functions:

- **Structural Integrity**
  The structure ensures the spacecraft can survive all load cases which occur during its lifetime. These loads can be static, dynamic or vibrational.
- **Envelope**
  The structure provides a fitting envelope for all other subsystems to be installed in.
- **Satellite Deployment**
  The structures subsystem includes a deployment mechanism for separation from the lunar orbiter. This system will safely store the spacecraft during the launch and transfer to lunar orbit and will separate the spacecraft from the lunar orbiter upon arrival in the preferred lunar orbit.
- **Mechanisms**
  The mechanisms subsystem includes all deployment mechanisms necessary for the correct functioning of the other subsystems, such as the deployment mechanism for the solar panels. The functional flow diagram of the mechanisms is given in figure 11.1.

- **Radiation Protection**
  The structure will adequately protect all subsystems from the harsh radiation environment in lunar orbit.

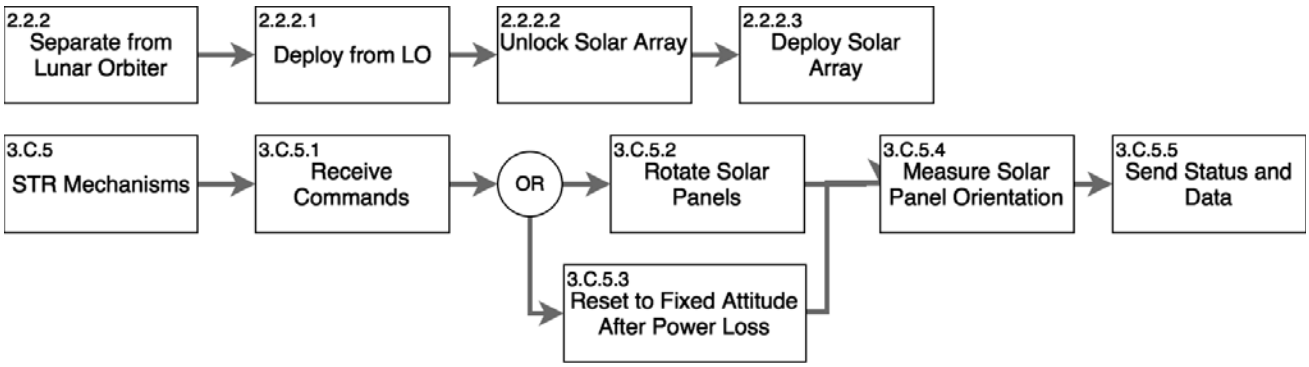

Figure 11.1: Flow diagram for the mechanisms

To ensure that the subsystem properly fulfills all of the aforementioned functions, first the choice has to be made between designing a structure or using a commercial CubeSat®™ structure. Commercial structures have several advantages over designing a structure. They have been adequately tested for common load cases and radiation and they come in standardized dimensions, which means they are easy to integrate with the commercial deployment systems and provide easy access to all components during assembly. These advantages make it preferable to use a commercial structure.
For the analysis of the aforementioned functions, a specific structure has to be decided upon. Several companies offer CubeSat®™ structures, but the choice goes out to ISIS® [108] as they have the most experience and the most flight-proven designs. The satellite will be deployed using a QuadPack® [109].

11.2 Design

In this section the design choices for the structures and mechanism will be explained.

11.2.1 Structural Integrity

To ensure that the spacecraft will survive the loads that occur during its lifetime, it was analyzed using Finite Element Analysis (FEA). The software tool chosen to perform this analysis was Ansys, as it is reliable, easy to use and has been extensively verified and validated. To begin with the analysis, a CAD model of the structure was needed. Since the ISIS® 12U structure [108] is still in the last phases of testing, no CAD files were available. Since the 6U structure did have CAD files, the decision was made to design the structure as two 6U structures attached to eachother. The structure was then simplified to reduce the computational workload of the analysis. This meant that all small holes were filled and small edge fillets were removed. An image of the structure used for analysis and the real structure can be seen in figure 11.2. The material for this structure was set to Aluminium 7075-T6 with a density of 2770 kg/m^3, a Young's Modulus of 72 GPa, a yield strength of 280 MPa, a thermal conductivity of 130 W/m $\cdot$ K, and a thermal expansion of 23 µm/m $\cdot$ K.

In order to analyse this structure, the loads first have to be determined. The assumption is made that the most significant loads occur during the launch phase and the separation from the lunar orbiter and the launch vehicle. These loads can be split into 4 main groups: quasi-static loads, acoustic loads, random vibrations, shock loads.

To determine these loads, a reference launcher was picked. The Proton-M launcher was chosen as this rocket has already been used by ESA and has Lunar Transfer Orbit capability. A summary of the Loads can be found in table 11.2. The next step in the analysis is then to apply the loads to the structure and to define the boundary conditions. The accelerations act on the entire body and the acoustic pressure is assumed to act on the outer surfaces of the structure only. The boundary

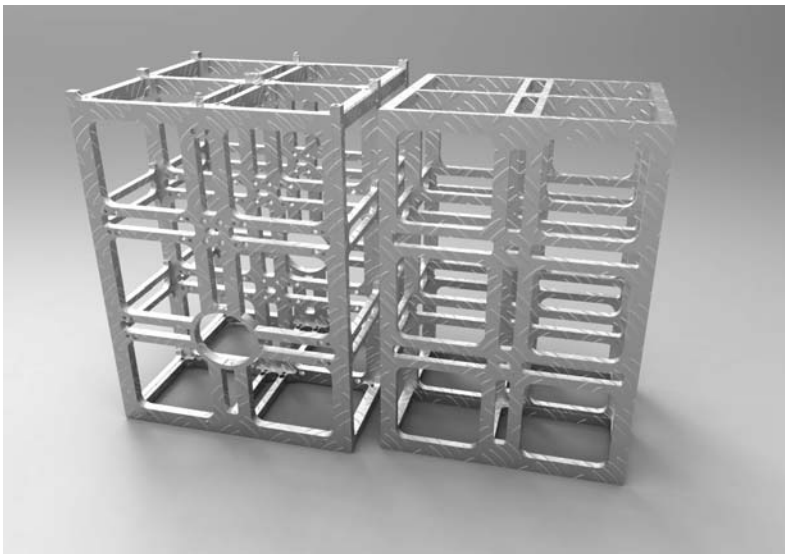

Figure 11.2: *Left:* Real satellite structure *Right:* Simplified satellite structure used for analysis

conditions are defined as follows: a fixed support is added to the bottom side of the structure and the top side is constrained in all directions except the z-direction. This means the structure is fixed in the transverse directions and free to move in the longitudinal direction. These conditions are derived from the way the satellite is stored in the deployment system.

Table 11.2: Load summary of launch with proton M

	Max. long. acc. [g]	**Max. transv. acc. [g]**	**Event**
Static Loads	3.6		Q_{max} before 1st stage booster separation
		1.1	Lift-off
	Max pressure [kPa]		**Event**
Acoustic Loads	83.0		Lift-off and Q_{max} before 1st stage booster separation

Table 11.3: Summary of the shock loads during separation. The shock loads vary linearly between these values.

Frequency [Hz]	**Shock Level [g]**
100	20
1000	2000
10000	2000

The vibrations during launch can be seen in figure 11.3.

The shock loads that occur during separation between launcher and lunar orbiter are shown in table 11.3.

The final step that needs to be taken before starting the analysis is the creation of the mesh. The mesh is an unstructured mesh and consists of tetrahedrons. The size function is set to 'adaptive', which means that the mesh is more refined around typically critical areas such as cut-outs or corners and coarser in the other areas. This allows for a more accurate analysis of the parts that are most likely to fail. A minimum edge length was chosen to be 2×10^{-4} m. This was done to keep the number of elements under 32 000 as this is the maximum problem size for the student's version of the software. A more detailed finite element analysis is recommended for further design phases.
The assumption is made that fatigue analysis is not necessary, since all relevant loads occur during the launch phase and will therefore have a very limited number of cycles. The loads occurring during

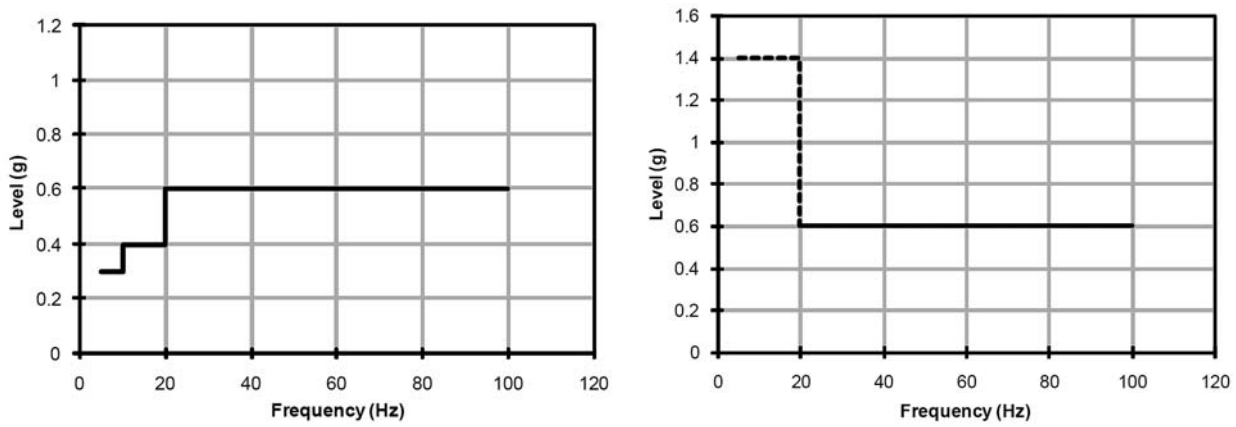

Figure 11.3: Lateral and longitudinal vibration levels during launch

the operational lifetime are too low to be considered.

FEA Results: The analysis was then performed on the structure under the aforementioned loads and vibrations. The structure never failed, which was to be expected as the 6U structure our structure was based on, was qualified to withstand higher launch loads. The resistance to loads was thus foreseen. A point of uncertainty that remained was the resistance of the structure to random vibrations. The fact that the structure was adapted from a 6U to a 12U structure could make for radically different behaviour when exposed to vibrations. The analysis however showed that the new structure would still withstand all vibrations occurring during transport and launch. The results of the FEA can be seen in figure 11.4 Finally, the structure was analysed to find the modal frequencies. These are listed in table 11.4 and are all well above the minimum of 25 Hz for the Proton-M launcher [110].

Mode	Frequency [Hz]
1	400.94
2	526.72
3	570.07
4	603.17
5	881.9
6	905.81

Table 11.4: Modal frequencies of the structure

11.2.2 Envelope

Another function of the satellite structure is to provide a fitting envelope for all other subsystems to be installed in. This process was done using CAD models of components to be able to clearly visualize the relative positions. The use of a CAD model also allowed to keep track of c.o.m. position and mass moments of inertia. Both of which are of large importance to other subsystems. The outer envelope of the structure is 226.3 mm x 226.3 mm x 340.5 mm, the inside 0.5 U envelope is 98.4 mm x 98 4 mm x 49.2 mm. The primary structure mass is 1500 g. When the secondary structure mass is added to that the total mass is 2000 g.

Table 11.5: Mass moments of inertia

Axis	Velocity	Normal	Body
Mass Moment Of Inertia [kgm^2]	1.208	1.213	2.015

The difference in location between the centre of mass and the thrust axis has been calculated using the CAD model and was found to be 0.1 mm after the placement of some components was changed

in order to symmetrise the satellite as much as possible. This means that, in combination with the low thrust, the moment will be small enough to be compensated for by the AOCS. Furthermore, it is assumed that during later design phases, the distance will even be lowered more, when cabling etc. can be decided upon. In table 11.5, the mass moments of inertia of the system are listed.

11.2.3 Satellite Deployment

The satellite also needs to be separated from the lunar orbiter upon delivery to the initial lunar orbit. This will be done using the ISIS® 12U Quadpack® Type 1-XL [109] since this is tailored to the size of the satellite structure. The Quadpack® provides another 10 mm of room on the sides of the structure, 25.4 mm on the top and room for five 30 mm long 'Tuna Cans' on the bottom. This deployment system produces very low intensity shocks of only 200g above 1000Hz.

11.2.4 Mechanisms

The structures and mechanisms subsystem also provides the appropriate mechanisms for the satellite subsystems. For this satellite only two mechanisms are used, the solar array deployment and solar array drive mechanism. These mechanisms deploy the folded solar panels after separation from the lunar orbiter and turn the solar array to point towards the sun. The mechanisms are based upon two articles concerning a deployable and rotating solar panel system for CubeSats® by Fabio Santoni et al. [102, 103]
The solar array deployment mechanism consists of two different spring loaded hinges, the first of which is connected to the solar array drive mechanism and connects the solar array to the satellite. The second hinge is used for the connection between two solar panels. The solar panels are stowed on the side of the satellite and each side has three panels, of which one is a 2SID.

The solar array drive mechanism consists of stepper motors and drive cylinders which are attached to the solar array deployment mechanism. These stepper motors rotate in fixed increments of 1 degree and have a fixed datum orientation to restore to in order of power loss and thus orientation knowledge loss. Furthermore, the stepper motors have proven to be reliable components and to reduce the impact of failure of a stepper motor, every solar array has its own motor, so that a failure will not affect the performance of the other solar arrays. An image of the solar array drive can be found in figure 11.5.

11.2.5 Radiation Protection

To protect the spacecraft against the harsh radiation environment in the earth-moon transfer orbit and in the lunar orbit, the structures subsystem shall include radiation shielding. From radiation measurements on board the Chandrayaan mission [111], an average ionising dose of 10 µGy/hr or a total ionising dose over the mission lifetime of 0.1752 Gy is found. This is not significantly higher than in earth orbit and therefore the decision was made to use standard aluminium radiation shields of 0.5 g/cm^2. Assuming a density of 2700 kg/m^2 this amounts to plates with a thickness of 1.78 mm which are mounted on the outside of the structure. The total ionising dose absorbed during the earth-moon transfer orbit will be roughly 1 Gy [111], most of which will be absorbed while passing through the Van Allen Belts. The proposed radiation shields should suffice for this dose as well.

When designing radiation protection measures, one should not only look at the total ionising dose but also at Single Event Effects (SEE). SEE's are high energy particles which can cause significant damage to particularly electronics. Structural protection is very ineffective for these kinds of radiation, but nonetheless extra radiation protection will be placed around the most sensitive electronic components, i.e. the OBC, the SD cards and the camera. Apart from this, the electronics will be designed to be radiation-tolerant rather than radiation hardened. This approach does not stop the particles from damaging components but will make the components resistant to the faults that occur due to the SEE's.

11.2.6 Mass and Power Budgets

The mass and power budgets of the structures and mechanisms of the CubeSats is presented in table 11.6.

Table 11.6: Mass & power budget of the structures and mechanisms subsystem.

Component	**Amount**	**Total Mass [kg]**	**Total Power [W]**
Structure	1	2	0
Radiation Shielding	1	2	0
Deployment Mechanism	1	1.5	0
	Total:	**5.5**	**0**

11.3 Verification

The FEA code does not need to be verified, since Ansys is extensively verified in the Ansys Workbench Verification manual [112]. The validation of the model can be done using testing for static loads and random vibrations. All structures delivered by ISIS® have been qualification tested for vibrations, mechanical shocks, thermal cycling and thermal vacuum. Only acceptance testing is still needed on the structure. This means that vibration and load tests will be performed on the structure after it is acquired from the company.

11.4 Sensitivity Analysis

The sensitivity of the structures and mechanisms subsystem is analysed in this section. When the loads on the structure are varied, the stresses will increase or decrease accordingly. However, since the structure cannot be changed because it is a commercial component, the structure can not be adapted to these new loads. The maximum stress that occurs was less than 75 % of the yield stress, this means that the structure will not fail unless the loads increase by a large amount. When the loads are lowered, no problems will occur but the structure will be overdesigned and the choice between a commercial and a structure of own design will have to be reconsidered.

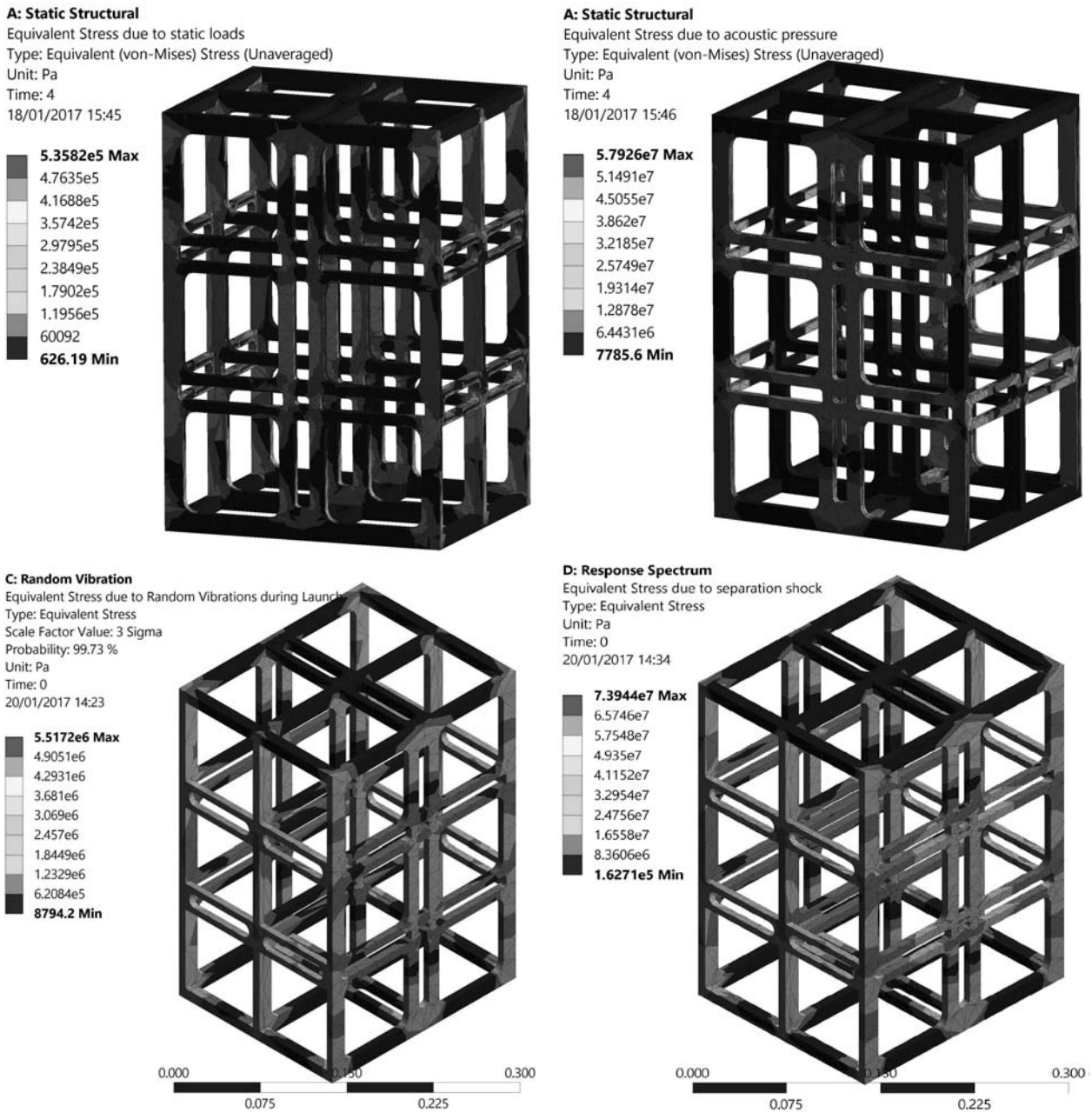

Figure 11.4: **FEA results:** *top left:* Equivalent stress due to static loads. *top right:* Equivalent stress due to acoustic pressure. *bottom left:* Equivalent stress due to launch vibrations. *bottom right:* Equivalent stress due to separation shocks.

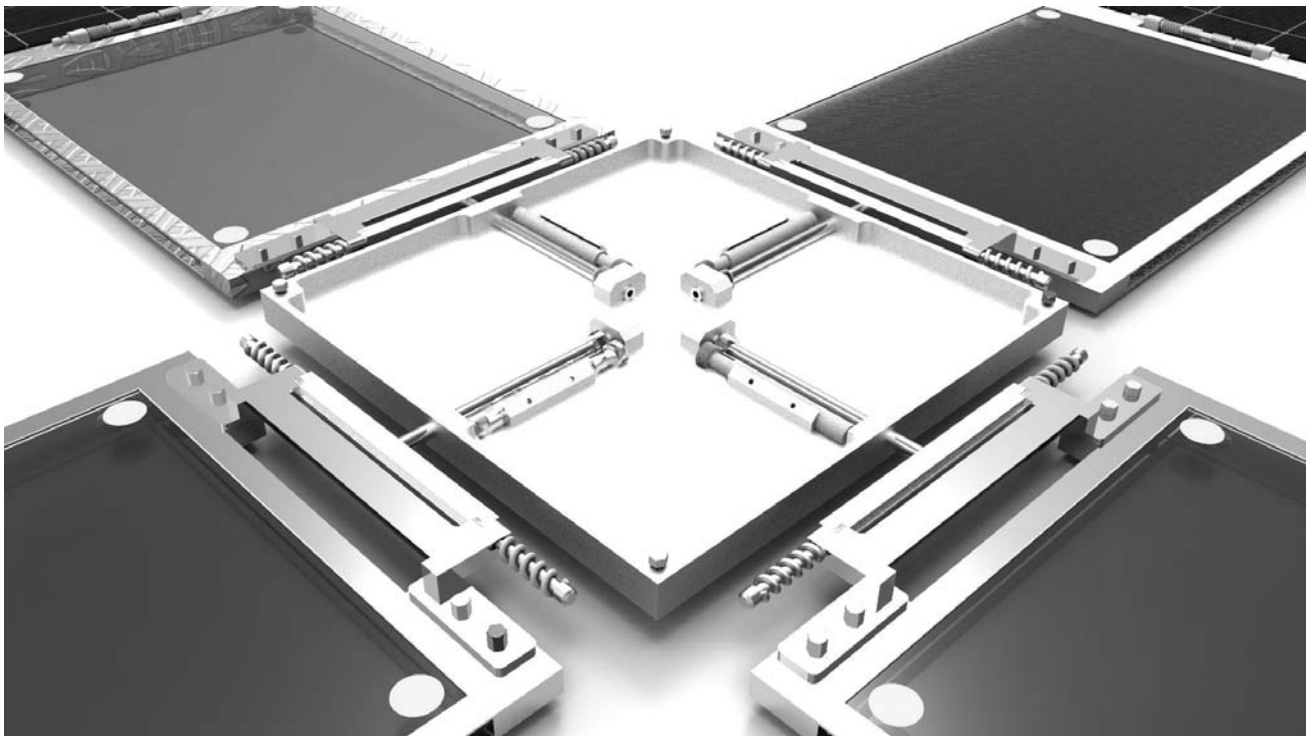

Figure 11.5: Solar array drive assembly

CHAPTER 12

Thermal Control System

This chapter discusses the design of the thermal control system (TCS) for the LUMID mission. The description of the TCS together with its requirements can be found in section 12.1, while the design and the verification are treated in sections 12.2 and 12.3 respectively.

12.1 Subsystem Description

Table 12.1 briefly lists the thermal control system's requirements.

Table 12.1: TCS requirements

Identifier	Requirement	Section	Compliance
R-SC-TC-1	The TC subsystem shall support the scientific payload's full operation for a temperature range of 0 °C to 40 °C.	12.2	✓
R-SC-TC-2	The TC subsystem shall maintain all subsystems within their pre-defined operating temperatures when the subsystem is operational.	12.2.3	✓
R-SC-TC-3	The TC subsystem shall maintain all subsystems whitin their pre-defines survival temperatures, when the subsystems are inoperative.	12.2.3	✓
R-SC-TC-4	The s/c shall survive the temperature range of −40 °C to 65 °C.	12.2.1	

The thermal control subsystem provides the ideal operational temperature for every component to operate in. There are different methods to control the temperature of the s/c, which can be passive or active. [113]

Passive methods are mostly preferred as they do not require power nor commands in order to function. *Heat insulation* is used to keep instruments warm and can be used to limit heat from propagating to heat-sensitive parts. Another well known passive method is changing the s/c's *coating* and its *surface materials* to have different values of absorptivity α and reflectivity ϵ.

Active methods include *heaters* to heat up the system in case of low temperatures. Those are mostly composed of an inefficient resistance which converts electricity to thermal radiation, and they are called electrical resistance heaters. They can be manufactured in a lot of different shapes and are thus flexible in use. The last discussed method are *heat pipes*. This are hollow pipes filled with a fluid which vapourises as it is exposed to a heat source and flows through the pipe where it radiates the heat into space at the cold end. Figure 12.1 shows this process.

12.2 Design

This section focuses on the design of the thermal control system (TCS), the results of which are discussed in section 12.2.3. The analysis of the temperature ranges of all the s/c components during the s/c's lifetime can be found in section 12.2.1.

12.2.1 Design Temperature Range

The LUMID spacecraft are composed out of multiple subsystems, everyone of which has its own temperature range for correct operation. Figure 12.2 shows the operational temperatures for each component of the s/c as well as the survival temperatures which they can withstand. For the payload

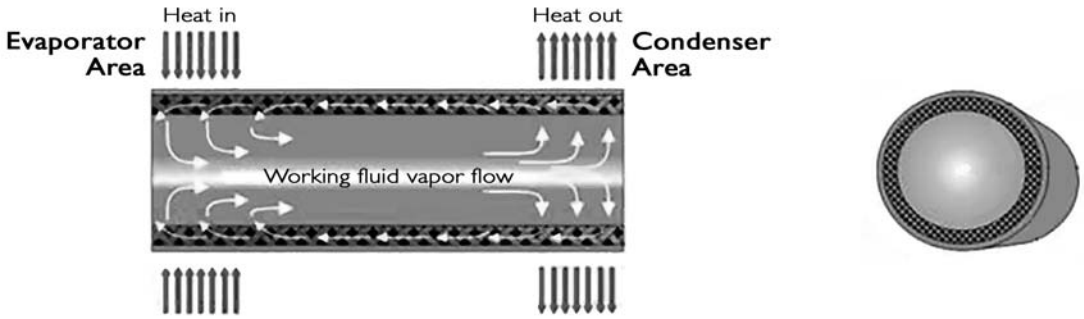

Figure 12.1: Cross section of a closed system heat pipe. The fluid vaporises and flows the heat from the evaporator to the condenser. (figure adapted from reference [114])

system (PLS) and the main thrusters these were known and shown with the dashed lines. The ones which were not specifically stated were assumed by using references [61, 115–117]. This was done by looking at the deviation from the operational temperature in the reference, and applying the same deviation to the known operational temperatures.

The black dashed line indicates the temperature for which the entire subsystem can survive. This temperature is −30 °C, which is 243 K. This means the TCS can not comply yet to requirement **R-SC-TC-4** without the need of heaters for every component of the AOCS. This can be done at a later stage of the design by splitting up the thermal radiation of the main heater into smaller heaters placed near the AOCS components.

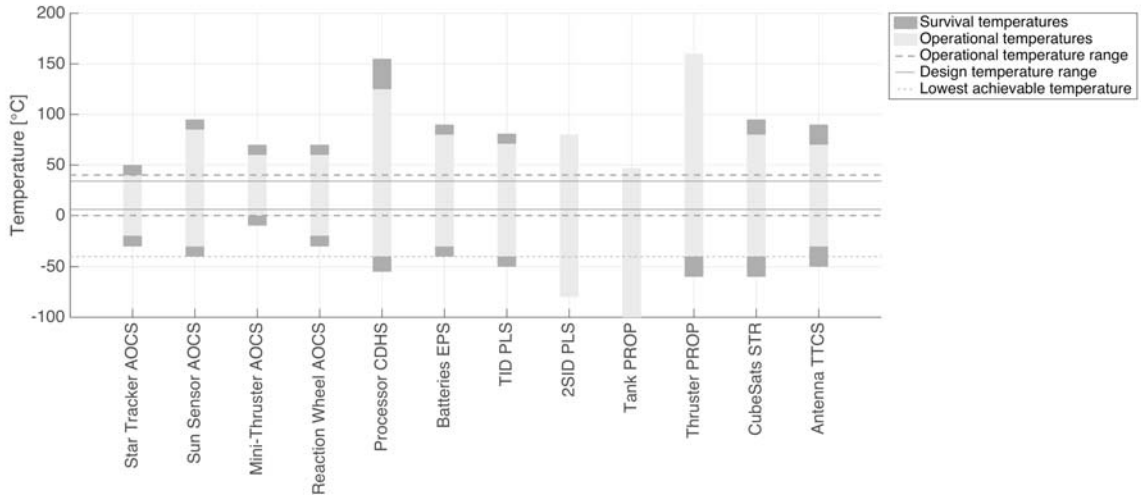

Figure 12.2: Temperature ranges of every component of the subsystems.

Design temperature range. As can be seen in figure 12.2 the operational temperature range of the entire system is 0 °C to 40 °C, which corresponds to 273 K to 313 K. To ensure the operational temperature is maintained at all times a margin of 15 % is used to calculate the design temperature range. This gives a temperature range of 6 °C to 34 °C or 279 K to 307 K, which are the temperatures used to design the TCS.

12.2.2 Lifetime Temperature Range

Heat in the system is provided by means of direct solar radiation, the albedo radiation and the Moon's thermal radiation in the infrared spectrum (see figure 12.3), as well as the internal heat produced by the s/c's subsystems. During periods of eclipse only the infrared's lunar radiation impacts the

s/c, while during the rest of the orbit the direct solar radiation and the reflecting radiation (albedo) are of main importance to the system's temperatures. The absorbing area of these radiations is estimated to be approximately the same as the solar panels' effective area together with the top part of the spacecraft. The heat then spreads through the spacecraft by conduction among the aluminum components.

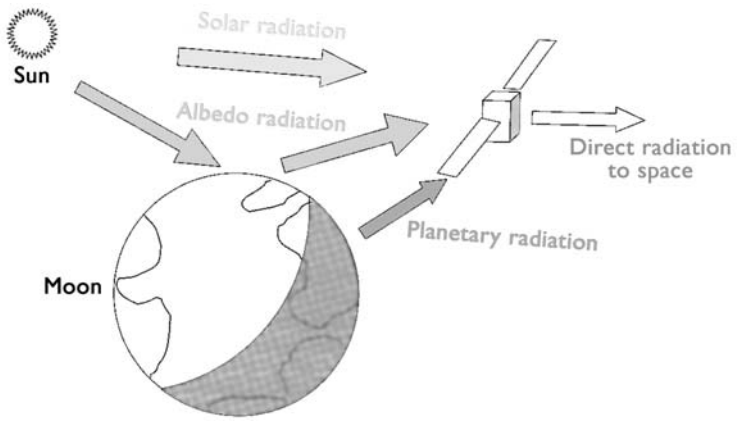

Figure 12.3: Radiations in a moon orbit (figure adapted from reference [118]).

When designing the mission those radiations were the inputs to the TCS model. Figure 12.4 shows the schematics of said model, which logic is used for all of the outputs in this chapter.

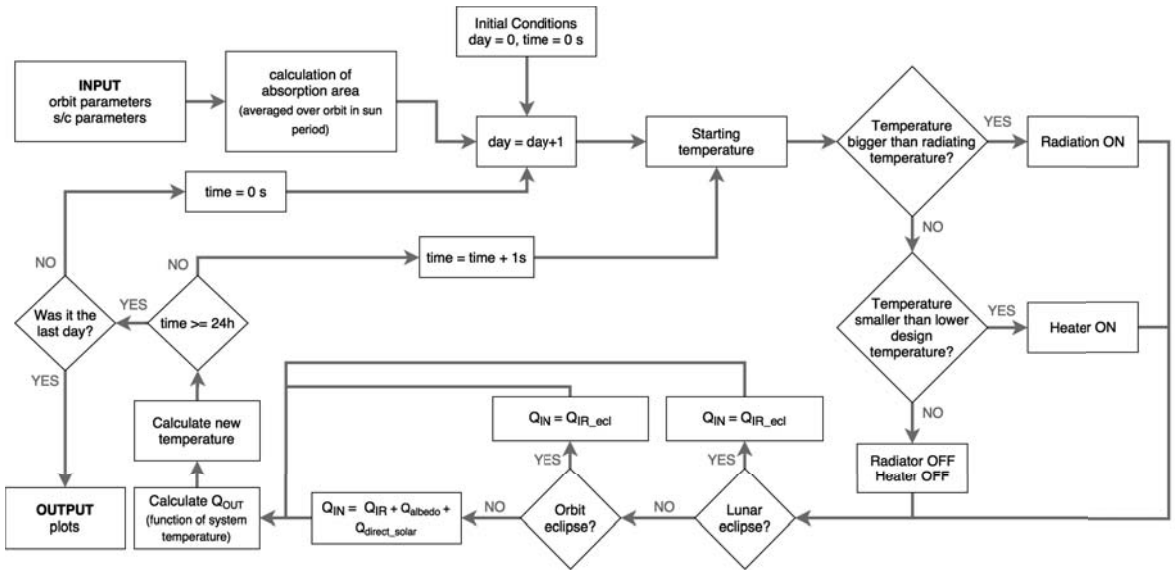

Figure 12.4: Schematic model representing the flow logic of the MATLAB script for the TCS.

Figure 12.5 shows the minimum and maximum temperature for every day during the s/c's lifetime of two years by accounting for the absorbed radiations and the internal heat production. The outgoing radiation is then calculated by using an emitting area equal to the system's total area. Day 1 is excluded from this figure as it is furtherly analysed in section 12.2.4 together with the lunar eclipses.

The oscillation in temperature with a period of ≈100 days is due to the beta angle, which is the angle between the orbital plane and the sun vector. The beta angle causes the time in eclipse of the satellite in each orbit to change, which causes the temperature to fluctuate. The system reaches lower temperatures when the eclipse times are greater, because it then spends more time in an area of the orbit where the emitted radiation is higher then the absorbed and the internal radiation together.

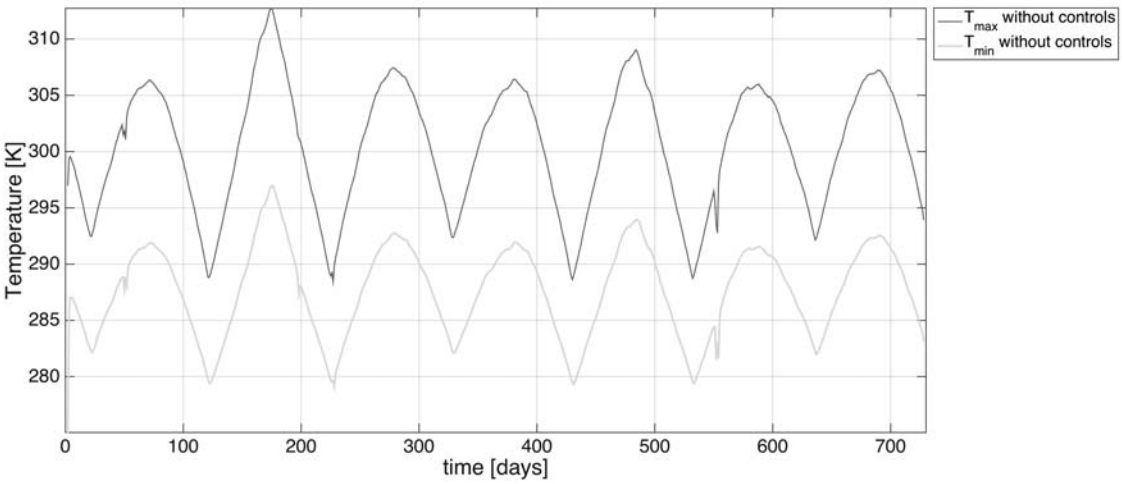

Figure 12.5: Maximum and minimum temperature for every day during the s/c's lifetime of two years.

12.2.3 Thermal Control Solutions

The TCS was sized according to its requirements as stated in section 12.1.

Assumptions

In order to start designing the system first some assumptions were made.

The internal energy dissipated by the subsystems as internal thermal radiation loss was assumed 15 W at all times. This value is used by analysing the energy requirements of the subsystems and accounting for an average loss during each orbit.

The temperature inside of the spacecraft is assumed to be constant across all subsystems, such that heat-sensitive components have no possibility to overheat. This assumption can later be discarded by placing the components across the system according to their temperature requirements. When the satellite goes in lunar eclipse a total eclipse time of 4 h is assumed. This accounts for the worst situation possible, as eclipses normally have shorter durations of approximately 2 h to 3.5 h and penumbral and partial eclipses are not as extreme.

TCS Components

The s/c has a design temperature range of 279 K to 307 K (see section 12.2.1). In order to comply to this requirement the design starts with the choice of a **coating**. This choice is affected by the ability of the coating to absorb and emitt radiation, due to its values of absorbivity α and emissivity ϵ respectively, in order to have the lowest reached temperature inside of the design temperature range. This decision is taken because of the need to switch on the heater in the case of temperatures lower than 279 K, which will consume a great amount of power and results in a heavier electrical power system. A 1 mm coating of Kapton Film with silver-Aluminum Oxide overcoating [119] was chosen for this mission, which has α of 0.08 and ϵ of 0.21.

To withstand the higher peaks in temperature a **radiating device** is chosen to be manufactured with a radiating area of 7.5×7.5 cm. This radiator has a coating (Teflon Aluminum backing) with high emissivity ($\epsilon = 0.87$, $\alpha = 0.13$) and it is placed on the outer side of the s/c. The radiator is connected to a set of heat pipes which act as conduction couplings, and take the heat out of the system towards the radiator. The active fluid inside of the heat pipes is chosen to be Acetone, which vapourises at temperatures of about 293 K. This means the radiator will only radiate heat to outer space when this temperature is reached and the acetone starts travelling inside of the heat pipes. This will slowly decrease the temperature to a maximum of 306.8 K. For the mass estimation the radiator is chosen to be stainless steel with a density of 7861.1 kg/m^3, because of its high conductivity values.

This is enough to have the spacecraft to stay in the design temperature range. There is however one major problem that needs to be accounted for, which is the temperature on day 1 and the lunar eclipse on May 26th, 2021 [120]. Those days the system reaches temperatures under 279 K, and need to be heated up. Heating happens by means of a 20 W **electrical resistance heater**. A commercially available option for this heater is not available at the moment, so a custom made design will need to be manufactured. The mass of this system is estimated to be 100 g as it just consists of light electrical components. To account for the single point of failure of the TCS, redundancy is reached by placing two heaters of the same wattage. These are never turned on together as the EPS does not allow for that. Therefore the power indicated in the subsystem's budget is 20 W and the mass doubles to 200 g. Together with the main system heater an extra 5 W heater needs to be placed.

The entire system can only function if the temperatures across the system are continuously measured by means of **temperature sensors**, placed across the system. The MEAS Space Qualified (Hi-Reliance) temperature sensors are chosen because of their reliance, light weight and ESA qualification. [121] The amount and the exact positioning of the sensors needs to be determined in the detailed design phase by taking into account redundancy and relevance of the measurement points.

12.2.4 Controlled System

Now that the TCS is formed, its functions are schematically shown in the subsystem's functional flow diagram displayed in figure 12.6. When the TCS is powered on, it first measures the temperature of the s/c and sends this measurement to the CDHS which tells the system to power on the heater if the temperature is lower than 279. Day 1 will need both heaters to function at the same time in order to bring the s/c's temperature to its desired value as fast as possible. A more detailed look at day 1 can be nd later in this section.

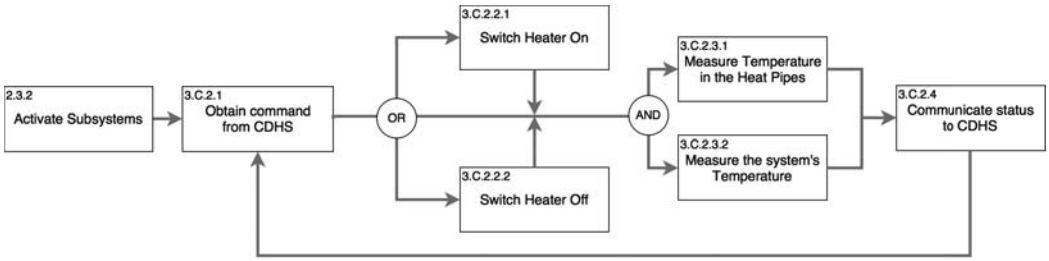

Figure 12.6: Functional flow of the TCS. The system receives commands from the CDHS to switch the heater ON/OFF or just keep it as is, after which it communicates the system's temperatures back.

Thermal Solution

Figure 12.7 shows how the combination of coating and radiator affect the temperature of the system. The dashed lines show the effective temperatures with only the coating applied, while the continuous ones show the iteration of the system's temperatures with the radiator radiating from a temperature of 293 onwards and the heater heating when the temperature drops more than 279 K. The result is the system staying right in the design temperature of 279 K to 307 K.

Day One

Day one is one of the most extreme days of the mission, where the temperature has to go from the starting temperature inside of 200 K inside of the Lunar Orbiter to the equilibrium temperature of ≈284 K. This takes the system up to 14 h after deployment. This means the spacecraft experiences temperatures lower than the lowest achievable temperature of 243 K during the first 6 h after deployment. This can not be issued two methods. One is to power a heating device from the Lunar Orbiter itself, or by having the payload storing temperature at 243 K or higher. The first 24 h iteration can be seen in detail in figure 12.8.

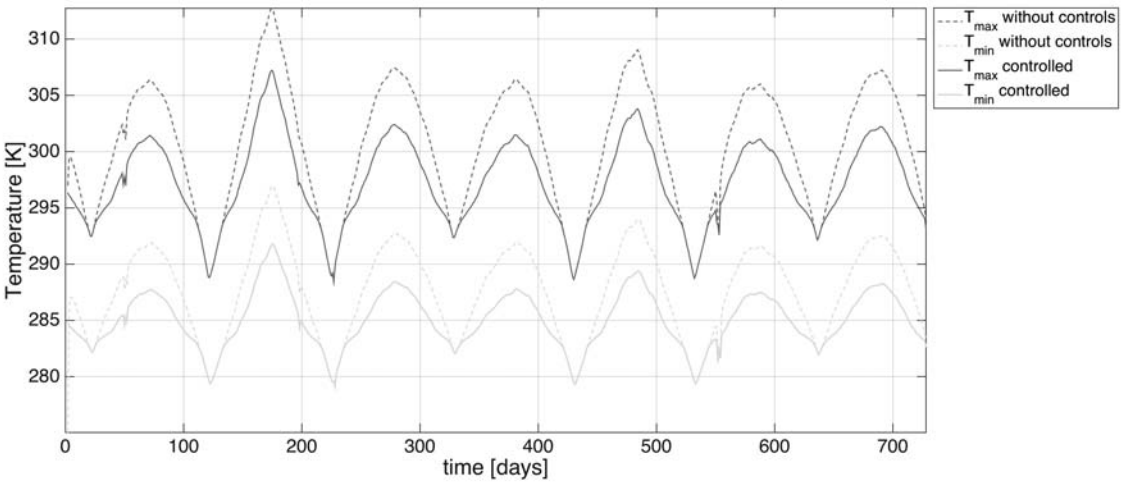

Figure 12.7: Mission lifetime thermal control iteration.

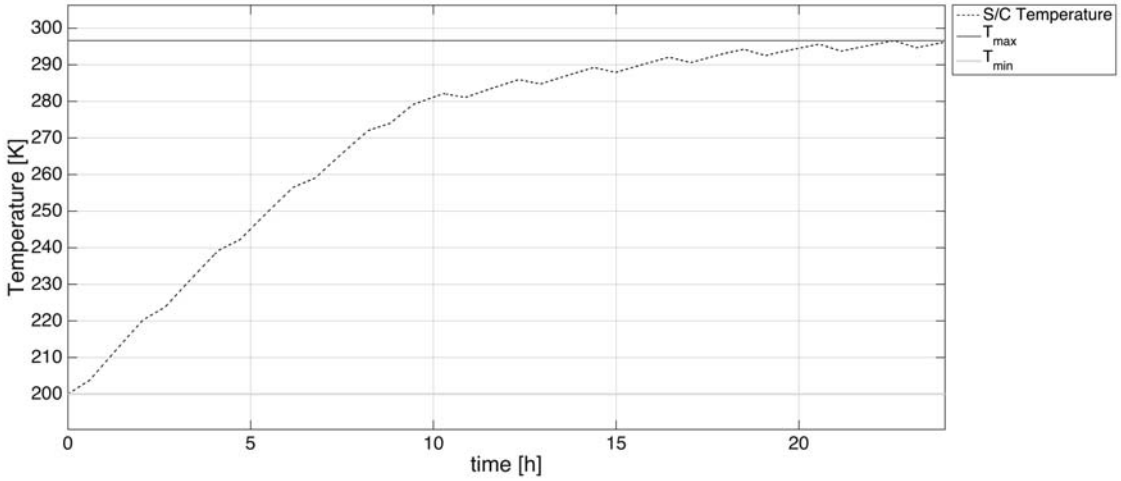

Figure 12.8: Convergence of the temperature on day 1. The temperature stabilises to 279 K in 9.5 hours, during which a 20 W heater is operating.

Lunar Eclipse

During the course of the LUMID mission planet Earth lies in-between the sun and the moon. This occurrence is called a lunar eclipse and is relevant for our mission as during this eclipse no sun radiation hits the s/c, influencing both the power generation as well as the thermal control. To make sure this parameter is fully taken into account, the eclipse calculation is taken apart and shown in figure 12.9 for the negative peak on day 552. Here it can be seen how the temperature drops 8 K during the full length of the eclipse.

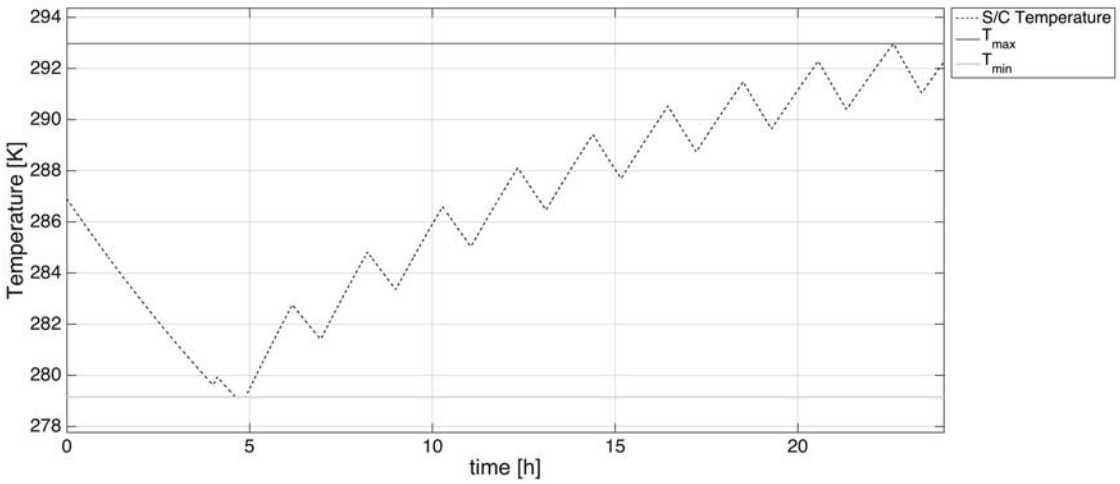

Figure 12.9: S/C temperature change for a total eclipse of 4 hours.

12.2.5 Mass and Power Budgets

The mass and power budgets for the TCS are shown in figure 12.2.

Table 12.2: Mass and power budgets for the thermal control subsystem.

Component	**Amount**	**Total Mass [kg]**	**Total Power [W]**
s/c heater	2	0.20	20
Mini-thruster heater	1	0.05	5
Coating & Heat pipes	x	1.00	0
Temperature sensors	3	0.03	0
Radiator	1	0.45	0
	Total:	**1.73**	**25**

12.3 Verification and Sensitivity Analysis

The main part on which verification and sensitivity analysis are performed is the temperature model that simulates the satellite's overall temperature during the LUMID's mission lifetime. This will be done by looking at the expected output on a given input. This also shows how sensitive the model is on a change of inputs.

12.3.1 Year Iteration Verification

To start off with the main model, the verification started with simplifying the model by keeping the beta angle constant over time. The end result is that the eclipse times do not change and the model outputs a straight line at the balance temperature. This is what is expected from the system.

To verify the capability of the heater to keep the temperature in-between the limits the heater and the radiator were switched off and the internal radiation was put to 0. The result is that the 20W heater jumps in to keep the temperature constant on the lower limit of the system. However, the big heater will not provide enough thermal radiation to have this temperature above the 279 K limit, and needs to be assisted by the smaller 5 W one. Figure 12.10 shows the response of the 20W heater to zero internal heat loss. A sensitivity analysis on the internal heat loss shows the system can take internal heat losses in the range of 0 W to 20 W.

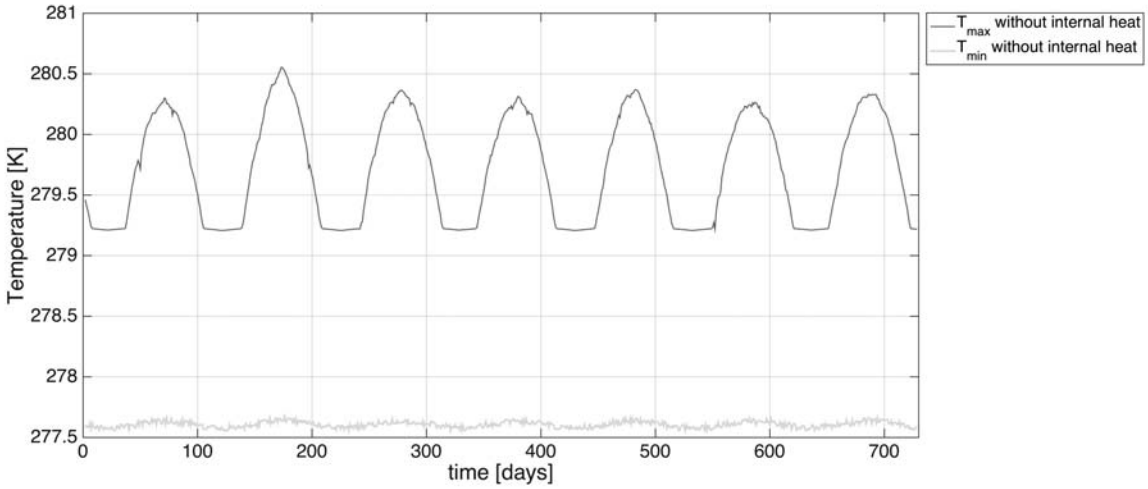

Figure 12.10: Response of the system's temperature to zero internal radiation.

12.3.2 Zero-input Test

An important step to verify the calculations for the total model was to simulate a "zero-input" environment. In this test, the spacecraft received no heat input at all and the corresponding output was expected to be a smooth decrease in temperature until reaching the space environment temperature. The actual model behaviour however is shown in figure 12.11, and here it can be seen that the model starts with a steep decay in temperature and slowly converges to the temperature of 29 K during a two year period. This is because of the outgoing radiation characterised by the system's temperature.

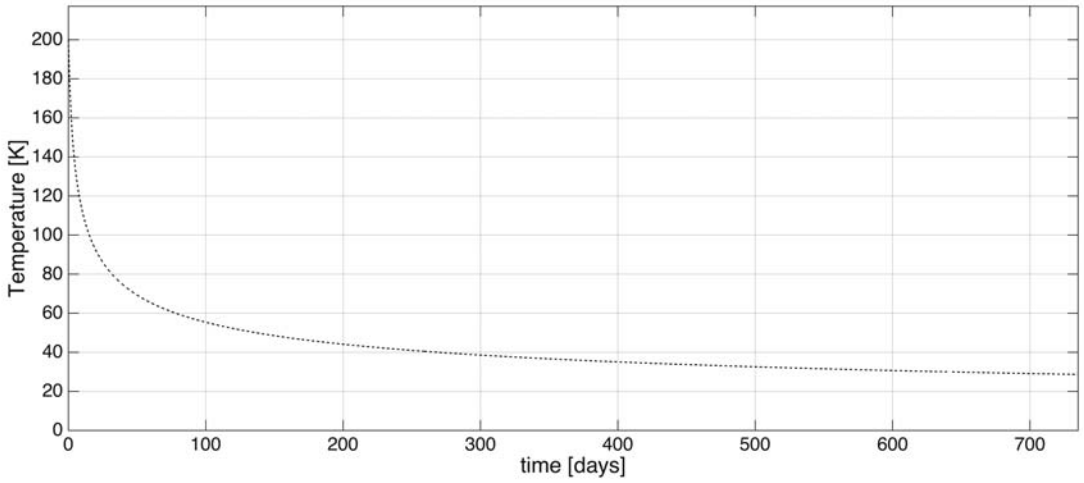

Figure 12.11: Zero-input test run over two years.

12.3.3 Day One Convergence

The day 1 convergence was simulated with multiple starting temperatures lower, equal to and higher then the convergence temperature. Every time the convergence was reached in the first two days without a heater, while it took the system ≈10 hours to converge with the heater radiating at full power.

CHAPTER 13

System Performance

This chapter will give all the information that can be given now that the design is complete.

13.1 Mass Budget

Now all the subsystems are defined a total picture of the mass budget is shown in table 13.1 and figure 13.1. The power in this table is not representative as the individual subsystems are not going to be switched on at the same time. This is just shown for reference over the power usage of each subsystem.

Table 13.1: Mass and power budgets

Subsystem	**Mass Budget [kg]**	**Power Budget [W]**
PLS	1.893	4.20
CDHS	1.030	8.00
TTCS	0.200	2.04
AOCS	3.532	4.53
PROP	1.686	107.14
EPS	2.523	n/a
STR	5.500	-
TCS	1.730	25.00
Total:	**18.094**	**150.91**

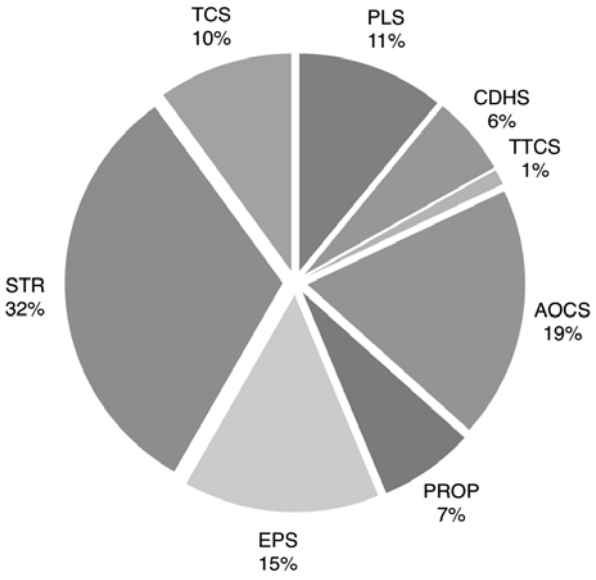

Figure 13.1: Mass distribution

Figure 13.1 shows the distribution of the subsystems' with respect to the total in a pie chart format. The heaviest subsystem is the structures and mechanisms one.

13.2 Mission Compliance Matrix

The mission compliance shows if and where the design requirements and constraints are being met. The parameters with <tbd> have not been specified as of now and will have to be complied during future phases. The missing compliances mostly concern the production phase, which is not relevant during the design phase of the project.

13.3 Sensitivity Analysis

The sensitivity of a change in major system parameters and the influence on the design will be addressed in this section. The parameters that will be considered are the orbit altitude, the maximum power, the maximum mass, the size of micrometeoroids that have to be detected and the lifetime.

Table 13.2: Mission compliance matrix

Identifier	Section	Compliance	Identifier	Section	Compliance
C-T-L-1	13.1	✓	C-T-SC-P-2	10.2.3	✓
C-T-L-2	13.1	✓	C-T-SC-P-3	6	✓
C-T-L-3	11.2.2	✓	C-T-SC-TC-1	12.2.1	✓
C-T-MI-1	3.4.2	✓	C-SH-1	14.2	✓
C-T-MI-2	3.4.2	✓	C-SH-2	14.2	✓
C-T-MI-3	3.4.2	✓	C-L-1	14.3	<tbd>
C-T-SC-TTC-1	6.2.1	✓	C-L-2	14.3	✓
C-T-SC-TTC-2	7.2	✓	C-RS-ST	13.5	✓
C-T-SC-TTC-5	7.2	✓	C-SD-1	13.7	✓
C-T-SC-TTC-6	7.2	✓	C-SD-2	13.7	✓
C-T-SC-TTC-7	7.2	✓	C-PROD-1	14.3	<tbd>
C-T-SC-TTC-8	7.2	✓	C-PROD-2	14.3	<tbd>
C-T-SC-TTC-9	7.2	✓	C-PROD-3	14.3	<tbd>
C-T-SC-P-1	11.2.3	✓			

13.3.1 Orbit Altitude

A change in orbit altitude would lead to significant changes in the design of the LUMID. The primary subsystem that would be influenced by an increase in altitude is the payload. The thermal imaging device as it is now can only function properly in a certain altitude range. At higher altitudes the resolution would be too large to be able to detect the micrometeoroid impacts, or would at least increase the minimum detectable size significantly. The choice then lies between either relaxing the requirement on minimum detectable size and thus drastically reducing the scientific return, or redesigning the payload system to continue functioning properly at this new altitude.
A redesign of the payload can be done in two different ways. The existing thermal imaging device can be adapted to work at this altitude, by e.g. choosing a different lens, which would decrease the ground resolution and therefore increase the detectability, but would decrease the field of view and thus the covered area and the scientific return of the system.
Another option is to choose a different component, e.g. a camera with a higher resolution, or a different detection method all together. A higher resolution camera will most likely have a higher power usage and a lower sensitivity. The consequences of changing the detection method are too far reaching to investigate, so this option will only be used as a last resort. The other subsystems that would be influenced directly are the PROP subsystem, since station-keeping manoeuvres will most probably have to occur at a lower frequency, the TTC, which will have to be designed for different contact times and the EPS which will have different eclipse ratios. Finally, all other subsystems will be influenced indirectly in some way through the change in the aforementioned subsystems.

13.3.2 Maximum Power

An increase in the required power would of course influence the EPS the most. The solar arrays and the batteries will have to get larger. The increase in solar array area will lead to a significant increase in the MMOI's of the spacecraft, which will then require the AOCS to provide more torques and thus increase the size of the reaction wheels. The added batteries and the extra mass of the solar panels and the AOCS will then require a larger thrust to provide the same Delta-V's for station-keeping. This will thus require a more powerful thruster, which will use more power and thus closing the circle at the increase in the batteries and solar panels that are needed to deliver this higher power to the thruster. This process has to be iterated over until convergence.

13.3.3 Maximum Mass

The consequences of a change in the mass of the spacecraft can be placed in the same iterative process that has been mentioned in 13.3.2. The sensitivity of the system to any of the changes that are mentioned in 13.3.2 is relatively high, due to the recurring nature of the changes.

13.3.4 Size of micrometeoroids to be detectable

A decrease of the required minimum detectable micrometeoroid size would lead to a change in the payload subsystem, Since the LUMID is now flying at a 15km periapsis, the orbit cannot be lowered anymore. The possibilities for changes in the payload system are already listed in 13.3.1.

13.3.5 Lifetime

An increase in the minimum lifetime requirement would most notably create a change in the required propellant for the station-keeping manoeuvres. Due to this, the iterative process in 13.3.2 is started again. A second impact of this change would be that some components would have to be replaced by others for increased reliability. An example of this might be the change of data storage method from SD-cards to a hard-drive which is less prone to failure due to radiation. Since the components of the satellite have been chosen to minimise the mass as much as possible, choosing a more reliable component will most probably increase the mass.

13.4 Risk Assessment

During the design process, the technical risks of the satellite have continuously been assessed. The overall risks have been discussed in the midterm report [105]. In this section an overview is given of the subsystem risks during the two main phases. Only the most threatening risks are discussed.

Risk events cannot entirely be avoided, therefore, risk mitigation is an integral part of the mission design. This can be done in two ways; reducing the impact or likelihood of a risk. The goal is to move the risks in table 13.3 in the direction of the lower left corner. The risk mitigation measures are directly indicated after the risk identification.

13.4.1 Payload Risks

[PLS1] Camera Failure The payload is to be functional at all time to enhance proper scientific data to be obtained. Failure of the camera therefore has a **catastrophic** impact since no data can be gathered then. The likelihood is estimated as **unlikely**. The catastrophic impact is mitigated since three cameras on different satellites are used. When one camera fails, the coverage reduces resulting in less data. However, the mission can still continue reducing the impact to **critical**.

[PLS2] Camera Degradation The camera can degrade over time by turning on and off during eclipse and day time respectively. Degradation will affect the lifetime and can affect the performance leading to a **moderate** impact since there is still data obtained but the quality will decrease slowly. The likelihood is estimated as **likely** since degradation of cameras for space missions is a well-known phenomenon. The camera degradation can be mitigated by going in safe/standby mode during the day instead of shutting down, reducing the likelihood to **moderate**.

[PLS3] Dead Pixels A dead pixel is a pixel that cannot change colour. In case of a black pixel it means that no MMs can be detected. A bright dead pixel is more critical since this would mean that constantly a MM is detected influencing the measured flux drastically. The impact would therefore be **catastrophic** while the likelihood is **unlikely** since the probability of a dead pixel for the total screen is guaranteed to be very low. A bright dead pixel can be prevented by implementing a pixel check, if a bright pixel exceeds a certain time duration, the data will not be taken into account. The impact will then reduce to **moderate**.

[PLS4] Noise Influencing the Data Noise can result in a missed or false detection leading to incorrect results. A flash is detected when the corresponding pixel is two times brighter than the surrounding pixels. Combined with the fact that random noise does not per definition make the pixel detectably brighter, leads to the classification of the likelihood as **moderate**. The impact is estimated

as **moderate** since the number of MMs impacting is high and missed and false detections will more or less average out resulting in a good flux approximation. The influence of noise can be mitigated by increasing the contrast ratio which will reduce the likelihood to **unlikely**. A noise filter is build in reducing the noise influence reducing the impact to **marginal**.

[PLS5] Radiation from other Subsystems Resulting in a Detection Error Radiation originating from other subsystems might produce heat leading to a detection error. The impact is estimated as **moderate** as is explained in [PLS4] where a detection error is dealt with as well. The likelihood is expected to be **moderate** since the temperature inside the satellite will be higher than the surroundings but it is difficult to predict the exact consequences. The likelihood can be reduced to **unlikely** by protecting the camera with a coating to block the radiation preventing detection errors from this source.

[PLS6] Two Stage Impact Detector Failure It is possible that the two stage impact detector will fail due to the impact of a too large MM, but the corresponding probability is low. Also, many MMs impacting leads to different holes in the first foil making the system less accurate. Since it is estimated that the number of MM impacts during the mission lifetime is low, the likelihood of both events is **unlikely**. The impact averaging both events is **critical**. Different two stage impact detectors are used introducing redundancy. However, the coverage will decrease and the amount of data obtained as well. Regarding this, the impact is brought down to **moderate**.

13.4.2 Command & Data Handling Risks

[CDHS1] Flipped Bits For the CDHS it is possible that flipped bits occur resulting in hard and software errors. The CDHS receives commands via the lunar orbiter from earth and distributes it along the whole spacecraft making the impact **critical** depending on the result of the error. Since the CDHS is complex the likelihood is estimated as **moderate**. To prevent flipped bits, radiation shielding is used. This measure reduces the likelihood to **unlikely**. To fix errors resulting from flipped bits, voting systems are used for error detection. This combined with the fact that radiation tolerant hard and software is used reduces the impact to **moderate**.

13.4.3 Telemetry, Tracking and Command Risks

[TTCS1] Insufficient Contact Time with Lunar Orbiter to Transmit all Obtained Data When the contact time with the lunar orbiter is insufficient to transmit all obtained data, a large data storage unit is necessary. Since the obtained data defines the scientific value of the mission the impact is classified as **critical**. The lunar orbiter is in a different orbit and is part of the time far away from the moon, this implies a likelihood of **likely**. The CDHS has a data storage large enough to store data when the contact time is to short to transmit all data. Moreover, all this stored payload data can be sent when the contact time is longer. Also, the data rate is designed that when the mission lifetime is completed, all obtained data is sent to earth via the lunar orbiter. All these applied solutions reduce the impact to **marginal** and the likelihood to **unlikely**.

13.4.4 Propulsion Risks

[PS1] Unforeseen station keeping When more and or longer adjustments are needed for station keeping this will demand more from the propulsion system. When station keeping cannot be performed this will have a **catastrophic** impact. Taking into account, as is stated in [OP2], that the satellites orbit is already simulated accurately in chapter 3 the likelihood is determined **unlikely**. The impact is lowered to **moderate** by incorporating additional propellant such that additional station keeping can be performed when necessary.

[PS2] Power Processing Unit Failure The possibility exists that the power processing unit (PPU) fails such that the thrusters are not controllable anymore. Station keeping cannot be performed from

that moment onwards, resulting in a **catastrophic** impact. The likelihood is estimated as **moderate**. The PPU is radiation hardened decreasing the radiation failure probability. Furthermore, the PPU is already flight-proven assuring reliability. This combination decreases the likelihood to **unlikely**.

13.4.5 Attitude Orbit and Control Risks

[AOCS1] Underestimation of External Momentum It is possible that the external momentum turns out to be higher than estimated leading to more propellant mass needed. The thrusters cannot compensate for the disturbances anymore resulting in a **catastrophic** impact. The likelihood is estimated as **moderate** since the estimation method is sensitive to the input parameters. In the estimation worst case parameters are assumed, reducing the likelihood that the external momentum is underestimated to **unlikely**. Another safety measure is that additional propellant is taken such that, even if the external momentum is underestimated this can still be dumped by the thruster units. This brings down the impact to **moderate**.

13.4.6 Electrical Power Risks

[EPS1] Meteoroid Impact The solar panels cover a large area of the satellite making the probability of a meteoroid impact relatively high. However, the probability of impact for a small size CubeSat® is still **unlikely**. The impact depends on the size, the velocity and the angle of impacting the solar panels. In any way, less power generation may have an effect on the functionality of the components inducing a **critical** impact. By connecting the solar cells to a certain extent in parallel instead of in series, the impact is reduced to **moderate** since the power consumption will not drop drastically and a safety margin is already incorporated. The likelihood cannot be brought down as is explained in [PLS6].

[EPS2] Solar Cell Degradation Resulting in a too low Power Generation near End-of-life A well known solar cell aspect is that the performance degrades slowly over time. During the whole mission lifetime power consumption and generation patterns will repeat. The likelihood that the lower power generation has consequences for the functionality of the components depends on the degradation rate and is estimated as **moderate**. The impact differences per component so is decided to be **critical**. The effect of solar cell degradation is taken into account in the power generated during the mission lifetime, as can be seen in figure [REF]. This measure reduces the likelihood to **unlikely**. The impact is lowered to **moderate** by evaluating the power consumption when operating and when in stand-by mode, such that the large power consuming systems are, as much as possible, not consuming much power in the same time period.

[EPS3] Fluctuating Current in the Spacecraft The use of a photo-voltaic battery system for the EPS makes an ideal case for fluctuating current. The power generation depends on the angle of incidence and the battery current depends on the state of charge at any point. With both main elements sensitive to the fluctuations, the likelihood can be stated as **Almost Certain**. The impact could be that the spacecraft generates too much or too little power, resulting in overcharging or undercharging. The combined impact is **Critical**. To mitigate this, the design of a Peak Power Tracker and a Battery (Dis-)Charge Regulator is proposed, making sure that the current output of both remains constant and reducing the likelihood to **Unlikely**.

13.4.7 Structures & Mechanisms Risks

[STR1] Failure of Stepper Motor The stepper motor is a relatively complex component since it has to actuate various times during orbit. Combined with a long lifetime for CubeSat® standards this leads to a likelihood of **likely**. The impact will only influence the power generation of one solar panel but a failure has a long term effect making the impact **moderate**. By extensively testing, especially for durability, the likelihood can be brought down to **moderate**. The impact will remain the same as reparation is not possible.

[STR2] Failure of Deployment Mechanism The deployment mechanism is of utmost importance resulting in a **catastrophic** impact. The deployment mechanism is normally a relatively complex system due to actuation. On the other hand, the system has to work only once, leading to a **moderate** occurrence probability. A spring loaded system is used,increasing the reliability and thus decreasing the likelihood to **unlikely**. Testing is, as holds for all components, another possibility to bring down the likelihood. The impact cannot be mitigated since the consequence remains the same.

[STR3] Unknown Solar Panel Orientation In case of power deficiency, the orientation of the solar panels will be unknown. When the power is available again, the orientation can be interpreted incorrectly resulting in a non optimal solar panel orientation for power generation. The impact depends on the power deficiency time and is estimated as **critical**. The likelihood is **moderate**. This risk is mitigated since the stepper motors have a fixed datum orientation to restore to in order of power loss decreasing the impact to **marginal** (subsection 11.2.4). The power is simulated accurately in 10 reducing the likelihood to **unlikely**.

[STR4] Underestimation of Launch Loads It may be possible that the launch loads turn out to be higher than expected damaging the structure. In an extreme case, this leads to a system failure, while (small) deformations to the structure are also an option. Combined the impact is set to **critical**. The likelihood is determined **moderate** due to the variations in launch loads and vibrations. The launch loads are elaborately investigated and modelled in 11. Also, the launch loads can be simulated by testing. This combined lead to a likelihood of **unlikely**. A safety factor incorporated for the launch loads reduces the impact to **moderate**.

13.4.8 Thermal Control Risks

[TCS1] Overheating of the Satellite Due to solar radiation and internal heat produced by different components the spacecraft heats up during the day. When the temperature becomes too high, components can stop functioning. The impact depends on the operational temperature of the main components and is therefore **moderate**. The likelihood is estimated **moderate** as well. A radiator is used to transport all produced heat to the environment when needed. This in combination with isolating the temperature sensitive components attenuates the likelihood to **unlikely**. The impact remains the same, since the consequence of too high temperatures will remain the same.

[TCS2] Under Cooling of the Satellite The lowest temperatures occur during lunar eclipses and may lead to under-cooling. The components which cannot withstand these low temperatures will not be operational anymore. The likelihood and impact are both estimated as **moderate**. The low temperatures are compensated by heaters which create internal heat, decreasing the likelihood to **unlikely**. The impact remains the same here as well, due to the fact that the consequence of too low temperatures will not change.

13.4.9 Risk Maps

The risk map before mitigation is given in table 13.3. After mitigation, the updated risk map is visualised in table 13.4. It is decided not to indicate the risk positions before mitigation in the table after mitigation for clarity. The same holds for indicating the risk position change by arrows.

13.5 Design RAMS

RAMS analysis contains the terms Reliability, Availability, Maintainability and Safety. These terms are defined as [122]:

Reliability can be defined as the probability that a system will perform in a satisfactory manner for a given period of time when used under specified operating conditions.

Table 13.3: Risk map: likelihood and impact of risks are represented by the horizontal and vertical axis, respectively.

Catastrophic		PO3, PLS1, PLS3, PS1	PS2, AOCS1, STR2	PO4, OP2, OP3	
Critical	PO2	PLS6, EPS1	PO1, PO5, CDHS1, EPS2, STR4	TTCS1	EPS3
Moderate			PLS4, PLS5, STR3, TCS1, TCS2	PLS2, STR1	
Marginal					
Negligible					
	Rare	Unlikely	Moderate	Likely	Almost Certain

Table 13.4: Risk map: likelihood and impact of risks are represented by the horizontal and vertical axis, respectively.

Catastrophic		PO3, PO4, OP3, PS2, STR2			
Critical		PO1, PO5, PLS1, EPS3			
Moderate	PO2	OP1, OP2, PLS3, PLS4, PLS5, PLS6, CDHS1, PS1, AOCS1, EPS1, EPS2, STR4, TCS1, TCS2	PLS2, STR1		
Marginal		TTCS1, STR3			
Negligible					
	Rare	Unlikely	Moderate	Likely	Almost Certain

Availability is often used as a measure of system readiness. The degree, percent, or probability that a system will be ready or available when required for use. Availability can be seen as the result of reliability and maintainability.

Maintainability pertains to the ease, accuracy, safety, and economy in the performance of maintenance actions. Maintainability is the ability of an item to be maintained, and like reliability, is an inherent characteristic of system design.

Safety is the freedom from hazards to human and equipment.

The success of the overall LUMID system depends on its availability for the intended use. The overall availability has two components: the reliability and the maintainability. For satellites once launched, the availability depends only on the reliability, as physical maintenance will be beyond reach. The RAMS requirements are given as:

R-RAMS-1: The spacecraft reliability shall exceed 95% during the mission lifetime.

R-RAMS-2: The spacecraft shall have no need of physical maintenance during its lifetime.

R-RAMS-3: The spacecraft shall allow for software maintenance during the mission lifetime.

The system reliability is based on probability of numerous components working together successfully over the entire mission duration. The reliability of a given component is derived from tests on a large number of identical components under actual operating conditions. In the spacecraft industry, an actual flight history is available on only a small number of satellites. Furthermore, CubeSats® have even less documentation available on their reliability and the LUMID mission is the first to attempt a mission lifetime of at least two years. These factors combined make actual reliability estimation difficult. However, the estimate is useful at least on a relative basis, in identifying and correcting weak links in the chain of reliability. The perspective of the system reliability developed during the process is perhaps more important than the final reliability number. The probability of failure of a component comes from four sources:

- Random failures, which is only dictated by probability.

- Wear-out failures, which corresponds to the amount of cycles a component has to endure during the mission lifetime.
- Design failures, where incorrect measurements of for example internal stresses or internal momentum result in exceeding the design limit.
- Manufacturing failures, where the actual property deviates from the initial design due to errors in the production process.

The design and manufacturing errors can be accounted for in the next design iterations by allowing design margins and ensuring proper quality control during the production process.

Wear-out failures occur after many cycles of product use. For example, the batteries and solar panels degrade over time and spacecraft components under constant stress will show fatigue.

Random failures form the largest risk during the mission lifetime. Where wear-out failures are fairly predictable, random failures occur only based on probability. The possibility of random errors is a major influence in the design. As an example of random failure rate estimation (and consequently, reliability estimation) will be discussed.

13.5.1 Electrical Components Example

The standard MIL-HDBK-217 establishes a uniform method of predicting reliability of military/space grade electronic parts, equipment, and systems. It lists the base failure rates of numerous parts under base thermal, electrical, and mechanical stresses. To give an example of the process of estimating the reliability of electrical components, the failure rate prediction of diodes is given in equation 13.1. All deviations from the base operating conditions alter the failure rate by the factors denoted by π. These are: temperature, electrical stress, conctact construction, part quality and environmental effects.

$$\lambda_p = \lambda_b \cdot \pi_T \cdot \pi_S \cdot \pi_C \cdot \pi_Q \cdot \pi_E \tag{13.1}$$

13.5.2 Influencing Reliability in Design

The overall reliability can be given as a function of the individual component reliabilities. The subsystems of the LUMID can be viewed in series according to equation 13.2 [122]. However, with the eight subsystems defined, it is necessary for every subsystem to be just over 99% reliable. The proposed solution within the spacecraft subsystems is to allow for redundancy. The reliability of a redundant component changes its reliability according to equation 13.3. For example, a fully redundant part (two components in parallel) of 95% reliability has an estimated 99.75% reliability.

$$R_{total} = R_{PLS} \cdot R_{CDHS} \cdot R_{TTCS} \cdot R_{AOCS} \cdot R_{PROP} \cdot R_{EPS} \cdot R_{STR} \cdot R_{TCS} \tag{13.2}$$

$$R_{parallel} = 1 - (1 - R)^n \tag{13.3}$$

Every subsystem reliability prediction will be a combination of series and parallel components. The actual reliability prediction is at this stage impossible, due to the design not being described to the lowest detail possible. However, the following list shows the redundancy implemented at this stage.

- PLS: Multiple piezo-electric sensors (full redundancy)
- CDHS: Functional redundancy on COTS PCB design
- TTCS: Multiple antenna's (full redundancy)
- PROP: Functional redundancy on COTS PPU design
- EPS: Multiple solar arrays, solar cell architecture, COTS battery architecture

For the STR and TCS subsystem, the main failure cause at this stage is the wear-out failure. For these subsystems, the COTS structure and the TCS radiator have included a design margin.

13.6 Market Analysis

Although the CubeSat® concept has existed for a long time, its implementation in high-complexity space missions is still at a novel and premature level. A CubeSat® has never been deployed to an alien celestial body to this date. This raises concerns about the place of the concept in the market world.

The subsequent sections investigate what the potential market opportunities for CubeSats® are and the market volume of CubeSats® at present and in the future. In addition, the market trends driving the development of CubeSats® are investigated and the profitability of CubeSats® is looked into, especially in terms of cost. This is also related to the Lunar micrometeoroid detector treated in this document.

Firstly, the market opportunity is explained in section 13.6.1, followed by the market size in section 13.6.2. Subsequently, the market trends and market and product profitability are explained in sections 13.6.3 and 13.6.4, respectively. A cost breakdown is made in section 13.6.7. The chapter then concludes with section 13.6.5, listing the possible stakeholders of the mission.

13.6.1 Market Opportunity

The current CubeSat® market focuses mainly on Earth orbiting satellites. Up until now there has not been any high demand for CubeSats® orbiting the Moon. However, as explained in [123] there is severe growth in the use of CubeSats® and it is expected to keep on growing in the future. As plans are made to operate a permanently manned base on the Moon, the first step of ESA's plan is to start putting satellites into lunar orbit [124]. These satelites should investigate the lunar environment. Using a CubeSat® to detect micrometeoroids, mapping the radiation pattern, solar illumination, as well as available water-ice packages are possible examples of lunar exploration missions.

The cost of getting a spacecraft in lunar orbit is significantly higher than that of an Earth orbit, therefore it is important to keep the cost of other aspects of the mission to a minimum. The best option is to minimise mass by using mass efficient designs and ensuring the satellites are durable. CubeSats® are particularly suitable in that regard. This suggests that it is beneficial, both from an engineering and an investor point of view, to break open the market for cost efficient lunar CubeSats®.

13.6.2 Market Size

As of September 2016, approximately 480 CubeSats® have been launched. It is expected, taking future planned missions into account, that over 3000 nano- or microsatellites will be launched from 2016 up to 2022. This generates a wide market range for CubeSats® orbiting the Earth. As for the Moon, only a limited number of large-scale satellites is currently orbiting it. Currently, there are over 18 different lunar missions planned until 2020. Some of them are private, but most are from various national space agencies. Current plans also project new crewed missions on the Moon by 2023. [123]

Although several missions have been planned already, the number of CubeSat® missions is still very limited. NASA has procured the "Skyfire" concept to Lockheed Martin, planning on delivering 12 CubeSats® into lunar orbit by 2018. The objective of this mission is to deliver key information on the characteristics of the Moon on solar illumination, as well as available water-ice packages. As plans are made to colonise the Moon, great knowledge is required of the lunar environment. A great opportunity to supply this knowledge lies in the use of CubeSats®, as these seem to be the most cost and weight efficient for this objective. This generates a great need and a wide market size for CubeSats® in for lunar exploration. The detection of MMI's to make a flux model is one of many possibilities to investigate the lunar environment. [123]

13.6.3 Market Trends

Two key trends have been identified helping to stimulate the growth in the nano- and microsatellite market: all-electric propulsion system for satellites, development of reusable space launch vehicles.

Since CubeSats® are very small, it is nearly impossible to apply traditional propulsion systems, like the ones with solid and liquid propellant. Only if micro-electric propulsion technologies advance, are CubeSats® expected to become more popular [125].

Also, reusable space launch vehicles are very important for CubeSats®. Launching satellites in a single-use rocket, is rather expensive. Reusable rockets would reduce the launching cost significantly, rendering the usage of CubeSats® more affordable [125]. This technology could potentially also be used on the Moon. Reusable rockets could take cargo there and then take off again.

13.6.4 Market Profitability

One of the main advantages of CubeSats® lies in their lower mass, moment of inertia and volume, in turn meaning they require less space in launchers, and therefore, are more affordable [126]. As a consequence, a mission to the Moon would be more affordable, because there could already be savings in launch costs.

The feasibility aspects of CubeSat® missions are continuously improving, as they take advantage of newer miniaturised consumer technologies. Constant improvements in price and performance in the consumer-electronics industry allow CubeSats® to perform as well as satellites that are many times larger and heavier, but at a far lower cost. In fact, a swarm of CubeSats® might outperform a traditional heavy satellite many times. They can also be built faster.

However, this does not automatically mean it is a highly profitable sector. The consumer-electronics industry is mainly for high volume markets such as smartphones and computers. Compared to that, the CubeSat® industry is a very low volume market. Finding a supply chain that is fitted to supply small volumes of high-tech components can be a big challenge for companies. Often, it is decided to keep production in-house, increasing CubeSat® production cost. In addition, satellite companies are often faced with minimum order quantities (MOQ). Often they have to buy more materials and equipment than they actually need, making the production of CubeSats® more expensive than necessary. To tackle the mass production effect, one needs to design missions that involves more production of components so that as little raw material as possible is wasted. A possible way to do this is making use of a constellation or a swarm.

13.6.5 Stakeholders

The main stakeholders in the mission of Moon exploration are the European Space Agency (ESA) as a customer, the scientific community as a user and all the companies that supply parts. An active stakeholder is Delft University of Technology. A passive stakeholder are the citizens of the European Union (EU).

ESA sets the requirements and the general theme for the Moon exploration mission. The scientific community would benefit from the information collected during the mission. It would gather knowledge on the Lunar environment and the information would also help develop future missions to the Moon. Delft University of Technology helps the team develop the mission along the way with its knowledge, infrastructure, and training program. That is why it is an active stakeholder. The EU citizens influence the mission indirectly, mainly via income from taxation and political support. If the public interest toward Moon exploration is high, ESA will have more financial resources to make it happen.

There is also a sustainability component related to the stakeholders which is important to look at when market analysis is performed. The environmental and economic sustainability, as well as impact on the society affect the aforementioned stakeholders. The sustainability aspects are further elaborated upon in chapter 9.

13.6.6 Return on Investment

The return on investment of a CubeSat® mission detecting micrometeoroid impacts in the lunar environment is considered to be mostly scientific. The three s/c generate data on the number of micrometeoroid impacts that occur on the satellites itself (insitu) and on the surface of the Moon.

This data is used to map a flux model of the number of micrometeoroids in the vicinity of the lunar surface. This flux model is of crucial importance for both future manned- and unmanned lunar exploration.

The flux model could be made much more reliable if more data can be delivered by the satellites. This can be done by increasing the mission time-line or by putting more satellites in orbit.

Overall the mission creates great opportunities for the scientific community to demonstrate how mass efficient CubeSats® can be placed in lunar orbit and what the challenges are that drive a CubeSat® mission to the Moon. This is also of great importance for future lunar exploration.

Furthermore the mission would not only stimulate the growth in the use of nano- and microsatelites. It would also allow for improvements in the aformentioned market trends. On business related benefit the mission would generate a coorporation between ESA and TU Delft as much as other stakeholders such as suppliers.

13.6.7 Cost Breakdown

To properly assess and optimise the profitability of the LUMID, the entire cost structure of the mission needs to be known. That will not only give an overall picture in terms of cost, it will also help identify the biggest cost drivers of the mission. In figure 13.2, one can see that the cost break down structure identifies and breaks down the costs of the entire mission from beginning to end of life. It is an AND tree. From there, one can see that the subsystems can be either bought off the shelf or produced independently. If one chooses to produce it independently, one needs to account for Direct Material, Direct Labour, and Manufacturing Overhead Cost. As the mission goes forward, the actual cost of the mission components will be determined. However, a first order estimation is of the three satellite and launching cost is presented in table 13.5. One can see there that the approximate cost for the mission is around 18 million Euros. A large part of the estimation was done using reference components from CubeSatShop®. [127] Since the mission here is quite, it becomes hard to make a proper cost estimation. However there is known that the Lunar CRater Observation and Sensing Satellite (LCROSS) Mission had a cost of around 74 million euros [128]. The GeneSat-1 mission that flew in LEO had a cost of around 4.7 million euros [128]. So total cost of the LUMID is expected to be in between the cost of these two missions and strongly leaning towards the LCROSS mission cost. Taking the cost estimation per Cubesat® (see table 13.5) into account, a total mission cost is estimated around 54 million euros. The two reference missions are used as a crude validation method for the mission cost estimation.

Table 13.5: Cost estimation per CubeSat®.

	Cost [€]
Project definition and initiation	100
Spacecraft construction	5 000 000
Structure	15 000
AOCS	480 000
Payload	500
CDH	6000
Thermal Control	4100
Propulsion	90 340
TTC	11 000
EPS	40 000
Overhead cost	45 000
Total satellite cost	5 692 040
Amount of satellites	3 units
Total satellite system cost	17 076 120
Transport to launch site	500 000
Launch cost	300 000
Total cost for launching procedure	304 000
Total cost:	**17876120**

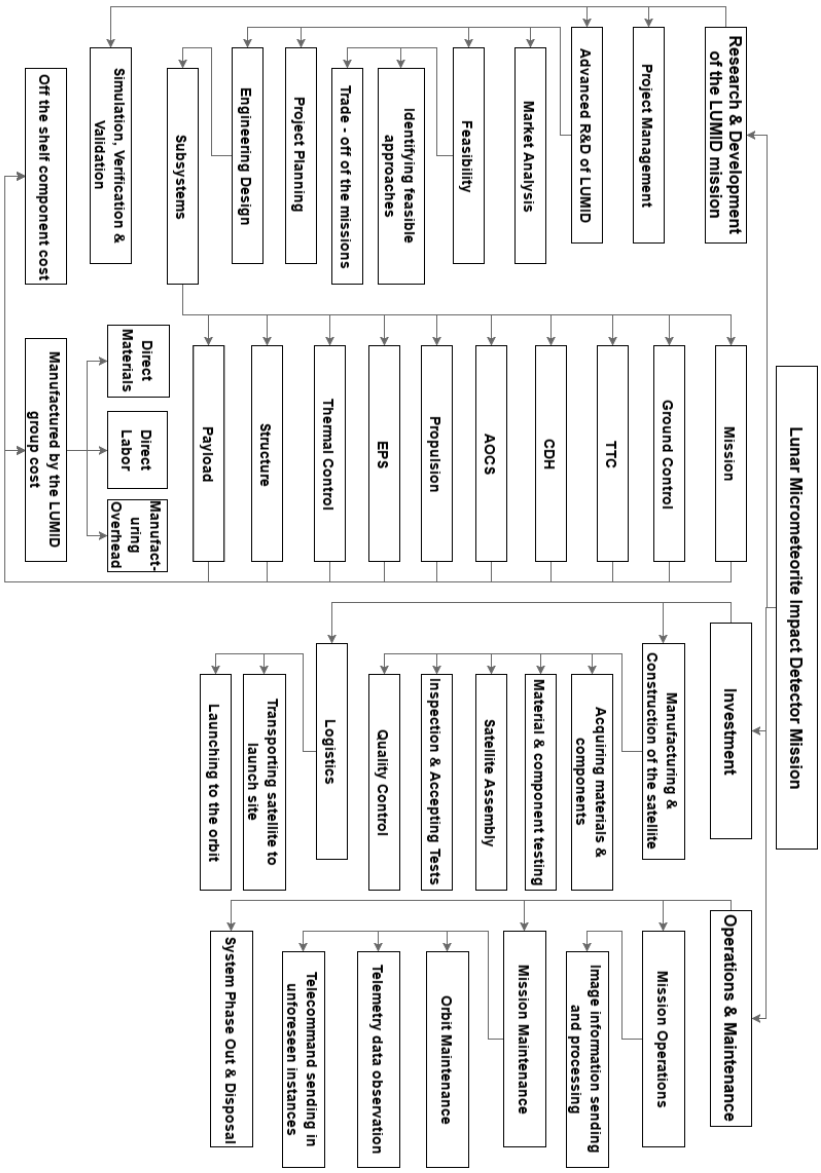

Figure 13.2: Cost break-down structure of the LUMID mission

13.7 Sustainability Plan

Spaceflight, with the large amounts of propellants associated with it, is inherently rather unsustainable. However, even though sending a satellite to the moon may be unsustainable, the scientific results produced by these missions have frequently resulted in creating sustainable technologies. In this section, various aspects of the LUMID mission which make it sustainable, are elaborated upon.

13.7.1 Modularity

The LUMID mission is designed as a CubeSat® mission. The CubeSat^{TM} platform, with its standard form factor and its commercial off the shelf components, was conceived to make spaceflight more accessible. The standardised structures make it so that components can easily be replaced at any given time. This makes the satellites modular. The LUMID satellite could easily be rebuilt with a different scientific payload installed. The stringent requirements stemming from the low altitude lunar orbit make it so that some of the orbital manoeuvring capabilities can be traded in for even more room for scientific payload. Furthermore, if intended for use in LEO, the AOCS thrusters can be replaced by much more power and mass efficient magnetorquers.

13.7.2 Green Propulsion

In 2013, the Chinese space ageny launched its first unmanned mission to the moon, the Chang'e 3 [129]. It was estimated that the amount of gases produced by the Chang'e 3 lander during descent to the Lunar surface was roughly equal to the Lunar exosphere. This fragile environment should be protected at least until thorough measurements have been made about it, which could increase the understanding of the Lunar environment. The LUMID mission will use Ion-thrusters, which use Xenon as a propellant and are extremely efficient. This will therefore cause a negligible disturbance on the Lunar exosphere. It should be noted that the choice for Ion-thrusters originated from other requirements, such as the maximum volume and mass for the satellite, as using traditional chemical propulsion would require far more propellant than a 12U CubeSat® structure could provide.

13.7.3 Piggyback Launch

The LUMID will travel to the moon using a piggyback launch. This means that it will travel along with a Lunar Orbiter, designed by ESA, as a secondary payload. This method of launching nano- and microsatellites can drastically decrease the cost and propellant requirements associated with satellite missions. This decrease in launch costs will create more possibilities for commercial space missions, which can lead to new and more sustainable technologies being developed.

13.7.4 End of Life

An important consideration for a sustainable space mission is the end of life, or EOL, strategy. The growing problem of space debris has not yet reached the lunar environment so this might come across as of lesser importance. Nothing is less true however. In order to avoid a similar situation to the LEO space debris, every spacecraft going to the Moon must have a sustainable EOL strategy. The several options for the EOL strategy are described in the IADC Space Debris Mitigation Guidelines. [130] This document states that "Spacecraft or orbital stages that are terminating their operational phases in other (than LEO or GEO) orbital regions should be manoeuvred to reduce their orbital lifetime, commensurate with LEO lifetime limitations, or relocated if they cause interference with highly utilised orbit regions." The aforementioned LEO lifetime limitations are generally accepted to be 25 years, which will not be a problem for the LUMID due to its low orbit. Also due to the many irregularities in the lunar gravity field, a small orbit manoeuvre will result in an impacting orbit. When the spacecraft has entered the impact trajectory, all components should be passivised. This means that as much as possible internal energy is dissipated to the environment. This can be done by expelling away all the propellant, despinning the reaction wheels, decharging the batteries, etc. This way the spread of shrapnel upon impact is contained as much as possible. Furthermore, special care has to be taken to avoid impacting on any areas with either historical or important scientific value. Finally, a strategy has to be designed for a premature EOL in case the spacecraft functions and resources approach the limit of what is needed for a successful de-orbit.

CHAPTER 14

Post-DSE Phase

The current report focuses on the design of a CubeSat® capable of detecting MMs in a lunar orbit. This space project however is not complete yet, as different phases (as explained in section 14.1) still need to be covered for a successful completion. Specifically, section 14.2 focuses on the detailed definition of the concept and section 14.3 explains how the operations and the logistics take over until the system's disposal.

14.1 Space Project Management

A mission like the LUMID mission can be subdivided according to the Project Phasing and Planning documents issued by the European Cooperation for Space Standardization [131]. This documents specifies six specific phases of space project management of which phase 0 up to and including phase B are already performed during this report:

- Phase 0: Mission Analysis/Needs Identification
  This phase identifies the requirements of the system by analysing its needs and the expected performance, together with finding the purpose of the mission. Also the major steps of project management are assessed within this phase.
- Phase A: Feasibility
  The so called feasibility phase is the mission's phase in which the feasibility of the mission is determined, both operationally and technically. This is generally done by trading off different concepts. This can be done by defining their level of uncertainty and their risks, quantifying their critical elements and identifying the technical and industrial feasibility.
- Phase B: Preliminary Definition (Project and Product)
  After a basic concept is chosen in phase A, phase B focuses on a preliminary definition of this concept. Its feasibility is confirmed and both the technical as well as the economic operating conditions are defined. This is backed by the assessment of techniques, technologies and means of implementation.
- Phase C: Detailed Definition (Product)
  This phase allows for a detailed study of the concept defined in the previous phases, to get a definitive standard ready for production of the first models.
- Phase D: Production/Ground Qualification Testing, product verification and validation.
  This phase is the phase where the methods and procedures used in the previous phases are confirmed. The product is produced and tested. If the requirements are met it gets a *design qualification*, while the *operational qualification* is reached if the product can be used operationally. At the end of phase D the product passes the Acceptance Review.
- Phase E: Utilisation
  This phase is composed out of two sub-phases, E1 and E2. Sub-phase E1 is an overall test and commissioning phase, which ends in the first In-Space Test Review. It is composed out of launch activities and in-flight qualification and acceptance tests of the system. Sub-phase E2 is the utilisation phase itself, which the system is designed for.
- Phase F: Disposal
  The disposal phase covers the end-of-life event until the final disposal of the product.

14.2 Project Design & Development Logic

This section focuses on the design work to be done in the phase following the work up until this reports, which focuses especially on the first three phases (Phase 0, A and B). Next on the schedule is the detailed definition of the product, also known as **Phase C**. The future work to be done after this report starts with this phase. Most of the work will go in iterating the design over and over again to find the most appropriate design to suit this mission. Moreover, detailed data sheets of off the shelf components need to be acquired and some components need detailed design for personalised manufacturing. Some chapters already specify the work to be done for the detailed design. A Gantt chart roughly indicating the times to be spend for the activities until the launch date of November the 22nd, 2019 is displayed in figure 14.1.

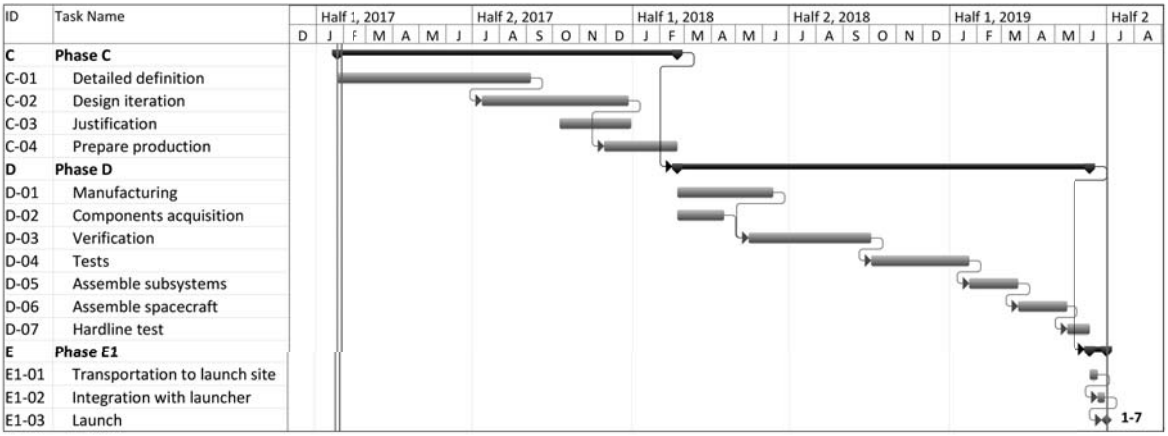

Figure 14.1: Gantt chart for the post-design phase.

14.3 Operations and Logistics

14.3.1 Phase D: Production/Ground Qualification Testing

In this phase the project is going to manufacture, assemble, integrate, and verify and conduct the Qualification Reviews. The manufacturing in specific is divided in the hardware and software manufacturing.

Since the LUMID will mostly use commercial off the shelf (COTS) components, the manufacturing phase will be short. Components that need to be produced are the fuel tank, the fuel tank clamps, the hinges for the solar array and the solar array drive mechanism. The design of these components should be such that they can be produced with commercially available tools and materials.

In parallel with the manufacturing, the component acquisition will take place. All commercial components will be ordered and acquired. Special care has to be taken in order to avoid any delays in delivery or damaged components. This can be done by choosing manufactures with good reputations and which are as close to the production site as possible.

Once all parts have been either manufactured or acquired, the components have to be tested to see if they fulfil all requirements. All manufactured components have to be tested extensively, but when it comes to the commercial components, most of them have been tested already.

After manufacturing, acquiring and testing all the necessary components, the spacecraft can be assembled. All components shall be assembled into subsystems and will consequently be installed inside the satellite structure. The satellite structure is built so that all components can be easily accessed and removed after assembly, which allows for a larger margin of error during assembly.

Some testing also takes place in between the assembly phase. Subsystems will be tested before being placed into the structure. After assembly the system will undergo one last test, the hardline test.

During the hardline test, a series of test inputs will be given to the CDHS, which will then send commands to the other subsystems and check if all subsystems and components perform correctly.

14.3.2 Phase E: Utilisation

Phase E will start assembly and testing. The satellite will be stowed inside the deployment mechanism and will start the transport towards the launch site. Since the launch will be provided by ESA, it will take place either at Kourou, French Guyana, or Baikonur, Kazakhstan. For transport to Kourou, transport by train is not an option. The choice then exists between air transport or transport by ship. Transport by ship will take considerably longer, but is still the preferred option, since vibrations will be smaller and the risk of damaged components decreases significantly. The transport on land will preferably happen by train, once again to reduce vibrations. In the case the launch will take place at Baikonur, the satellite will be transported entirely by train.

Once the satellite arrives on the launch site, it will be installed on the lunar orbiter, after which the launch procedure can be started. Once again, two options exist. The launcher will first enter a circular parking orbit around earth, after which it will either deliver the lunar orbiter into an earth-moon transfer orbit, or after which the lunar orbiter will enter the transfer orbit on it's own, using a kicker stage. After transfer, the lunar orbiter will enter a circular orbit at roughly 500 km altitude and an inclination of 50° to 90° and the satellite will separate from the lunar orbiter using its deployment system. The satellite will then have to wait for 15 minutes before it can start transmitting and will have to act autonomously during this period. Once transmission has been established, the satellite will communicate his status to the ground station, via the lunar orbiter. After this, the transfer to and insertion into the science orbit can start.

The science phase of the mission then begins. The satellite orbits the moon in a (15×300) elliptical orbit at an inclination of 50°. It will detect MMI's using its thermal imaging device every time it is on the dark side of the moon and below a certain altitude. The two stage impact detectors will function continuously starting from the transfer to the science orbit.

In the science orbit, two main phases can be distinguished. The eclipse phase and the illuminated phase. During eclipses, the thermal imaging device will perform measurements, if it is at a low enough altitude. During illuminated phases, the solar panels are pointed towards the sun to maximimise power generation. Each orbit, a small station-keeping manoeuvre will be carried out to prevent orbital decay. The manoeuvres shall preferably be carried out at the apoapsis.
If during the mission, unforeseen circumstances occur, information will be saved and transmitted. If these circumstances pose a threat to the survival of the satellite, the s/c can enter safe mode, in which the functionality of the s/c is reduced to increase survivability. The safe mode can be ended by a command from the ground station.

14.3.3 Phase F: Disposal

The mission has been designed to include an end of life strategy, consisting of a controlled impact on the lunar surface. The required lifetime for the satellite is at least 2 years. The satellite will therefore carry enough propellant to stay in orbit for two years. If however, due to unforeseen circumstances, the projected lifetime decreases during the mission, the satellite will enter its impact trajectory earlier. This will be done by calculating the minimum amount of fuel that is needed to perform an impact manoeuvre. Once the propellant levels drop below that specific level, the end of life phase will commence. The desired orbit for impact will be calculated on earth and the necessary commands to inject the satellite into this orbit will be sent to the lunar orbiter. Special care will be taken to avoid any places of historical or scientific value. Once the satellite is in the impact orbit, it will be passivized. This means that as much internal energy as possible will be dissipated. This will be done through de-charging the batteries, de-spinning the reaction wheels, and thrusting away any remaining fuel. The passivisation of the satellite will contain the shrapnel upon impact as much as possible.

After impact, the complete project inventory will be reviewed to determine the success of the mission and possible future use.

CHAPTER 15

Conclusions and Recommendations

The design treated in this document set out with the aim to create a CubeSat® system to contribute to the human exploration of the Moon. Among a vast array of options, the designers opted to focus on a major threat to interplanetary human exploration: impacts by micrometeoroids. A system needed to be put together to characterise the flux of these tiny rock fragments on the lunar surface and the LUMID mission has been developed to fill this gap.

The preliminary design outcome indicates that a CubeSat® mission to the Moon is already well within the realm of feasibility. A total of three identical, yet independently functioning CubeSats® will be deployed at a 50° inclination at a 15×300 elliptical orbit. Each will use a remote-sensing thermal imaging instrument to register the heat radiated upon an impact event, as well as an onboard 2-stage impact detector for in-situ measurements. Covering a total of 5 billion km^2 and detecting micrometeors smaller in size than 1 µg, it is estimated that over its 2-year duration, the mission will gather enough data to help re-evaluate existing statistical models and to cast light upon this field, which has for decades been been impeded by a veil of uncertainty and lack of comprehensive data.

In addition to its purely scientific value, the mission aims to make a number of breakthroughs in the CubeSat® engineering world. Never before has a constellation of nanosatellites been deployed in orbit around an alien body, nor has it used a larger orbiter as a communications relay station. For the first time will a CubeSat® use a pair of ion-gridded thrusters for orbit control, as well as the Deep Space Network for navigating in an interplanetary environment. Eventually, a successful LUMID mission would establish the capacity of nanosatellites for interplanetary mission at the fraction of the cost of larger modules and open new frontiers in the rapidly developing CubeSat® market.

Furthermore, special reference is due to the sustainability aspects of the design. These aspects materialise both via direct and indirect measures. Directly, by virtue of applying technologies such as the green-technology ion thrusters that eliminate the need for toxic propellants or by avoiding the generation of orbital debris upon decommission. Indirectly, by investing in the modularity of its design that facilitates increased flexibility, reliability and cost-efficiency and by utilising the piggybacking concept, which drastically decreases both the mission costs and the environmental footprint of the design.

As final conclusive remarks, a number of practical considerations are listed below:

- The scientific output of the mission is highly dependent on chance. The payload needs to be at the right place at the right time for an impact to be registered and the probability of this event can only be statistically predicted
- While in theory, a wide range of inclinations is feasible for the placement of the orbit, in practise only a handful of them is appropriate in terms of mission duration, Δv budget and scientific relevance.
- The development of the mission largely depends on external factors. As a characteristic example, the execution of the mission depends on the availability of a host orbiter and none is expected in the foreseeable future for the European Space Agency. As such, negotiations with foreign space agencies are to be made. A further example concerns the start epoch on the mission, dependent not only on the host orbiter, but also on the availability of an appropriate launcher vehicle.

A number of recommendations are also due, listed below:

- **Mission Design:** The preliminary nature of the design, as well as the uncertainty surrounding the configuration of the Lunar Orbiter does not allow for a comprehensive configuration of the

operations sequence. A more thorough research into this aspect is necessary during the next stage of the design.

- **Astrodynamics:** The accuracy of the Δv budgets listed in this report is questionable. Finite burns have not been simulated and the computed Δv values have not accounted for gravity losses. It is a necessary step for the subsequent design phase, that all manoeuvres are simulated by virtue of optimised finite burn sequences. In pursuit of the highest fidelity, a more accurate gravity model is suggested (with emphasis on the latest models produced by NASA's GRAIL mission), as well as more robust numerical schemes and optimisation techniques,
- **Payload:** To better tackle motion blur, an investigation into active stabilisation methods and algorithms is advised. A more thorough research into the component options for the composition of the instrument is also strongly suggested. Lastly, the simulation technique can be enhanced by improving the modelling of the vibration modes and refining the statistical determination approach of the noise sources.
- **S/C Subsystems:**
  - Attitude and Orbit Control system: Current work has focused mostly on qualitatively assessing the type, number and positioning of sensors and actuators needed for attitude determination and control, respectively. As the design process will progress and the configuration of the s/c and/or the mission will evolve, it will be necessary to update the model with new pointing accuracy requirements, inertia characteristics, etc. Also, the coordination of the various sensors in the context of the s/c environment and the reference coordinate system is to be defined with greater clarity, to achieve higher fidelity of the model.
  - Guidance & Navigation hardware: The main candidates have been presented in this report, but a final choice has not been made. Since this constitutes one of the system's most essential components, it needs to be resolved at the earliest opportunity. Accordingly, the rest of the subsystems are to update their configurations to accommodate for it, since it has currently been excluded from the general s/c configuration.
  - Propulsion system: Since the selected thruster is in the final stages of its design, a number of its performance parameters remain unknown. Thrust coefficients, exact thrust and Isp values, as well as accurate power-per-operation-mode values are yet to be determined. Close consultation with the supplier company is advised for the rest of the design process, to ensure the final configuration is consistent with the thruster's performance.
  - Electrical Power system: A number of simplifying assumptions have been included in the current model. Updated values for the illumination beta angles, burn durations and eclipse characteristics are to be accounted for, should a high-fidelity model be desired.
  - Thermal control system: In absence of sufficient data per subsystem, the design of this system has taken a collective approach in its sizing, rather than adapting the design for the needs of every subsystem separately. As such, the heat distribution and dissipation needs are not accurately accounted for, a point for future improvement.
- **Sustainability:** The notion of sustainability is a rather broad one. There are various methodologies for limiting the negative footprint of the design that are not limited to green propellant technologies or space debris prevention. Indicatively, a "lean approach" to the development process [132], usage of state-of-the-art production techniques, innovative end-of-life disposal protocols, etc are all decisive steps towards rendering the concept more sustainable.

Bibliography

[1] J. Carpenter, R. Fisackerly, S. Espinasse and the Lunar Exploration Definition Team, "Lunar Exploration Objectives and Requirements Definition," February 2010. Last visited.

[2] S. Loff and R. Lind, "Lunar Exploration Objectives." https://www.nasa.gov/exploration/home/why_moon_process.html, December 2006. (last visited on December 2, 2016).

[3] E. Kulu, "Nanosatellite database the world's largest database of nanosatellites, more than 1600 nanosats and cubesats." http://www.nanosats.eu/, January 2017. (last visited on December 2, 2016).

[4] D. K. Lynch, "The leonid meteoroid shower: Lessons learned from 19977 and plans for 1998-2001," *Acta Astronautica*, vol. 47, No.11, pp.831-838, June 2000. 10.1016/S0094-5765(00)00134-X.

[5] H. Pettersson, "Cosmic spherules and micrometeoroid dust," *Scientific American, Inc*, vol. 202, No. 2, pp. 123–132, February 1960.

[6] A. Snelling and D. Rush, "Moon dust and the age of the solar system," *Creation Ex-Nihilo Technical Journal*, vol. 7, No. 1, pp. 2–42, 1993.

[7] F. Horz, D. A. Morrison, D. E. Gault, V. R. Oberbeck, W. L. Quaide, D. E. Brownlee, and J. B. Hartun, "The micrometeoroid complex and evolution of the lunar regolith," tech. rep., National Administration Of Aeronautics and Astronautics (NASA), 1977.

[8] E. J. Speyerer, R. Z. Povilaitis, M. S. Robinson, P. C. Thomas, and R. V. Wagner, "Quantifying crater production and regolith overturn on the moon with temporal imaging," *Nature*, vol. 538, pp. 215–218, October 2016. 10.1038/nature19829.

[9] "Apollo to the Moon - Lunar Rocks." https://airandspace.si.edu/exhibitions/apollo-to-the-moon/online/science/lunar-rocks.cfm. (last visited on January 2017, 2017).

[10] J. Woerner, "Moon village: A vision for glabal cooperation and space 4.0." http://blogs.esa.int/janwoerner/2016/11/23/moon-village, November 2016. (last visited on January 24, 2017).

[11] C. R. Tooley, M. B. Houghton, R. S. S. Jr., C. Peddie, D. F. Everett, C. L. Baker, and K. N. Safdie, "Lunar reconnaissance orbiter mission and spacecraft design," *Springer Science*, January 2010. 10.1007/s11214-009-9624-4.

[12] P. O. Hayne1 and B. A. Cohen and R. G. Sellar and R. Staehle and N. Toomarian and D. A. Paige, "Lunar Flashlight: Mapping Lunar Surfac Volatiles Using a CubSat," *Annual Meeting of the Lunar Exploration Analysis Group*, 2013.

[13] C. R. Coombs and B. R. Hawke, "A Search for Intact Lava Tubes on the Moon: Possible Lunar Base Habitats," *2nd Conference on Lunar Bases and Space Activities*, 1992.

[14] C. L. York and B. Walden and T.L. Billings and P. D. Reeder, "Lunar Lava Tube Sensing," *2nd Conference on Lunar Bases and Space Activities*, 1992.

[15] G. de Angelis and J.W. Wilson and M. S. Clowdsley and J. E. Neal and D. H. Humes and J. M. Clems, "Lunar Lava Tube Radiation Safety Analysis," *The Japan Radiation Research Society*, 2002.

[16] B. Walden and T. Billings and S. Gillett, "Utility of Lava Tubes on Other Worlds," *Workshop on ISRU Construction*, February 1998.

[17] R. V. Wagner and M. S. Robinson, "Distributiion, Age and Formation Mechanisms of Lunar Pits," 2015. (last visited on January 24, 2016).

[18] C. Duncan, "Iris V2 CubeSat Deep Space Transponder," 2014. (last visited on January 24, 2016).

[19] M. Beckman, "Mission design for the lunar reconnaissance orbiter," *29th Annual AAS Guidance And Control Conference*, February 2006.

[20] P. D. Tompkins and R. Hunt and M. D'Ortenzio and J. Strong and K. Galal and J. L. Bresina and D. Foreman and R. Barber and M. Shirley and J. Munger and E. Drucker, "Flight Operations for the LCROSS Lunar Impactor Mission," *National Aeronautics and Space Agency*, 2010.

[21] J. C. Fusco, S. S. M. Swei, and R. H. Nakamura, "Sun safe mode controller design for ladee," *AIAA Guidance, Navigation, and Control Conference*, June 2015. 10.2514/6.2015-2011.

[22] P. Fortescue, G. Swinerd, and J. Stark, *Spacecraft System Engineering*. Wiley, 4th ed., 2011. 9780470750124.

[23] A. Perez, "Lunar orbit stability for small satellite mission design," tech. rep., 4th Interplanetary Cubesat Workshop, NASA Ames Research Center, May 2015.

[24] J. Melosh, *Planetary Surface Processes*. Cambridge University Press, 2011. 978-0-521-51418-7.

[25] D. Folta and D. Quinn, "Lunar frozen orbits," *AIAA/AAS Astrodynamics Specialist Conference and Exhibit*, August 2006. 10.2514/6.2006-6749.

[26] D. Folta, K. Galal, and D. Lozier, "Lunar prospector frozen orbit mission design," *AIAA*, 1998. 10.2514/6.1998-4288.

[27] G. H. Heiken, D. T. Vaniman, and B. M. French, *Lunar Sourcebook - A User's Guide to the Moon*. Cambridge University Press, 1991. 0-521–33444-6.

[28] K. F. Wakker, *Fundamentals of Astrodynamics*. Institutional Repository Delft University of Technology, 2015. 978-94-6186-419-2.

[29] Y. Jian-Guo, P. Jin-Song, L. Fei, and W. Wei, "Analyzing the character of lunar gravity field bylp165p model and its effect on lunar satellite orbit," *CHINESE JOURNAL OF GEOPHYSICS*, vol. 48, no. 2, pp. 348–355, 2006. 10.1002/cjg2.844/.

[30] E. C. Vilana, "Study of spacecraft orbits in the gravity field of the moon." http://upcommons.upc.edu/bitstream/handle/2099.1/15241/Memoria.pdf, January 2012. (last visited on December 21, 2016).

[31] "Gmat user guide." http://gmat.sourceforge.net/docs/R2016a/html/index.html, 2011-2016. (last visited on January 23, 2017).
[32] American Institute of Aeronautics and Astronautics, V.A. Chobotov, *Orbital Mechanics - Third Edition*. American Institute of Aeronautics and Astronautics, 2002. 1-56347-537-5.
[33] "Meteor shower calendar." http://www.amsmeteors.org/meteor-showers/meteor-shower-calendar/, July 2013-2017. (last visited on January 19, 2017).
[34] "Taosi observatory." http://www.phisicalpsience.com/public/Taosi_Observatory/Taosi_Observatory.html, June 2011-2016. (last visited on January 24, 2017).
[35] "Lro images." https://www.nasa.gov/mission_pages/LRO/multimedia/lroimages/lroc-20101027-highest.html, November 2010. (last visited on January 31, 2017).
[36] C. Brunt, B. van Dam, H. Frericks, A. Karagiannis, T. Koppenaal, B. Krijnen, M. Misin, P. Sengalrayan, A. Vandenberghe, J. Vanwesenbeeck, and J. Westenberger, "Moonsat, designing a cubesat system that contributes to lunar exploration, baseline report." Faculty of Aerospace Engineering, Delft University of Technology, November 2016.
[37] S. Bouley, D. Baratoux, J. Vaubaillion, A. Mocquet, M. L. Feuvre, F. Colas, Z. Benkhaldoun, A. Daassou, M. Sabil, and P. Lognonné, "Power and duration of impact flashes on the moon: Implication for the cause of radiation," *Elsevier*, 2012.
[38] A. Watts, "Unified theory of climate: Reply to comments," *watssupwiththat.com*, 2012.
[39] G. Matthews, "Celestial body irradiance determination from an underfilled satellite radiometer: application to albedo and thermal emission measurements of the moon using ceres," *Applied Optics*, vol. 47, Issue 27, pp. 4981–4993, 2008.
[40] "Cosmic infrared background radiation." http://www.astro.ucla.edu/~wright/CIBR/, October 2001. (last visited on Jan 23, 2017).
[41] D. Malacara, *Physical Optics and Light Measurements*. Academic Press, 1988. ISBN 9780124759718.
[42] Photovoltaic Education Network, "Energy of photon." http://www.pveducation.org/pvcdrom/2-properties-sunlight/energy-photon. (last visited on December 8, 2016).
[43] K. Janschek, V. Tchernykh, and S. Dublenko, "Integrated camera motion compensation by real-time image motion tracking and image deconvolution," *International Conference on Advanced INtelligent Mechantronics*, 2005.
[44] FLIR, "Flir tau swir datasheet." http://www.flir.com/uploadedFiles/OEM/Products/SWIR-Cameras/New-Tau-SWIR/FLIR-Tau-SWIR-SIC-200-Datasheet-EN.pdf, July 2016. (last visited on December 8, 2016).
[45] Edmund Optics, "Edmund optics ir lenses." http://www.edmundoptics.com/optics/optical-lenses/ir-lenses/. (last visited on December 2, 2016).
[46] R. D. Corsaroa, F. Giovane, Jer-Chyi, L. Mark, J. Burchell, M. J. Cole, E. G. Williams, N. Lagakos, A. Sadilek, and C. R. Anderson, "Characterization of space dust using acoustic impact detection," *The Journal of the Acoustical Soeciety of America*, May 2016.
[47] G. Ribay, S. Catheline, D. Clorennec, R. K. Ing, N. Quieffinand, and M. Fink, "Acoustic impact localization in plates: Properties and stability to temperature variation," *ieee transactions on ultrasonics, ferroelectrics, and frequency control*, February 2007.
[48] M. Ercegovac, T. Land, and J. H. Moreno, *Introduction to Digital Systems*. John Wiley & Sons Inc., 1999. 978-0-471-52799-2.
[49] L. Foschini, "Electromagnetic interference from plasmas generated in meteoroids impacts," *IOP Science*, March 1998.
[50] D. C. Giancoli, *Physics for Scientists & Engineers*, vol. 2. Pearson, 2008. 978-013-227559-0.
[51] "Grün interplanetary flux model." https://www.spenvis.oma.be/help/background/metdeb/metdeb.html, December 2026. (last visited on January 23, 2017).
[52] J. R. Wertz and W. J. Larson, *Space Mission Analysis and Design*. Kluwer Academic Publishers, 3rd ed., 2005. 1-881883-10-8.
[53] Cobham Gaisler, "Gr740 data sheet and user's manual." http://www.gaisler.com/doc/gr740/GR740-UM-DS.pdf, 2016. (last visited on December 15, 2016).
[54] T. Scholz, "Qb50 whole orbit data packet format," tech. rep., Von Karman Institute for Fluid Dynamics, 2013.
[55] A. D. Corporation, "Uhf patch antenna for space." http://www.antdevco.com/, 2014. (last visited on January 10, 2017).
[56] I. S. in Space, "Deployable uhf and vhf turnstile antenna." https://www.isispace.nl/brochures/, 2014. (last visited on January 11, 2017).
[57] P. P. Sundaramoorthy, "MoonSat Project Description (AE3-200 course)." Faculty of Aerospace Engineering, Delft University of Technology, 2016.
[58] D. Cavallo, "Lecture 09 – Guiding and Radiating: Antennas and Radiation(EE3-330 course)," tech. rep., Faculty of Aerospace Engineering, Delft University of Technology, 2015.
[59] A. Cervone, "Lecture 05. Spacecraft Telecommunications (AE2-111 course)." Faculty of Aerospace Engineering, Delft University of Technology, 2014.
[60] A. Cervone, "Lecture 04. Spacecraft Telecommunications (AE2-111 course)." Faculty of Aerospace Engineering, Delft University of Technology, 2014.
[61] J. R. Wertz, D. F. Everett, and J. J. Puschell, *Space Mission Engineering: The New SMAD*. Microcosm Press, 1st ed., 2011. 978-1-881-883-15-9.
[62] "Luna's (earth's moon) thermal environment." http://www.tak2000.com/data/planets/luna.htm, December 2008. (last visited on December 22, 2017).

[63] "Reaction wheels." http://bluecanyontech.com/portfolio-posts/reaction-wheels/, 2016. (last visited on November 29, 2016).

[64] "Vacco standard micropropulsion system." http://www.cubesat-propulsion.com/wp-content/uploads/2015/10/standard-micro-propulsion-system.pdf, 2016. (last visited on November 29, 2016).

[65] "Nanosatellite micropropulsion system." https://www.cubesatshop.com/product/nanosatellite-micropropulsion-system/, 2016. (last visited on November 29, 2016).

[66] NASA, "Measuring earth's albedo." http://earthobservatory.nasa.gov/IOTD/view.php?id=84499, 2014. (last visited on 14 December 2016).

[67] "nanossoc-a60." http://www.solar-mems.com/smt_pdf/Brochure_NanoSSOC-A60.pdf, 2016. (last visited on November 29, 2016).

[68] "Star tracker st400 and st200." https://www.berlin-space-tech.com/portfolio/star-tracker-st400-and-st200/, 2016. (last visited on November 29, 2016.

[69] M. D. Guman, D. C. Roth, R. Ionasescu, A. H. Taylor, and J. B. Jones, "Cassini orbit determination from first venus flyby to earth flyby," tech. rep., California Institute of Technology, January 2000.

[70] "Space engineering propulsion general requirements." http://everyspec.com/ESA/download.php?spec=ECSS-E-ST-35C_REV-1.048206.pdf. (last visited on January 19, 2017).

[71] R. P. Welle, "Propellant storage considerations for electric propulsion." http://erps.spacegrant.org/uploads/images/images/iepc_articledownload_1988-2007/1991index/IEPC1991-107.pdf, 2007. (last visited in January 19, 2017).

[72] Busek Co. Inc., "Bit 3.2 datasheet." http://www.busek.com/index_htm_files/70010819%20RevA%20Data%20Sheet%20for%20BIT-3%20Ion%20Thruster.pdf, 2014. (last visited on January 11, 2017).

[73] Busek Co. Inc., "Neutraliser datasheet." http://www.busek.com/index_htm_files/70008509B.pdf, 2014. (last visited on January 11, 2017).

[74] Busek Co. Inc., "Thrusters and neutralisers." http://www.busek.com/index.htm, 2016. (last visited on January 11, 2017).

[75] M. J. Patterson and S. W. Benson, "Next ion propulsion system development status and performance." https://www.grc.nasa.gov/www/ion/pdfdocs/AIAA-2007-5199.pdf, 2007. (last visited in January 18, 2017).

[76] D. M. Tsay, J. Frongillo, J. Model, J. Zwahlen, and L. Paritsky, "Flight development of iodine bit-3 rf ion propulsion system for sls em-1 cubesats." http://digitalcommons.usu.edu/cgi/viewcontent.cgi?article=3471&context=smallsat, 2016. (last visited on January 18, 2017).

[77] RE Smith, "Quick reference for rs485, rs422, rs232 and rs423." http://www.rs485.com/rs485spec.html, 2016. (last visited on January 25, 2017).

[78] M. M. Micci and A. D. Ketsdever, "Micropropulsion for small spacecraft," 2000.

[79] B. C. Inc., "Lunarcube: A deep space 6u cubesat with mission enabling ion propulsiontechnology." file:///C:/Users/Jorn/Downloads/AM%208.00%20-%20LunarCube-%20A%20Deep%20Space%206U%20CubeSat%20with%20Mission%20Enabling%20Ion%20Propulsion%20Technology.pdf, 2015. last visited January 31 2017.

[80] M. R. Patel, *Spacecraft Power Systems*. CRC Press, 2005. 0-8493-2786-5.

[81] T. L. Fifer, "Radiation effects on multi-junction solar cells," Master's thesis, Monterey, California. Naval Postgraduate School, December 2001.

[82] D. J. Flood and I. Weinberg, "Advanced solar cells for satellite power systems," tech. rep., NASA - Lewis Research Center, Cleveland, Ohio, Nov 1994.

[83] C. Fetzer, B. Jun, K. Edmondson, S. Khemthong, K. Rouhani, R. Cravens, R. Bardfield, and M. Gillanders, "Production ready 30% efficient triple junction space solar cells," 2008.

[84] "11. solar array performance." ftp://cdsarc.u-strasbg.fr/ftp/more/HIP/cdroms/docs/vol2/ch11.pdf. (last visited on December 23, 2016).

[85] R. R. King, C. M. Fetzer, D. C. Law, K. M. Edmondson, H. Yoon, G. S. Kinsey, D. D. Krut, J. H. Ermer, P. Hebert, B. T. Cavicchi, and N. H. Karam, "Advanced iii-v multijunction cells for space," May 2006.

[86] S. Kasap and P. Capper, *Springer Handbook of Electronic and Photonic Materials*. Springer Science, 2006. 0-387-26059-5.

[87] M. A. Green, K. Emery, Y. Hishikawa, W. Warta, and E. D. Dunlop, "Solar cell efficiency tables (version 45)," *Progress in Photovoltaics: Research and Applications*, vol. 23 No. 1, December 2014.

[88] G. A. L. James R. Woodyard, "Radiation resistance of thin-film solar cells for space photovoltaic power," tech. rep., NASA Technical Memorandum 103715, Jan 1991.

[89] I. Weinberg and D. J. Brinker, "Progress in inp solar cell research," tech. rep., NASA Technical Memorandum 100914, August 1988.

[90] A. Shah, *Thin film silicon solar cells*. EPFL Press, 2010. 978-2-940222-036-0.

[91] "Cadmium telluride." https://www.energy.gov/eere/sunshot/cadmium-telluride. (last visited on January 20, 2017).

[92] K. S. Jefferies, "Analysis of costs of gallium arsenide and silicon solar arrays for space power applications," tech. rep., NASA Technical Paper 1811, March 1981.

[93] "Copper indium gallium selenide (cuingase2) semiconductors." http://www.azom.com/article.aspx?ArticleID=8493, Aug 2013. (last visited on January 20, 2017).

[94] C. Kittel, *Introduction to Solid State Physics*. New York:John Wiley, 1986. 6th Edition.

[95] J. Ayre, "New cigs solar cell record." https://cleantechnica.com/2014/09/27/new-cigs-solar-cell-record-21-7-cigs-cell-conversion-efficiency-achieved-zsw/, Sept 2014. (last visited on January 21, 2017).
[96] T. S. Shirou Kawakita, Mitsuru Imaizumi, "Super radiation tolerance of cigs solar cells demonstrated in space by mds-1 satellite." http://ieeexplore.ieee.org/document/1305376/, May 2003.
[97] "Space products: faq." http://www.spectrolab.com/faqs-space.htm, 2009. (last visited on January 12, 2017).
[98] "30% triple junction gaas solar cell type: Tj solar cell 3g30c - advanced." http://www.azurspace.com/index.php/en/products/products-space/space-solar-cells, Aug 2016. (last visited on January 23, 2017).
[99] "26.8% improved triple junction (itj) solar cells." http://www.spectrolab.com/solarcells.htm, Apr 2008.
[100] "28.3% ultra triple junction (utj) solar cells." http://www.spectrolab.com/solarcells.htm, Oct 2010.
[101] "29.5% next triple junction (xtj) solar cells." http://www.spectrolab.com/solarcells.htm, Sep 2012.
[102] F. Santoni, F. Piergentili, G. P. Candini, and M. Marino, "An orientable solar panel system for nanospacecraft," *Acta Astronautica*, vol. 101, pp. 120–128, 2014.
[103] F. Santoni, F. Piergentili, S. Donati, and M. Marino, "An innovative deployable solar panel system for cubesats," *Acta Astronautica*, vol. 95, pp. 210–217, 2014.
[104] "What's the best battery." http://batteryuniversity.com/learn/archive/whats_the_best_battery.
[105] C. Brunt, B. van Dam, H. Frericks, A. Karagiannis, T. Koppenaal, B. Krijnen, M. Misin, P. Sengalrayan, A. Vandenberghe, J. Vanwesenbeeck, and J. Westenberger, "Lumid, conceptualisation of the lunar micrometeoroid impact detector." Faculty of Aerospace Engineering, Delft University of Technology, December 2016.
[106] M. W. Lund, "Nimh battery charging basics." http://www.powerstream.com/NiMH.htm.
[107] S. B. Peterson, J. Apt, and J. Whitacre, "Lithium-ion battery cell degradation resulting from realistic vehicle and vehicle-to-grid utilization," *Journal of Power Sources*, vol. 195, pp. 2385–2392, 2009.
[108] "Isis cubesat structures brochure." https://www.cubesatshop.com/wp-content/uploads/2016/06/ISIS_CubeSat-Structures_Brochure_v.7.11.pdf, July 2011. (last visited on December 5, 2016).
[109] ISIS, "QuadPack CubeSat deployer." https://www.isispace.nl/product/quadpack-cubesat-deployer/, August 2016. (last visited on December 9, 2016).
[110] "Proton launch system mission planner's guide." http://www.ilslaunch.com/sites/default/files/pdf/Proton%20Mission%20Planner%27s%20Guide%20Revision%207%20%28LKEB-9812-1990%29.pdf, October 2009.
[111] S. Vadawale, J. Goswami, T. Dachev, B. Tomov, and V. Girish, "Radiation environment in earth-moon space: Results from radom experiment onboard chandrayaan-1," in *Advances in Geosciences, Planetary Science (PS). Vol. 25. Edited by Anil Bhardwaj. Singapore: World Scientific, 2011, p. 121*, vol. 25, p. 121, 2011.
[112] "Ansys workbench verification manual." 148.204.81.206/Ansys/150/ANSYS%20Workbench%20Verification%20Manual.pdf, 2016. (last visited on January 19, 2017).
[113] "Emc and thermal analysis." http://www.space.aau.dk/cubesat/documents/psu/Chapter5.pdf.
[114] "Emc and thermal analysis." http://cooltechnologiesinc.com/thermal-dispersion/heat-pipes/.
[115] "Autonomous star trackers: A-str and aa-str," 2016. MM07786.
[116] VACCO, "Polar micro propulsion system.." http://www.cubesat-propulsion.com/palomar-micro-propulsion-system/. (last visited on January 18, 2017).
[117] "Sitael obdh," 2015.
[118] B. T. C. Zandbergen, "Aerospace Design & Systems Engineering Elements I (AE1-222 course)." Faculty of Aerospace Engineering, Delft University of Technology, November 2015.
[119] J. H. Hemmer, "Solar absorptance and thermal emittance of some common thermal-control spacecraft coatings." https://ntrs.nasa.gov/archive/nasa/casi.ntrs.nasa.gov/19840015630.pdf, April 1984.
[120] "Lunar ecipses: 2021-2030." https://eclipse.gsfc.nasa.gov/LEdecade/LEdecade2021.html, December 2013. (last visited on January 22, 2017).
[121] T. Connectivity, "Te sensors solutions." http://www.te.com/content/dam/te-com/documents/sensors/global/SSTSTE100/TE-SensorSolutions_SS-TS-TE100.pdf, November 2015. (last visited on January 22, 2017).
[122] R. J. Hamann and M. J. L. van Tooren, "Systems Engineering & Technical Management Techniques (AE3-S01 course)." Faculty of Aerospace Engineering, Delft University of Technology, January 2006.
[123] SpaceWorks, "Nano/microsatellite market forecast." http://spaceworksforecast.com/docs/SpaceWorks_Nano_Microsatellite_Market_Forecast_2016.pdf, 2016. (last visited on January 18, 2017).
[124] ESA, "Lunar exploration objectives and requirements definition," 2010. (last visited on January 18, 2017).
[125] Technavio, "Three trends influencing market growth for nano and micro satellites." http://www.technavio.com/blog/three-trends-influencing-market-growth-for-nano-and-microsatellites, 2015.
[126] J. Rotteveel, A. Bonnema, and J. Hennequin, "Nano-profitability-a review of the financial success of nanosattelite industrial companies," *Conference on Small Satellites*, 2016.
[127] "Cubesatsearch." https://www.cubesatshop.com/. (last visited on January 25, 2017).
[128] J. Colen, "Areas of ames ingenuity: Low-cost missions." https://www.nasa.gov/centers/ames/research/area-low-cost-missions.html. Page Last Updated: July 31, 2015.
[129] L. David, "China's 1st moon lander may cause trouble for nasa lunar dust mission," 2013.
[130] S. Group and W. G. 4, "IADC space debris mitigation guidelines," tech. rep., Inter-Agency Space Debris Coordination Committee, September 2007.
[131] *ECSS-M-30A*. ESA–ESTEC Requirements & Standards Division, ESA Publications Division, 19 April 1996.
[132] J. P. Womack and D. T. Jones, *Lean Thinking*. Free Press, 2003. 0-7432-4927-5.

APPENDIX A

Large Tables

Table A.1: Mission requirements and constraints.

Identifier	Requirement
R-MI-L-1	The mission shall reach space using an already existing launching system
R-MI-TR-1	The s/c shall be transferred to its initial lunar orbit in a piggyback to a larger Lunar Orbiter.
R-MI-LO-1	Upon deployment from the mothership, the s/c shall acquire the initial orbit by virtue of their own propulsion system.
R-MI-SM-1	The mission shall produce measurements of the impact flux of micrometeoroids in the mass range of 1 mg to 1 g.
R-MI-EOL-1	Upon completion of the mission, the s/c shall perform a controlled impact.
R-MI-LT-1	Spacecraft lifetime shall be greater than two years
R-MI-EOL-2	Spacecraft shall not pollute the lunar environment with hazardous substances in case of an end-of-mission impact (hazardous as defined by the ESA Safety Standards).
C-T-L-1	In case a distributed-system concept is used, the total mass for all s/c units shall not exceed 60 kg, excluding their initial orbit deployment systems.
C-T-L-2	Each s/c injected by the Lunar Orbiter shall have a mass that does not exceeds 24 kg, excluding deployment system.
C-T-L-3	Each small spacecraft injected by the Lunar Orbiter shall have dimensions up to, and including, 12U CubeSat® form factor or custom form factor with equivalent volume.
C-T-MI-1	The s/c shall be inserted into a lunar orbit by the Lunar Orbiter providing transportation and data relay services.
C-T-MI-2	The s/c shall be injected into an orbit at an orbit inclination between 50-90 deg.
C-T-MI-3	The s/c shall be injected into a circular orbit with an altitude of at least 500 km.
C-T-SC-TTC-1	The s/c shall be able to survive for 10 days in the lunar vicinity without contact with the Lunar Orbiter.
C-T-SC-TTC-2	The s/c shall provide its own on-board communication subsystem or use an optional UHF transponder card furnished by the lunar data relay service provider.
C-T-SC-TTC-5	The s/c shall not turn on its transmitter(s) for 10 minutes after deployment.
C-T-SC-TTC-6	Each s/c shall receive equal contact time.
C-T-SC-TTC-7	The s/c shall use the CCSDS proximity-1 protocol at UHF frequencies as per Recommendation SFCG 32-2R1 (390-405 MHz TC and 435-450 MHz TM) for communications with the Lunar Orbiter.
C-T-SC-TTC-8	The capability of the UHF link to support ranging shall be .
C-T-SC-P-1	Each s/c shall procure its own deployment system that shall be mounted externally on the Lunar Orbiter during the 1 month transfer from launch to the lunar injection orbit.
C-T-SC-P-2	The s/c shall have a 5V power interface during stowed condition for battery charging and flight software update.

C-T-SC-P-3	The s/c shall have a CAN/UART (TBC) data interface during stowed condition for battery charging and flight software update.
C-T-SC-TC-1	The s/c shall be able to survive temperatures ranging between -40°C and +65°C during stowage in the Lunar Orbiter.
C-SH-1	The s/c shall be available for launch by.
C-SH-2	The s/c shall be in position to initiate the mission no later than .
C-L-1	All aspects of the entire mission development and execution shall adhere to the European and International law.
C-L-2	All aspects of the entire mission development and execution shall adhere to the regulations posed by the ECSS.
C-RS-ST	All aspects of the entire mission development and execution shall adhere to the European Space Agency's safety regulations.
C-SD-1	The mission shall comply to the European Space Agency's policy for sustainable development.
C-SD-2	The mission shall have no impact to the Lunar environment other than non-hazardous debris on a area on the ground after the end of life.
C-PROD-1	The s/c hardware shall use off-the-shelf components in the cases when this option exists.
C-PROD-2	The s/c hardware shall be producible with already existing manufacturing equipment.
C-PROD-3	All production-related aspects of the mission's hardware shall adhere to the constraints posed by ESA and the ECSS.

Table A.2: Deployment variation

Inclination [°]	Δv **over 2 months**	**Difference in total Δv with respect to 50° inclination over 2 years**	**Is an inclination change manoeuvre desired**
45	37,889	54,625	
46	36,376	36,467	
47	36,414	36,923	possibly
48	34,871	18,409	yes
49	32,139	-14,376	yes
50	33,337	0,000	
51	32,087	-14,998	yes
52	33,167	-2,033	yes
53	31,957	-16,559	possibly
54	35,525	26,261	possibly
55	32,866	-5,651	
56	32,892	-5,336	
57	33,220	-1,400	
58	34,089	9,023	
59	33,814	5,731	
60	35,640	27,640	
61	36,338	36,017	
62	35,510	26,075	
63	36,522	38,227	
64	37,122	45,428	
65	44,621	135,407	yes
66	39,333	71,954	
67	44,987	139,798	yes
68	42,430	109,122	
69	52,470	229,601	
70	52,640	231,644	
71	59,817	317,768	
72	63,146	357,708	
73	64,940	379,236	
74	67,252	406,980	
75	67,416	408,954	
76	66,432	397,148	
77	65,341	384,049	
78	64,044	368,482	
79	59,622	315,422	
80	58,079	296,904	
81	54,004	248,009	
82	52,355	228,221	
83	46,624	159,442	yes
84	42,842	114,064	yes
85	36,574	38,852	
86	34,529	14,306	
87	30,923	-28,960	
88	29,275	-48,739	
89	24,798	-102,468	
90	27,447	-70,674	

APPENDIX B

Individual Contribution Table

Table B.1: Individual contribution table

Name	**Contributions**
C.C. Brunt	Ch. 3, sole author: Subsecs. 3.3.2, 3.3.4, 3.4.4
B. van Dam	Secs. 10.1, 10.3, 10.4, Subsecs. 10.2.1, 10.2.2, 11.2.4, fig 14.1
H. Frericks	Ch. 8, Sec. 13.4
A. Karagiannis	Sole author: Summary, Chs. 1, 2, 15; Partly: Secs. 3.1, 3.2
T. Koppenaal	All flow diagrams, Ch. 4, Subsecs. 10.2.2, 10.2.3, Secs. 13.2, 13.5
B. Krijnen	3, sole author: Subsecs. 3.3.1, 3.3.3
M. Misin	Ch. 7, Subsecs. 9.2.1, 13.6.7
P.S. Sengalrayan	Preface, Ch. 12, Ch. 14: Secs. 14.1, 14.2
A.F. Vandenberghe	Ch. 6 (all but subsystem description), Ch. 11, Secs. 13.3, 13.7, 14.3
J. Vanwesenbeeck	Ch. 9, Secs. 6.1, 13.6, List of Symbols, List of Abbreviations, Subsec. 7.2.1,
J.M. Westenberger	Ch. 5